

NMR Characterization of Pathological Disease States: Monitoring Response to Single-Dose Radiotherapy in a RIF-1 Tumor Model and the Role of Spreading Depression in the Evolution of Ischemic Stroke

A dissertation submitted to the faculty of
Worcester Polytechnic Institute and University of Massachusetts Medical School
in partial fulfillment of the requirements for the degree of
Doctor of Philosophy in Biomedical Engineering and Medical Physics

By

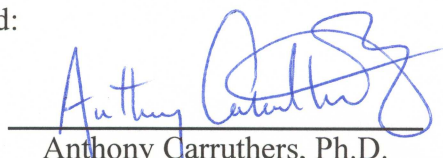

Erica C. Henning

May 2005

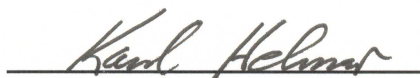
Approved:



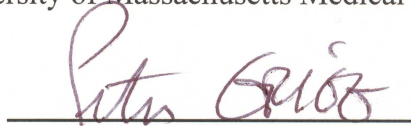
Christopher H. Sotak, Ph.D.
Professor and Head, Major Advisor
Biomedical Engineering Department
Worcester Polytechnic Institute



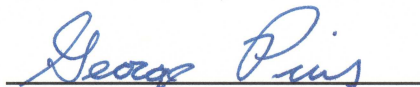
Anthony Carruthers, Ph.D.
Dean, Graduate School of Biomedical Sciences
Professor, Department of Biochemistry and
Molecular Pharmacology
University of Massachusetts Medical School



Karl G. Helmer, Ph.D.
Research Assistant Professor
Biomedical Engineering Department
Worcester Polytechnic Institute



Peter Grigg, Ph.D.
Professor, Committee Chair
Department of Physiology
University of Massachusetts Medical School



George D. Pins, Ph.D.
Assistant Professor
Biomedical Engineering Department
Worcester Polytechnic Institute



Chieko Azuma, BVSc, Ph.D.
Assistant Professor
Department of Clinical Sciences
Tufts University School of Veterinary Medicine

ACKNOWLEDGEMENTS

I would like to thank my major advisor, Chris Sotak, who has given me the opportunity to grow and expand as a researcher within the field of MR. Chris, I am humbled by your wealth of knowledge, as well as the prestige you have attained in both research and academia. I feel very lucky to have made a contribution to your work in the areas of stroke and cancer. Thank you so much for your support and guidance over the past five years. You have served not only as a mentor, but also as a colleague and a friend.

I would like to thank Karl Helmer, who has also provided me the opportunity for development as a researcher within the field of MR. Karl, our conversations, whether about the intricacies of MR and its various applications, or simply about whether I was doing well, kept me motivated during my time here. I am happy to have been able to contribute to your work in MR and its applications to oncology. Thank you for your guidance and friendship.

I would like to thank George Pins for his collaboration on the RIF-1 project. George, thank you for allowing me access to the personnel and resources of your laboratory. Thanks to you, as well your graduate students (Brett, Kevin, and Katie), for help in optimizing the histological protocol. Brett and Kevin, thank you for your energy and enthusiasm—it kept me motivated during the labor-intensive processing of my histology.

I would like to thank Chieko Azuma for her collaboration on the RIF-1 project. Chieko, thank you for allowing me access to the radiation therapy personnel and resources through Tufts. Without your participation, this research would not have been successful.

I would like to thank Marc Fisher for surrounding the NMR group with superior personnel and resources contributing to the stroke research. Specific thanks to Xiangjun Meng and James Bouley. Xiangjun's and Jamie's knowledge of the animal model and their surgical ability permitted a joint effort for the work on cortical spreading depression. Thank you for teaching me the surgical techniques required. In addition to their skills as

scientists, I am happy to call Xiangjun and Jamie my friends. I wish them both continued success.

I would like to thank Matthew Silva and Jeremy Wellen for their camaraderie. Although I broke the laboratory trend of being the oldest sibling in ones family and hating tomatoes (I am the youngest and love tomatoes), Matt and Jeremy accepted me without reservation. Matt and Jeremy, thank you both for your guidance in the laboratory, for answering my endless questions, and most of all, for your friendship. Having both of you in the lab kept things fun and interesting, a nice respite from experiments and data analysis. I look forward to working with you in the future. Additional thanks to Deirdre and Dave for entertaining conversations, and Dave, for his collaborative efforts on the optimization of BBB-opening experiments.

Finally, I would like to thank my parents and my brother for their continued love and support. Without them I would not be where I am today. Thank you for listening to my frustrations through failure, and joy from accomplishment that came throughout this whole process. I appreciate everything you have done for me, thank you from the bottom of my heart.

TABLE OF CONTENTS

Abstract	vi
1 Principles of Nuclear Magnetic Resonance	
1.1 Introduction	1
1.1.1 Magnetic Resonance Imaging: A Historical Introduction	1
1.2 Basic Physical Principles	2
1.2.1 Electromagnetic Theory	2
1.2.2 Nuclear Angular Momentum	4
1.2.3 Nuclear Magnetic Dipole Moment	4
1.2.4 Directional Dependence of μ and p	5
1.2.5 Nuclear Energy States	7
1.2.6 Motion of Magnetic Dipole Moments	9
1.2.7 Free Induction Decay	13
1.3 Relaxation Processes	15
1.3.1 Spin-Lattice (T_1) Relaxation	16
1.3.2 Spin-Spin (T_2) Relaxation	19
1.3.3 Relaxation Mechanisms and Generation of Tissue Contrast	21
1.4 Magnetic Resonance Imaging	27
1.4.1 Underlying Signal Composition: Phase, Frequency, and Amplitude	27
1.4.2 Slice Selection and Slice Offset	29
1.4.3 Frequency-Encoding and Phase-Encoding	32
1.4.4 Rephasing Gradients	35
1.4.5 Signal Processing: Conversion Between K-Space and Image Space	36
1.5 Imaging Methods	39
1.5.1 Spin-Echo (SE) Imaging	39
1.5.2 Gradient-Echo (GE) Imaging	42
1.5.3 Echo-Planar Imaging (EPI)	43
1.5.4 Diffusion-Weighted Imaging	47
1.5.5 Dynamic Contrast-Enhanced Perfusion Imaging	52
References	53
2 History of Cancer: Progression and Prognosis	
2.1 Background	55
2.1.1 Pathophysiology of Cancer Progression	55
2.1.2 Tissue Hypoxia and the Formation of Necrosis	58
2.1.3 Apoptotic Cell Death	58
2.1.4 Necrosis and Apoptosis	60
2.2 Current Therapeutic Targets	62
2.2.1 Radiotherapy	62
2.2.2 Chemotherapy	63
2.2.3 Anti-angiogenic Therapy	64

2.2.4	Gene-specific Therapy	64
2.3	Current MRI Methods	65
2.3.1	Diffusion-weighted Imaging	65
2.3.2	Dynamic Contrast-Enhanced (DCE) MRI	66
2.3.3	Metabolic Imaging	67
	References	68
3	Multispectral Quantification of Tissue Types in a RIF-1 Tumor Model with Histological Validation	
	Abstract	74
3.1	Introduction	75
3.1.1	Tumor Heterogeneity	75
3.1.2	Tumor Tissue Characterization with DWI	77
3.1.3	Limitations of a Single Parameter Approach	80
3.1.4	Multispectral Tissue Characterization	81
3.1.5	MS Analysis with Histological Validation	82
3.2	Methods	83
3.2.1	Animal Preparation	83
3.2.2	Radiotherapy	84
3.2.3	MRI Measurements	85
3.2.4	Data Analysis	87
3.2.5	K-means Clustering	88
3.2.6	Histological Analysis	89
3.2.7	Statistical Analysis	91
3.3	Results	92
3.3.1	Optimization of KM Method	92
3.3.2	KM Segmentation Results	95
3.3.3	Correlation with Histology	98
3.3.4	Temporal Evolution of KM Volume	104
3.4	Discussion	106
3.4.1	Determination of Optimum KM Method	106
3.4.2	KM Delineation Between Viable Tissue and Necrosis	107
3.4.3	KM Identification of Hypoxic Tissue	108
3.4.4	Temporal Evolution of KM Volume	110
3.4.5	Utility of the KM Method	110
	Acknowledgements	111
	References	111
4	Multispectral Tissue Characterization in a RIF-1 Tumor Model: Monitoring Response to Single-Dose (1000cGy) Radiotherapy	
	Abstract	118
4.1	Introduction	120
4.1.1	DWI Assessment of Treatment Response	120
4.1.2	Multispectral Tissue Characterization	122
4.1.3	Tumor Growth Kinetics	123
4.1.4	Monitoring Response to Radiotherapy	124

4.2	Methods	125
4.2.1	Animal Preparation	125
4.2.2	Radiotherapy	125
4.2.3	MRI Measurements	126
4.2.4	Data Analysis	127
4.2.5	K-means Clustering	127
4.2.6	Kinetic Modeling	128
4.2.7	Histological Analysis	128
4.2.8	Statistical Analysis	131
4.3	Results	131
4.3.1	KM Segmentation Results	131
4.3.2	Results: Control Group (Untreated)	136
4.3.3	Results: Radiotherapy Group (Treated)	136
4.3.4	Tumor Growth Kinetics (Control vs. Radiotherapy)	140
4.3.5	KM Volume and Treatment Response: TGD and Cell Kill	142
4.3.6	KM Volume and Treatment Response: Evolution of ADC and T ₂	144
4.4	Discussion	146
4.4.1	KM Segmentation Results	146
4.4.2	KM Results: Control versus Radiotherapy	146
4.4.3	KM Contributions to TGD and Cell Kill	148
4.4.4	Underlying Contributions to the ADC Response	149
4.4.5	Utility of the KM Method	149
	Acknowledgements	150
	References	150
5	History of Cerebral Ischemia: Evolution and Outcome	
5.1	Background	153
5.1.1	Healthy versus Ischemic Brain Tissue	153
5.1.2	Viability Thresholds in Cerebral Ischemia	154
5.1.3	Tissue Characterization: Core and Penumbra	156
5.2	Current Therapeutic Targets	157
5.2.1	Recombinant Tissue Plasminogen Activator (rt-PA) Therapy	157
5.2.2	Neuroprotective Therapy	157
5.2.3	Anti-inflammatory Agents	159
5.3	Current MRI Methods	160
5.3.1	Diffusion-weighted Imaging	160
5.3.2	Perfusion-weighted Imaging	161
5.3.3	Metabolic Imaging	162
	References	162
6	Visualization of Experimental Cortical Spreading Depression (CSD) Using Manganese-Enhanced MRI (MEMRI)	
	Abstract	167
6.1	Introduction	168
6.1.1	Pathophysiology of Cortical Spreading Depression	168
6.1.2	Role of CSD in Neurological Disorders	169

6.1.3	MRI of Experimental CSD	169
6.1.4	Manganese as a Paramagnetic Calcium Analog	172
6.2	Methods	174
6.2.1	Animal Preparation	174
6.2.2	MnCl ₂ Administration	174
6.2.3	Glutamate Administration	175
6.2.4	Experimental Cortical Spreading Depression	175
6.2.5	MRI Measurements	177
6.2.6	Data Analysis	177
6.3	Results	179
6.3.1	MEMRI Enhanced Regions	179
6.3.2	Quantitative Summary	181
6.4	Discussion	182
6.4.1	Cellular Uptake of Manganese	182
6.4.2	Validation of Method	183
6.4.3	Derivation of Activation Scheme	185
6.4.4	MEMRI Integration Effect	185
6.4.5	Role of Apical Dendrites	187
6.4.6	Cortical-Subcortical Neuronal Connectivity	189
6.4.7	MEMRI or DWI?	194
	Acknowledgements	195
	References	195
7	Manganese-Enhanced MRI (MEMRI) of Cerebral Ischemia: Role of Peri-Infarct Depolarizations (PIDs) in the Progression to Infarct	
	Abstract	198
7.1	Introduction	199
7.1.1	Peri-Infarct Depolarizations	199
7.1.2	Role of PIDs in Cerebral Ischemia	200
7.1.3	MRI Identification of PIDs	200
7.1.4	Manganese as a Paramagnetic Calcium Analog	204
7.2	Methods	207
7.2.1	Animal Preparation	207
7.2.2	Optimization of BBB Opening	207
7.2.3	MCAO Procedure	208
7.2.4	MRI Measurements	210
7.2.5	Data Analysis	211
7.2.6	Tissue Characterization	213
7.3	Results	214
7.3.1	Optimization of BBB Opening	214
7.3.2	Temporal Evolution of Ischemia	217
7.3.3	MEMRI and Ischemia	222
7.4	Discussion	224
7.4.1	Cellular Uptake of Manganese	224
7.4.2	Heterogeneity of BBB Opening	225
7.4.3	Temporal Evolution of Ischemia	227

7.4.4	MEMRI and Ischemia	227
7.4.5	Utility of MEMRI for PID Identification	228
	Acknowledgements	229
	References	229
8	Summary	233
Appendix		
	Curriculum Vitae	
	Publications and Selected Conference Proceedings	

ABSTRACT

Part 1: Monitoring Response to Single-Dose (1000cGy) Radiotherapy in a RIF-1 Tumor Model

The current standard of measure for monitoring chemotherapeutic and radiotherapeutic treatment response is tumor volume. Unfortunately, changes in tumor volume are generally slow and tumor volume does not necessarily indicate the degree of tumor viability. The development of marker(s) with the ability to detect an early therapeutic response would greatly aid in patient management, opening the possibility for both rapid dose optimization and replacement of ineffective therapies with alternative treatment. Previous studies have shown that diffusion measurements using magnetic resonance imaging (MRI) techniques are sensitive to therapy-induced changes in cellular structure, allowing demarcation between regions of necrosis and viable tumor tissue. This sensitivity, based on the correlation between water apparent diffusion coefficient (ADC) values and tumor cellular density, may allow diffusion measurements to be employed in non-invasive monitoring of treatment response. Therapy-induced increases in tumor ADC preceding tumor regression have been reported in a variety of experimental tumor models and several human brain tumors. Despite the demonstrated diffusion sensitivity to therapeutic response in these particular studies, shortcomings still remain that hinder the efficacy of clinical application in oncology. Earlier studies have concentrated on the mean ADC present within the tumor, either within the entire tumor volume or a region-of-interest (ROI) defined by the user, and their evolution pre-treatment and post-treatment. Because of inter- and intra-tumor heterogeneity, volume-averaged ADC measurements suffer from poor correlation with treatment efficacy. In addition, most studies make little or no attempt to characterize the entire tumor volume (necrotic, viable, edema). The identification of regions of differing tissue viability should aid in the staging of treatment, therefore making accurate and reproducible tissue segmentation an important goal.

The results of earlier, single-parameter studies indicate that a multi-parametric approach in which several MR parameters are monitored (ADC, T_2 , M_0) may provide greater power than that of the single parameter approach. A multi-parametric or multi-spectral (MS) analysis uses pattern-recognition techniques, such as clustering, for image segmentation. Clustering algorithms use characteristics of the multiple MR-parameter dataset to group tissue of similar type, e.g., fat, muscle, viable tumor, necrosis. Specifically, k-means (KM) is an unsupervised segmentation algorithm that groups together similar tissue based on the difference in MR parameter space between the image voxel of interest and the mean parameter values of the voxels in that cluster. In the first step of the classification algorithm, it is applied to separate the data into two clusters ($k = 2$), tissue and background noise voxels. All voxels classified as background noise are set to zero and removed from further processing. In the second step, KM is applied to the remaining tissue voxels to segment the data into multiple tissue types. In the case of tumors, it is not clear in advance how many different types of tissue exist. The number of clusters, k , should be varied to ensure that all relationships between tissues are found. In the final step, the resulting KM maps may be compared to histological slices taken from the same tissue as the imaging slices in order to identify the tissue type of each cluster.

In line with the studies and analyses described above, quantitative MRI was performed to investigate the spatial correlation between ADC, spin-spin (T_2) relaxation times, and proton density (M_0) in murine radiation-induced fibrosarcoma (RIF-1) tumors following single-dose (1000cGy) radiotherapy using the KM algorithm (Chapters 3 and 4) and different combinations of features and/or clusters. For all cluster/feature combinations, an in-depth comparison between KM-derived volume estimates and conventional histology via the hematoxylin-eosin (H&E) staining procedure (for identification of viable tumor versus necrosis), as well as via hypoxic-inducible factor-1 α (HIF-1 α) immunohistochemistry (for identification of regions of hypoxia versus well-oxygenated tissue) was performed (Chapter 3). The optimal cluster/feature combination was determined by minimizing the sum-of-squared-differences (SSD) between the actual datapoints and the ideal one-to-one correlation that should exist between KM-derived volume estimates and histology-derived volume estimates. The optimal cluster/feature

combination was determined to be a 2-feature (ADC, T_2) and 4-cluster (2 regions each of viable tissue and necrosis) segmentation. This KM method was then applied in analysis of the radiotherapeutic response: first, to gain insight into the various processes whose combination yield the total ADC response over time; second, to identify the contribution of tissue heterogeneity to the treatment response and changes in tumor growth kinetics and cell kill (Chapter 4). Comparisons between control and various time-points out to 14 days post-radiotherapy permitted more accurate tissue characterization and prediction of therapeutic outcome over analysis using ADC alone.

The results based on histological validation demonstrated: (1) MS analysis provides an improved tissue segmentation method over results obtained from conventional methods employing ADC alone; (2) MS analysis permits subdivision based on the degree of necrosis, as well as delineation between well-oxygenated and hypoxic viable tissue; and (3) Individual KM volumes corresponded well with both H&E volumes and regions with increased HIF-1 α expression. The results based on the radiotherapeutic response demonstrated: (1) MS analysis provides a method for monitoring the range of tissue viability as a function of time post-treatment; (2) MS analysis permits assessment of the various contributions to the total ADC response post-treatment; (3) The relative fractions of well-oxygenated (i.e., radiosensitive) versus hypoxic (i.e., radioresistant) tissue pre-treatment may be predictive of treatment response; and (4) The early ADC increase did not seem to be a result of radiation-induced vasogenic edema, but instead was most likely due to a slight reduction in cellular density following therapy. These studies provide a non-invasive method of tissue characterization that may be used in monitoring treatment response and optimizing drug dose-timing schemes, with the potential for predicting treatment efficacy.

Part 2: Role of Spreading Depression in Ischemic Stroke

Stroke is a prevalent disease that ranks as the 3rd leading cause of death and disability in the United States, according to NIH statistics, costing millions of dollars in medical costs and lost wages. At present, the mechanism by which focal ischemia evolves into infarction remains poorly understood. By determining the patho-physiological

mechanisms involved in the evolution of focal brain ischemia, therapeutic strategies may be designed for instances of acute ischemic stroke. In the late 1980s, researchers discovered MRI techniques that allow the detection of stroke very early after onset. Such techniques as diffusion-weighted imaging and perfusion-weighted imaging (DWI and PWI) have been applied both clinically and experimentally. Previous studies employing these techniques suggest that cortical spreading depression plays a detrimental role in the evolution of focal brain ischemia. Spreading depression (SD) is characterized by a spontaneous and reversible depression of cortical electrical activity that spreads from the site of onset as a wave with a speed of 2-5 mm/min. It is accompanied by an ionic redistribution, with efflux of potassium ions (K^+) and influx of sodium, chloride, and calcium (Na^+ , Cl^- , Ca^{2+}) ions, as well as water. This results in cellular swelling and a decreased extracellular space (ES), yielding a decline in ADC. A positive correlation between the number of both spontaneous and induced SDs and infarct volume has well been documented, supporting the idea that SD inhibition might be neuroprotective if initiated early after ischemic onset.

Even though these studies show promise in their ability to track SD using diffusion mapping, changes in ADCs reflect cytotoxic edema and do not necessarily correspond to SD or SD-like depolarizations or calcium (Ca^{2+}) influx, leading to cell death. Recent studies have reported the use of manganese ions (Mn^{2+}) as a depolarization-dependent contrast agent in monitoring brain activation through the application of glutamate, as well as in the study focal ischemia. Since extracellular accumulation of potassium (K^+) ions or glutamate in ischemic tissue is believed to play a central role in the initiation and propagation of SDs, and knowing that Mn^{2+} , having an ionic radius similar to that of Ca^{2+} , is handled in a manner similar to Ca^{2+} , these studies suggest the possible use of manganese ions (Mn^{2+}) in tracking SD or SD-like depolarizations in the evolution of focal brain ischemia.

In order to determine the utility of Mn^{2+} as a marker for SD, two sets of T_1 -weighted MRI experiments were performed before applying Mn^{2+} in an experimental stroke model (Chapter 6). First, for verification purposes, a glutamate administration group was

evaluated to validate our use of the manganese-enhanced MRI (MEMRI) method previously developed by Aoki *et al*, a modification of the original by Lin and Koretsky. When satisfied that the contrast enhancement was specific to glutamate only, a second set of experiments was performed. Here, experimental SD was elicited by chemical stimulation (direct application of concentrated potassium chloride [KCl] on the exposed cortical surface) and compared with control conditions (perfusion of sodium chloride [NaCl] on exposed brain cortex). This study demonstrated: (1) Mn^{2+} , specific to Ca^{2+} channel activity, is a more accurate marker for SD than DWI or T_2^* methods; (2) Cortical restriction of MEMRI enhancement supports the contention that apical dendrites are necessary for SD propagation; (3) Subcortical enhancement is a result of cortical-subcortical neuronal connectivity; and (4) Because of the relatively slow clearance of Mn^{2+} , MEMRI permits higher spatial resolution and signal-to-noise ratios (SNRs) via increased signal averaging. Based on these results, preliminary experiments involving the study of SD in focal ischemia using Mn^{2+} were performed (Chapter 7). Initial results indicate: (1) MEMRI of ischemia, when compared with standard DWI/PWI methods, may provide a method for estimating the likelihood of progression to infarct at acute time points post onset of stroke. These studies provide a foundation for further investigation into the role of SD in stroke, and the application of Mn^{2+} towards the design of therapeutic strategies targeting SD inhibition.

Conclusions and Medical Significance

The research within this dissertation employed magnetic resonance imaging techniques for monitoring the temporal evolution of pathological disease states such as focal ischemia and cancer, with and without therapeutic intervention. Optimization of these techniques in experimental models will open the possibility for future application in a clinical setting. Clinical availability of these non-invasive methods, with the ability to detect an early therapeutic response or to provide staging and prediction of tissue fate, would greatly aid in patient management of both cancer and stroke.

CHAPTER 1

PRINCIPLES OF NUCLEAR MAGNETIC RESONANCE

Basic Physical Principles

- Electromagnetic Theory
- Nuclear Angular Momentum
- Nuclear Magnetic Dipole Moment
- Directional Dependence of μ and p
- Nuclear Energy States
- Motion of Magnetic Dipole Moments
- Free Induction Decay

Relaxation Processes

- Spin-Lattice (T_1) Relaxation
- Spin-Spin (T_2) Relaxation
- Generation of Tissue Contrast

Magnetic Resonance Imaging

- Slice-Selection
- Frequency- and Phase-Encoding
- Signal Processing and Fourier Reconstruction

Imaging Methods

- Spin-Echo Imaging
- Gradient-Echo Imaging
- Echo-Planar Imaging
- Diffusion Imaging
- Perfusion Imaging

1.1 Introduction

This chapter will discuss the principles of nuclear magnetic resonance (NMR), beginning with a historical introduction describing the discovery and development of magnetic resonance imaging (MRI). Section 1.2 will describe basic physical concepts, such as electromagnetic (EM) theory and the origin of the NMR signal, combining classical and quantum mechanical NMR descriptions. An overview of relaxation processes, specifically T_1 (spin-lattice), T_2 (spin-spin), and T_2^* in Section 1.3 will build on this foundation. The ability of specific NMR parameters, such as repetition time (TR) and echo time (TE), to generate tissue-specific contrast will also be discussed. Next, the basis of MRI in terms of slice-selective gradients, frequency-encoding, phase-encoding, and Fourier reconstruction will be covered in Section 1.4. The final section of this chapter will detail current imaging pulse sequences starting with the spin-echo, the oldest imaging method used, and ending with newer methods like echo-planar imaging and diffusion imaging. By the end of this chapter the reader should have a good grasp of NMR theory and its evolution. Several sources of information were used in preparation of this chapter, in particular books by Gadian (1), Callaghan (2), Hashemi *et al.* (3), Bernstein *et al.* (4), and Schmitt *et al.* (5).

1.1.1 Magnetic Resonance Imaging: A Historical Introduction

Nuclear magnetic resonance (NMR) is a powerful technique for the investigation of chemical and physical properties at the molecular level. Independently discovered by Bloch *et al.* (6) and Purcell *et al.* (7) in 1946, NMR began as an analytical tool used primarily by chemists for the determination of molecular structure and configuration. It wasn't until the 1970s, with Lauterbur's generation of the first two-dimensional NMR image (8), that NMR evolved into an imaging modality. The development of basic imaging techniques by Kumar *et al.* (9) and Mansfield (10), along with the necessary imaging hardware, transformed magnetic resonance imaging (MRI) into a non-invasive method capable of providing anatomical contrast superior to computed tomography (CT) without the problem of ionizing radiation. Since the 1980s, MRI has served as an indispensable diagnostic tool, with unlimited applications to the fields of biology, chemistry, physics, and engineering.

1.2 Basic Physical Principles

In order to understand the NMR phenomenon a review of the basic physical principles, beginning with electromagnetic (EM) theory, is needed. Some of these principles are best explained with Newtonian physics and others using quantum mechanics. For all intents and purposes, the message conveyed is the same in either case.

1.2.1 Electromagnetic Theory

Wave Concept of EM Radiation

EM radiation travels through space in the form of waves. It consists of an electric field component, **E**, a magnetic field component, **B**, and a velocity of propagation, **C**, equivalent to the speed of light (Fig. 1-1). The electric and magnetic field components are orthogonal and have the same frequency. They may be characterized by the classical wave equation:

$$v = \frac{c}{\lambda} \quad (1.1)$$

where c is the speed of light (3.0×10^8 m/s), λ is the wavelength (m) and v is the frequency (s^{-1}).

Particle Concept of EM Radiation

Certain EM radiation reacts with matter as if it were particles rather than waves. These particles, discrete packets of energy called quanta, are characterized by a specific frequency of radiation. Using this frequency and Planck's constant, the actual energy may be calculated:

$$E = h\nu \quad (1.2)$$

where h is Planck's constant (4.13×10^{-18} keV·s), ν is the frequency (s^{-1}), and E is the energy (keV).

MRI and the EM Spectrum

Different branches of NMR study molecular phenomena associated with the absorption of particular frequency components, typically 5 to 200 MHz, in the radiofrequency (RF) portion of the EM spectrum. This is why the EM pulses used to generate the MRI signal are called RF pulses. The various regions of the EM spectrum, radiowaves, microwaves, visible light, and x-rays are diagrammed in Fig. 1-2.

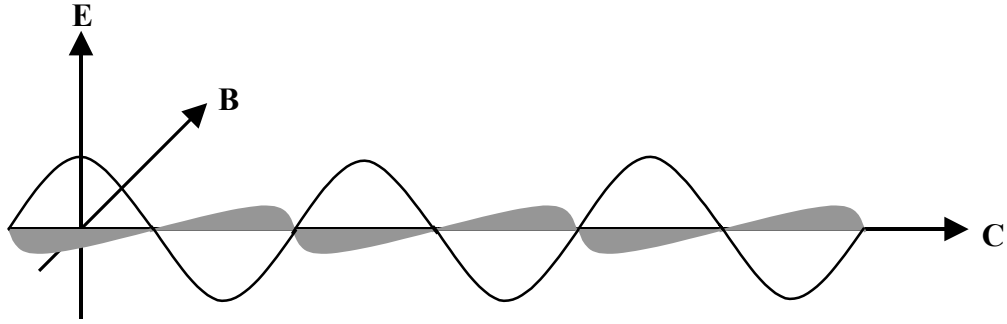


Figure 1-1: Individual components of the electromagnetic (EM) wave. E is the electric component and B is the magnetic component. These two components are perpendicular, have the same frequency, and travel at the speed of light, C.

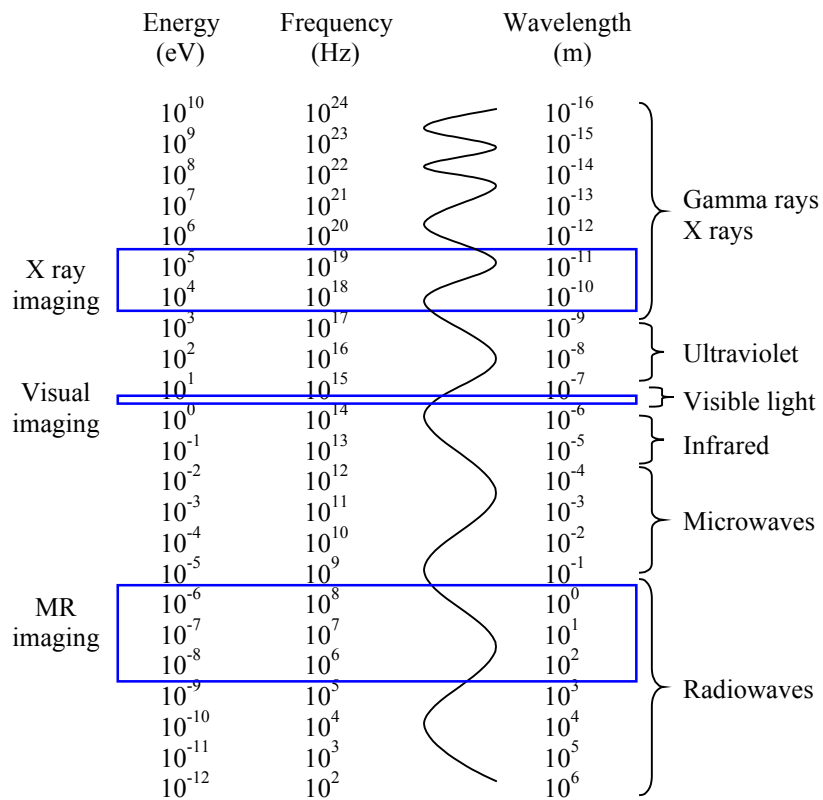


Figure 1-2: The electromagnetic (EM) spectrum. The imaging windows for radiowaves, x-rays, and visible light are outlined in blue. The various types of EM radiation are noted on the right, starting with high-energy gamma rays and x-rays at the top, and ending with the low-energy radiowaves at the bottom.

1.2.2 Nuclear Angular Momentum

Angular momentum is necessary for nuclear detection by NMR. The total angular momentum of a particle arises from two types of rotational motion, orbital rotational motion and spin rotational motion. While orbital rotational motion depends on the particle's mass, velocity, and radius of orbit, spin rotational motion is an intrinsic property of the particle itself. For a nucleus, the orbital motion of the nucleons (both protons and neutrons) is caused by the spinning motion of the entire nucleus rather than the orbital motion of its individual constituents. The orbital angular momentum may be represented by:

$$p = mr^2\omega = n\hbar \quad (1.3)$$

where m is the mass (kg), r is the radius of orbit (m), ω is the angular velocity ($\text{rad}\cdot\text{s}^{-1}$), and p is the orbital angular momentum ($\text{kg}\cdot\text{m}^2\cdot\text{s}^{-1} = \text{J}\cdot\text{s}$). This portion of the equation is the classical representation. The quantum mechanical representation, given by $n\hbar$, is the principle quantum number n multiplied by \hbar , Planck's constant h ($6.6 \times 10^{-34} \text{ J}\cdot\text{s}$) divided by 2π . Based on Equation 1-3, the orbital angular momentum has discrete values (is quantized) in integral multiples of \hbar . Similarly, spin angular momentum is also quantized in units of \hbar and may be defined as:

$$p = \hbar[I(I+1)]^{1/2} \quad (1.4)$$

where \hbar is Planck's constant h ($6.6 \times 10^{-34} \text{ J}\cdot\text{s}$) divided by 2π , I is the spin quantum number (unitless), and p is the spin angular momentum ($\text{J}\cdot\text{s}$). The value of I is dependant on the nuclear structure. Protons, neutrons, and electrons, each having a spin of $\frac{1}{2}$, pair with themselves, spin-up ($+\frac{1}{2}$) and spin-down ($-\frac{1}{2}$), canceling one another out. The protons and neutrons that remain unpaired determine the total spin angular momentum of the nucleus. For nuclei to be NMR observable, they must have an odd number of protons and/or neutrons to have a non-zero value of the spin quantum number, I (^1H , ^{19}F , and ^{31}P are examples of spin $\frac{1}{2}$ nuclei). I is zero for nuclei with even numbers of both protons and neutrons (^{12}C and ^{16}O have zero spin and are not NMR observable).

1.2.3 Magnetic Dipole Moment

A nucleus having net spin angular momentum (i.e., $I \neq 0$), generates an EM field whose magnetic component causes it to act like a bar magnet. The nuclear magnetic dipole

moment, μ , describes the magnitude and direction of this local magnetic field. For a single spinning, positively-charged proton, the magnetic dipole moment (J/T) created may be described in terms of the spin angular momentum p (J·s) and the gyromagnetic ratio γ , a proportionality constant unique to a given nucleus:

$$\mu = \gamma p \quad (1.5)$$

Certain nuclei possess a magnetic dipole moment (MDM), such as ^1H , ^{19}F , ^{31}P , ^{23}Na , ^{13}C , and ^{17}O . ^1H , ^{19}F , and ^{31}P are of particular interest in light of their natural abundance and large gyromagnetic ratios (Table 1-1). Both properties yield a larger MDM and, therefore, a larger possible NMR signal.

Table 1-1. Table of Nuclear Properties

Nucleus	# Protons	# Neutrons	Spin Quantum Number (I)	% Natural Abundance	Gyromagnetic Ratio* (MHz/T)
^1H	1	0	1/2	99.985	42.58
^{13}C	6	7	1/2	1.10	10.71
^{17}O	8	9	5/2	0.038	5.77
^{19}F	9	10	1/2	100	40.08
^{23}Na	11	12	3/2	100	11.27
^{31}P	15	16	1/2	100	17.25

*Note that the gyromagnetic ratios reported here are expressed in terms of $\gamma/2\pi$.

1.2.4 Directional Quantization of μ and p

Directional Dependence of p

In addition to magnitude, the nuclear spin angular momentum p has a directional component, p_z . Classically, p_z could take on any value between p and $-p$. However, remembering that the spin angular momentum p is limited to the discrete values given by equation 1-4, it is also the case that the vector is limited to directions corresponding to:

$$p_z = \hbar m_l \quad (1.6)$$

where p_z is the component of the spin angular momentum along the z-axis (J·s), \hbar is Planck's constant h (6.6×10^{-34} J·s) divided by 2π , and m_l is the directional spin quantum number. In this equation, m_l may take on values from $-I, -I+1, \dots, I-1, I$. For a spin- $1/2$ nucleus such as ^1H , $I = 1/2$, therefore, m_l may be $+1/2$ or $-1/2$, allowing only two possible orientations of p_z .

Directional Dependence of μ

Recalling the quantization of p (given by Eq. 1-4), and the relationship between p and μ defined in Eq. 1-5, the magnetic dipole moment μ may be redefined as:

$$\mu = \gamma\hbar[I(I+1)]^{1/2} \tag{1.7}$$

The orientation of μ is thus also limited to discrete values determined by μ_z , the z-component of the MDM:

$$\mu_z = \gamma p_z = \gamma\hbar m_l \tag{1.8}$$

Similarly, for a spin $1/2$ nucleus such as ^1H , $I = 1/2$, therefore, m_l may be $+1/2$ or $-1/2$, allowing only two possible orientations of μ_z . Fig. 1-3 illustrates the two possible orientations of μ and p for a spin- $1/2$ nucleus, termed spin-up and spin-down, in addition to the orientation angle, θ , between these vectors and the z-axis.

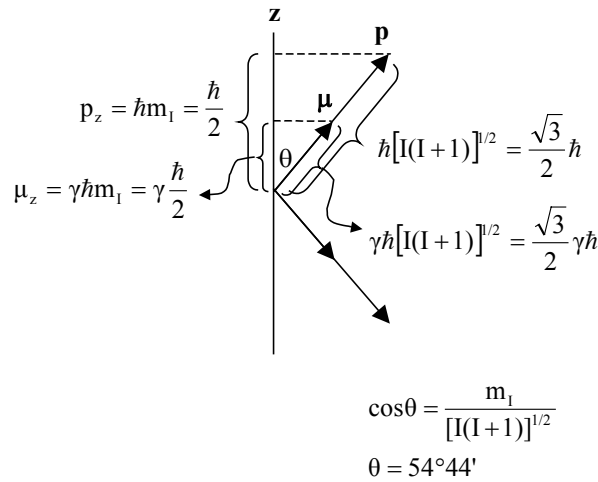


Figure 1-3: Quantization of the nuclear spin angular momentum p and the nuclear magnetic dipole moment μ for the ^1H -nucleus. The magnitudes for each vector, p and μ , as well as the magnitudes for their projection onto the z-axis, p_z and μ_z , are shown.

1.2.5 Nuclear Energy States

B₀ Field Energy Level Dependence

The nuclear spin angular momentum p and the nuclear magnetic dipole moment μ are restricted to $(2I+1)$ possible orientations or states. In the absence of an external magnetic field, the energies of the $(2I+1)$ states, independent of the orientation of μ , are degenerate (i.e., have the same value). If instead the nuclei are introduced into an external magnetic field, B_0 , this degeneracy is removed. The interaction between μ and this B_0 field (known as the Zeeman effect) has an associative potential energy E given by:

$$E = \mu_z B_0 \quad (1.9)$$

where μ_z is the component of the MDM along the z-axis (J/T), B_0 is the external magnetic field (also oriented along the z-axis, expressed in units of T), and E is the potential energy (J). For a spin- $\frac{1}{2}$ nucleus, the energy levels associated with the two orientations of μ_z (defined in Eq. 1.8 and diagrammed in Fig. 1-3) are given by:

$$E = \pm \frac{\gamma \hbar B_0}{2} \quad (1.10)$$

where the negative term is the lower energy state (aligned with, or parallel to, the B_0 field) and the positive term is the upper energy state (aligned against, or anti-parallel to, the B_0 field). These are also termed ‘spin-up’ and ‘spin-down’, respectively (Fig. 1-4).

Energy Level Transitions

For transitions (also referred to as spin flips) between energy levels, EM radiation in the RF spectrum must be absorbed or emitted, depending on whether there is a transition from the lower-to-upper or upper-to-lower energy state. The quantum of radiation required for a single transition has a characteristic frequency (Eq. 1.2) and a magnitude equivalent to the energy difference between the two states, $\gamma \hbar B_0$. From conservation of energy, this frequency may be redefined as:

$$\nu_0 = \frac{\gamma}{2\pi} B_0 \quad (1.11)$$

where ν_0 is the frequency of absorbed or emitted radiation ($\text{rad}\cdot\text{s}^{-1}$), γ is the gyromagnetic ratio (MHz/T), and B_0 is the magnetic field strength (T). Since the gyromagnetic ratio is intrinsic of nuclei, each nucleus will have a unique resonance frequency in a given B_0 field.

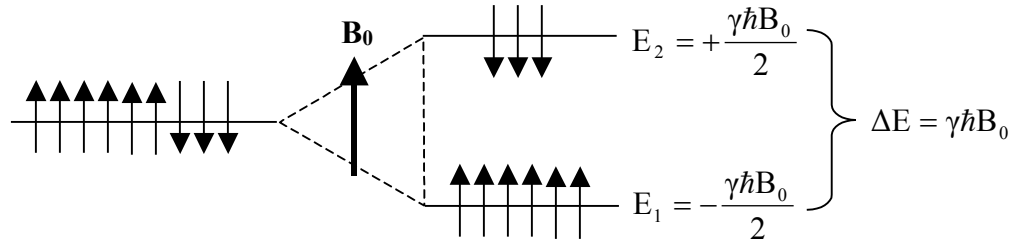


Figure 1-4: Zeeman effect: quantization of nuclear energy states. For a collection of protons in the presence of an external magnetic field B_0 , the degeneracy between energy levels is removed. The ‘spin-up’ orientation of μ_z (parallel to B_0) is of lower energy and this state contains more protons than the higher energy, ‘spin-down’ configuration.

Spin-State Populations: The Boltzmann Distribution

In NMR, the proton signal is measured from a large collection of spins distributed between the two energy levels (defined in Eq. 1.10). The detected signal is a result of the population difference between these two states, α (E_1) and β (E_2), and may be described in terms of the Boltzmann distribution:

$$N_I = e^{-E_I/KT} \quad (1.12)$$

where E_I is the energy of state I (J), K is the Boltzmann constant ($1.38 \times 10^{-23} \text{ J K}^{-1}$), T is the temperature (K) and N_I is the population of nuclei in state I. If this equation is used to calculate the populations of spins for α and β , then the ratio of the two will yield the population difference between the two energy states:

$$\Delta n = \frac{N_T \Delta E}{2KT} \quad (1.13)$$

where $\Delta E = \gamma\hbar B_0$ and N_T is the total number of nuclei. This population difference yields a total magnetic moment of the system, or net magnetization, M_z , equivalent to the sum of all of the z-components of the individual nuclear magnetic dipole moments:

$$M_z = \sum_{m=-I}^I N_m \mu_{z,m} \quad (1.14)$$

where N_m is equal to the population of nuclei in state m and $\mu_{z,m}$ is the z-component of the individual nuclear magnetic moment in state m (J/T). The number of states is equivalent to $(2I+1)$, where I is the spin quantum number of the nucleus.

The NMR signal, which is proportional to Δn and equivalent to M_0 (the total magnetization at the Boltzmann equilibrium), increases with increasing field strength (B_0), and is greater for nuclei possessing larger gyromagnetic ratios (i.e., ^1H , ^{19}F , etc).

1.2.6 Motion of Magnetic Dipole Moments

Classical Approach

In the presence of an external magnetic field, B_0 , a magnetic dipole moment μ will experience a torque L that tends to tip the magnetic moment towards B_0 :

$$L = \frac{dp}{dt} = \mu \times B_0 \quad (1.15)$$

From this equation, the torque L is equal to the time rate of change of the angular momentum p . Recalling the relation between μ and p in Eq. 1.5, the motion of μ may be described further by:

$$\frac{d\mu}{dt} = \gamma \frac{dp}{dt} = \gamma \mu \times B_0 \quad (1.16)$$

Here, the time rate of change of the MDM is equal to the time rate of change of the angular momentum (Eq. 1.15) multiplied by the gyromagnetic ratio. In the presence of this static magnetic field, the torque L induces the precession of μ about B_0 at a particular frequency, ω_0 (Fig. 1-5a). The rate or frequency of precession is proportional to the strength of the magnetic field and is expressed by the Larmor equation:

$$\omega_0 = \gamma B_0 \quad (1.17)$$

where γ is the gyromagnetic ratio (MHz/T), B_0 is the magnetic field strength (T) and ω_0 is the Larmor frequency (MHz). This frequency is directly related to the frequency described in Eq. 1.11 (by a factor of $1/2\pi$); therefore, EM radiation in the RF spectrum satisfies the resonance condition and may be applied to perturb the system from equilibrium. In the presence of an applied RF field, B_1 , with frequency ω , the motion of μ is from interaction with the static magnetic field B_0 , as well as the applied RF field, B_1 . This motion is described by:

$$\frac{d\mu}{dt} = \gamma \frac{dp}{dt} = \gamma \mu \times (B_0 + B_1) \quad (1.18)$$

Here, μ precesses about the effective magnetic field, B_{eff} , which is the resultant of B_0 , B_1 , and a “fictitious” field ω/γ (11). This is viewed most easily in the rotating frame (Fig. 1.5b). If ω_r of the rotating frame is equal to the Larmor frequency ω_0 , then the effective magnetic field ‘seen’ by μ is equal to the applied field B_1 . Further consideration of RF perturbations to a collection of nuclei will be discussed in more detail using the quantum-mechanical approach.

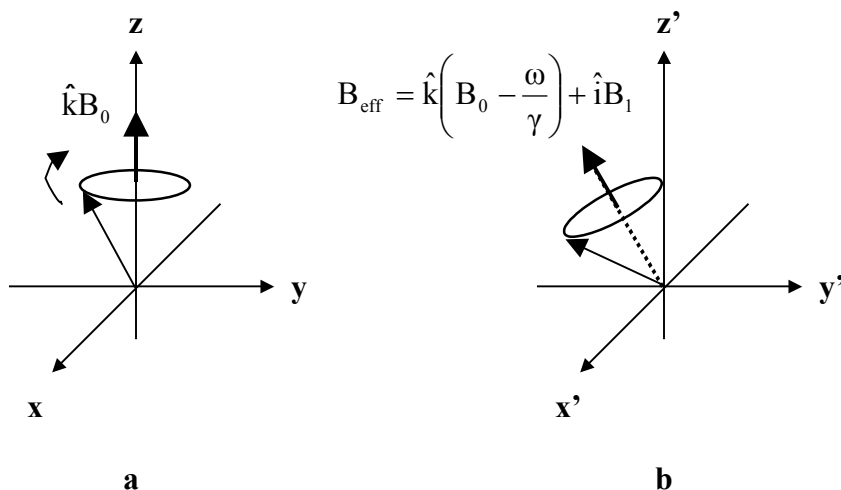


Figure 1-5: Precession of an individual nuclear magnetic moment μ about B_0 in the laboratory frame (a) and the precession of an individual nuclear magnetic moment μ about the effective magnetic field in the rotating frame (b). In the presence of an external magnetic field, B_0 , μ precesses at the Larmor frequency, ω_0 , given by $\omega_0 = \gamma B_0$. With an additional applied RF field, B_1 , the precession depends on the interaction of μ with both B_0 and B_1 , termed the effective static magnetic field, B_{eff} .

Quantum-Mechanical Approach

Although the classical model describing the motion of an individual nuclear magnetic moment is useful in understanding the NMR phenomenon, it has limitations in terms of effectively explaining the interactions between nuclei. To overcome the limitations of the classical model, Felix Bloch developed a set of differential equations describing the dynamics of nuclear magnetization. For a collection of spins, the vector sum of the individual MDMs yields the net magnetization, M , the total magnetic moment of the system. In the absence of an external magnetic field, B_0 , the individual MDMs will have

random spin vector orientations whose sum yields a net magnetization equal to zero. In the presence of an external magnetic field, B_0 , each MDM precesses about B_0 at the Larmor frequency, ω_0 . Based on the Boltzmann distribution, more nuclei are parallel versus anti-parallel to B_0 (i.e., in the lower-energy state versus the higher-energy state), resulting in a net longitudinal or z-magnetization, M_0 . The vector sum of the transverse or xy-components of M results in the phase cancellation of the nuclei and no coherent transverse magnetization, M_{xy} , at the Boltzmann equilibrium. Therefore, the remaining longitudinal magnetization M_0 (also known as M_z) has constant magnitude, and is parallel to B_0 . These microscopic and macroscopic concepts of the net magnetization are diagrammed in Fig. 1-6.

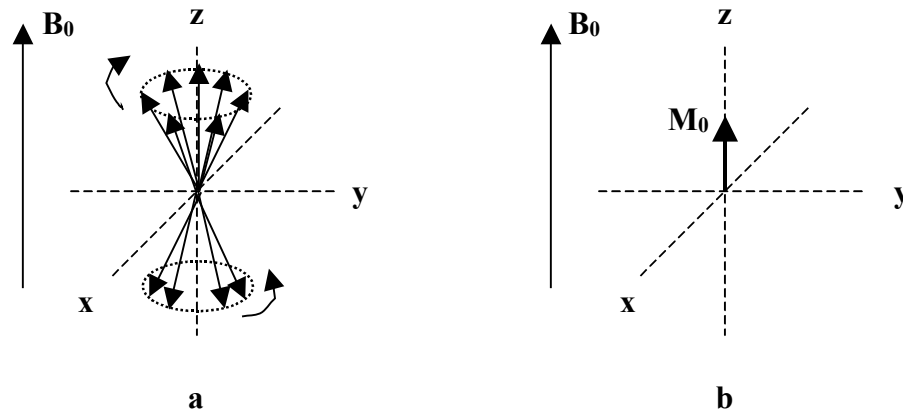


Figure 1-6: Microscopic (a) and macroscopic (b) pictures for a collection of protons in the presence of an external magnetic field, B_0 . The individual magnetic dipole moment (MDM) of each proton precesses about B_0 at the Larmor frequency, ω_0 . The protons will appear to precess on the surface of two ‘cones’, one with a positive z-component and one with a negative z-component. Because there are more protons in the upper ‘cone’, there will be a nonzero vector sum M_0 , or net longitudinal magnetization, of constant magnitude, parallel to B_0 . Note that the sum of the transverse components of individual MDMs results in phase cancellation and thus no residual transverse magnetization M_{xy} .

At the Boltzmann equilibrium the motion of the net magnetization M , the vector sum of the individual magnetic moments, may be described by the time rate of change of M :

$$\frac{dM}{dt} = \gamma(M \times B_0) \quad (1.19)$$

Upon application of an RF field, B_1 , the net magnetization M is rotated away from the z -axis by some angle θ . When viewed from the laboratory frame, the net magnetization M precesses about B_0 at the Larmor frequency ω_0 and angle θ with respect to the z -axis. In the rotating frame ($\omega_r = \omega_0$), M ‘experiences’ no torque and therefore, appears stationary. This is illustrated in Fig. 1-7.

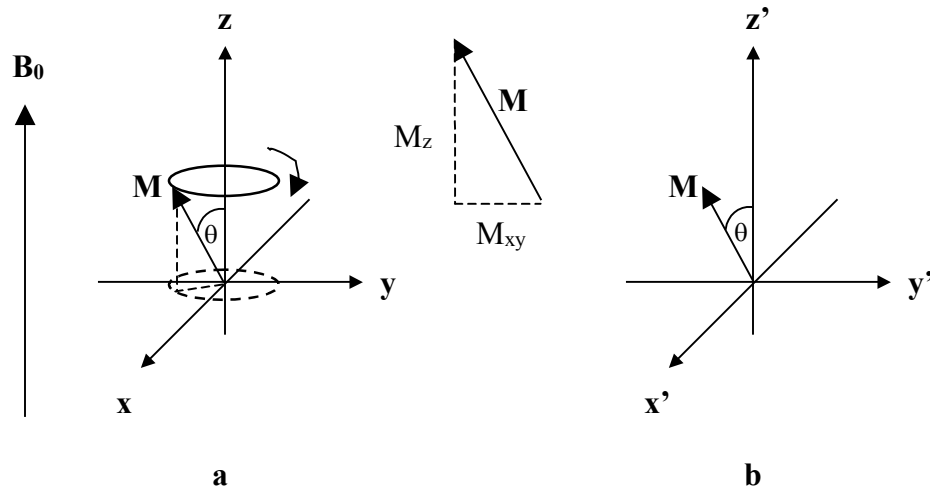


Figure 1-7: Visualization of the net magnetization M in the laboratory frame (a) and the rotating frame (b). In the laboratory frame, M precesses about B_0 at the Larmor frequency. In the rotating frame, since the rotational frequency ω_r is equal to the Larmor frequency ω_0 , M ‘experiences’ no torque and appears stationary. Following application of the B_1 field, the net magnetization M is at some angle θ with respect to B_0 and the z -axis. The z -component of the magnetization M is called the longitudinal magnetization and is termed M_z . The xy -component of the magnetization M is called the transverse magnetization and is termed M_{xy} .

In the presence of an RF field, B_1 , Eq. 1.19 must be modified for the inclusion of the external magnetic field, B_0 , and the applied RF field, B_1 :

$$\frac{dM}{dt} = \gamma(M \times B) \tag{1.20}$$

Here, B consists of both B_0 and B_1 . By expanding the cross product in Eq. 1.20, time derivatives may be written for each component of M :

$$\frac{d\mathbf{M}}{dt} = \gamma(\mathbf{M} \times \mathbf{B}) = \gamma \begin{vmatrix} \hat{i} & \hat{j} & \hat{k} \\ M_x & M_y & M_z \\ B_x & B_y & B_z \end{vmatrix} =$$

$$\underbrace{\gamma(M_y B_z - M_z B_y)}_{\frac{dM_x}{dt}} \hat{i} - \underbrace{\gamma(M_x B_z - M_z B_x)}_{\frac{dM_y}{dt}} \hat{j} + \underbrace{\gamma(M_x B_y - M_y B_x)}_{\frac{dM_z}{dt}} \hat{k} \quad (1.21)$$

Since \mathbf{B} consists of the static field, B_0 , and the RF field, B_1 , the individual components of \mathbf{B} (B_x , B_y , and B_z) are equal to:

$$\begin{aligned} B_x &= B_1 \cos \omega t \\ B_y &= B_1 \sin \omega t \\ B_z &= B_0 \end{aligned} \quad (1.22)$$

Upon perturbation from thermal equilibrium by an RF field, B_1 , the net magnetization \mathbf{M} will return to equilibrium via T_1 and T_2 relaxation processes (to be discussed further in Section 1.3). The inclusion of these relaxation processes yields the full Bloch equations in the laboratory frame:

$$\begin{aligned} \frac{dM_x}{dt} &= \gamma B_0 M_y + \gamma B_1 \sin \omega t M_z - \frac{M_x}{T_2} \\ \frac{dM_y}{dt} &= -\gamma B_0 M_x + \gamma B_1 \cos \omega t M_z - \frac{M_y}{T_2} \\ \frac{dM_z}{dt} &= -\gamma (\sin \omega t M_x + \cos \omega t M_y) - \frac{(M_z - M_0)}{T_1} \end{aligned} \quad (1.23)$$

In NMR, it is convenient to describe the net magnetization, \mathbf{M} , using the rotating frame. Here, the z-axis, parallel to B_0 , is the axis of rotation while the x and y axes rotate at the Larmor frequency, ω_0 . By this convention, M_0 is invariant in terms of magnitude, as it is parallel to B_0 and the rotational axis. For all subsequent discussions of M_0 , the rotating frame of reference with the rotational axis parallel to B_0 will be used when describing the motion of nuclei.

1.2.7 Free Induction Decay

In Fourier transform NMR experiments, RF pulses of set duration, τ , are used to generate a magnetic field, B_1 , orthogonal to the static B_0 field. This B_1 field rotates the net

magnetization M away from the z -axis (Fig. 1-8). The degree of rotation, θ , also termed the flip angle, is dependent on both the strength of the applied RF field, B_1 , as well as the duration over which it is applied:

$$\theta = \gamma B_1 \tau \quad (1.24)$$

Depending on the experiment, θ will either be 90° (flipping M into the transverse plane) or 180° (flipping M onto the negative z -axis). The importance of RF pulses in NMR lies in the ability to create a transverse component of the net magnetization. This is because the net magnetization in the XY plane (M_{xy}) is the only component of magnetization that induces a NMR signal.

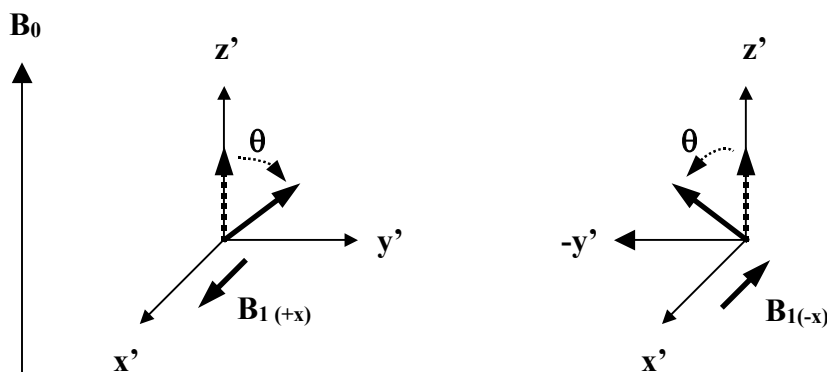


Figure 1-8: Application of a B_1 field flips the net magnetization, M , from equilibrium along the z -axis by an angle θ that is dependent on the strength of the B_1 field and the duration over which it is applied. In addition, it is important to note that the direction that M moves away from the z -axis by the angle θ is dependent on the direction along which the B_1 field is applied.

Upon application of an RF pulse producing a given flip angle, θ , perturbation of the net magnetization yields a transverse component (M_{xy}) that is detected by an RF receive coil encompassing the sample-of-interest. This transverse component arises from the phase coherence to the spins comprising the xy -magnetization. Over time, the spin system will return to the Boltzmann equilibrium, the xy -plane phase coherence will be lost, and the transverse magnetization will decay to zero. Remembering that the net magnetization is precessing about the z -axis at the Larmor frequency, the measured evolution of the transverse signal is an exponentially-decaying sinusoid called a free induction decay, or FID (Fig. 1-9). The loss of phase coherence and exponential decay of the transverse

magnetization is from the relaxation processes (T_2/T_2^*) upon return to equilibrium. T_2^* contributions include the intrinsic T_2 relaxation from nuclear interactions, as well as contributions from magnetic susceptibilities, B_0 -field inhomogeneities, and molecular diffusion. Section 1.3 will further detail T_2 and T_2^* relaxation.

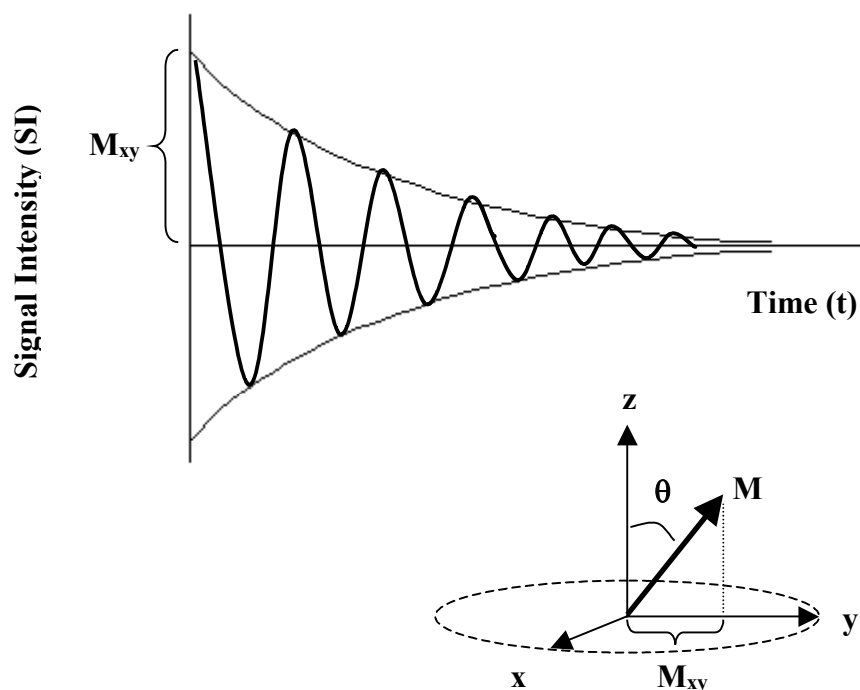


Figure 1-9: Sample free induction decay (FID) signal following application of a RF pulse with a set flip angle θ . As θ moves from 0° to 90° , the component of magnetization in the transverse plane increases, yielding larger FID amplitude.

1.3 Relaxation Processes

The two main relaxation mechanisms in NMR are spin-lattice (T_1) relaxation and spin-spin (T_2) relaxation. Following perturbation by a magnetic field, B_1 , the net magnetization of the spin system will return to the Boltzmann equilibrium via exponential decay processes. The exponential process whereby the longitudinal magnetization, M_z , returns to its equilibrium state (along the z -axis) is measured by the time constant T_1 . Similarly, the exponential process whereby the transverse magnetization, M_{xy} , decays to zero from its starting value (based on the flip angle θ) is

measured by the time constant T_2 . These time constants, T_1 and T_2 , vary based on tissue type, disease state, etc., allowing their manipulation to generate tissue contrast in magnetic resonance imaging (MRI) applications. The following sections will describe T_1 and T_2 relaxation processes, as well as the generation of tissue contrast in MR images.

1.3.1 Spin-Lattice (T_1) Relaxation

T_1 is called the longitudinal relaxation time because it refers to the time taken for realignment of the net magnetization with the longitudinal z-axis. It is also known as the spin-lattice relaxation time, referring to the time taken for the spins to transfer the absorbed energy from the applied RF pulse to their surroundings (the “lattice”) in order to return to the Boltzmann equilibrium. From the Bloch equations for the laboratory frame (Eq. 1.23), the longitudinal component arising from relaxation processes is:

$$\frac{dM_z}{dt} = -\frac{M_z - M_0}{T_1} \quad (1.25)$$

Solving this equation, the exponential growth of the longitudinal magnetization may be described by:

$$M_z(t) = M_0 \left(1 - \alpha e^{-t/T_1} \right) \quad (1.26)$$

where t is the time following the RF pulse, M_0 is the value of the magnetization at Boltzmann equilibrium prior to the RF pulse, T_1 is the time required for the longitudinal component to return to 63% of its original value, and $M_z(t)$ is the change in the longitudinal magnetization over time. In Eq. 1.27, α is dependent on the type of pulse applied—for a 90° pulse, $\alpha = 1$, for a 180° pulse $\alpha = 2$.

Progressive Saturation

Progressive saturation is one of several methods used for measuring the T_1 relaxation time of the sample-of-interest. It involves the application of two 90° pulses separated by a waiting period $t = TR$, termed the repetition time. Following application of the first 90° pulse to flip the magnetization from the longitudinal z-axis to the transverse xy plane, the spin system has phase coherence and there is no remaining longitudinal magnetization ($M_z = 0$). Over the time $t = TR$, the longitudinal component (M_z) recovers to the longitudinal z-axis. The amount of recovery is dependent on the ratio of TR to the T_1 of the sample-of-interest, and is measured by applying a second 90° pulse to flip the

recovered longitudinal magnetization into the transverse plane for receipt by the RF receive coil. Through acquisition of several FIDs at varying TRs, the signal amplitude of the FID versus repetition time (TR) may be plotted for calculation of T_1 . The progressive saturation method is diagrammed in Fig. 1.10.

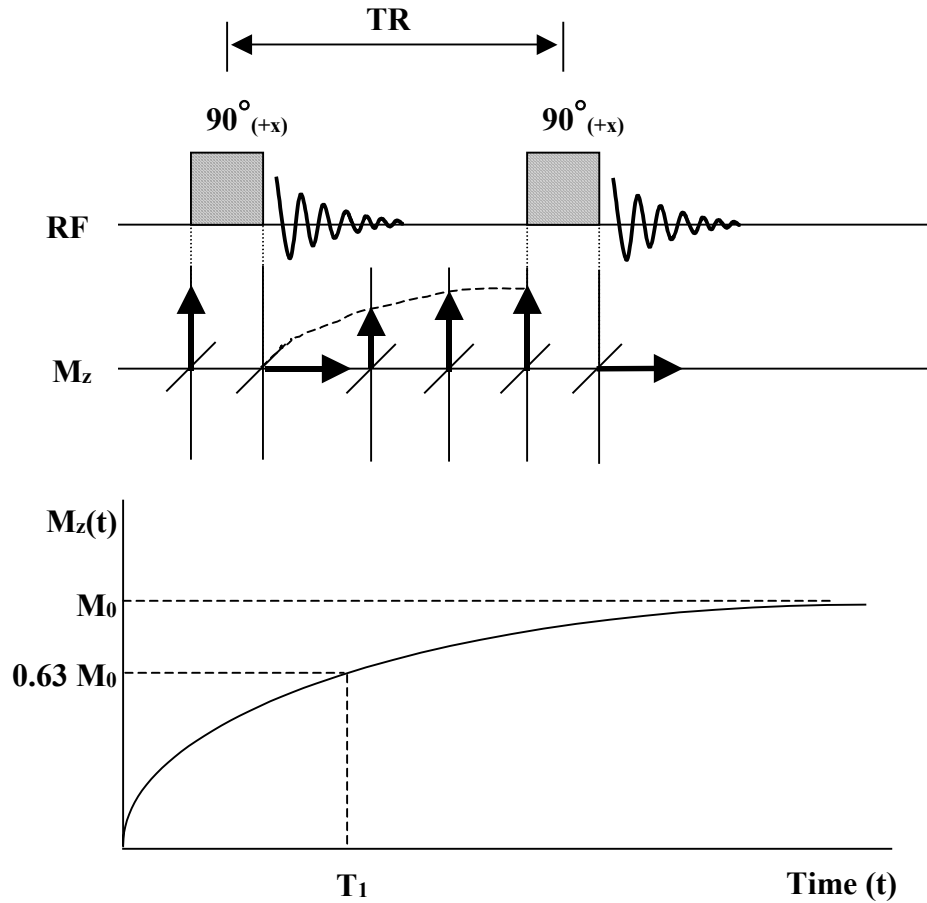


Figure 1-10: Progressive saturation method for the measurement of T_1 relaxation. Top: PS pulse sequence for T_1 measurement. Middle: The changes in the net magnetization, M , are diagrammed by the arrows. Bottom: Sample plot of signal intensity versus time (with increasing TR).

Inversion Recovery

Inversion recovery, like progressive saturation, is a method used for measuring the T_1 of the sample-of-interest. This particular method involves the application of a 180° pulse and a 90° pulse, separated by a waiting period $t = TI$, termed the inversion time. The application of the 180° pulse serves to flip the magnetization from the longitudinal $+z$ -

axis to the longitudinal $-z$ -axis. Over the time $t = T_1$, the longitudinal magnetization will recover by a given amount, dependent on the ratio of T_1 to the T_1 of the sample-of-interest. This recovery is measured by applying a 90° pulse to flip the recovering longitudinal magnetization into the transverse plane for detection by the RF receive coil. Through acquisition of several FIDs at varying T_1 s, the signal amplitude of the FID versus inversion time (T_1) may be plotted for calculation of T_1 . The inversion recovery method is diagrammed in Fig. 1.11.

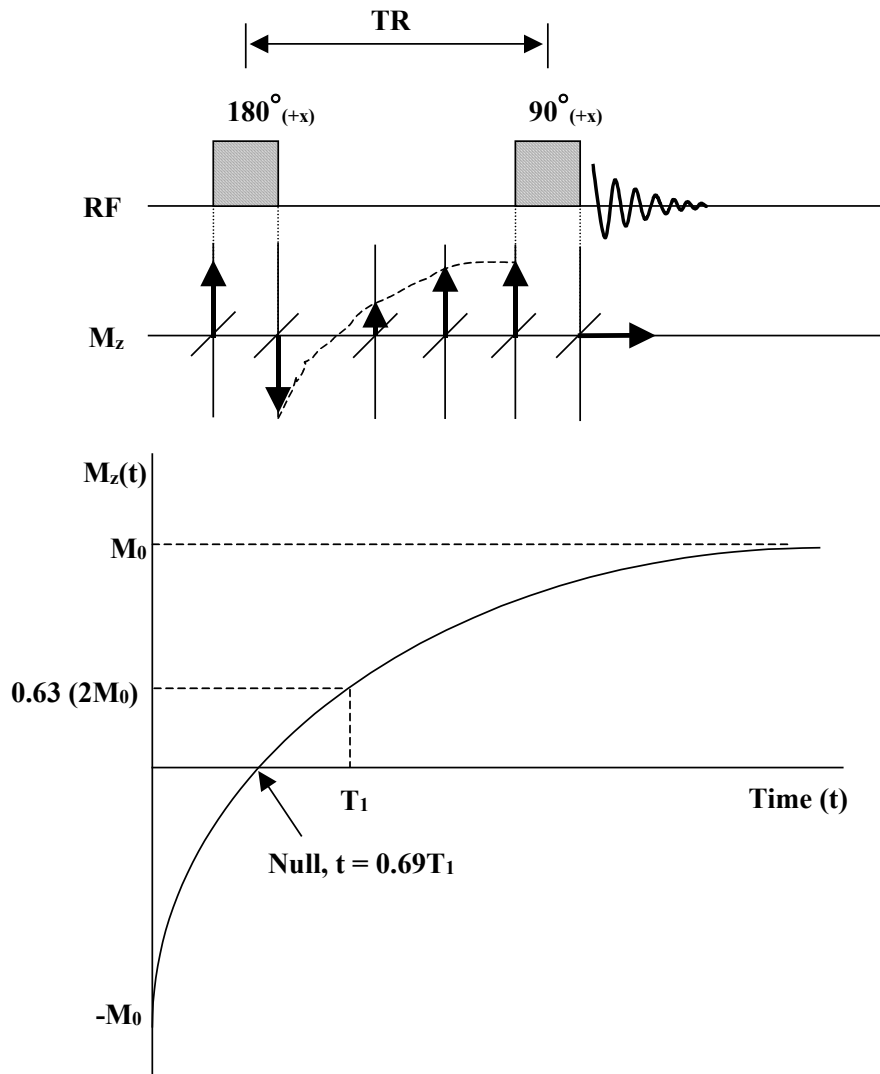


Figure 1-11: Inversion recovery method for the measurement of T_1 relaxation. Top: IR pulse sequence for T_1 measurement. Middle: The changes in net magnetization, M , are diagrammed by the arrows. Bottom: Sample plot of signal intensity versus time (increasing T_1).

1.3.2 Spin-Spin (T_2) Relaxation

The transverse relaxation time, T_2 , refers to the time taken for the exponential decay of the transverse component of the net magnetization. It is also known as the spin-spin relaxation time, referring to the time taken for dephasing of the spins via spin-spin interactions, in order to return to the Boltzmann equilibrium. In addition to dephasing from spin-spin interactions, other contributions exist from B_0 field inhomogeneities, differences in magnetic susceptibility, and molecular diffusion effects. All these sources contribute to the total transverse relaxation time, T_2^* :

$$\frac{1}{T_2^*} = \frac{1}{T_2} + \frac{1}{T_2^{IH}} + \frac{1}{T_2^{MS}} + \frac{1}{T_2^{MD}} \quad (1.27)$$

where T_2^{IH} is the dephasing time due to B_0 field inhomogeneities, T_2^{MS} is the dephasing time due to magnetic susceptibility differences, and T_2^{MD} is the dephasing time from molecular diffusion effects. From the Bloch equations for the laboratory frame (Eq. 1.23), the change in the transverse component arising from relaxation processes is:

$$\frac{dM_{xy}}{dt} = -\frac{M_{xy}}{T_2} \quad (1.27)$$

Following application of a single 90° pulse, the decay of the transverse magnetization follows an exponential process with the time constant of T_2^* rather than just T_2 :

$$M_{xy}(t) = M_0 e^{-t/T_2^*} \quad (1.28)$$

where t is the time following the RF pulse, M_0 is the Boltzmann equilibrium value of the z-magnetization just prior to the 90° RF pulse, T_2^* is the time required for the transverse component to decay to 37% of its original value, and $M_{xy}(t)$ is the change in the transverse magnetization over time.

Hahn Spin Echo

The Hahn spin echo is a method that eliminates contributions from B_0 field inhomogeneities and magnetic susceptibilities, allowing the measurement of T_2 for a sample-of-interest. This particular method involves the application of a 90° pulse and a 180° pulse, separated by a waiting period $t = TE/2$, with TE termed the echo time. The application of the 90° pulse serves to flip the z-magnetization to the transverse xy plane. Immediately after the pulse is turned off, the spins are in phase with one another (i.e., M_{xy}

is a maximum). Over the time $t = TE/2$, spin dephasing will occur through T_2^* relaxation processes. Application of the 180° pulse reverses the phases of individual spins relative to the Larmor frequency. Another delay of $t = TE/2$ allows for rephrasing of the spin system, after which the remaining transverse magnetization (known as a spin-echo) is measured by the RF receive coil. During the two $TE/2$ time periods, the sources of dephasing from B_0 field inhomogeneities and magnetic susceptibilities are constant, therefore, they are phase cancelled at $TE/2$ following the 180° pulse. Through acquisition of several spin echoes at varying TEs, the signal amplitude of each echo versus echo time (TE) may be plotted for calculation of T_2 . The Hahn spin echo method is diagrammed in Fig. 1.12.

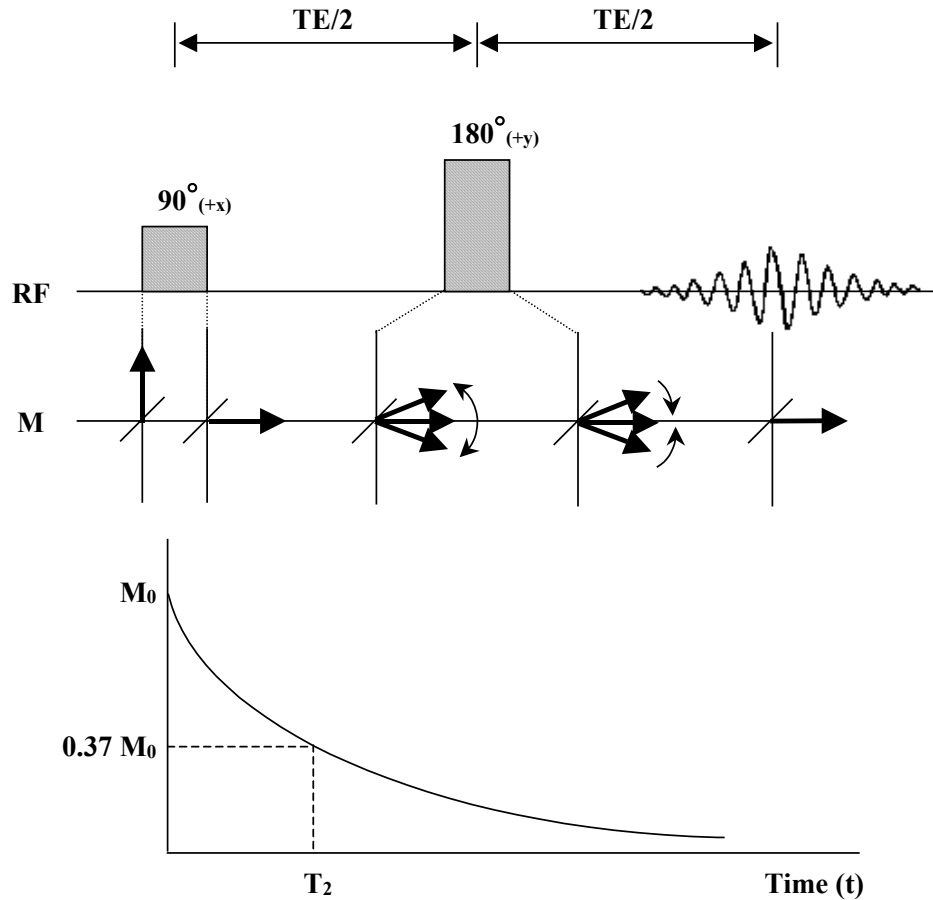


Figure 1-12: Hahn spin echo method for the measurement of T_2 relaxation. Top: HSE pulse sequence for T_2 measurement. Middle: The changes in the net magnetization, M , are diagrammed by the arrows. Bottom: Sample plot of signal intensity versus time (increasing TE).

1.3.3 Relaxation Mechanisms and Generation of Tissue Contrast

Molecular Motions and Dipole-Dipole Coupling

In NMR, dipole-dipole coupling modulated by rotational and translational molecular motions is the major contributor to T_1 and T_2 relaxation, and therefore, the ability to generate tissue contrast for a sample-of-interest. In terms of rotational motion, the time required for a molecule to rotate $1/2\pi$ (1 radian) is termed the correlation time, or τ_c . It also indicates the time between molecular collisions, which may be interpreted as the time a molecule remains in one state of motion. The correlation time τ_c has an associated range of frequencies (0 to $1/\tau_c$ Hz), a subset of which are of particular interest when at or near the Larmor frequency.

Static Component of Dipole-Dipole Coupling

When two protons are placed near one another (e.g., in a water molecule) they couple, each experiencing a small contribution δB from the other proton in addition to the external magnetic field B_0 . For bulk water at room temperature, the molecules' rapid isotropic movements ($\tau_c \sim 10^{-12}$ sec) result in averaging of the positive and negative phase contributions and zero contribution to T_2 decay. In contrast, water molecules bound to macromolecules such as globular proteins have significantly longer correlation times ($\tau_c \sim 10^{-5}$ - 10^{-8} sec). The slow rotational rate of the bound system results in a small contribution to the total magnetic field due to interactions with its neighbors (no motional averaging), leading to T_2 relaxation from dephasing and a non-zero static component of dipole-dipole coupling.

Dynamic Component of Dipole-Dipole Coupling

Translational motion and rotational tumbling motion, the sources of the dynamic component of dipole-dipole coupling, contribute to both T_1 and T_2 decay. For an individual water molecule, the total magnetic field experienced by each nucleus is the sum of the external magnetic field B_0 and the local contribution δB from its neighbor. These fluctuations in the magnetic field behave similar to the B_1 field generated by an RF pulse. When exposed to a fluctuating magnetic field, the nuclei may absorb energy from the field and change spin states. Following this exchange there is random dephasing of the transverse magnetization (T_2 relaxation) as well as energy transfer to the lattice with recovery of the longitudinal magnetization (T_1 relaxation).

Spectral Density Distribution

The molecular motions within a system (i.e., a collection of molecules) may be represented by a uniform distribution of molecules rotating at frequencies ranging from zero to $\omega = 1/\tau_c$. This frequency distribution is represented by the spectral density function, $J(\omega)$:

$$J(\omega) = \frac{\tau_c}{1 + \omega^2 \tau_c^2} \quad (1.29)$$

where τ_c is the correlation time and ω is the rotational frequency of the molecule. Fig. 1-13 diagrams the relationship between $J(\omega)$ and ω for three different molecular environments—large molecules (i.e., proteins), medium-sized molecules (i.e., lipids), and small molecules (i.e., water). For a sample in a given magnetic field, the measured relaxation rates (T_1 and T_2) depend on the fluctuations in the local magnetic field at or near the Larmor frequency. In other words, only molecules with motional frequencies near the resonance frequency ω_0 contribute significantly to the T_1 and T_2 values measured with NMR. Since ω_0 is B_0 field dependent, the fraction of molecules with motional frequencies equal to ω_0 generally decreases with increasing B_0 , causing a reduction in relaxation rate.

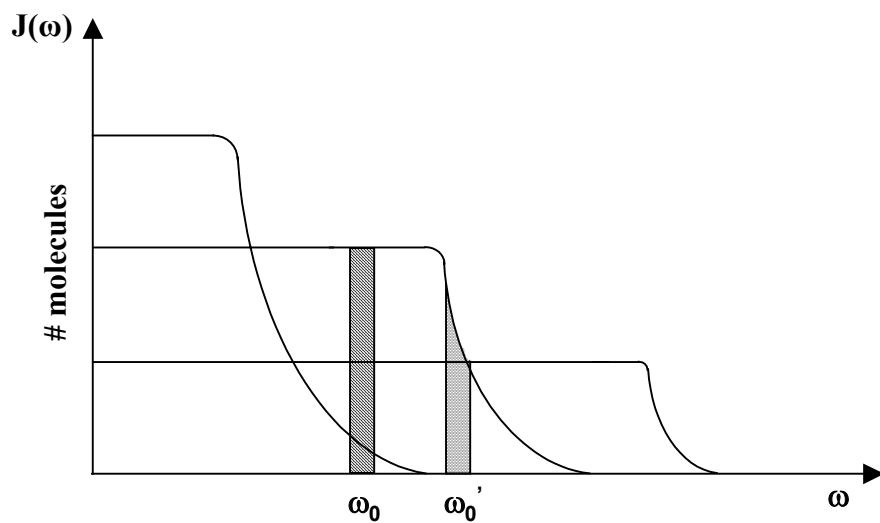
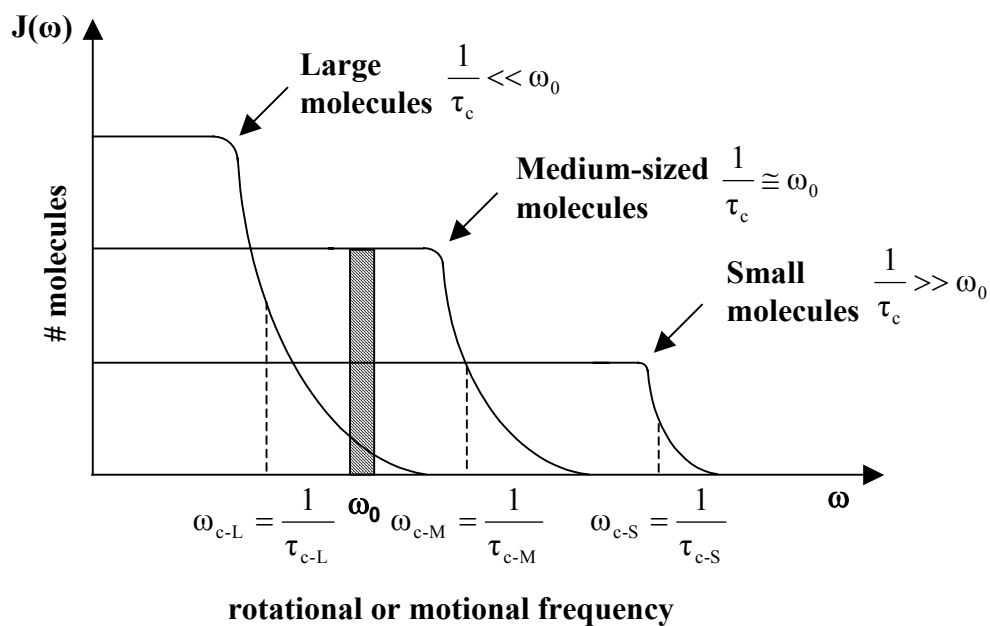


Figure 1-13: Relationship between the spectral density function $J(\omega)$ and the rotational or motional frequency (ω). Top: For increasing molecular size, there is a corresponding increase in correlation time τ_c and a smaller range of permitted rotational frequencies. Bottom: For increasing B_0 field, there is a corresponding increase in ω_0 and generally a reduction in the fraction of molecules with motional frequencies having significant contribution to the relaxation rates.

MRI Tissue Contrast: Exploiting Differences in T_1 and T_2

The resultant differences in T_1 and T_2 values from molecular motions and dynamic dipole-dipole coupling permit generation of tissue contrast. These differences allow delineation between tissues such as fat, soft tissue, water, and proteinaceous fluid. They also allow delineation between healthy soft tissue and pathological lesions, as well as between white matter, gray matter, and cerebrospinal fluid (CSF) in the brain. Exploitation of T_1 - and T_2 -weighting for differentiating between brain tissues and for lesion identification (i.e., tumors) will be shown in the following sections.

T_1 -weighting: Short TR/Short TE

In the brain, the myelin sheath of white matter has similar properties to fat, whereas gray matter is closer to soft tissue. This yields a shorter T_1 in white matter versus that of gray matter. CSF, on the other hand, has a long T_1 . On a T_1 -weighted image (acquired using a short TR and a short TE) the white matter would be bright (i.e., high signal intensity), the gray matter would be intermediate in intensity, and the CSF would be dark (Fig. 1-14).

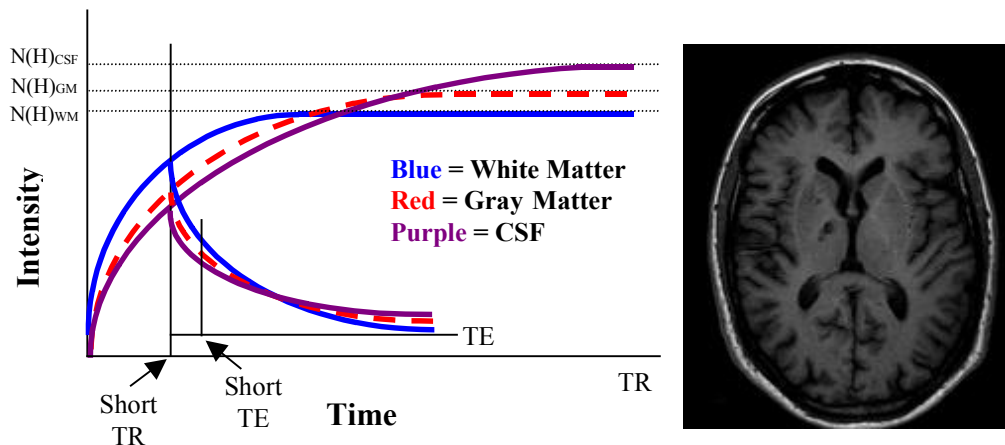


Figure 1-14: T_1 -weighted contrast. Left: T_1 -recovery and T_2 -decay curves of white matter, gray matter, and CSF. For short TR and short TE values, the contrast between these tissues is maximized based on their differences in T_1 . The T_2 effect is minimized by using a short TE value. Right: T_1 -weighted image of the human brain. T_1W image reproduced from http://www.mr.ethz.ch/3t/patient_2.html.

For healthy soft tissue versus pathological lesions (i.e., tumors), the difference in signal intensities on a T_1 -weighted image is minimal. The best contrast for distinguishing tumors from surrounding tissue is T_2 -weighted imaging. Since tumors tend to have

higher water content (due to edema from inflammatory processes), they have increased T_1 and T_2 relaxation times in comparison to normal healthy tissue.

T₂-weighting: Long TR/Long TE

In the brain, white matter has a slightly shorter T_2 than gray matter. CSF, on the other hand, has the least dephasing and therefore the longest T_2 of the three tissues. On a T_2 -weighted image (acquired using a long TR and a long TE) the white matter would be dark, the gray matter would be intermediate in intensity, and the CSF would be bright (Fig. 1-15, top). In tumors, the T_2 tends to be longer than healthy soft tissue. This is because of the reduced dephasing from decreased cell density and increased water content. This allows for differentiation between the tumor and the surrounding tissue (Fig. 1-15, bottom). Diffusion-weighted imaging also provides contrast between lesions and soft tissue. This particular type of contrast will be discussed in detail in Chapter 2.

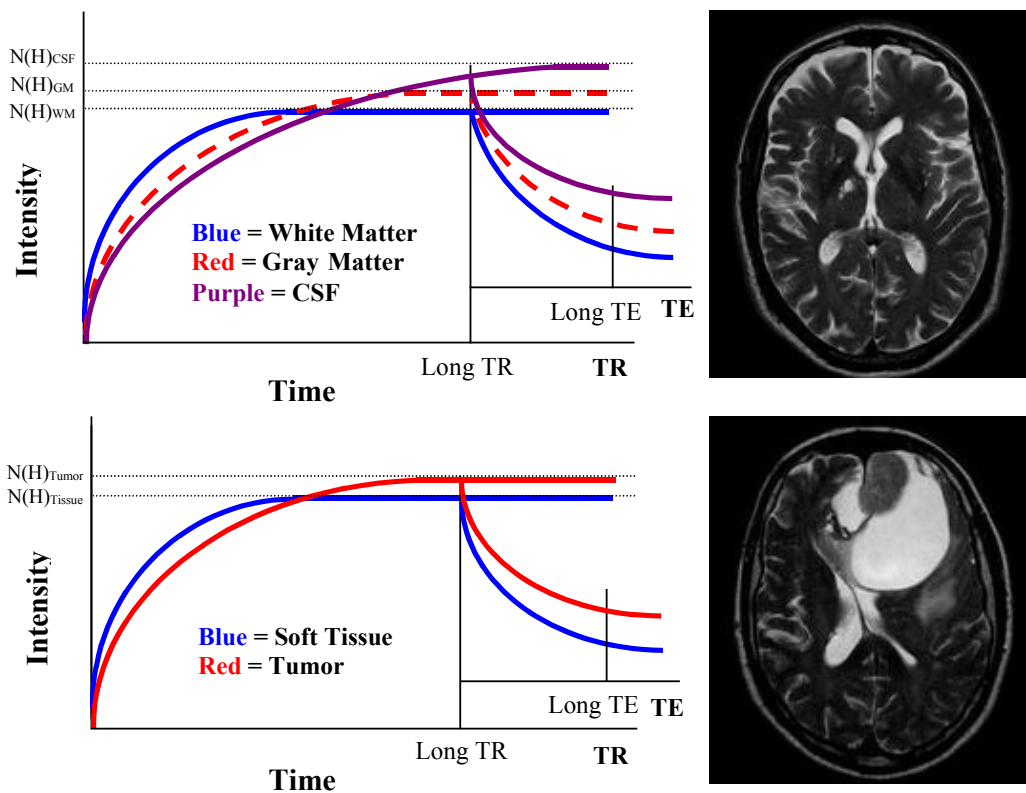


Figure 1-15: T_2 -weighted contrast. Top Left: T_1 -recovery and T_2 -decay curves of white matter, gray matter, and CSF. Bottom Left: T_1 -recovery and T_2 -decay curves of soft tissue and tumor. For long TR and long TE values, the contrast between these tissues is maximized based on their differences in T_2 . The T_1 effect is minimized by using a long TR value. Top Right: T_2 -weighted image of the human brain. Bottom Right: T_2 -weighted image of a human brain tumor. Images reproduced from http://www.mr.ethz.ch/3t/patient_2.html and http://www.mr.ethz.ch/3t/patient_3.html.

Proton Density: Long TR/Short TE

In the brain, if a very short TE is chosen in combination with a long TR value, the signal intensities for the individual tissues (white matter, gray matter, and CSF) will reflect their respective proton densities (i.e., M_0) (Fig. 1-16). This type of weighting is many times used to compare the relative water content of two tissues or regions of interest.

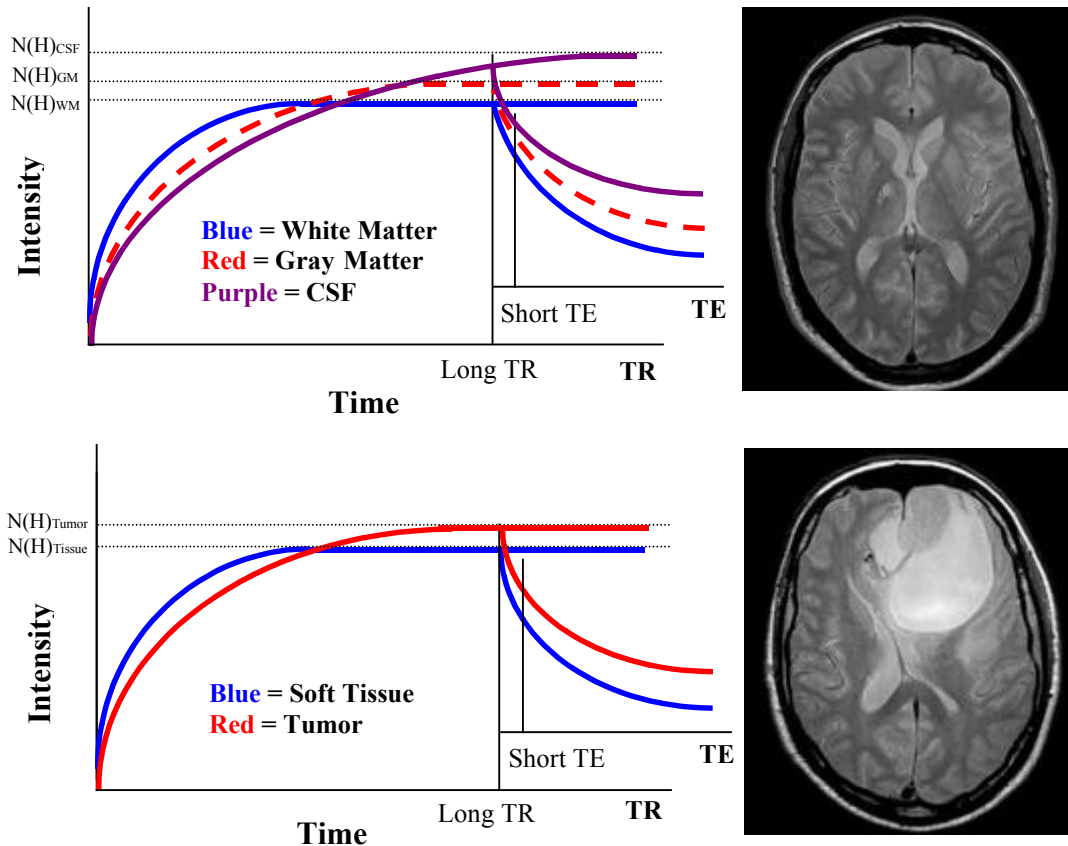


Figure 1-16: Proton Density-weighted contrast. Left: T₁-recovery and T₂-decay curves of white matter, gray matter, and CSF. For a long TR and short TE, the contrast between these tissues is maximized from their differences in proton density (i.e., M_0). The T₂ effect is minimized by using a short TE value. Right: Proton Density-weighted image of the brain. Images reproduced from http://www.mr.ethz.ch/3t/patient_2.html and http://www.mr.ethz.ch/3t/patient_3.html.

1.4 Magnetic Resonance Imaging

In order to translate from magnetic resonance spectroscopy (MRS) techniques to MRI, several important steps are required, most importantly, spatial encoding. In this section, signal composition (frequency, phase, amplitude) will be discussed prior to that of specific image acquisition and processing techniques. The methodology behind slice selection and slice offset, the concepts of frequency encoding and phase encoding, as well as the rephasing gradients necessary will also be covered.

1.4.1 Underlying Signal Composition: Phase, Frequency, and Amplitude

NMR signals are measured with respect to the rotating frame of reference; therefore, their oscillation frequencies are represented by $\omega_0 \pm \omega$. During the acquisition phase of the NMR experiment, a RF receive coil measures the total signal (FID) with respect to time (Fig. 1-17). This FID has phase, frequency, and amplitude. Since the FT permits transformations between time and frequency space, a 1D-FT taken of the FID will yield a plot of signal amplitude with respect to frequency. If the FID's composition contains a single frequency of oscillation, there will be one Lorentzian-shaped peak located symmetrically about that frequency and whose full-width-at-half-maximum height (FWHM) is related to the time constant for exponential decay. If instead the FID's composition has two frequencies of oscillation, there will be two Lorentzian-shaped peaks, both symmetrically disposed about their individual resonance frequencies. NMR signals many times are composed of signals with varying frequency and amplitude, a direct result of tissue heterogeneity (fat, muscle, etc). For MRS, these principles of 1D-FT NMR allow investigation of chemical composition, structure, etc. In terms of MRI, the application of a sinc-shaped RF pulse is only half of the picture. The second half involves application of a non-uniform field (linear field gradient) for spatial encoding.

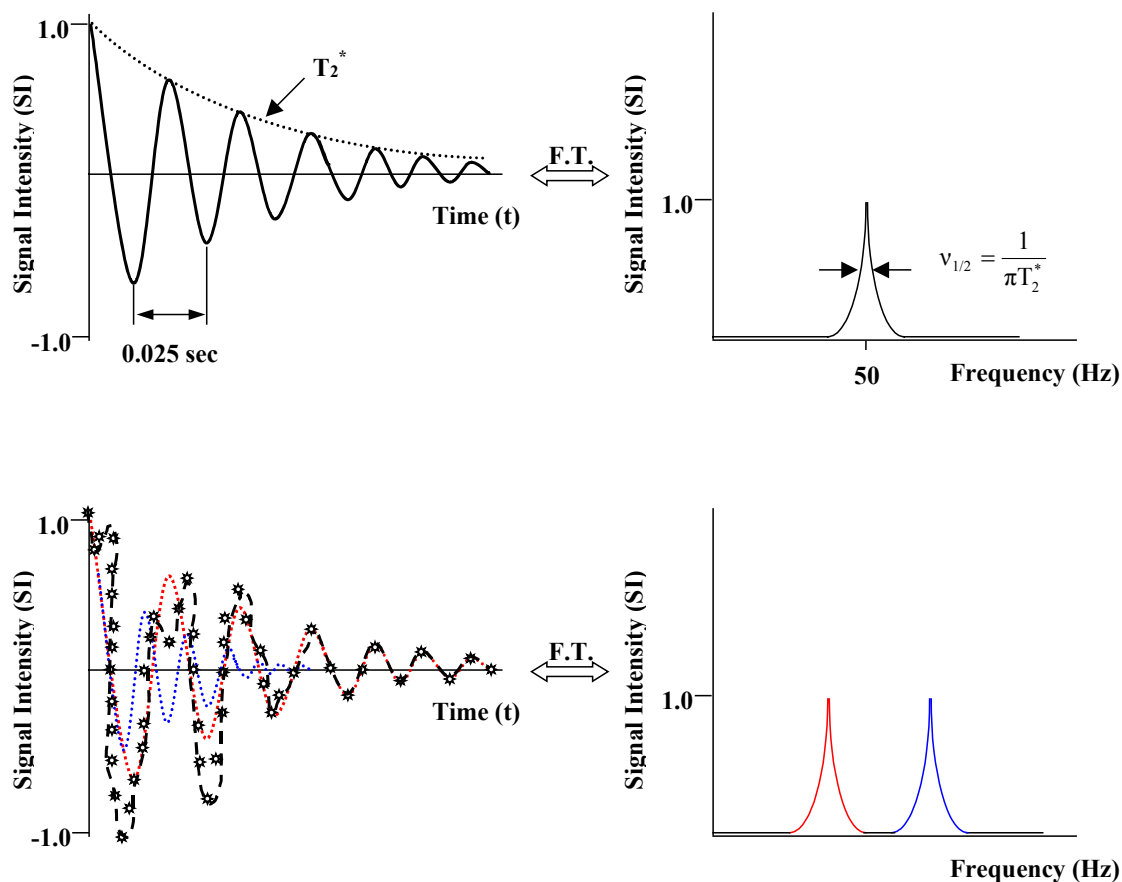


Figure 1-17: Sample FIDs and their 1D Fourier transformations (FT). Top: Conversion of a single exponentially-damped sinusoid between time and frequency space. The full-width-at-half-maximum height (FWHM) is inversely proportional to the exponential decay constant, in this case T_2^* , times $1/\pi$. Bottom: Conversion of two exponentially-damped sinusoids between time and frequency space. The black dashed line is the total FID, equivalent to the sum of the individual components (red, blue). These represent the two frequency components (red = low, blue = high).

1.4.2 Slice Selection and Slice Offset

For excitation of a particular range of frequencies (i.e., bandwidth), a sinc-shaped ($\sin(x)/x$) RF pulse of a particular duration is applied. The sinc pulse, usually on the order of three to four milliseconds in duration, corresponds to a rectangular shaped excitation (power spectrum) in the frequency domain (Fig. 1-18, top). Slice selection is performed through the application of a linear magnetic field gradient during the RF excitation, yielding dependence of the Larmor frequency on the spatial location of the nuclei:

$$\omega(z) = \gamma(B_0 + G_z z) \quad (1.30)$$

where γ is the gyromagnetic ratio, B_0 is the external magnetic field, G_z is the linear gradient applied along the z-direction, z is the position along the gradient direction, and $\omega(z)$ is the angular frequency corresponding to a particular location along the z-axis. This gradient, often referred to as a slice-select gradient, may be applied along the x, y, or z axes depending on the desired slice orientation. If the slice-select gradient is applied during RF pulse transmission, the range of frequencies (i.e., bandwidth = $\Delta\omega$) excited corresponds to a range of magnetic field strengths proportional to the slice thickness, Δz (Fig. 1-18, bottom):

$$\Delta z = \frac{\Delta\omega}{\gamma G_z} \quad (1.31)$$

where γ is the gyromagnetic ratio, G_z is the linear gradient applied along the z-direction, $\Delta\omega$ is the bandwidth, and Δz is the slice-thickness.

Slice Thickness Adjustment

In order to change the slice thickness, either the bandwidth or the strength of the slice-select gradient must be changed. In MRI, the bandwidth (and hence the RF pulse duration) is usually kept constant while the slice-select gradient strength is increased or decreased depending on the desired slice thickness. In order to decrease the slice thickness, a stronger (i.e., steeper) gradient is used.

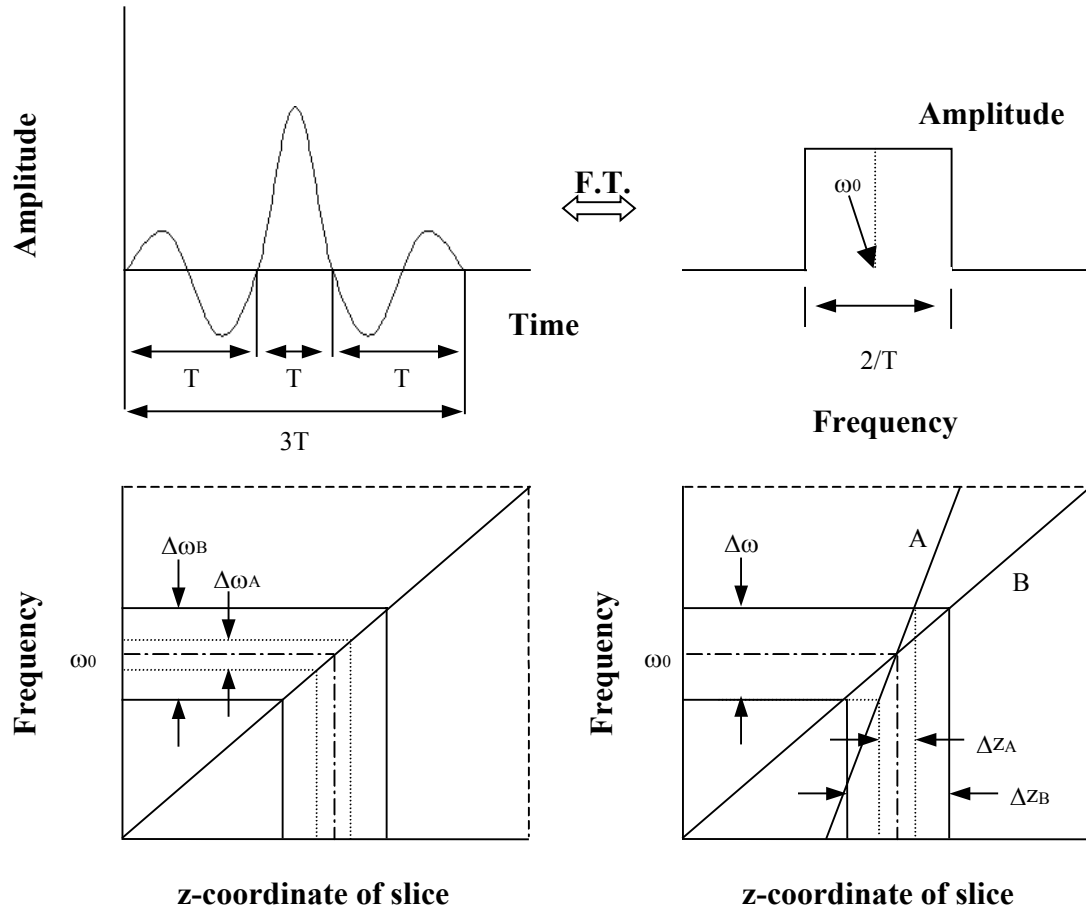


Figure 1-18: Slice-selection methods. Top: To excite a particular range of frequencies, a sinc ($\sin(x)/x$) pulse is applied. This sinc pulse in the time domain corresponds to a rectangular excitation profile in the frequency domain. Top Left: Time-domain, 3-lobe, sinc pulse of duration $3T$. Top Right: Frequency-domain rectangular excitation profile. Bottom: To change the slice thickness, the bandwidth ($\Delta\omega$) or the strength of the linear gradient (G) needs to be altered. In MRI, the bandwidth is generally kept constant and the magnetic field gradient is changed to obtain the desired slice thickness. Bottom Left: A narrower bandwidth is used to decrease the slice thickness ($\Delta z_A < \Delta z_B$). Bottom Right: At a specific bandwidth ($\Delta\omega$), a steeper magnetic field gradient (line A) is used to decrease the slice thickness (Δz_A). By lowering the strength of the magnetic field gradient (line B), a thicker slice may be obtained (Δz_B).

Slice Offset

To change the slice position, the RF pulse frequency (i.e., carrier frequency) must be increased by a set amount relative to ω_0 . This frequency offset is dependent on the strength of the slice-select gradient and may be represented by the following equation:

$$\omega(z) = \gamma G_z z \tag{1.32}$$

equivalent to the latter half of Eq. 1.30. For example, for a slice offset of 1 cm in the presence of a 1 G/cm gradient, the frequency of the RF pulse must be increased by a value of 4258 Hz.

Image Acquisition: Addition of Slice-Select Gradients

With the addition of the slice-select gradients, the MRI pulse sequence diagram for a standard spin-echo experiment will include the slice-selective 90° and 180° RF pulses, the slice-select gradients, and the signal-acquisition period (Fig. 1-19). The frequency-encoding gradients and phase encoding gradients, as well as the rephasing gradients, still remain to be discussed.

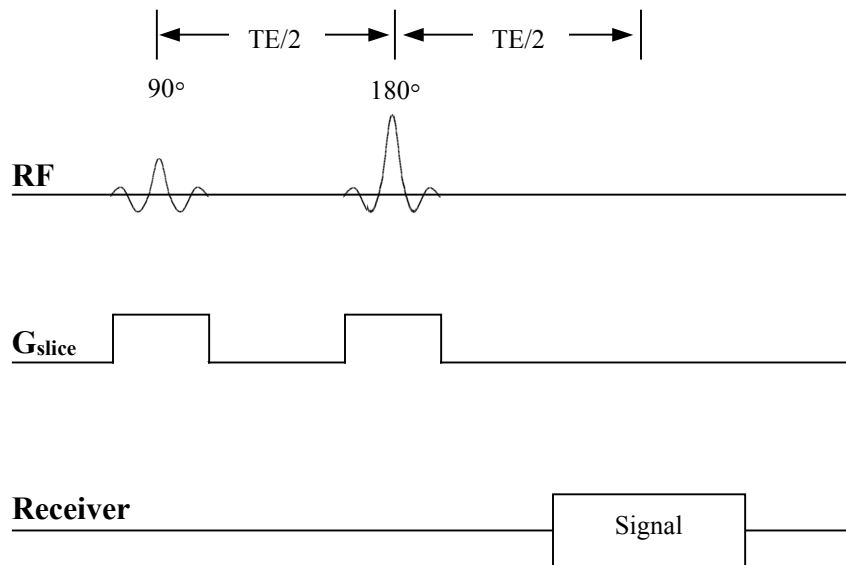


Figure 1-19: Spin-echo pulse sequence diagram with the 90° and 180° slice-selective RF pulses, the slice-select gradients, and the signal-acquisition period.

1.4.3 Frequency-Encoding and Phase-Encoding

In order to further encode the spatial information within each slice, in particular, the amount of signal corresponding to each voxel (volume element) of interest, frequency-encoding and phase-encoding techniques are employed. Signal composition (phase, frequency, and amplitude), described briefly in section 1.4.1, is extremely important to spatial localization methods. The measured signal from a single-slice MRI experiment, without frequency-encoding or phase-encoding gradients, is the signal from the *entire* slice.

Frequency-Encoding

In order to obtain the spatial information along the x-direction of the slice plane, for example, a gradient G_x is applied during acquisition of the echo. This is termed the frequency-encoding or read-out gradient. Based on the spatial extent of the nuclei, the application of this gradient changes the B_{eff} experienced for each voxel, and, therefore, the precessional frequency, ω_{eff} . Again, there will be a range of frequencies (signal bandwidth) corresponding to the spatial location of the nuclei, and dependent on the gradient amplitude. This relationship, a variation of Eq. 1.31, is equivalent to:

$$\text{FOV}_x = \frac{\text{BW}}{\gamma G_x}, \quad \text{with } \text{BW} = \frac{N_{\text{freq}}}{\text{AT}} \quad (1.33)$$

where γ is the gyromagnetic ratio (Hz/G), BW is the signal bandwidth (Hz), G_x is the gradient amplitude (G/cm), and FOV_x is the field of view along the readout or x-direction in this case (cm). BW, which is usually user specified, is dependent on the number of points sampled (N_{freq}) and the acquisition time (AT). From Eq. 1.33, increased spatial resolution in the readout direction may be obtained via the following methods: decreased FOV_x with a corresponding increase in G_x , increased N_{freq} , or decreased BW. For a constant BW, increasing the N_{freq} will increase the AT and yield a reduction in the SNR for each sampling point (i.e., the greater the number of points sampled, the lower the available signal on a point-by-point basis). Similarly, decreasing BW increases the SNR by reducing the available noise on a point-by-point basis. In general, the resolution is greater for adjustment of the gradient amplitude (G_x) than that of the BW. With this in mind, BW (and hence AT) is usually kept constant in MRI experiments and G_x is varied based on the desired FOV_x .

Image Acquisition: Addition of Frequency-Encoding Gradients

With the addition of the frequency-encoding (readout) gradients, the MRI pulse sequence diagram for a standard spin-echo experiment will include the slice-selective 90° and 180° RF pulses, the slice-select gradients, the readout gradients, and the signal acquisition period (Fig. 1-20). The phase-encoding gradients as well as the rephasing gradients still remain to be discussed.

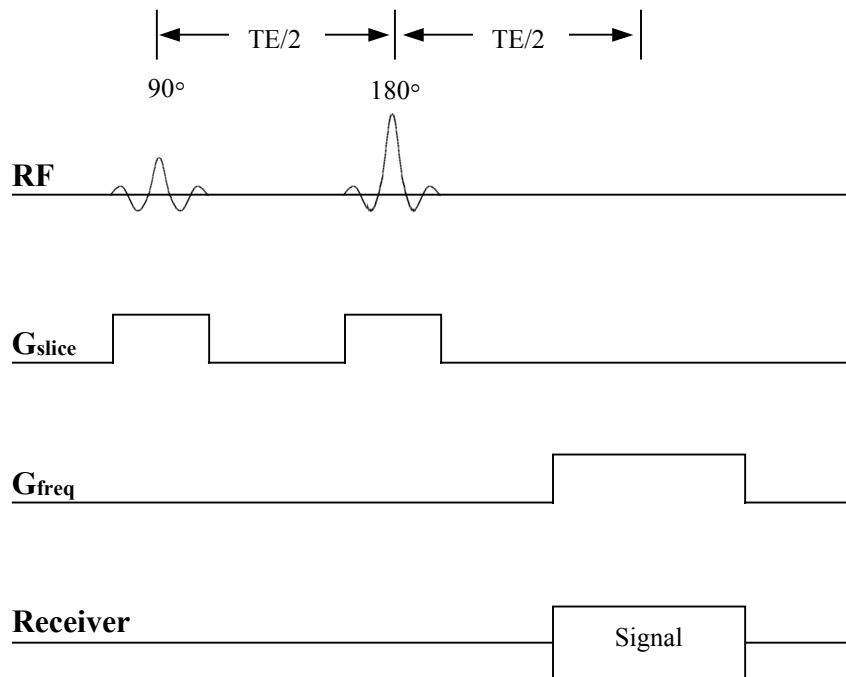


Figure 1-20: Spin-echo pulse sequence diagram with the 90° and 180° slice-selective RF pulses, the slice-select gradients, the frequency-encoding (readout) gradients, and receiver channels.

Phase-Encoding

In order to get the spatial information along the y-direction of the slice plane, a gradient G_y is applied. This is termed the phase-encoding gradient. G_y is usually applied between the slice-selective RF pulses—in the case of the spin-echo experiment the phase-encoding gradient would be applied between the 90° and 180° pulses. Although G_y may also be applied after the slice-selective RF pulses, it must be applied prior to the echo or

readout. Based on the spatial extent of the nuclei, application of this gradient induces a phase-shift for each voxel. Again, there exists a range of precessional frequencies corresponding to the spatial location of the nuclei, dependent on the gradient amplitude:

$$\omega(y) = \gamma G_y y \quad (1.34)$$

where γ is the gyromagnetic ratio (Hz/G), G_y is the gradient amplitude (G/cm), y is the position along the phase-encoding or y -direction (cm), and $\omega(y)$ is the frequency of precession experienced at the y -position (Hz). Exposure to G_y for a period of time t generates a phase shift, $\Delta\phi$, of specific magnitude:

$$\Delta\phi = \gamma G_y y t \quad (1.35)$$

where γ is the gyromagnetic ratio (Hz/G), G_y is the gradient amplitude (G/cm), and y is the position along the phase-encoding or y -direction (cm). Since the phase information imparted to the nuclei is retained through the experiment, it is standard practice to repeat the pulse sequence a number of times (N_{phase}) using an equivalent number of phase-encoding gradient increments ($G_{y\text{-inc}}$). In MRI, a bipolar phase-encoding gradient is used, meaning the phase imparted will be $\pm 180^\circ$, with a -180° phase shift and a $+180^\circ$ phase shift experienced by the near and far edges of FOV_y , respectively. With this in mind, $G_{y\text{-inc}}$ may be defined as:

$$G_{y\text{-inc}} = \frac{1}{\gamma \text{FOV}_y t} \quad (1.36)$$

where γ is the gyromagnetic ratio, FOV_y is the field of view in the phase-encoding or y -direction, and t is the time of $G_{y\text{-inc}}$ application. From Eq. 1.35 and the number of phase-encoding steps (N_{phase}), the maximum amplitude (positive or negative) of $G_{y\text{-inc}}$ may be determined.

Image Acquisition: Addition of Phase-Encoding Gradients

With the addition of the phase-encoding gradients, the MRI pulse sequence diagram for a standard spin-echo experiment will include the slice-selective 90° and 180° RF pulses, the slice-select gradients, the readout gradients, the phase-encoding gradients, and the signal acquisition period (Fig. 1-21). The rephasing gradients still remain to be discussed.

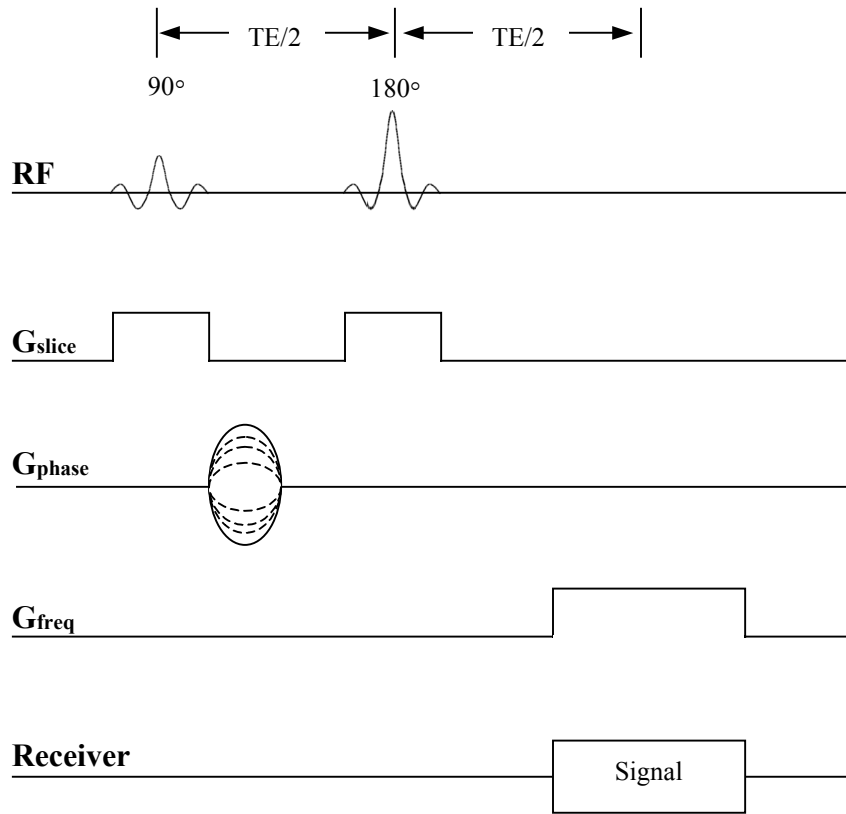


Figure 1-21: Spin-echo pulse sequence diagram with the 90° and 180° slice-selective RF pulses, the slice-select gradients, the phase-encoding gradients, the frequency-encoding (readout) gradients, and the signal acquisition period.

1.4.4 Rephasing Gradients

Although it would seem that the MRI pulse sequence diagram is now complete for a standard spin-echo experiment, without rephasing gradients for both slice-selection and readout the acquired signal and final image intensity would be diminished. Because there is dephasing of the nuclei during application of the slice-select gradient, a rephasing gradient is applied after the fact for phase-shift correction (i.e., all the nuclei should have the same phase). Dephasing is also present during the application of the readout gradient. In order to have the nuclei in phase at the midpoint of readout (i.e., the echo is centered during signal acquisition), a rephasing gradient is applied prior to application of the readout gradient. The addition of the rephasing gradients to the pulse sequence diagram for the standard spin-echo experiment is diagrammed in Fig. 1-22.

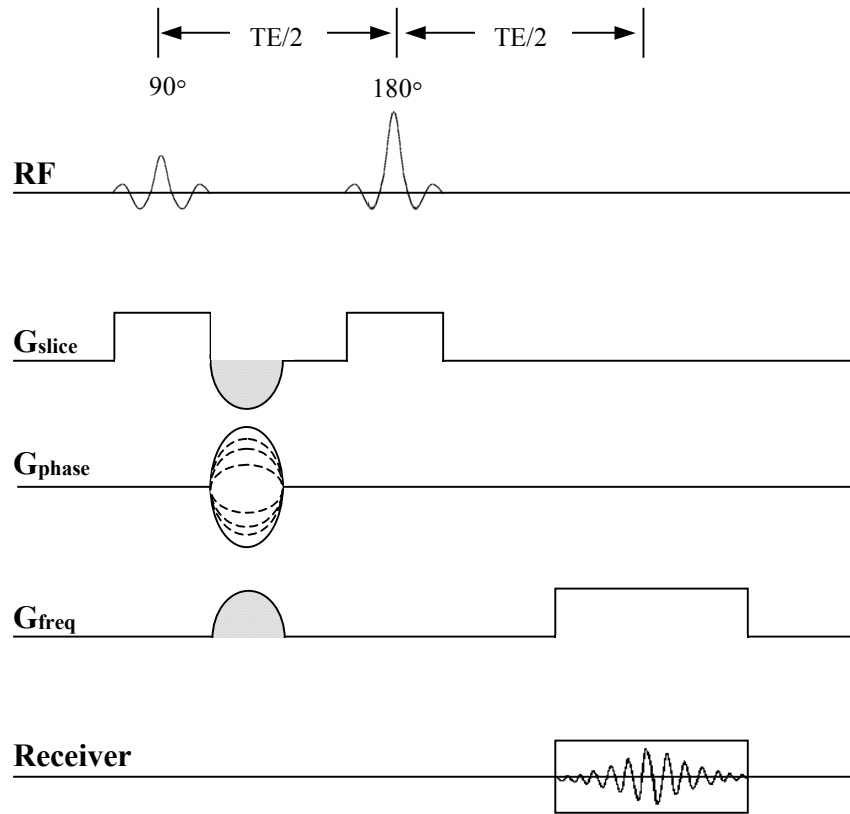


Figure 1-22: Complete spin-echo pulse sequence diagram. Individual components include: the 90° and 180° slice-selective RF pulses, the slice-select gradients, the phase-encoding gradients, the frequency-encoding (readout) gradients, the rephasing gradients (shaded gray), and receiver channel (with the resultant signal acquisition period).

1.4.5 Signal Processing: Conversion Between K-Space and Image Space

Besides a thorough coverage of MRI image acquisition techniques, a methodological discussion of the conversion between data space and image space is warranted. A brief description of the utility of 1D-FT for NMR spectroscopic methods was given in section 1.4.1, and will be expanded upon here. Specifically, the properties of k-space and the use of the 2D-FT for conversion from k-space to image space will be discussed.

What is K-Space?

K-space is a 2D presentation of the raw data, with frequency-encoding (Hz) along the first axis and phase-encoding along the second. Both axes have inclusion of time. As the

frequency-encoding axis (ν) is traversed, each step or increment is a single sampling point. The total length of the axis is equivalent to the number of sampling points N_{freq} acquired over the acquisition time AT . As the phase-encoding axis (ϕ) axis is traversed, each step or increment is a single phase-encoding increment (ϕ_{inc}) related to the increment of the gradient amplitude, $G_{y\text{-inc}}$, and the total number of increments (N_{phase}). Overall, the matrix size associated with the k-space representation of the data is equivalent to $N_{\text{freq}} \times N_{\text{phase}}$.

K-Space Composition

Since a rephasing gradient is applied in order to center the echo in the acquisition window, it follows that individual rows of k-space along the frequency direction have the weakest amplitude at the beginning and end of each row (i.e., high frequencies). In contrast, the center of each row of k-space (zero frequency) has maximal amplitude because it contains the signal contribution of the spin echoes (i.e., where the nuclei are in phase). Additionally, since the phase-encoding gradient dephases the signal, it follows that individual rows acquired with higher amplitude phase gradients have greater signal dephasing and smaller amplitude than those acquired with a lower amplitude phase gradients. Overall, the center of k-space (where the phase and frequency shifts are near zero) contains maximal signal intensity. In this case, the central portion of k-space may appear more important than the remainder as it contains the majority of the spatial information. However, if the peripheral regions of k-space (i.e., the edges) are disregarded, the fine detail (i.e., high frequency information) of the image is lost and the sharp interfaces between various regions are degraded. The idea of k-space and the importance of the central and peripheral regions to image quality are diagrammed in Fig. 1-23.

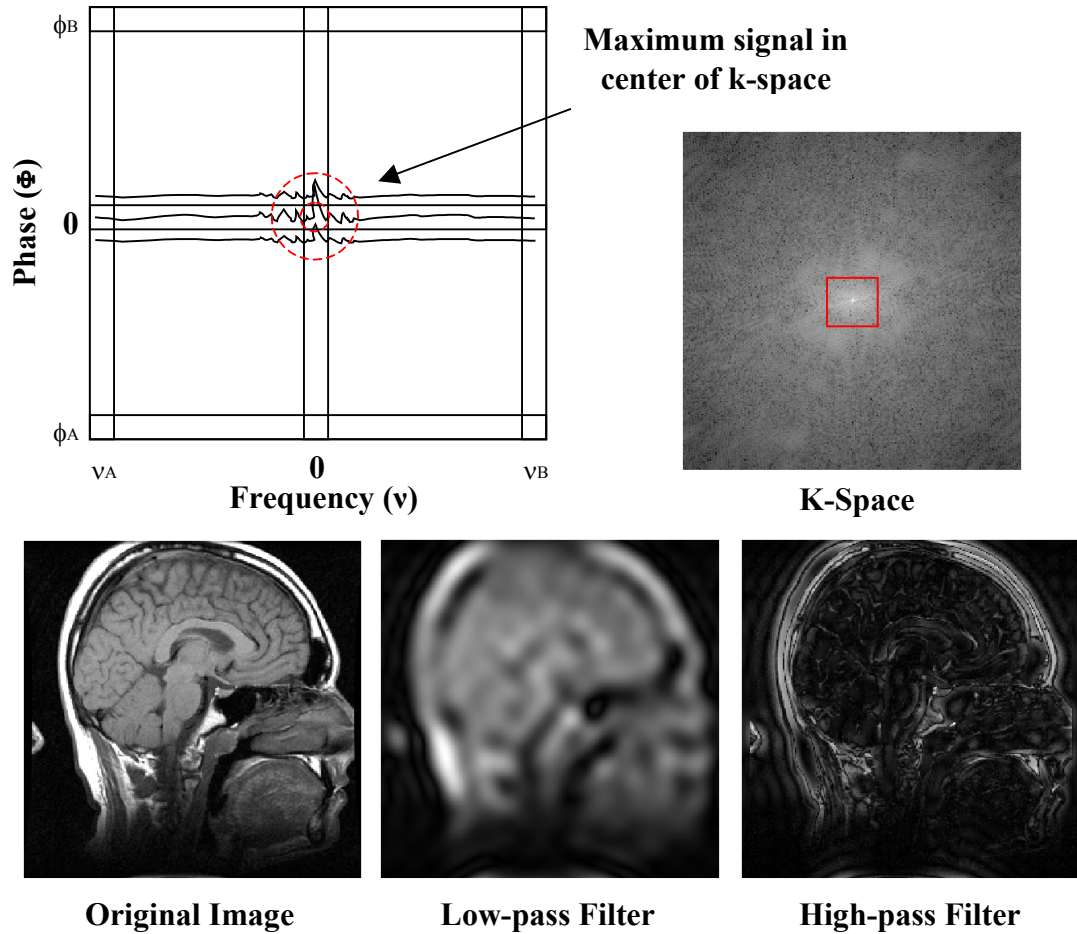


Figure 1-23: K-space composition and importance of both low- and high-frequency regions. Top Left: k-space is the 2D raw data with dimensions a function of frequency and phase. The center of each row of k-space (i.e., zero frequency) has the maximum amplitude because it contains the signal contribution of the spin echoes (i.e., where the nuclei are in phase). Moving away from the center of each row, the nuclei become progressively more out of phase, decreasing the signal amplitude. Frequencies at ν_a and ν_b have the weakest signal. Since the phase-encoding gradient dephases the signal, rows acquired with higher phase-encoding gradient (i.e., at ϕ_a or ϕ_b) have increased dephasing from the additional phase imparted to the nuclei. Top Right: Sample k-space data. Bottom Left: Corresponding image. Bottom Middle: Image constructed from only data at the center of k-space. Bottom Right: Image constructed from only data at the edges of k-space.

Fourier Reconstruction

The 2D k-space representation of the data may be converted into image space using a 2D-FT. Application of a 2D-FT permits conversion of the frequency and phase information into an image with signal amplitude dependent on spatial location, similar to application of the 1D-FT for conversion of NMR spectroscopic data from the time domain to the frequency domain (described in Section 1.4.1). Most MRI systems perform a 2D-FT using the fast Fourier transform (FFT), a faster method than that of the digital Fourier transform (DFT). As the signal (FID) is sampled at a constant interval, each data point making up the total FID will have discrete amplitude and time values. Therefore, for a DFT the number of calculations required to solve the series of delta functions from k-space for image formation is $N_{\text{freq}} \times N_{\text{phase}}$. For the FFT, the required number of calculations is instead $N_{\text{phase}} \times \log_2 N_{\text{freq}}$. In order for $\log_2 N_{\text{freq}}$ to be a whole number, the N_{freq} needs to be a power of 2 (i.e., 64, 128, 256, etc.) when the FFT is used. It is usually standard to then use an equivalent N_{phase} for a square matrix and FOV, or an N_{phase} that is at least a power of 2 if not equivalent to N_{freq} . Matrices that are 64×64 , 128×128 , 256×256 are standard in animal MRI studies as the FOVs are at least an order of magnitude smaller than in the clinical setting.

1.5 Imaging Methods

With the growing number of MRI pulses sequences in practice today an understanding of the fundamentals, such as spin-echo (SE) imaging and gradient-echo (GE) imaging, as well as fast imaging techniques such as echo-planar imaging (EPI), is necessary. In addition to these methods, employed for generation of T_1 , T_2 , and T_2^* contrast, diffusion-weighted imaging (DWI) and perfusion-weighted imaging (PWI) methods will be discussed. This information will provide suitable background for the MRI methods applied in later chapters (specifically Chapters 3-4 and Chapters 6-7).

1.5.1 Spin-Echo (SE) Imaging

Hahn Spin-Echo (HSE)

The mechanisms of spin-echo formation through application of 90° and 180° RF pulses were described previously in Section 1.3.2, with a step-by-step discussion of the spin-

echo pulse sequence for image acquisition in Section 1.4. This type of spin-echo, first discovered by Hahn in 1950 (12), involves application of two slice-selective RF pulses ($\sin x/x$), a 90° and a 180° , separated by a time $t = TE/2$ (Fig. 1-22). During the transmit phase, the slice-selective gradients are applied in order to excite a specified frequency bandwidth (BW). Application of the 90° RF pulse flips the longitudinal magnetization into the transverse plane. Immediately following the 90° RF pulse, a rephasing gradient is applied to remove the dephasing effect of the slice-select gradient. Concomitant with this rephasing gradient, the first increment of the phase-encoding gradient is applied, giving a specific amount of phase to the nuclei dependent on their spatial location along the phase or y-direction. Following the $t = TE/2$ period, the 180° RF pulse is applied to flip the magnetization about one of the transverse axes (x or y). Prior to acquisition of the echo, a pre-dephasing gradient is applied along the frequency-encoding direction. This is done to dephase the transverse magnetization and counteract the dephasing effects of the subsequent frequency-encoding gradient. Next, the receiver is turned on and the frequency-encoding gradient is applied, exciting a specific bandwidth (BW) based on the spatial location along the frequency or x-direction. At a time $t = TE/2$ following the 180° RF pulse, the echo formation reaches a maximum (i.e., the nuclei are in phase with one another). The total acquisition time (AT) is based on the receiver bandwidth (BW) and the number of sampling points (N_{points}) dependent on Nyquist's theorem. In order to obtain all of the spatial information for the phase-encoding direction, the pulse sequence is iterated N_{phase} times, equivalent to the total number of phase-encoding steps. The time for each of these iterations is termed the repetition time (TR); therefore, the total experiment time is $N_{\text{phase}} \times TR$.

Carr-Purcell-Meiboom-Gill (CPMG)

Performing image acquisition (either single-slice or multi-slice) according to the HSE method for a single TE value takes a reasonable amount of time. Difficulty in maintaining good temporal resolution arises when multiple images of varying TE value are desired for determination of T_2 . This may be overcome using the Carr-Purcell-Meiboom-Gill (CPMG) method (13,14) characterized by a single 90° RF pulse followed by a train of 180° RF pulses (N_{echoes}). The 90° and first 180° RF pulses are separated by a time $t = TE/2$, with each additional 180° spaced at time intervals $t = TE$. Multiple spin-

echoes occur (one after each 180° RF pulse) that are modulated by a T_2 -relaxation envelope. Application of the slice-select gradients, frequency- and phase-encoding gradients, and the rephasing gradients are diagrammed in Fig. 1-24. SE imaging via the HSE, CPMG, or fast imaging methods (to be discussed in the latter portion of Section 1.5) is of particular interest for identifying abnormalities from healthy tissue based on differences in T_2 relaxation.

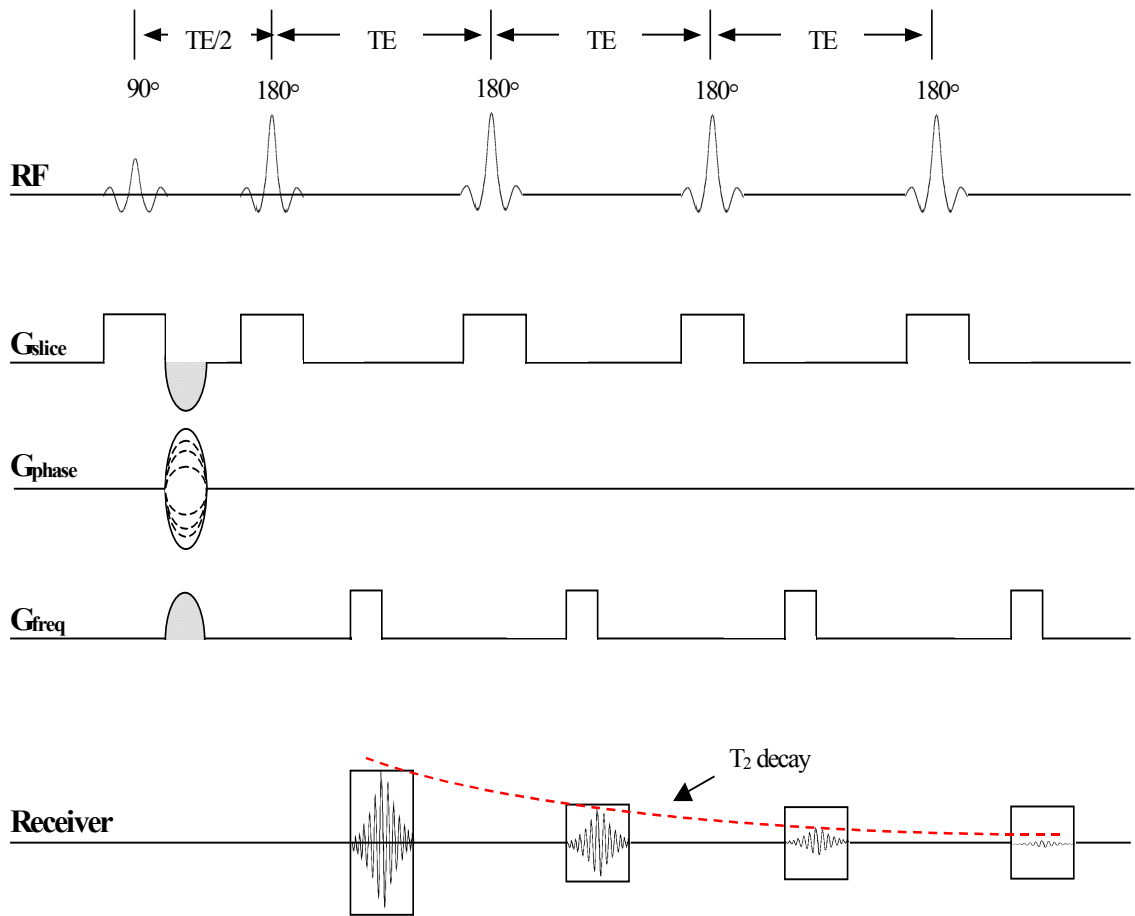


Figure 1-24: Carr-Purcell-Meiboom-Gill (CPMG) pulse sequence diagram. Individual components include: the 90° and 180° slice-selective RF pulses, the slice-select gradients, the phase-encoding gradients, the frequency-encoding (readout) gradients, the rephasing gradients (shaded gray), and receiver channels (with the resultant signal acquisition periods for individual spin-echoes).

1.5.2 Gradient-Echo (GE) Imaging

The mechanisms of gradient-echo (GE) formation involve application of a single RF pulse having a flip angle θ that is usually less than 90° . This partially flips the longitudinal magnetization into the transverse plane. Over time, dephasing from B_0 field inhomogeneities, magnetic susceptibility effects, and molecular diffusion effects induces decay of the transverse magnetization. This decay, termed T_2^* , was mentioned briefly in Section 1.3.2. After a time $t = TE$, echo formation is at a maximum. Similar to the HSE and CPMG sequences, the GE pulse sequence is repeated N_{phase} times, with a repetition time (TR) for each increment. Again, the total experiment time is $N_{\text{phase}} \times TR$. Since GE imaging uses a reduced-flip-angle RF pulse, it may be performed using much shorter TR values than the HSE or CPMG methods, significantly reducing the experiment time. GE imaging is of particular interest for applications using contrast-enhancement, such as vascular and perfusion imaging. The GE pulse sequence is diagrammed in Fig. 1-25.

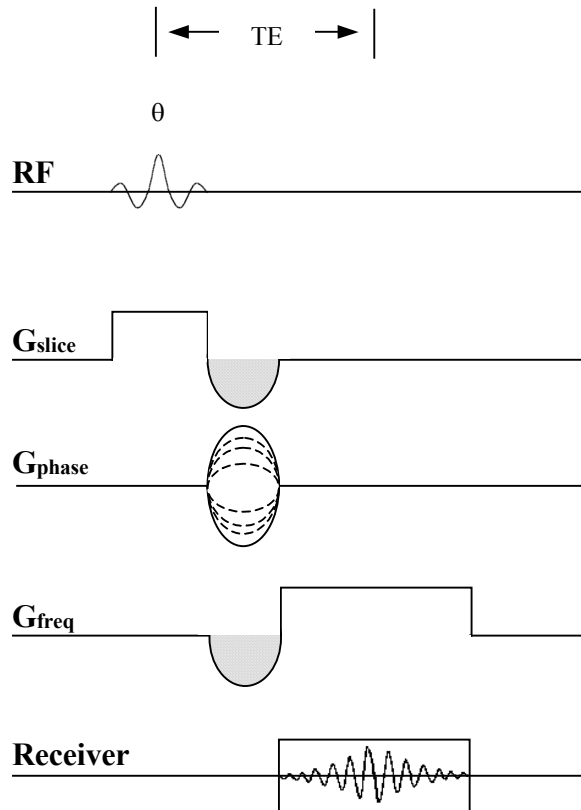


Figure 1-25: Gradient-echo (GE) pulse sequence diagram. Individual components include: the slice-selective RF pulse of flip angle θ , the slice-select gradient, the phase-encoding gradients, the frequency-encoding (readout) gradients, the rephasing gradients (shaded gray), and receiver channel (with the resultant signal acquisition period).

Optimization of Flip Angle θ

The SNR may be optimized for the GE sequence by employing the Ernst angle relationship. For a given TR and T_1 value, the maximum signal will be obtained using a flip angle equivalent to the Ernst angle (θ_E):

$$\cos \theta_E = e^{-TR/T_1} \quad (1.37)$$

where TR is the repetition time and T_1 is the spin-lattice relaxation. For long T_1 's, the maximum signal will occur at low flip angles ($\sim 30^\circ$).

1.5.3 Echo-Planar Imaging (EPI)

Prior to introduction of fast-imaging techniques, experiment times were on the order of 5-25 minutes depending on the FOV, number of slices, user-specified TR/TE values, and the number of averages (NEX) desired. In 1977, Peter Mansfield introduced a method now commonly known as echo-planar imaging, or EPI (10). Because of hardware limitations, it wasn't until the late 1980s that EPI became technically feasible, transforming it into the standard that exists today.

Single-shot EPI

Conventional MRI methods acquire k-space data on a line-by-line basis separated by a TR period (usually 10msec-3000msec), resulting in experiment times on the order of several minutes. In contrast, EPI acquires the k-space data in a single acquisition (one TR period). Since a single TR period is used, it is important to make sure that the total spatial encoding process is completed in the shortest time possible (i.e., using a short TE) in order to minimize effects of T_2/T_2^* decay. The EPI pulse sequence begins with application of the slice-select RF pulses and slice-select gradients, similar to the SE and GE methods described in Sections 1.5.1 and 1.5.2, respectively. The primary difference is the method of frequency-encoding and phase-encoding employed for fast imaging. The frequency-encoding gradient is applied in an alternating fashion (by switching the gradient polarity) for traversing k-space. In terms of the phase-encode gradients, two methods are common, one using a blipped gradients, the second using a ramped gradient. Application of the blipped phase-encode gradient occurs between the alternating application of the frequency-encode gradient, adding a small phase increment for each step. This is analogous to the approach used for phase-encoding in conventional MRI

(Fig. 1-26). For the ramped phase-encode gradient, constant gradient amplitude is applied during the alternating application of the frequency-encode gradient, permitting a 'zig-zag' pattern of traversing k-space (Fig. 1-27).

Optimizing EPI Image Quality

Imaging artifacts could potentially present a problem depending on the EPI sequence used. Although this is the case, the choice of parameters, image orientation, and hardware help in producing consistent image quality. Some sources of artifacts are: sensitivity to field inhomogeneities (particularly important in GE-EPI), phase-encode blurring, and ghosting. For SE-EPI, the latter two issues should be kept in mind. Phase-encode blurring occurs from T_2/T_2^* signal decay during readout. This may be minimized through reduction in the acquisition time (AT) by using a higher bandwidth (BW) for a given number of points sampled (N_{freq}). A shorter TE value should also be used to increase the overall SNR. Ghosting occurs from problems in collection of the echoes during readout. This is because odd and even echoes are acquired with alternating gradient polarity; therefore, any mismatch between them will result in a duplicate image of the object. These are referred to as N/2 or Nyquist ghosts. In order to reduce the potential of having Nyquist ghosts, gradient stability is important as well as minimized eddy currents. The analog-to-digital converter (ADC) rate should also match the rate of data collection (i.e., centering the echoes in the acquisition window).

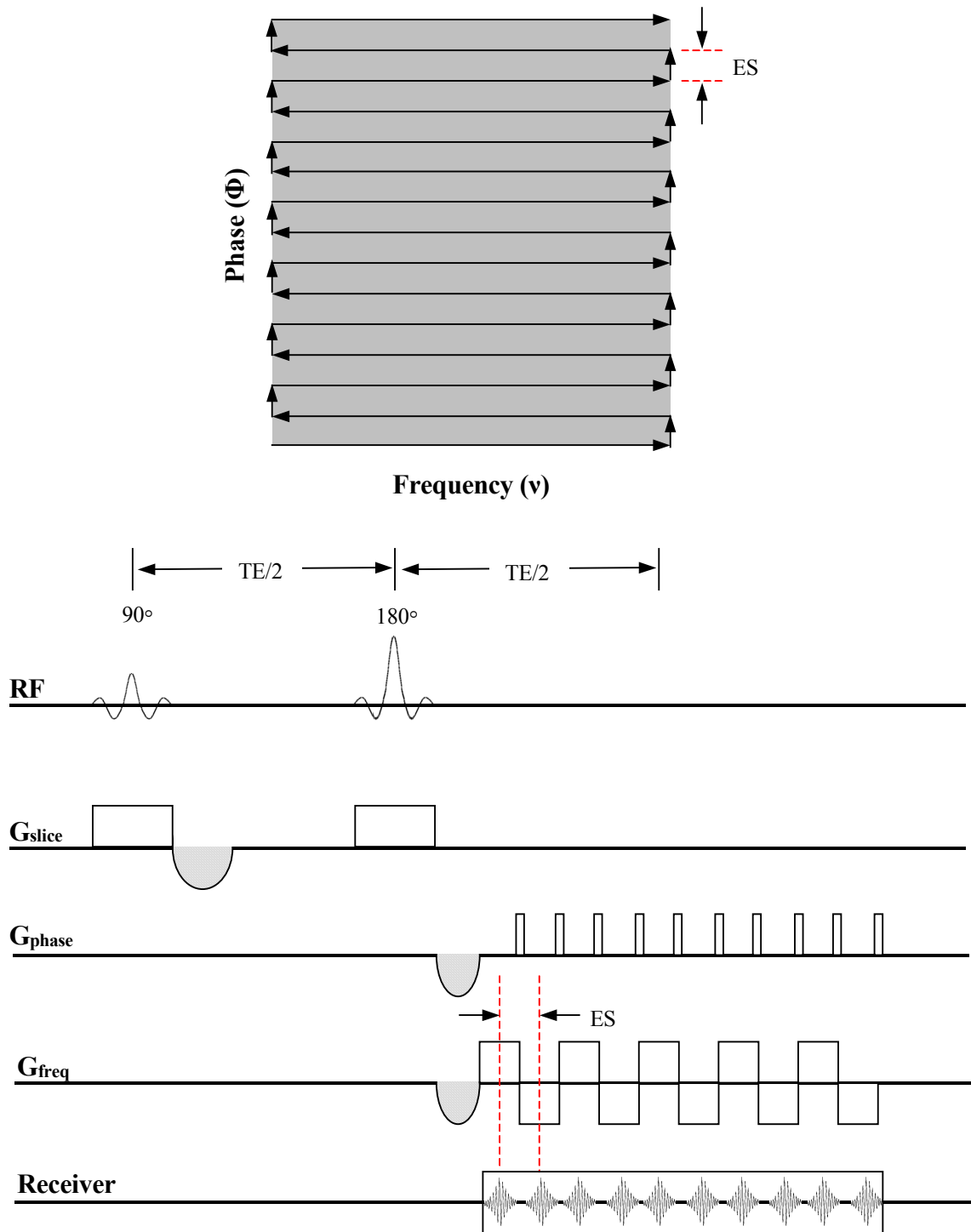


Figure 1-26: Spin-echo, echo-planar imaging (SE-EPI) pulse sequence diagram with blipped phase-encode gradient. Individual components include: the 90° and 180° slice-selective RF pulses, the slice-select gradients, the phase-encoding gradients, the frequency-encoding (readout) gradients, the rephasing gradients (shaded gray), and receiver channel (with the resultant signal acquisition period).

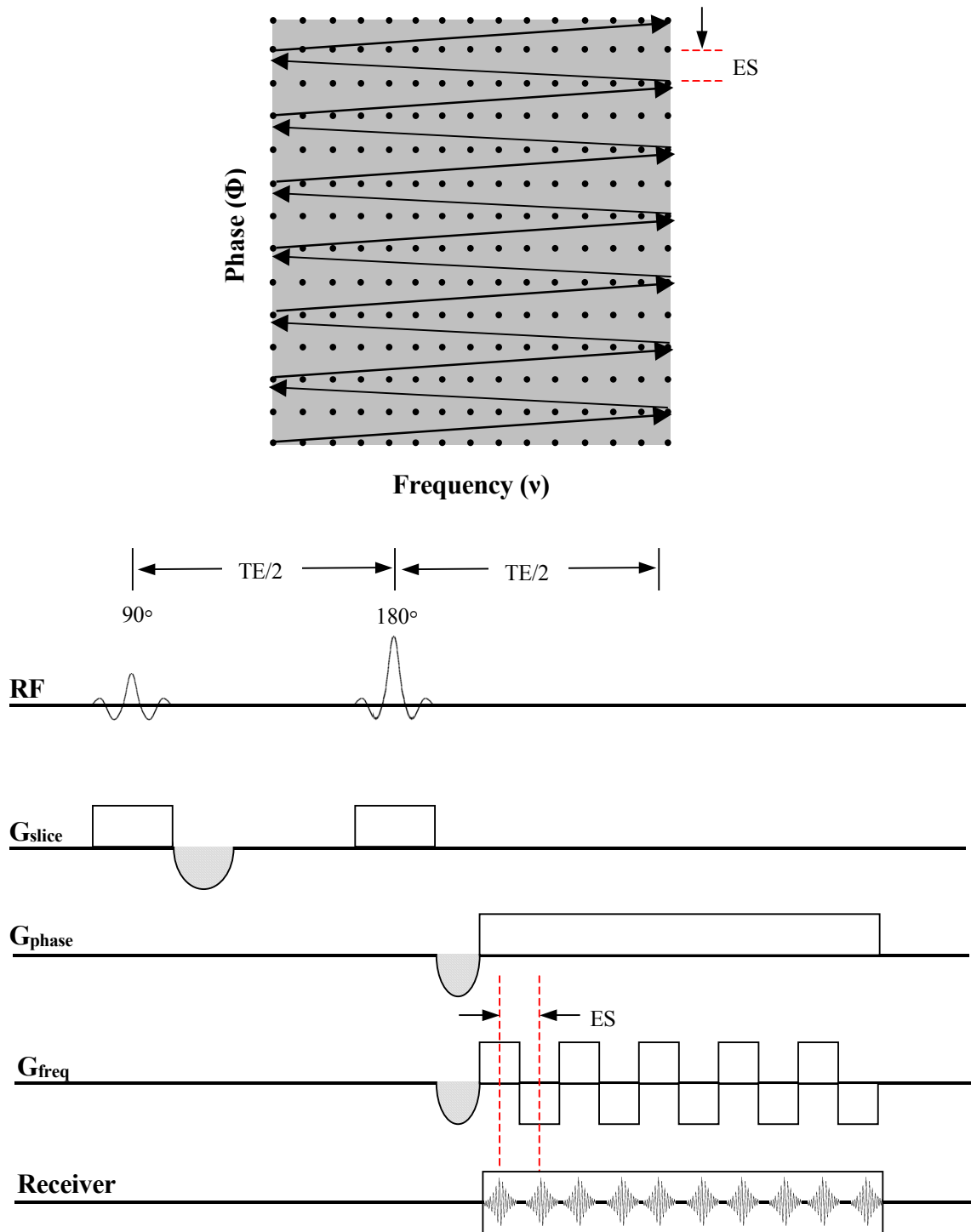


Figure 1-27: Spin-echo, echo-planar imaging (SE-EPI) pulse sequence diagram with a ramped phase-encode gradient. Individual components include: the 90° and 180° slice-selective RF pulses, the slice-select gradients, the phase-encoding gradients, the frequency-encoding (readout) gradients, the rephasing gradients (shaded gray), and receiver channel (with the resultant signal acquisition period).

1.5.4 Diffusion-Weighted Imaging

What is Diffusion?

Diffusion is the process of random molecular motion (termed Brownian motion) driven by the inherent thermal energy of a system. For unrestricted self-diffusion, as is the case in bulk-water, Einstein showed that the mean squared displacement is related to the elapsed time t (i.e., the diffusion time, t_{dif}):

$$\langle (r - r')^2 \rangle = 2nD_0 t_{\text{dif}} \quad (1.38)$$

where n is the number of dimensions and D_0 is the free diffusion coefficient. With an increase in t_{dif} there is a corresponding increase in the mean-squared displacement. In other words, there is a larger displacement based on initial (r) and final (r') positions because of the increased time allotted for diffusion. Because diffusion is limited in biological tissue (from presence of macromolecules, organelles, cell membranes, etc), measurement of the true diffusion coefficient D_0 is not possible. Instead, the apparent diffusion coefficient (ADC) is used to characterize the water mobility in tissue.

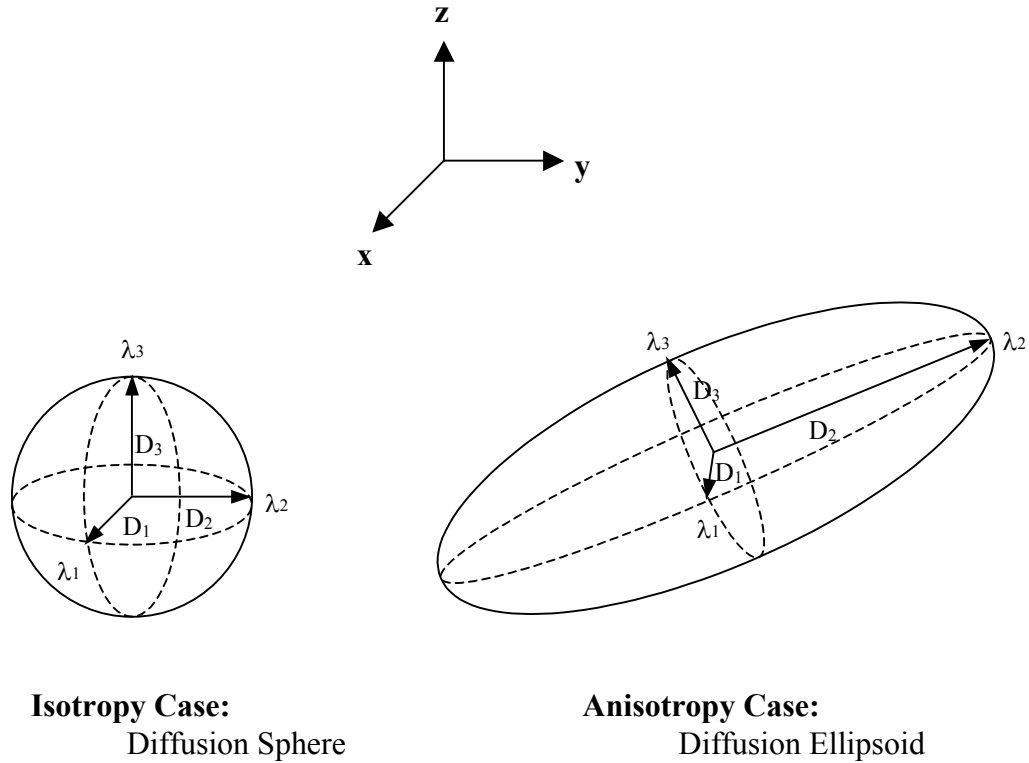
Isotropic and Anisotropic Diffusion

In the case of isotropic diffusion the ADC is independent of spatial orientation, meaning it may be measured along any direction and the same value will be obtained. Generally, the restrictions imposed in biological tissue introduce a dependence of the ADC on the spatial orientation. This is known as diffusion anisotropy. In this case, the directional dependence is described using a 2nd-rank tensor known as the diffusion tensor:

$$\bar{D} = \begin{bmatrix} D_{xx} & D_{xy} & D_{xz} \\ D_{yx} & D_{yy} & D_{yz} \\ D_{zx} & D_{zy} & D_{zz} \end{bmatrix} \quad (1.39)$$

Six of the nine elements of this 3×3 matrix represent an independent measure of diffusion. The elements along the diagonal are measurements of diffusion along the three principal axes (x , y , and z in Cartesian coordinates). The off-diagonal elements represent the degree of correlation between random motion along two of the principal directions. Using Eq. 1.38 and the diffusion values along the principal axes, displacement values for each direction may be obtained. These are diagrammed in Fig. 1-28 for the cases of isotropic diffusion and anisotropic diffusion. For isotropic diffusion (i.e., in CSF) the

diffusion tensor in Eq. 1.38 reduces to a single diffusion coefficient where $D_{xx} = D_{yy} = D_{zz} = D$ with all off-diagonal elements equal to zero. For anisotropic diffusion, at least one of the diffusion values along the principal axes is unequal to the remaining two.



Isotropy Case:
Diffusion Sphere

Anisotropy Case:
Diffusion Ellipsoid

Figure 1-28: Isotropic and anisotropic diffusion described by a diffusion sphere and diffusion ellipsoid, respectively. The semiaxes are equal to the amplitude of the diffusion tensor eigenvalues D_1 , D_2 , and D_3 , with the directions of the three axes coincident with the eigenvectors λ_1 , λ_2 , and λ_3 . For isotropic diffusion, $D_1 = D_2 = D_3 = D$. For anisotropic diffusion, at least one of the diffusion values (D_1 , D_2 , D_3) differs from the remaining two.

Indices of Isotropy and Anisotropy

In order to eliminate the diffusion dependence based on sample placement with respect to the applied magnetic-field gradients, measurement of the average ADC may be performed. The average ADC, also termed the mean diffusivity, is calculated using the trace of the diffusion tensor:

$$\langle D \rangle = \frac{\text{Tr}(\bar{D})}{3} = \frac{D_1 + D_2 + D_3}{3} \tag{1.40}$$

with $D_1 = D_{xx}$, $D_2 = D_{yy}$, and $D_3 = D_{zz}$ (D_1 , D_2 , and D_3 are often referred to as the principal diffusivities). This provides a scalar measure for isotropic diffusion. In addition, two indices of anisotropy, relative anisotropy (RA) and fractional anisotropy (FA), permit estimation of diffusion anisotropy and, therefore, a measure sensitive to tissue fiber orientation and connectivity (15). The RA index provides a ratio between the anisotropic and isotropic components:

$$RA = \frac{1}{\sqrt{3}\langle D \rangle} \sqrt{\sum_{i=1}^3 (D_i - \langle D \rangle)^2} \quad (1.41)$$

The RA index is a dimensionless quantity that yields values between 0 and $\sqrt{2}$, representing purely isotropic diffusion and purely anisotropic diffusion, respectively. The FA index is similar to the RA index in the respect that it is based on the standard deviations of the principal diffusivities from the mean diffusivity, but differs by method of normalization:

$$FA = \sqrt{\frac{3}{2}} \frac{\sqrt{\sum_{i=1}^3 (D_i - D_{\text{avg}})^2}}{\sqrt{\sum_{i=1}^3 D_i^2}} \quad (1.42)$$

The FA index is a dimensionless quantity that yields values between 0 and 1, representing purely isotropic diffusion and purely anisotropic diffusion, respectively.

Diffusion-Imaging

The method of diffusion-weighted imaging (DWI) was first introduced by Stejskal and Tanner in the 1960s (16), with in vivo DWI coming into practice in the 1980s (17). It involves the application of a pair of gradient pulses of particular amplitude (G) and duration (δ) separated by a time Δ , resulting in an effective diffusion time t_{dif} equal to $\Delta\delta/3$ and $\Delta\delta/4$ for rectangular-shaped and sine-shaped gradients, respectively. The application of the first gradient imparts phase (ϕ) to the nuclei:

$$\phi_1 = \int_0^T \omega dt = \gamma \int_0^T G x(t) dt = \gamma G [x(T) - x(0)] \quad (1.39)$$

where ω is the precessional frequency, dt is the time derivative, γ is the gyromagnetic ratio, G is the gradient applied (usually along the x , y , or z axes, but potentially any

direction), x_0 is the initial position of the nuclei, and $x(t)$ is the position of the nuclei at a time t . Next, the nuclei are allowed to diffuse for a time t_{dif} , after which a second gradient is applied. This gradient removes the phase imparted by the first gradient:

$$\phi_2 = -\int_T^{2T} \omega dt = -\gamma \int_T^{2T} G x(t) dt = \gamma G [x(T) - x(2T)] \quad (1.40)$$

If the nuclei did not move, the phase accumulation would be zero:

$$\phi_1 + \phi_2 = \gamma G [x(0) - x(T)] + \gamma G [x(T) - x(2T)] = 0 \quad (1.41)$$

With no movement, $x(0) = x(2T)$, and all terms cancel. If the nuclei do move, there will be the two phase terms ϕ_1 and ϕ_2 will not cancel. This net phase accumulation is equivalent to the following:

$$\phi_1 + \phi_2 = \gamma G [x(0) - x(2T)] \neq 0 \quad (1.42)$$

Any phase accumulation resulting from the movement of the nuclei yields exponential attenuation of the MRI signal:

$$M = M_0 e^{-bD} = M_0 e^{-(\gamma^2 G^2 \delta^2) t_{\text{dif}} D} \quad (1.43)$$

where M and M_0 are the signal intensities with and without diffusion, respectively, D is the diffusion coefficient along the direction of the applied diffusion gradient, b is the b-value or b-factor that controls the diffusion-weighting in individual images, and t_{dif} is the diffusion time. The b-value is user-defined by the gyromagnetic ratio γ , the gradient strength G , the duration of the diffusion gradients δ , and the diffusion time t_{dif} . A spin-echo, diffusion-weighted imaging (SE-DWI) pulse sequence is diagrammed in Fig. 1-29. Diffusion weighting may be incorporated into any imaging technique, although it is mainly used with spin-echo imaging methods (such as HSE and SE-EPI). In the SE-DWI method, there is additional signal decay based on T_1 and T_2 effects; therefore, the signal intensity M will be weighted to some degree based on the chosen TR and TE values. To reduce these effects a long TR and short TE are generally used.

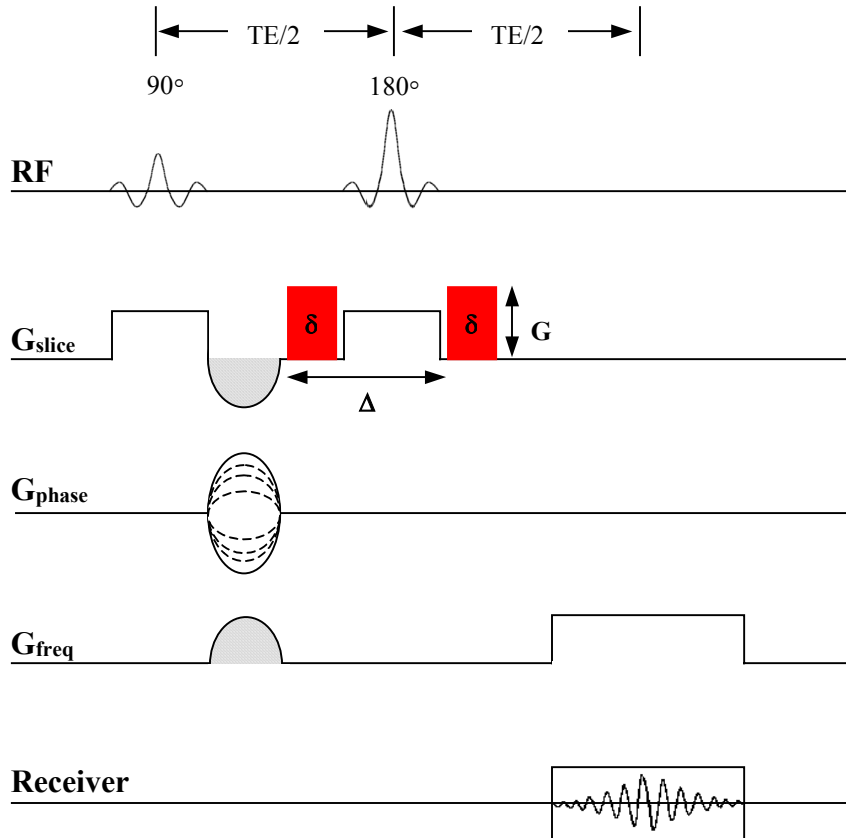


Figure 1-29: Spin-echo, diffusion-weighted imaging (SE-DWI) pulse sequence diagram. Individual components include: the 90° and 180° slice-selective RF pulses, the slice-select gradients, the phase-encoding gradients, the frequency-encoding (readout) gradients, the rephasing gradients (shaded gray), and receiver channel (with the resultant signal acquisition period). The diffusion gradients (highlighted red) of amplitude G and duration δ are separated by a time Δ , resulting in an effective diffusion time t_{dif} (equal to $\delta\Delta/3$ and $\delta\Delta/4$ for rectangular-shaped and sine-shaped gradients, respectively). Although they are diagrammed along the slice direction, the diffusion gradients may be applied along any direction.

1.5.5 Dynamic Contrast-Enhanced Perfusion Imaging

What is Perfusion?

Perfusion refers to the blood flow of a system (i.e., a specific tissue or organ). Changes in vascular morphology within that system induce alterations in blood flow and may be characterized using contrast enhancement. Rosen *et al.* (18,19) employed T_2^* -weighted EPI for dynamic contrast-enhanced perfusion imaging using a gadolinium chelate. NMR contrast agents such as gadolinium-based chelates cause reductions in T_1 and T_2 through alterations in the local magnetization following bolus-injection via the bloodstream. Based upon the relaxivity R_2 and concentration $[Gd]$ of the contrast agent, the T_2 changes in the following manner:

$$\frac{1}{T_2} = \frac{1}{T_2^0} + R_2 \times [Gd] \quad (1.44)$$

where T_2^0 is the transverse relaxation time of blood in the absence of contrast agent. Rapid acquisition of images both pre- and post-contrast injection (i.e., using EPI) permit tracer kinetic analysis and estimations of parameters such as relative cerebral blood volume (rCBV) and vascular transit time (VTT). These two parameters, rCBV and VTT, allow calculation of a cerebral blood flow index (CBF_i).

Extraction of Tracer Kinetic Parameters

Following acquisition of a series of EP images during bolus administration of the contrast agent, the changes in the T_2 relaxation rate, $\Delta R_2(t)$, may be obtained:

$$\Delta R_2(t) = -\frac{1}{TE} \times \ln \left[\frac{M(t)}{M_0} \right] \quad (1.45)$$

where $M(t)$ is the signal intensity at a time t during bolus passage of the contrast agent and M_0 is the signal intensity value at baseline pre-contrast. Fitting the data using a gamma-variate function and non-linear regression (20), integration of the $\Delta R_2(t)$ curve yields a measure of rCBV over the course of the entire experiment (in time T):

$$rCBV = \int_{\tau}^{\tau+T} \Delta R_2(t) dt \quad (1.46)$$

Further estimation of VTT is obtained from the first moment of the $\Delta R_2(t)$ curve:

$$rCBV = \int_{\tau}^{\tau+T} \Delta R_2(t) dt \quad (1.47)$$

Per previous discussion by Hamberg *et al.* (21), the perfusion-weighted image series, along with Eqs. 1.46 and 1.47, are used to calculate the CBF index:

$$CBF_i = \frac{rCBV}{VTT} \quad (1.48)$$

Perfusion Imaging

For rapid acquisition of an image series, either SE-EPI or GE-EPI may be employed. Although contrast agents alters both T_2 and T_2^* , SE-EPI for T_2 -weighted imaging has the advantage of increased SNR without the problem of magnetic field inhomogeneities or susceptibility effects (as is the case in GE-EPI for T_2^* -weighted imaging). The SE-EPI method has been diagrammed previously in Fig. 1-27. The number of repetitions (N_{rep}) may be specified such that the total experiment time is equal to the N_{rep} multiplied by the TR value, with an image taken at every TR increment.

References

1. Gadian DG. Nuclear magnetic resonance and its applications to living systems. Oxford: Oxford University Press; 1995.
2. Callaghan PT. Principles of nuclear magnetic resonance microscopy. Oxford: Clarendon Press; 1991.
3. Hashemi RH, Bradley WG, Lisanti CJ. MRI: the basics. Baltimore: Lippincott Williams & Wilkins; 2003.
4. Bernstein MA, King KF, Zhou XJ. Handbook of MRI pulse sequences. New York: Academic Press; 2004.
5. Schmitt F, Stehling MK, Turner R. Echo-planar imaging: theory, technique and application. New York: Springer; 1998.
6. Bloch F, Hansen WW, Packard M. Nuclear Induction. Phys Rev 1946;69:127.
7. Purcell EM, Torrey HC, Pound RV. Resonance absorption by nuclear magnetic moments in a solid. Phys Rev 1946;69:37.
8. Lauterbur PC. Image formation by induced local interactions: examples employing nuclear magnetic resonance. Nature 1973;242:190-191.
9. Kumar A, Welti D, Ernst RR. NMR fourier zeugmatography. J Magn Reson 1975;18:69-83.
10. Mansfield P. Multi-planar image formation using NMR spin echoes. J Phys C: Solid State Phys 1977;10:L55-L58.
11. Farrar TC, Becker ED. Pulse and Fourier transform NMR: introduction to theory and methods. New York: Academic Press; 1971.
12. Hahn EL. Spin echoes. Phys Rev 1950;80:580-594.

13. Carr HY, Purcell EM. Effects of diffusion on free precession in nuclear magnetic resonance experiments. *Phys Rev* 1954;94:630-638.
14. Meiboom S, Gill D. Modified spin-echo method for measuring nuclear relaxation times. *Rev Sci Instr* 1958;29:688-691.
15. Bassar PJ, Pierpaoli C. Microstructural and physiological features of tissues elucidated by quantitative-diffusion-tensor MRI. *J Magn Reson* 1996;111:209-219.
16. Stejskal EO, Tanner JE. Spin diffusion measurements: spin echoes in the presence of a time-dependent field gradient. *J Chem Phys* 1965;42:288-292.
17. Le Bihan D, Breton E, Lallemand D, Grenier P, Cabanis E, Laval-Jeantet M. MR imaging of intravoxel incoherent motions: application to diffusion and perfusion in neurologic disorders. *Radiology* 1986;161:401-407.
18. Rosen BR, Belliveau JW, Chien D. Perfusion imaging by nuclear magnetic resonance. *Magn Reson Q* 1989;5:263-281.
19. Rosen BR, Belliveau JW, Vevea JM, Brady TJ. Perfusion imaging with NMR contrast agents. *Magn Reson Med* 1990;14:249-265.
20. Benner T, Heiland S, Erb G, Forsting M, Sartor K. Accuracy of gamma-variate fits to concentration-time curves from dynamic susceptibility-contrast enhanced MRI: influence of time resolution, maximal signal drop, and signal-to-noise. *Magn Reson Imaging* 1997;15:307-317.
21. Hamberg LM, Macfarlane R, Tasdemiroglu E, Boccacini P, Hunter GJ, Belliveau JW, Moskowitz MA, Rosen BR. Measurement of the cerebrovascular changes in cats after transient ischemia using dynamic magnetic resonance imaging. *Stroke* 1993;24:444-451.

CHAPTER 2

HISTORY OF CANCER: PROGRESSION AND PROGNOSIS

Background

- Pathophysiology of Cancer Progression
- Tissue Hypoxia and the Formation of Necrosis
- Apoptotic Cell Death
- Necrosis and Apoptosis

Current Therapeutic Targets

- Radiotherapy
- Chemotherapy
- Anti-angiogenic Therapy
- Gene-specific Targets

Current MRI Methods

- Diffusion-weighted Imaging
- Perfusion-weighted Imaging
- Metabolic Imaging

2.1 Background

The formation and progression of cancer (i.e., carcinogenesis) is generally accepted as a multi-stage process, involving four major steps: initiation, promotion, malignant conversion, and tumor progression (1). Once malignancy is present, the likelihood of the cancer becoming invasive and metastatic increases dramatically, decreasing the potential for long-term patient survival. With this in mind, early diagnosis previous to any infiltration into the surrounding normal tissue is necessary. Hand in hand with early diagnosis are treatment provision and determination of efficacy. Current therapeutic options include surgery, fractionated radiotherapy, chemotherapy, anti-angiogenic therapy, photodynamic therapy, gene-specific therapy, or combination therapy. Therapeutic assessment of solid tumors is generally performed through noninvasive monitoring of tumor volume by ultrasound, CT, or MRI. Unfortunately, changes in tumor volume are generally slow and do not necessarily indicate tumor viability. Methods investigating physiologic-based changes that precede a change in tumor volume while also addressing the issue of tumor heterogeneity should aid in patient management. Rapid identification of the therapeutic response would permit both optimization of drug dose and delivery and the replacement of ineffective treatment with alternative measures. Since 1971 and Damadian's (2) discovery of tumor detection using nuclear magnetic resonance, MRI has come to serve as a powerful diagnostic tool in clinical oncology. In order to understand the applicability of MRI methods to tumor tissue characterization and the determination of therapeutic efficacy, a discussion of the pathophysiology of cancer progression and the inherent heterogeneity intra- and inter-tumorally is required. Additionally, a discussion of viable tissue versus formation of necrosis and well-oxygenated versus radioresistant hypoxic tissue as they pertain to the cytotoxic response will be covered. This chapter should provide sufficient background for the research presented in Chapters 3 and 4.

2.1.1 Pathophysiology of Cancer Progression

Initiation, promotion, and malignant conversion are necessary for a benign growth (i.e., adenoma) to become malignant (i.e., carcinoma). Initiation involves genetic changes such as DNA strand breaks that lead to sequence additions or deletions, altered

nucleotides, or frameshift mutations. The genetic replication of such errors is dependent on the dynamic between cell replication and standard DNA repair processes—if replication is faster than the repair process, the error may become permanent. Following such a mutation, specific promoters stimulate cell proliferation and hasten the movement from a benign to hyperplastic lesion. One group of promoters are the growth regulatory proteins, including fibroblast growth factor (FGF), epidermal growth factor (EGF), platelet-derived growth factor (PDGF), and vascular endothelial growth factor (VEGF) to name a few (1). The up-regulation of these proteins, along with the loss of tumor suppressor genes (i.e., p53) leads to malignant conversion and ultimate tumor progression.

The Angiogenic Switch

Tumors can grow to approximately 1-2 mm in diameter and remain quiescent for years. It isn't until the switch to an angiogenic phenotype (i.e., vascularization), first hypothesized by Folkman in 1971 as a potential therapeutic target (3), that further growth occurs. This was confirmed by subsequent studies following identification of the first angiogenic factor, VEGF (4), and the anti-tumor effects of VEGF inhibition (5). Tumor angiogenesis may be stimulated by various mechanisms: neovascularization in adjacent vascular beds, fibroblast/macrophage overexpression of angiogenic factors (i.e., VEGF), or incorporation of pre-existing vessels. The regulation of these mechanisms is controlled by promoters (i.e., proto-oncogenes) and inhibitors (i.e., suppressor genes), and may be further modified by the tumor physiologic state (6).

Surrounding Tissue Infiltration and Metastatic Cascade

Concomitant with the angiogenic switch is tumor metastasis. Several studies have shown a strong correlation between intra-tumoral microvessel density (MVD) in primary tumors and the formation of local (lymph nodal) or distant metastasis (7-9). Additionally, O'Reilly *et al.* (10) demonstrated that removal of the primary tumor, and therefore, the removal of natural angiogenic inhibitors produced by that tumor, induces rapid growth of distant metastasis. These studies indicate a specific role of angiogenic factors, both stimulatory and inhibitory, to the cascade of events required for secondary tumor formation. Because newly formed capillary vessels often have gaps between endothelial cells and a discontinuous or absent basement membrane (11), they are structurally weak

and the resulting increase in vascular permeability promotes the migration of cancer cells into the circulation. The overall metastatic cascade is diagrammed in Fig. 2-1.

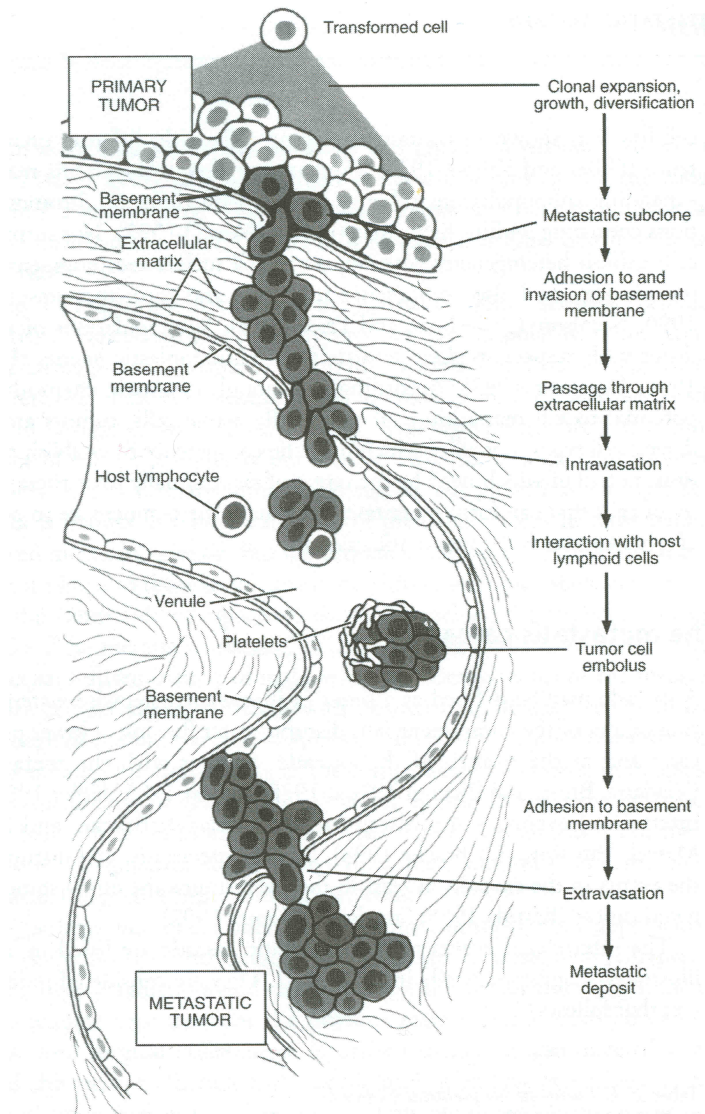


Figure 2-1. Metastatic cascade of events. A primary tumor contains cells able to give rise to metastatic colonies, which must bind and disrupt the basement membrane, invade the extracellular matrix, penetrate the vascular system, circulate, arrest themselves at a distant site by adhesion to the basement membrane, and finally exit the vessel (extravasation) for formation of metastasis [Reprinted from Coltran RS, Kumar V, Robbins SL. Pathological Basis of Cancer, 5th ed. Philadelphia: W.B. Saunders Co., 1994.]

2.1.2 Tissue Hypoxia and the Formation of Necrosis

Tumor vessels are structurally and functionally abnormal. The tumor vasculature, in contrast to normal vessels, is chaotic and tortuous. Its vessels have endothelial fenestrae, widened interendothelial junctions, and a discontinuous or absent basement membrane, resulting in vascular hyperpermeability (12-14). As a tumor increases in size, there is an increase in interstitial pressure from plasma buildup—a direct result of the inherently leaky tumor vasculature and a non-functional lymphatic system. This increase in pressure is greatest at the tumor center, and may lead to compression of local microvessels (15) and restricted oxygen delivery (16). As all cells require oxygen and nutrients for their survival, and since the mean oxygen diffusion distance is only 50 to 200 μm , regions lacking local blood vessels within this proximity are likely to develop tissue hypoxia. Regions of chronic hypoxia many generally result in formation of necrosis. Necrotic cell death (17) is a process whereby cells lose their ability to maintain membrane integrity, leading to Ca^{2+} influx, increased enzymatic activity, and failed energy metabolism. The cells then swell and burst, releasing enzymes such as lipases, proteases, and nucleases as well as reactive oxygen species (ROS) into the extracellular (EC) space, extending the damage to neighboring cells. An inflammatory response is initiated to clean up the dead cells, but further damage is caused from neutrophils and macrophages recruited to the area. For this reason, the central region of necrosis that forms usually extends radially from the site of origin, with a region of semi-necrosis at its edge surrounded by viable tissue that is hypoxic, and well-oxygenated, well-vascularized tissue at the periphery.

2.1.3 Apoptotic Cell Death

Any cellular injury can result in apoptotic cell death. Apoptosis, otherwise known as programmed cell death, is a response to specific stimuli whereby a cell decides to die rather than repair itself (Fig. 2-2).

Bcl-2 and Bax: Their Respective Roles in Apoptosis

Following cellular damage, if the Bcl-2 gene family is underexpressed or absent, channels can form in mitochondria (termed permeability transition (PT)), resulting in ion gradient failure, ROS production, and oxidative injury (18). In addition, the release of

Ca^{2+} and proteins (cytochrome c and apoptotic inducible factor (AIF)) into the cytoplasm leads to caspase activation, a group of enzymes that cleave structural proteins and DNA. Loss of membrane integrity ultimately yields cellular collapse and phagocytosis by neighboring viable tumor cells or macrophages. If instead Bcl-2 is overexpressed, it prevents the cleavage and activation of various caspases, dysregulating the apoptotic pathway. In contrast, if Bax is overexpressed it promotes PT transition in mitochondria and the processing and activation of various caspases, aiding continuation of the apoptotic cascade.

p53 and Apoptosis

Besides Bcl-2 and Bax, p53 also plays an important role in apoptosis. Stimulated expression of p53 can cause cell-cycle arrest and DNA-damage-induced apoptosis (19). Since p53 deficiency in mice leads to spontaneous tumors (20), and as p53 inactivation by mutation exists in a variety of tumor types, p53 is a target of particular interest for gene-specific therapies.

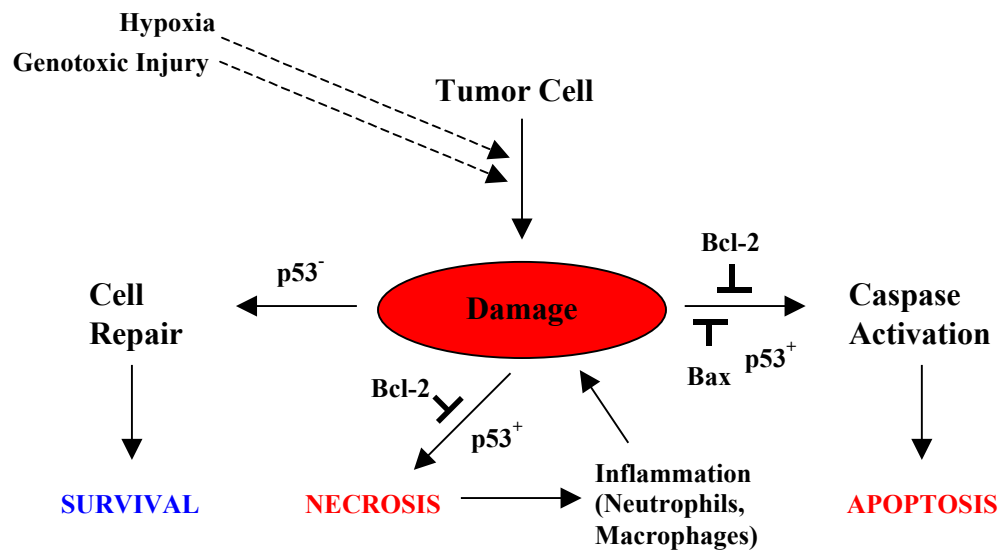


Figure 2-2. Mechanisms of cell death: apoptosis and necrosis. Following a major insult such as hypoxia or genotoxic injury (i.e., from therapeutic intervention), cellular damage occurs. Several mechanisms are involved in the decision to survive or to proceed along the pathway to cell death. Bcl-2 expression dysregulates apoptosis and necrosis through inhibition of caspase processing and activation. In contrast, Bax expression triggers caspase activation and subsequent apoptotic death. p53 on the other hand, has a dual role. The downregulation or absence of p53 permits cell repair, survival, and tumor progression. The upregulation of p53 triggers further processes that induce cell-cycle arrest, DNA damage-induced apoptosis, and necrotic cell death.

2.1.4 Necrosis and Apoptosis

Since there are two modes of cell death, namely necrotic cell death and apoptotic cell death, it is important to be able to differentiate between them. In the case of necrosis, cells have critically damaged membranes and organelles and exhibit a high degree of swelling prior to bursting their contents into the EC space. The cellular debris is then phagocytosed by local macrophages and neutrophils, leaving an acellular zone (Fig. 2-3, light pink region labeled 'N' for necrosis). As necrosis and the inflammatory response induce further damage to neighboring cells, apoptosis in proximity to regions of necrotic formation is not uncommon, leading to a region of semi-necrosis (Fig. 2-3, between the solid white arrows). During apoptosis, cells shrink, condense, and detach themselves from their viable neighbors prior to phagocytosis by lysosomes and/or local macrophages. The identification of cells undergoing various stages of apoptosis, whether proximal or distal to regions of necrosis, is possible by staining for differences in genetic expression (i.e., levels of Bcl-2 or p53 expression), or changes in morphology (i.e., nuclear fragmentation using the TUNEL assay). Apoptotic cells may be identifiable via hematoxylin-eosin (H&E) staining, although this method is much more cumbersome for quantitative versus qualitative analyses.

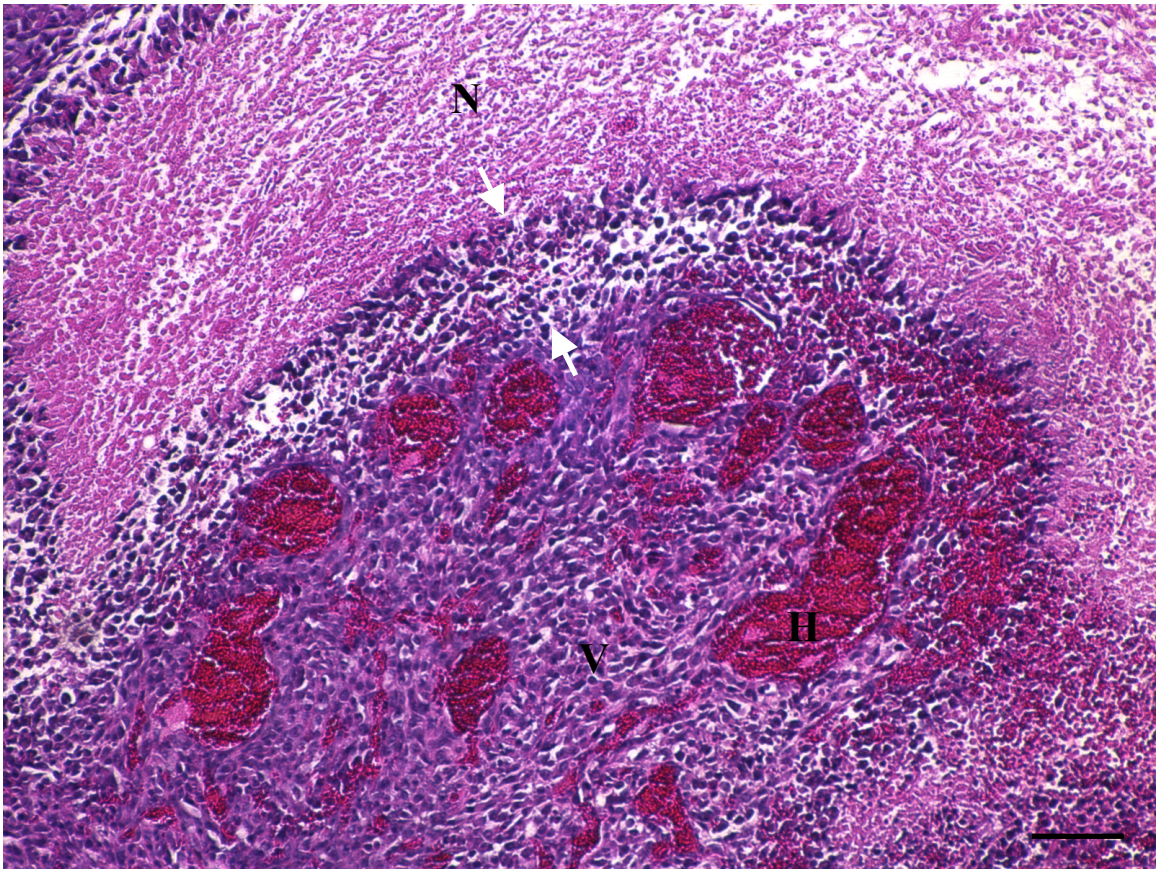


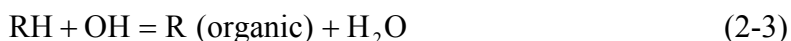
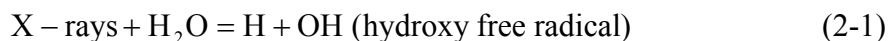
Figure 2-3. Patterns of cell death for a RIF-1 tumor. Hematoxylin-Eosin staining of $6\mu\text{m}$ sections ($10\times$). A zone of necrosis (N) is visible, surrounded by a region of multi-focal necrosis (between the solid white arrows) at the interface with viable tissue (V). Some regions of hemorrhage (H) within the neoplastic proliferation were also present. Scale bar = $100\mu\text{m}$.

2.2 Current Therapeutic Targets

Current therapeutic measures are generally directed at one of two cellular targets: the tumor cells, or the endothelial cells of the vasculature supplying the tumor with oxygen and nutrients for continued proliferation. Radiotherapy and chemotherapy are mainly directed at tumor cells. Anti-angiogenic therapy combats the blood supply by directly or indirectly attacking vascular endothelial cells. The standard therapies (i.e., radiotherapy, chemotherapy) will be discussed in detail, with a brief coverage of anti-angiogenic therapy and gene-specific therapy. The overall therapeutic goal is to induce tumor clonogenic death, regression and remission. This is usually done via total or partial tumor resection, followed by fractionated treatment over a period of several weeks to months.

2.2.1 Radiotherapy

Roentgen's discovery of x-rays in the late 19th century was and still remains the cornerstone of radiotherapy as a form of cancer treatment. Following irradiation, the majority of cellular damage is caused by the formation of free radicals from x-ray interaction with the target tissue (21):



The free radicals formed in Equations 2-1 through 2-4 are the hydroxy, hydroperoxy, organic, and peroxy free radicals. Since free radicals contain unpaired electrons, they are highly reactive and can interact via oxidation-reduction processes, damaging DNA, proteins, and membrane integrity. It is important to note that hydroperoxy and peroxy free radical production are oxygen-dependent processes. For this reason, well-oxygenated tissue generally responds well to radiotherapy, whereas hypoxic tissue does not (22).

Tumor Hypoxia and Radioresistance

Tumor hypoxia contributes to both tumor progression and radioresistance (22-27). During hypoxia, hypoxic-inducible-factor-1 α (HIF-1 α) protein is upregulated in order for

cell adaptation to oxygen deficiency (28). Increased HIF-1 α triggers production of various growth factors (i.e., VEGF and FGF), stimulating angiogenesis for enhanced oxygen delivery, glucose transport, and a switch to anaerobic glycolysis via changes in gene expression. In addition, HIF-1 α overexpression enhances radioresistance through suppression of apoptosis (25). In light of these findings it is not surprising that, depending on the severity of tissue hypoxia and the extent of HIF-1 α overexpression, radiotherapy may be ineffective (i.e., in terms of tumor regression and patient survival). Burri *et al.* (24) reported a significant correlation between HIF-1 α expression and outcome following radiotherapy in cervical cancer. Additional clinical studies report HIF-1 α as a prognostic marker of therapeutic efficacy (23,26,27). Further studies investigating the role of HIF-1 α in tumor progression should aid in the development of hypoxic-specific targets, making non-invasive imaging methods monitoring HIF-1 α expression important for determining therapeutic response.

2.2.2 Chemotherapy

The development of novel chemotherapeutics, termed cytotoxic drugs, act by disrupting the genetic integrity of cells. They may or may not be directed against the cell cycle. Those that act against the cell cycle target DNA replication (S-phase or synthesis) and cell division (M-phase or mitosis), the two main processes within the cell cycle itself. Several drugs in prevalent use today are cyclophosphamide (Cp), 5-Fluorouracil (5-FU), bischloroethylnitrosourea (BCNU), and Paclitaxel. Cp and BCNU are cell-cycle non-specific. In contrast, 5-FU and Paclitaxel are cell-cycle specific, most sensitive during S-phase and M-phase, respectively. It is important to note that chemotherapy agents are unable to distinguish between normal healthy cells and malignancy, making them more toxic than radiotherapy with a higher incidence of unwanted side effects. For this reason, fractionated-drug delivery is usually given to prevent or, at a minimum, diminish any potential adverse effects.

Hypoxia and chemotoxic resistance

Cells experiencing either chronic or intermittent hypoxia may exhibit resistance to anti-cancer drugs. First, anti-cancer drugs are targeted at rapidly dividing cells. Second, anti-cancer drugs must traverse the chaotic tumor vasculature to reach the tumor cells. Since

most hypoxic cells have retarded cell division and are located distal to capillary beds, therapeutic efficacy will decrease as a function of distance from the vasculature (29). Recent studies have reported that overexpression of HIF-1 α , a hypoxic marker, contributes to chemotoxic resistance (30), and that high levels of HIF-1 α are associated with more aggressive tumors and treatment failure (31). For this reason, investigation of anti-cancer drugs that are toxic only under hypoxic conditions (i.e., Tirapazamine (TPZ)) may be desirable.

2.2.3 Anti-angiogenic Therapy

Since conventional cancer therapy and current anti-cancer drugs fail to cure approximately 50% of cancers, it is extremely important to develop novel therapeutic approaches that are more effective, less toxic, and less susceptible to failure. One particular avenue of research that has emerged over the last decade is anti-angiogenic therapy, therapies specifically targeted at destroying the tumor blood supply.

Direct versus Indirect Inhibitors

Angiogenesis inhibitors are either direct or indirect. Direct anti-angiogenic therapies specifically target endothelial cells and tend to induce little or no drug resistance (32,33). Two examples are angiostatin and endostatin, both manufactured by Entremed. Indirect anti-angiogenic therapies, in contrast, target the tumor cell's production of an angiogenic factor or block its receptor on endothelial cells. Because tumor cells have high mutation rates, there is a high risk of relapse for indirect versus direct methods. Two examples are Interferon-alpha (commercially available) and Avastin (anti-VEGF; Genentech), which inhibit bFGF production and VEGF production, respectively.

2.2.4 Gene-specific Therapy

In addition to anti-angiogenic therapy, gene-specific therapy has raised a great deal of interest. The transfer or replacement of a gene offers the possibility of a "magic bullet", in which cell death may be induced or a genetic mutation may be reversed. This type of therapy would spare normal host cells, but current methods of delivery require further optimization and testing. In general, a gene is transferred to recipient cells by agents called vectors. These vectors may be viral (i.e., adenoviruses or retroviruses) or non-viral (i.e., liposomes). Since p53 is the most frequently mutated gene in human cancers, gene

replacement therapy of p53 has been under investigation in several cancer cell lines (34-36). These studies have identified that replacement of p53 in combination with chemotherapy is more efficacious than either alone, reinforcing the importance of p53 regulation of apoptosis and other anti-tumor mechanisms.

2.3 Current MRI Methods

MRI techniques such as DWI, dynamic contrast-enhanced (DCE) MRI, and metabolic imaging permit the rapid identification of tumor morphological features such as cellular density (for differentiation between viable tissue versus necrosis) as well as physiologic-based parameters, namely tumor blood flow, vascular permeability, oxygenation, pH, and lactate accumulation. These methods are not only useful in investigating the pathophysiology of tumor progression, but also in monitoring therapeutic efficacy and optimizing drug dose and delivery.

2.3.1 Diffusion-weighted Imaging

With the development of DWI methods and their utility in cerebral ischemia (37), researchers over the past decade have been investigating the application of DWI in the study of experimental tumor models (38-45) and in the clinical setting (46,47).

Identifying Tumor Heterogeneity

Variations in ADCs, caused by differences in cellular density, permit tumor tissue characterization and volumetric analysis. Lyng *et al.* (43) reported that viable tissue and necrosis could be delineated from one another based on ADCs. The authors also noted a strong correlation between ADC values and cellular density, similar to previous reports (40,46). Although studies employing T₂-weighted MRI are able to identify tumor tissue from surrounding healthy tissue, conventional imaging is unable to accurately subdivide the tumor into various regions based on morphological characteristics. This is because T₂-weighted MRI, which detects alterations in tissue water content, is less sensitive than DWI. T₂ changes may not be readily apparent until sufficient formation of necrosis or during therapeutically-induced vasogenic edema. DWI, on the other hand, is able to detect evidence of small changes in cellular density, providing a tool for addressing the issue of tumor heterogeneity. Carano and coworkers (45) reported the delineation

between viable tissue, necrotic tissue, and subcutaneous adipose tissue using a multidimensional feature space (ADC, T_2 , M_0) and cluster analysis. Comparison of MR parameter maps with histology indicates that regions with elevated ADCs and T_2 values denote regions of necrosis (zones that are generally acellular), whereas regions with normal to moderately elevated ADCs and normal T_2 values denote viable tissue. Although previous studies have employed similar methods for assessing the temporal evolution of cerebral ischemia (48-51), as well as in breast (52) and brain cancer (47), this was the first study to report multispectral analysis for quantification of tumor tissue populations.

Predicting Therapeutic Efficacy Based on ADC Changes

In 1996, Zhao *et al.* (39) reported a significant increase in ADC previous to any change in tumor volume, indicative of the cytotoxic response following Cp treatment. The authors suggested that ADC changes might serve as a marker for monitoring treatment response, based on changes in cellularity and the integrity of cellular membranes. Soon after, Chenevert *et al.* (46) demonstrated the utility of DWI for determining therapeutic efficacy in both an experimental 9L glioma model and the clinical setting. Individuals who were responsive to therapy showed significant increases in ADCs post-therapy, whereas non-responders showed little to no change in ADCs. Galons *et al.* (42) reported similar ADC changes in human breast cancer tumor xenografts following paclitaxel treatment. These results indicate that DWI may serve as an early noninvasive indicator of therapeutic response for a variety of tumors. Therefore, multispectral analysis that includes ADC may provide further information into the physiological mechanisms involved, as well as the morphological changes that take place, post-therapeutic intervention.

2.3.2 Dynamic Contrast-Enhanced (DCE) MRI

Since the emergence of anti-angiogenic therapies, methods for the non-invasive monitoring of changes in the tumor vasculature were needed. Dynamic contrast-enhanced MRI, described in the latter part of Chapter 1, permits measurement of mean transfer time (MTT), relative tumor blood volume (rTBV), relative tumor blood flow (rTBF), vascular permeability (PS), and a tortuosity index. The quantitative assessment of these metrics should help assess the role of the vasculature in maintaining tumor

viability, determine any changes induced following therapeutic intervention, and potentially aid in prediction of therapeutic response.

Identifying Tumor Heterogeneity

Because tumoral angiogenesis is chaotic, the tumor vasculature itself is tortuous with non-functional and immature vessels, abrupt shunting, and increased permeability due to large endothelial cell gaps or fenestrae. These result in intermittent or unstable flow in areas of low vascular density and the potential for transient episodes of hypoxia and upregulation of angiogenic factors. Since tumor vascularity is spatially heterogeneous, rTBF, rTBV, and PS measurements may permit differentiation between benign growths versus malignancy. Knopp *et al.* (53) reported a significantly lower exchange rate (k_{21}) in benign versus malignant breast cancer, with a dependence on VEGF expression. A subsequent study by van Dijke and coworkers (54) demonstrated that these tumors may be subclassified into slow-growing and fast-growing (aggressive) based on PS. The authors noted a strong correspondence between PS and histologic MVD, the current standard of measure for angiogenesis.

Predicting Therapeutic Efficacy Based on DCE-MRI Changes

Pham *et al.* (55) demonstrated the utility of DCE-MRI measurements of PS in monitoring the response to anti-VEGF treatment in implanted human breast cancer line MDA-MB-435 in rats. The authors reported significant reductions in tumor growth rate and PS values following administration of anti-VEGF, indicative of reduced angiogenic activity. Gossmann *et al.* (56) reported similar results in a xenograft model of glioblastoma multiforme. Since the level of angiogenic activity pre-treatment has been shown to be a prognostic indicator of therapeutic response, the non-invasive assessment of rTBF, rTBV, and PS using DCE-MRI would permit tumor diagnosis and grading, providing the clinician with a tool for patient management and treatment planning. In addition to its diagnostic utility, DCE-MRI may serve as an early noninvasive indicator of tumor response to antiangiogenic therapy.

2.3.3 Metabolic Imaging

Besides changes in cellular density and hemodynamic parameters such as rTBF, rTBV, and PS, tumor oxygenation and metabolism play an important role in tumor progression and individual responsiveness to therapy. Tumors tend to have high interstitial fluid

pressure from plasma buildup in the interstitial space and a non-functional lymphatic system. This increase in pressure leads to compression of the blood vessels at the tumor interior, resulting in zones of chronic or acute hypoxia. Concomitant with tumor hypoxia is a transition to anaerobic glycolysis, tissue acidosis, and lactate accumulation. Accurate assessment of these processes (oxygenation, glycolysis, and lactate accumulation) should provide a method for noninvasively monitoring the early response to therapy. Poptani and coworkers (57,58) employed MR spectroscopic methods and DCE-MRI for the investigation of tumor oxygenation, glycolytic rates, and lactate levels following Cp treatment in a RIF-1 tumor model. In these two studies, the authors noted a significant decrease in glycolysis, tissue pO_2 , and lactate levels, and a significant increase in Gd-DTPA uptake kinetics at 24-hours post-treatment. The authors also suggested that these changes are indicative of increased aerobic metabolism and lactate clearance, owing to an increase in tumor perfusion and subsequent tumor reoxygenation. These results suggest that MRS methods monitoring tumor metabolism, in combination with DCE-MRI, may be used for early assessment of therapy.

References

1. Cohen SM, Ellwein LB. Genetic errors, cell proliferation, and carcinogenesis. *Cancer Res* 1991;51:6493-6505.
2. Damadian R. Tumor detection by nuclear magnetic resonance. *Science* 1971;171:1151-1153.
3. Folkman J. Tumor angiogenesis: therapeutic implications. *N Engl J Med* 1971;285:1182-1186.
4. Leung DW, Cachianes G, Kuang WJ, Goeddel DV, Ferrara N. Vascular endothelial growth factor is a secreted angiogenic mitogen. *Science* 1989;246:1306-1309.
5. Kim KJ, Li B, Winer J, Armanini M, Gillett N, Phillips HS, Ferrara N. Inhibition of vascular endothelial growth factor-induced angiogenesis suppresses tumor growth in vivo. *Nature* 1993;362:841-844.
6. Folkman J. Angiogenesis. In: Braunwald E, Fauci AS, Kasper DL, Hauser SL, Longo DL, Jameson JL, editors. *Harrison's textbook of internal medicine*: McGraw-Hill; 2001. p 517-530.
7. Gasparini G, Weidner N, Bevilacqua P, Maluta S, Dalla Palma P, Caffo O, Barbareschi M, Boracchi P, Marubini E, Pozza F. Tumor microvessel density, p53 expression, tumor size, and peritumoral lymphatic vessel invasion are relevant prognostic markers in node-negative breast carcinoma. *J Clin Oncol* 1994;12:454-466.

8. Weidner N, Semple JP, Welch WR, Folkman J. Tumor angiogenesis and metastasis: correlation in invasive breast carcinoma. *N Engl J Med* 1991;324:1-8.
9. Li VW, Folkherth RD, Watanabe H, Yu C, Rupnick M, Barnes P, Scott RM, Black PM, Sallan SE, Folkman J. Microvessel count and cerebrospinal fluid basic fibroblast growth factor in children with brain tumours. *Lancet* 1994;344:82-86.
10. O'Reilly MS, Holmgren L, Shing Y, Chen C, Rosenthal RA, Moses M, Lane WS, Cao Y, Sage EH, Folkman J. Angiostatin: a novel angiogenesis inhibitor that mediates the suppression of metastases by Lewis lung carcinoma. *Cell* 1994;79:315-328.
11. Ausprunk DH, Folkman J. Migration and proliferation of endothelial cells during preformed and newly formed blood vessels during tumor angiogenesis. *Microvasc Res* 1977;14:53-65.
12. Hobbs SK, Monsky WL, Yuan F, Roberts WG, Griffith L, Torchilin VP, Jain RK. Regulation of transport pathways in tumor vessels: role of tumor type and host microenvironment. *Proc Natl Acad Sci USA* 1998;95:4607-4612.
13. Dvorak HF, Nagy JA, Feng D, Brown LF, Dvorak AM. Vascular permeability factor/vascular endothelial growth factor and the significance of microvascular hyperpermeability in angiogenesis. *Curr Top Microbiol Immunol* 1999;237:97-132.
14. Hashizume H, Baluk P, Morikawa S, McLean JW, Thurston G, Roberge S, Jain RK, McDonald DM. Openings between defective endothelial cells explain tumor vessel leakiness. *Am J Pathol* 2000;156:1363-1380.
15. Jain RK. Determinants of tumor blood flow: a review. *Cancer Res* 1988;48:2641-2658.
16. Baxter LT, Jain RK. Transport of fluid and macromolecules in tumors. I. Role of interstitial pressure and convection. *Microvasc Res* 1989;37:77-104.
17. Martin SJ. Apoptosis and cancer: an overview. In: Martin SJ, editor. *Apoptosis and cancer*. San Diego: Karger Landes Systems; 1997. p 1-24.
18. Reed JC. Bcl-2 family proteins: role in dysregulation of apoptosis and chemoresistance in cancer. In: Martin SJ, editor. *Apoptosis and cancer*. San Diego: Karger Landes Systems; 1997. p 64-97.
19. Sluss HK, Jones SN. Analysing p53 tumour suppressor functions in mice. *Expert Opin Ther Targets* 2003;7:89-99.
20. Donehower LA, Harvey M, Slagle BL, McArthur MJ, Montgomery Jr. CA, Butel JS, Bradley A. Mice deficient for p53 are developmentally normal but susceptible to spontaneous tumours. *Nature* 1992;356:215-221.
21. Prasad KN. Cellular Radiation Damage. *Handbook of Radiobiology*. Boca Raton: CRC Press; 1995. p 49-59.
22. Gray LH. Concentration of oxygen dissolved in tissues at the time of irradiation as a factor in radiotherapy. *Br J Cancer* 1953;26:638-648.
23. Rofstad EK, Sundfor K, Lyng H, Trope CG. Hypoxia-induced treatment failure in advanced squamous cell carcinoma of the uterine cervix is primarily due to hypoxia-induced radiation resistance rather than hypoxia-induced metastasis. *Br J Cancer* 2000;83:354-359.
24. Burri P, Djonov V, Aebersold DM, Lindel K, Studer U, Altermatt HJ, Mazzacchelli L, Greiner RH, Gruber G. Significant correlation of hypoxia-

- inducible factor-1 α with treatment outcome in cervical cancer treated with radical radiotherapy. *Int J Radiat Oncol Biol Phys* 2003;56:494-501.
25. Akakura N, Kobayashi M, Horiuchi I, Suzuki A, Wang J, Chen J, Niizeki H, Kawamura K, Hosokawa M, Asaka M. Constitutive expression of hypoxia-inducible factor-1 α renders pancreatic cancer cells resistant to apoptosis induced by hypoxia and nutrient deprivation. *Cancer Res* 2001;61:6548-6554.
 26. Fyles AW, Milosevic M, Wong R, Kavanagh MC, Pintilie M, Sun A, Chapman W, Levin W, Manchul L, Keane TJ, Hill RP. Oxygenation predicts radiation response and survival in patients with cervix cancer. *Radiother Oncol* 1998;48:149-156.
 27. Nordsmark M, Overgaard M, Overgaard J. Pretreatment oxygenation predicts radiation response in advanced squamous cell carcinoma of the head and neck. *Radiother Oncol* 1996;41:31-39.
 28. Wang GL, Jiang BH, Rue EA, Semenza GL. Hypoxia-inducible factor 1 is a basic-helix-loop-helix-PAS heterodimer regulated by cellular O₂ tension. *Proc Natl Acad Sci USA* 1995;92:5510-5514.
 29. Brown JM. Exploiting the hypoxic cancer cell: mechanisms and therapeutic strategies. *Mol Med Today* 2000;6:157-162.
 30. Erler JT, Cawthorne CJ, Williams KJ, Koritzinsky M, Wouters BG, Wilson C, Miller C, Demonacos C, Stratford IJ, Dive C. Hypoxia-mediated down-regulation of bcl-2 and bax in tumors occurs via hypoxic-inducible factor 1-dependent and -independent mechanisms and contributes to drug resistance. *Mol Cell Biol* 2004;24:2875-2889.
 31. Birner P, Schindl M, Obermair A, Breitenecker G, Oberhuber G. Expression of hypoxia-inducible factor 1 α in epithelial ovarian tumors: its impact on prognosis and response to chemotherapy. *Clin Cancer Res* 2001;7:1661-1668.
 32. Kerbel RS. Inhibition of tumor angiogenesis as a strategy to circumvent acquired resistance to anticancer therapeutic agents. *Bioessays* 1991;13:31-36.
 33. Boehm T, Folkman J, Browder T, O'Reilly MS. Antiangiogenic therapy of experimental cancer does not induce acquired drug resistance. *Nature* 1997;390:404-407.
 34. Quist SR, Wang-Gohrke S, Kohler T, Kreienberg R, Runnebaum IB. Cooperative effect of adenoviral p53 gene therapy and standard chemotherapy in ovarian cancer cells independent of the endogenous p53 status. *Cancer Gene Ther* 2004;11:547-554.
 35. Yoo GH, Piechocki MP, Oliver J, Lonardo F, Zumstein L, Lin HS, Kim H, Shibuya TY, Shehadeh N, Ensley JF. Enhancement of Ad-p53 therapy with docetaxel in head and neck cancer. *Laryngoscope* 2004;114:1871-1879.
 36. Eisold S, Linnebacher M, Ryschich E, Antolovic D, Hinz U, Klar E, Schmidt J. The effect of adenovirus expressing wild-type p53 on 5-fluorouracil chemosensitivity is related to p53 status in pancreatic cancer cell lines. *World J Gastroenterol* 2004;10:3583-3589.
 37. Moseley ME, Cohen Y, Mintorovitch J, Chileuitt L, Shimizu H, Kucharczyk J, Wendland MF, Weinstein PR. Early detection of regional cerebral ischemia in cats: comparison of diffusion- and T₂-weighted MRI and spectroscopy. *Magn Reson Med* 1990;14:330-346.

38. Helmer KG, Dardzinski BJ, Sotak CH. The application of porous-media theory to the investigation of time-dependent diffusion in in vivo systems. *NMR Biomed* 1995;8:297-306.
39. Zhao M, Pipe JG, Bonnett J, Evelhoch JL. Early detection of treatment response by diffusion-weighted ¹H-NMR spectroscopy in a murine tumour in vivo. *Br J Cancer* 1996;71:61-64.
40. Chenevert TL, McKeever PE, Ross BD. Monitoring early response of experimental brain tumors to therapy using diffusion magnetic resonance imaging. *Clin Cancer Res* 1997;3:1457-1466.
41. Helmer KG, Han S, Sotak CH. On the correlation between the water diffusion coefficient and oxygen tension in RIF-1 tumors. *NMR Biomed* 1998;11:120-130.
42. Galons JP, Altbach MI, Paine-Murrieta GD, Taylor CW, Gillies RJ. Early increases in breast tumor xenograft water mobility in response to paclitaxel therapy detected by non-invasive diffusion magnetic resonance imaging. *Neoplasia* 1999;1:113-117.
43. Lyng H, Haraldseth O, Rofstad EK. Measurement of cell density and necrotic fraction in human melanoma xenografts by diffusion weighted magnetic resonance imaging. *Magn Reson Med* 2000;43:828-836.
44. Helmer KG, Meiler MR, Sotak CH, Petruccelli JD. Comparison of the return-to-the-origin probability and the apparent diffusion coefficient of water as indicators of necrosis in RIF-1 tumors. *Magn Reson Med* 2003;49:468-478.
45. Carano RA, Ross AL, Ross J, Williams SP, Koeppen H, Schwall RH, van Bruggen N. Quantification of tumor tissue populations by multispectral analysis. *Magn Reson Med* 2004;51:542-551.
46. Chenevert TL, Stegman LD, Taylor JMG, Robertson PL, Greenberg HS, Rehemtulla A, Ross BD. Diffusion magnetic resonance imaging: an early surrogate marker of therapeutic efficacy in brain tumors. *J Natl Cancer Inst* 1997;92:2029-2036.
47. Tzika AA, Astrakas LG, Zarifi MK, Petridou N, Young-Poussaint T, Goumnerova L, Zurakowski D, Anthony DC, Black PM. Multiparametric MR assessment of pediatric brain tumors. *Neuroradiology* 2003;45:1-10.
48. Carano RA, Takano K, Helmer KG, Tatlisumak T, Irie K, Petruccelli JD, Fisher M, Sotak CH. Determination of focal ischemic lesion volume in the rat brain using multispectral analysis. *J Magn Reson Imaging* 1998;8:1266-1278.
49. Carano RA, Li F, Irie K, Helmer KG, Silva MD, Fisher M, Sotak CH. Multispectral analysis of the temporal evolution of cerebral ischemia in the rat brain. *J Magn Reson Imaging* 2000;12:842-858.
50. Jacobs MA, Zhang ZG, Knight RA, Soltanian-Zadeh H, Goussev AV, Peck DJ, Chopp M. A model for multiparametric MRI tissue characterization in experimental cerebral ischemia with histological validation in rat: part 1. *Stroke* 2001;32:943-949.
51. Jacobs MA, Mitsias P, Soltanian-Zadeh H, Santhakumar S, Ghanei A, Hammond R, Peck DJ, Chopp M, Patel S. Multiparametric MRI tissue characterization in clinical stroke with correlation to clinical outcome: part 2. *Stroke* 2001;32:950-957.

52. Jacobs MA, Barker PB, Bluemke DA, Maranto C, Arnold C, Herskovits EH, Bhujwala Z. Benign and malignant breast lesions: diagnosis with multiparametric MR imaging. *Radiology* 2003;229:225-232.
53. Knopp MV, Weiss E, Sinn HP, Mattern J, Junkermann H, Radeleff J, Magener A, Brix G, Delorme S, Zuna I, van Kaick G. Pathophysiologic basis of contrast enhancement in breast tumors. *J Magn Reson Imaging* 1999;10:260-266.
54. van Dijke CF, Brasch RC, Roberts TP, Weidner N, Mathur A, Shames DM, Mann JS, Demsar F, Lang P, Schwickert HC. Mammary carcinoma model: correlation of macromolecular contrast enhanced MR imaging characterizations of tumor microvascular and histologic capillary density. *Radiology* 1996;198:813-818.
55. Pham CD, Roberts TP, van Bruggen N, Melnyk O, Mann J, Ferrara N, Cohen RL, Brasch RC. Magnetic resonance imaging detects suppression of tumor vascular permeability after administration of antibody to vascular endothelial growth factor. *Cancer Invest* 1998;16:225-230.
56. Gossman A, Helbich TH, Kuriyama N, Ostrowitzki S, Roberts TP, Shames DM, van Bruggen N, Wendland MF, Israel MA, Brasch RC. Dynamic contrast-enhanced magnetic resonance imaging as a surrogate marker of tumor response to anti-angiogenic therapy in a xenograft model of glioblastoma multiforme. *J Magn Reson Imaging* 2002;15:233-240.
57. Poptani H, Bansal N, Jenkins WT, Blessington D, Mancuso A, Nelson DS, Feldman M, Delikatny EJ, Chance B, Glickson JD. Cyclophosphamide treatment modifies tumor oxygenation and glycolytic rates of RIF-1 tumors: ¹³C magnetic resonance spectroscopy, eppendorf electrode, and redox scanning. *Cancer Res* 2003;63:8813-8820.
58. Poptani H, Bansal N, Graham RA, Mancuso A, Nelson DS, Glickson JD. Detecting early response to cyclophosphamide treatment of RIF-1 tumors using selective multiple quantum spectroscopy (SelMQC) and dynamic contrast enhanced imaging. *NMR Biomed* 2003;16:102-111.

CHAPTER 3

MULTISPECTRAL QUANTIFICATION OF TISSUE TYPES IN A RIF-1 TUMOR MODEL WITH HISTOLOGICAL VALIDATION

Introduction

- Tumor Heterogeneity
- Tumor Tissue Characterization with DWI
- Limitations of a Single Parameter Approach
- MS Tissue Characterization
- MS Analysis with Histological Validation

Methods

- Animal Preparation
- Radiotherapy
- MRI Measurements
- Data Analysis
- K-Means Clustering
- Histological Analysis
- Statistical Analysis

Results

- Optimization of KM Method
- KM Segmentation Results
- Correlation with Histology
- Temporal Evolution of KM Volume

Discussion

- Determination of Optimum KM Method
- KM Delineation Between Viable Tissue and Necrosis
- KM Identification of Hypoxic Tissue
- Temporal Evolution of KM Volume
- Utility of the KM Method

Multispectral Quantification of Tissue Types in a RIF-1 Tumor Model with Histological Validation

Erica C. Henning¹, Chieko Azuma², Christopher H. Sotak^{1,3,4}, Karl G.
Helmer¹

Departments of Biomedical Engineering¹ and Chemistry & Biochemistry³

Worcester Polytechnic Institute

Worcester, Massachusetts 01609

Department of Clinical Sciences²

Tufts University Veterinary School of Medicine

North Grafton, Massachusetts

Department of Radiology⁴

University of Massachusetts Medical School

Worcester, MA 01655

Part of this work was presented at the 12th and 13th annual meetings of the International Society of Magnetic Resonance in Medicine, Kyoto, Japan, 2004 and Miami Beach, FL, USA, 2005.

Manuscript in Progress

Abstract

Accurate assessment of therapeutic efficacy is confounded by intra- and inter-tumor heterogeneity. Variable pre-treatment tissue composition, tumor size, and growth kinetics, as well as post-treatment cell kill and tumor regrowth, complicate dose-optimization and comparative treatment regimens in animal oncological studies. In order to address this issue, multispectral (MS) analysis using ADC, T_2 , and M_0 and the k-means (KM) clustering algorithm was employed for identification of multiple compartments within both viable and necrotic tissue in a radiation-induced fibrosarcoma (RIF-1) tumor model receiving single-dose (1000cGy) radiotherapy. Optimization of the KM method was performed through histological validation via hematoxylin-eosin (H&E) staining and hypoxic-inducible factor-1 α (HIF-1 α) immunohistochemistry. The optimum KM method was determined to be a 2-feature (ADC, T_2) and 4-cluster (two regions each of viable tissue and necrosis) segmentation. KM volume estimates, both viable ($r = 0.94$, $p < 0.01$) and necrotic ($r = 0.76$, $p < 0.01$), were highly correlated with their H&E counterparts. Comparison of HIF-1 α immunohistochemistry and standard H&E showed that HIF-1 α expression tended to be concentrated in peri-necrotic regions, correlating to viable 2 and supporting the subdivision of the viable tissue into well-oxygenated (viable 1; V1) and hypoxic (viable 2; V2) regions. Since both necrosis and hypoxia have been implicated in poor treatment response and reduced patient survival, the quantification of the amount of necrosis and the severity of hypoxia may aid in assignment of a more aggressive treatment regimen. This method may potentially provide a tool for therapeutic monitoring, assessment of treatment efficacy, and optimization of drug-dose and timing schemes, particularly in pre-clinical animal models of disease.

Keywords: RIF-1, tumor, diffusion, multispectral analysis, HIF-1

3.1 Introduction

Accurate assessment of therapeutic efficacy is confounded by intra- and inter-tumor heterogeneity. Variable pre-treatment tissue composition, tumor size, and growth kinetics, as well as post-treatment cell kill and tumor regrowth, complicate dose-optimization and comparative treatment regimens in animal oncological studies. This chapter will address the application of multispectral (MS) analysis using ADC, T_2 , and M_0 and the k-means (KM) clustering algorithm for identification of multiple compartments within both viable and necrotic tissue. Histological validation was performed via hematoxylin-eosin (H&E) staining and hypoxic-inducible factor-1 α (HIF-1 α) immunohistochemistry. The optimum KM method determined here was applied in Chapter 4 for an in-depth investigation of the radiotherapeutic response.

3.1.1 Tumor Heterogeneity

Tumors are inherently heterogeneous, and tend to be characterized by a chaotic vasculature with intermittent and/or reduced blood flow (1,2). These perfusion abnormalities result in inefficient cellular delivery of oxygen and nutrients, thereby inducing regions of either transient or chronic hypoxia. Cellular hypoxia triggers a physiological cascade leading to one of two outcomes: 1) cellular repair (if necessary) and survival; or 2) cell death (apoptotic or necrotic) and a reduction in cellular density. If a cell ‘chooses’ to survive, it is generally through altered gene expression mediated by HIF-1 α , or hypoxic-inducible factor (3). This protein, upregulated during hypoxia, induces the transcription of a variety of genes specific to glucose uptake and metabolism (4), iron metabolism (5), and vascularization (6-8) in order to adapt to a low oxygen environment.

Tumor Hypoxia and Radioresistance

Tumor hypoxia has long been implicated in the non-responsiveness of tumors to radiotherapeutic intervention (9). Reduced oxygen availability decreases the generation of reactive oxygen species (ROS) following irradiation and the damage caused by free radicals (10). Several clinical studies in cervical (11-13), head and neck (14), and esophageal (15) cancers have shown good correlation between hypoxia and poor prognosis, specifically in terms of radiation response and tumor relapse. Additional

studies in experimental tumor models (16,17) indicate similar results of hypoxia-induced radioresistance. Cerniglia *et al.* (16) reported a significant increase in radiation sensitivity following carbogen breathing, based on an increase in tissue oxygen tension (pO_2) from ranges of 1-8 Torr to 5-15 Torr, well above the 5 Torr limit for radiation sensitivity. Zips *et al.* (17) demonstrated that tumors under clamp hypoxia, versus normal physiological conditions, required a higher dose (tumor control dose TCD₅₀ of 40% versus 29%) for local tumor control. These studies confirm the importance of tissue oxygenation to radiosensitivity and the overall prognostic outcome following radiotherapeutic intervention.

Tumor Hypoxia, Drug Resistance, and Tumor Progression

Besides its contributions to radioresistance, hypoxia may play an important role in drug resistance (18,19), and has recently been suggested as a major contributor in malignant progression (20,21). In instances of hypoxia, HIF-1 tends to be upregulated, promoting cell proliferation, tumor progression, and the formation of metastasis (22,23). Zhong *et al.* (24), in a study of 19 different tumor types, found a significant correlation between HIF-1 upregulation, p53 accumulation, and cell proliferation. The authors also noted the strongest HIF-1 expression in glioblastoma multiforme, the most malignant tumor of the central nervous system. Since cell acclimatization to hypoxia requires HIF-1 upregulation, and because increased HIF-1 activity is concomitant with tumor progression, HIF-1 may serve as a prognostic marker as well as a potential therapeutic target.

Formation of Necrosis and Tumor Progression

Necrotic cell death or the formation of necrosis, a direct result of chronic hypoxia, has been shown to correlate with tumor aggressiveness and, therefore, results in poor prognosis. Chia *et al.* (25) and Vleugel *et al.* (26) reported similar results of carbonic-anhydrase-9 (CA-9) expression in peri-necrotic regions, with strong correlation to tumor necrosis, tumor grade, and a higher relapse rate in invasive breast cancer. Vleugel *et al.* (26) also showed an association between HIF-1 expression and CA-9, an expected result as CA-9 is a hypoxic-regulated marker. A similar study by Giatromanolaki and coworkers (27) employing CA-9 in non-small cell lung cancer also reported a strong association between chronic hypoxia, necrosis, and poor patient outcome. These results

indicate that assessment of necrosis, for certain types of cancer, may aid in patient management and the assignment of a more aggressive treatment regimen.

3.1.2 Tumor Tissue Characterization with DWI

Because hypoxia and necrosis are interrelated, and based on their respective roles in tumor progression and/or resistance to therapy, the delineation between well-oxygenated and hypoxic tissue, as well as the identification of viable tissue versus necrotic formation, would aid in patient management. At this time, standard methods for assessing hypoxia and necrotic fraction are performed invasively using Eppendorf needle electrodes (28,29). Unfortunately, this method is extremely invasive, is limited to more superficial tumors, and has reduced reliability at low pO_2 values (< 10 Torr). Non-invasive methods able to quantify tumor morphology and oxygenation status, without the shortcomings of current invasive methods, would provide a safer alternative.

DWI Assessment of Tumor Morphology

Over the past decade, diffusion imaging has emerged as a powerful contrast mechanism for tissue characterization in both experimental tumor models (30-35) and the clinical setting (36,37). Diffusion, based on the random translational motion of molecules due to thermal energy (termed Brownian motion), permits the differentiation between viable and necrotic tissue based on changes in cellular density. In regions with high cellularity (i.e., viable tissue) diffusion will be restricted by barriers such as cell membranes, organelles, etc. In regions with low cellularity (i.e., necrosis), diffusion is less restricted and can be close to that of bulk water. Therapeutically-induced changes in cellular density and/or vasogenic edema may therefore, be detected using DWI and/or quantitative ADC measurements, permitting treatment monitoring (38-43) and the potential for prediction of therapeutic efficacy (44-46).

DWI Identification of Necrosis

Following the seminal study by Zhao *et al.* (38), reporting an early post-treatment increase in tumor spectroscopic ADC, Chenevert and coworkers (44,45) investigated the contribution of tumor physiology to this ADC change by comparison of the temporal evolution of the therapy-induced ADC increase with histological examination on a timepoint-by-timepoint basis. The authors reported a strong correlation between the mean ADC of the total tumor volume and cellular density calculations derived from

histological examination of hematoxylin-eosin (H&E) stained sections in a rat 9L glioma model. They concluded the early ADC increase was a result of reduced cellular density concomitant with formation of necrosis. This is diagrammed in Fig. 3-1. Lyng et al. (32) confirmed this correlation between ADC, cellular density, and necrotic fraction in four human xenograft lines, although the degree of correlation was dependent on the size of the necrotic fraction. The authors reported a significant correlation between total tumor ADC and necrotic fraction in the D-12 line that tended to form a large central region necrosis, but not with the other three lines that tended to form areas of point necrosis. They suggested this lack of correlation was likely a result of partial volume effects and inclusion of viable tumor in the small regions of necrosis characteristic of these lines. ADC parameter maps and the corresponding H&E sections for two of the xenografts are diagrammed in Fig. 3-2.

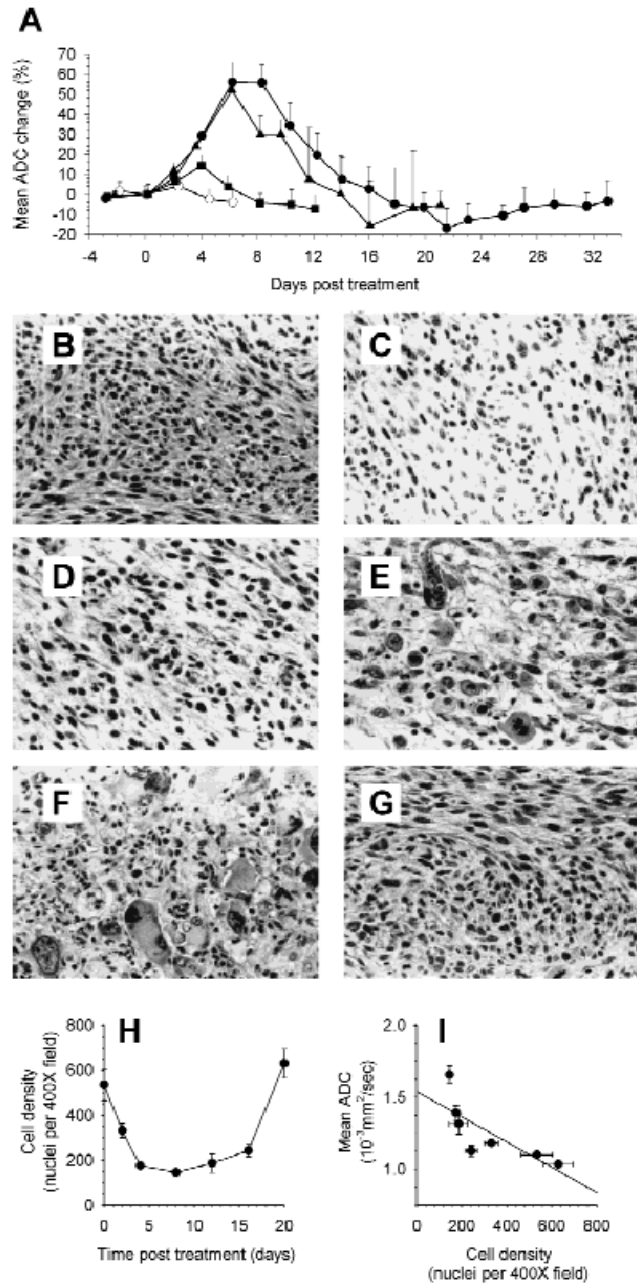


Figure 3-1. Evolution of tumor ADC and the corresponding changes in cellular density. (a) dose dependence of BCNU, given at 6.6 ($0.5 \times \text{LD}_{10}$, solid square), 13.3 ($1.0 \times \text{LD}_{10}$, solid triangle), and 26.6 ($2.0 \times \text{LD}_{10}$, solid circle) mg/kg and the corresponding change in ADC. (b) through (g) correspond to histopathological changes seen on H&E stained sections at days 2, 4, 8, 16, and 20 post-treatment. (h) cell density measurements for the $2.0 \times \text{LD}_{10}$ dose of BCNU. (i) correlation plot of ADC versus cell density ($r = 0.78$). Figure reproduced from reference (45).

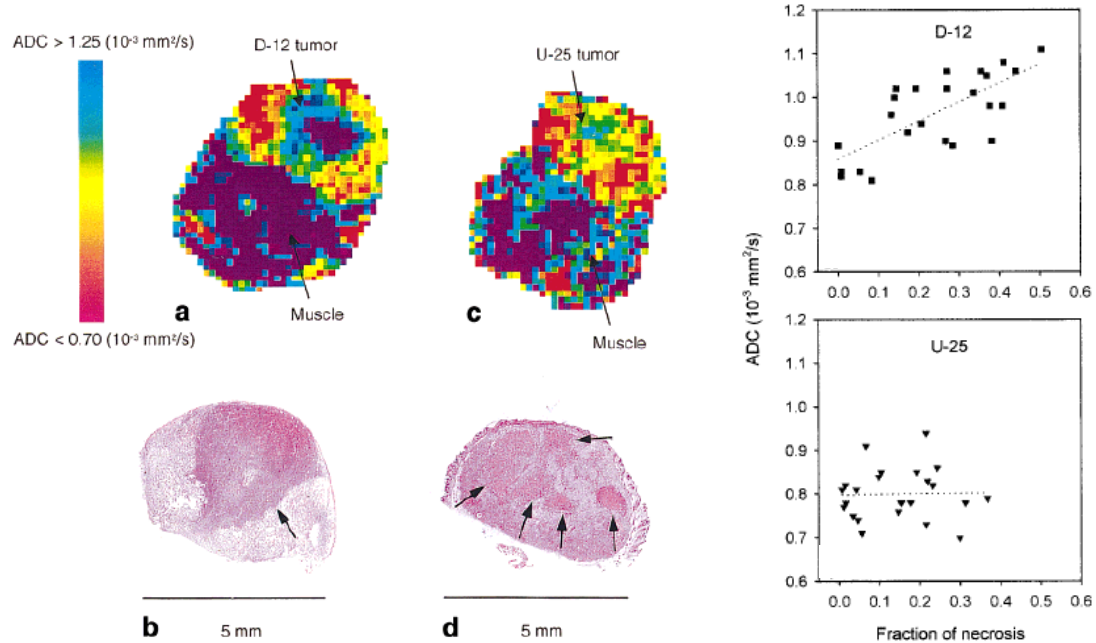


Figure 3-2. Left: ADC parameter maps (a, c) and the corresponding H&E stained sections (b, d) of a D-12 (a, b) and U-25 (c, d) human melanoma xenograft tumor. Red pixels represent ADCs below $0.70 \times 10^{-3} \text{ mm}^2 \text{ s}^{-1}$, whereas purple pixels represent ADCs above $1.25 \times 10^{-3} \text{ mm}^2 \text{ s}^{-1}$. Arrows indicate regions of necrosis. Right: Total tumor ADC versus necrotic fraction for D-12 and U-25 human melanoma xenograft tumors. Each point represents the ADC of an individual MR slice and the corresponding necrotic fraction on H&E. Figure adapted from reference (32).

3.1.3 Limitations of a Single Parameter Approach

Although these reports provide strong evidence that a significant ADC increase correlates with changes in cellular density and formation of necrosis, mean ADC calculations based on total tumor volume do not address or identify tissue heterogeneity, and therefore mask the underlying changes in tumor tissue viability. Helmer *et al.* (47) reported a correlation between ADC and necrotic fraction in a radiation-induced fibrosarcoma (RIF-1) tumor model, but only used tissue regions clearly viable or clearly necrotic in the analysis. Regions of mixed tissue were excluded from further analysis. The authors suggested that multiple MR parameters should increase the ability to identify these regions, although success will depend on both the size of necrotic regions and image resolution.

3.1.4 Multispectral Tissue Characterization

Intra- and inter-tumor heterogeneity complicate tumor tissue characterization and comparison of treatment regimens for drug dose optimization in pre-clinical cancer models. With this in mind, a multispectral (MS) approach that can identify tissue heterogeneity should provide greater power than previous single-parameter studies. Recent multiparametric studies in brain (48,49) show promise in their ability to separate tumor from surrounding healthy tissue and in potential tumor grading (i.e., level of malignancy). A similar MS approach used in breast cancer (50) was able to distinguish benign lesions from malignancy and surrounding adipose tissue. Following these studies, a novel method combining multispectral (MS) analysis using ADC, T_2 , and M_0 parameter maps was shown to aid in the differentiation between viable and necrotic tissue, as well as in the identification of multiple compartments within necrotic tissue (51). Example results from (51) have been reproduced in Fig. 3-3. Because T_2 is based on the interaction between water molecules and macromolecules, regions characterized by hemorrhage, upregulated angiogenesis, or an inflammatory response should have shorter T_2 values. In the case of hemorrhage and/or upregulated angiogenesis, T_2 shortening is caused by local inhomogeneities in the magnetic field from presence of paramagnetic molecules (i.e., deoxyhemoglobin). If inflammation is present, slow exchange between water molecules and proteins (i.e., a result of neutrophil action) lengthens the correlation times (τ_c), also reducing T_2 . Although the addition of T_2 permitted subdivision of the necrotic tissue population, Carano and coworkers (51) reported that the extraction of the MS viable volume provided a more stable efficacy endpoint than total necrotic fraction. The authors suggested that the similarities in percent necrosis seen by day 10 between groups, regardless of the presence or type of therapeutic intervention, may be characteristic of the COLO205 cell line used—these types of tumors tend to grow rapidly, exceeding their blood supply and forming large regions of necrosis. Nevertheless, this study provides a foundation for future methods employing an MS approach to tumor tissue characterization.

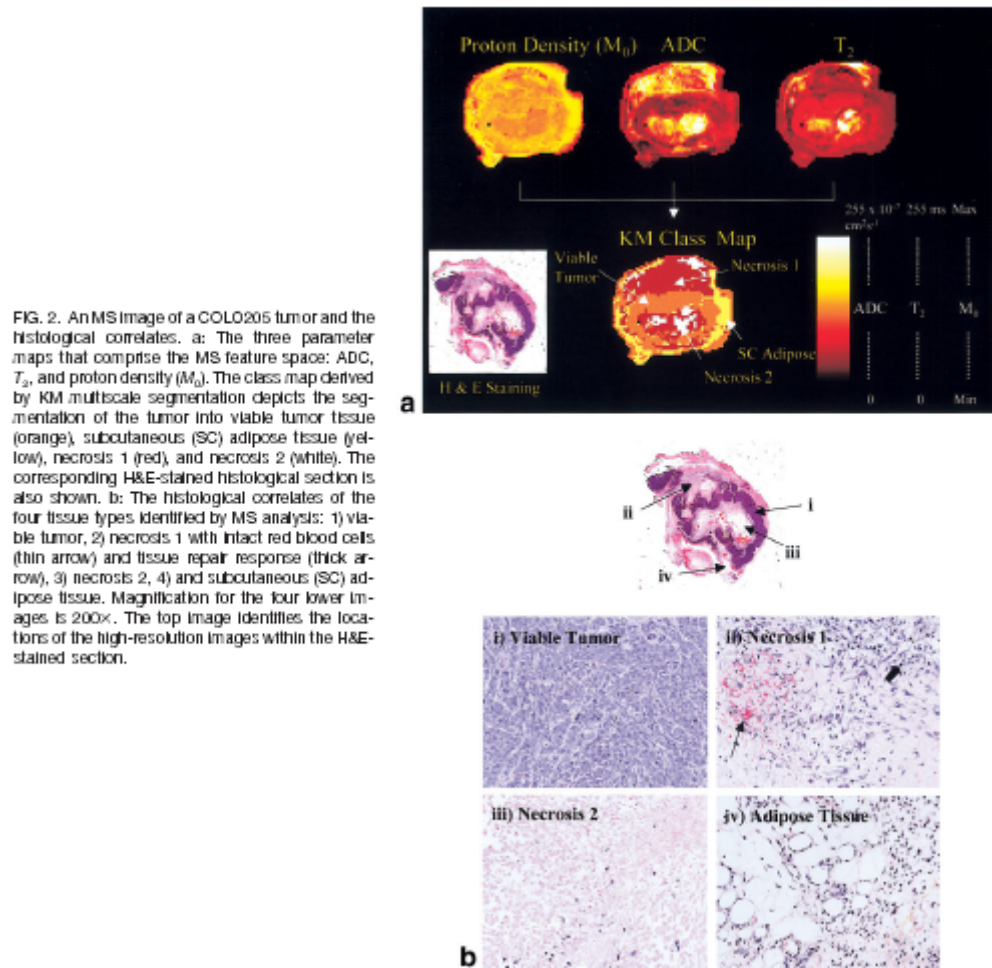


Figure 3-3. Multispectral (MS) tissue characterization using the KM clustering procedure and a feature space containing ADC, T_2 , and M_0 . Figure reproduced from reference (51).

3.1.5 MS Analysis with Histological Validation

In order to gain insight into the various processes whose combination yield the total ADC response over time, as well as the contribution of tissue heterogeneity (viable, necrotic) to the treatment response, we performed MS analysis using ADC, T_2 , and M_0 using the KM clustering algorithm (52) for identification of multiple compartments within both viable and necrotic tissue. The KM clustering algorithm is an unsupervised classification technique that has been utilized in past studies of cerebral ischemia (53,54) and tumor chemotherapeutic response (51). In order to use KM, the number of clusters, k , is

determined a priori. In this study, the number of clusters was determined based on reproducibility and the correlation between KM parameter maps and the corresponding histology. The utility of adding T_2 and M_0 for more accurate identification of individual tissue populations, versus ADC alone, was assessed based on minimization of the sum of squared differences (SSD) for KM volume estimates and their corresponding histological volumes. Hematoxylin-eosin (H&E) staining was performed for identification of viable tissue (broken into two sub-regions; V1, V2) versus regions of necrosis (broken into two sub-regions; N1, N2). Immunohistochemical staining for hypoxic-inducible factor-1 alpha (HIF-1 α) was performed to validate the subdivision of viable tissue into well-oxygenated (V1) and hypoxic (V2) regions. MS tissue characterization was performed accordingly following optimization of method.

3.2 Methods

3.2.1 Animal Preparation

The present study was approved by the Institute Animal Care and Use Committee (IACUC) of the University of Massachusetts Medical School (IACUC protocol A-544). Twenty-nine 6-8 week-old female C3H mice (20-25g; Taconic Farms, Germantown, NY) were initially anesthetized with an intraperitoneal injection of ketamine/zylazine (100 mg/kg:10 mg/kg). All mice were inoculated with 1×10^6 RIF-1 cells (0.15 ml), delivered through a subcutaneous injection into the right hind leg. Tumors were allowed to develop for 3-4 weeks, yielding an approximate 1.0 cc starting volume. Tumor volume was determined from caliper measurements, taken 2-3 times per week, of the three perpendicular axes (length, width, height) and the equation for calculating the volume of an ellipsoid, where $V = (\pi/6) (l \times w \times h)$. Animals were subsequently divided into two groups: a control group (N = 16) and a treatment group (N = 13). For the control group (N = 16), tumors of varying volumes (1.0 cc to 2.0 cc) were imaged at a single timepoint and then extracted for histological examination. For the treatment group (N = 13), tumors of an approximate 1.0 cc starting volume were irradiated with 1000 cGy at a rate of 300 cGy/min (Siemens Mevatron 77, 6 MeV electrons, Tufts University School of Veterinary Medicine, North Grafton, MA). Imaging for the treatment group was

performed at 1d pre-treatment, 5 hr, 1d, 2d post-treatment, and every 2d thereafter until tumor doubling (maximum 14d post-treatment) or until tumors reached a 2.0 cc volume (considered a burden for the animal).

3.2.2 Radiotherapy

Prior to radiotherapy, animals were anesthetized with an intraperitoneal injection of ketamine/xylazine (100 mg/kg:10 mg/kg). Animals were placed prone on a plastic board, with movement restricted by securing the forepaws and hindlegs using medical tape (Fig. 3-4a). The right hind leg was pulled away from the body in preparation for the procedure. First, a 0.5-cm-thick bolus of tissue-substitute (Bolx-II, MED-TEC, Inc., Orange City, IA), with the center cut out, was placed around the tumor and filled with gel (Fig. 3-4b). In order to deliver the desired dose to the tumor center without exposing the underlying tissue and bone, an additional 0.5-1.0 cm thick bolus of tissue-substitute was placed over the top, depending on the measured tumor height (Fig. 3-4c). Based on tumor length and width, custom-made cutouts from 2.0-3.0 cm in diameter were used for the cone size in order to limit the radiation to the tumor versus the surrounding tissue (Fig. 3-4d). Following preparation, tumors were irradiated with 1000 cGy at a rate of 300 cGy/min (Siemens Mevatron 77, 6 MeV electrons, Tufts University School of Veterinary Medicine, North Grafton, MA). At the conclusion of single-dose radiotherapy, animals were returned to their cage where they recovered from anesthesia and were provided with food and water.

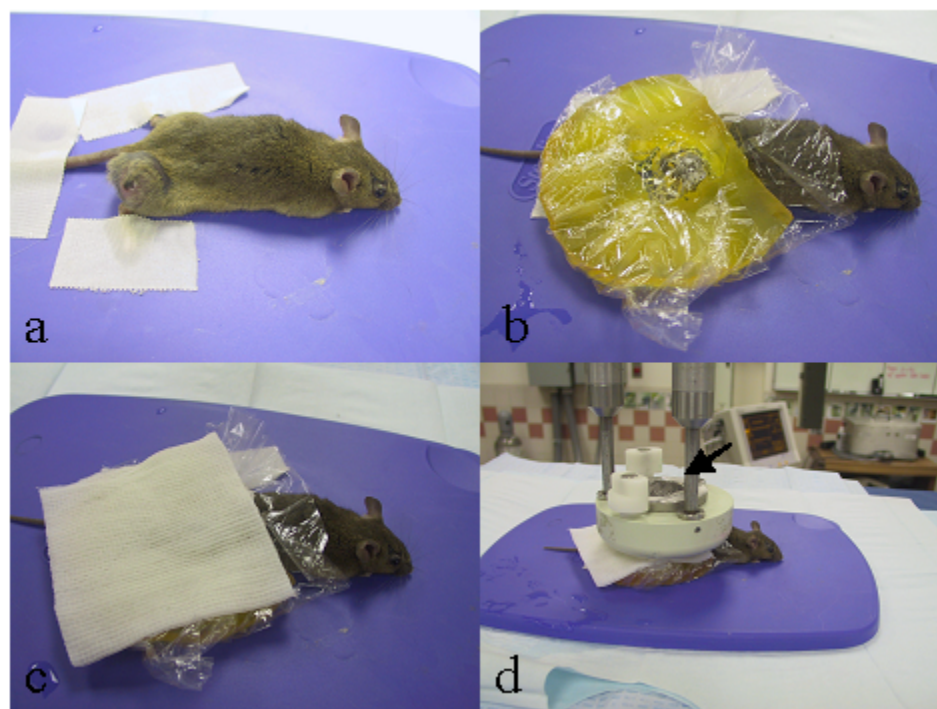


Figure 3-4. Animal preparation for receipt of single-dose radiotherapy. (a) The animal's right hind leg was pulled away from the body and secured with medical tape. (b) The tumor was surrounded by a 0.5-cm-thick-bolus of tissue-substitute (Bolx-II; MED-TEC, Inc., Orange City, IA) (c) An additional 0.5-1.0-cm-thick bolus of tissue-substitute was added, depending on the tumor height, in order to deliver the desired radiation dose to the tumor center. (d) Custom-made cutout (arrow) and positioning of setup for tumor irradiation.

3.2.3 MRI Measurements

MRI experiments were performed with a Bruker Biospin 2.0T/45cm imaging spectrometer operating at 85.56 MHz for ^1H and equipped with ± 20 G/cm self-shielded gradients (Fig. 3-5). The experiments involved multi-slice image acquisition along the coronal plane [matrix size = 128×128 , FOV = $3\text{cm} \times 3\text{cm}$, slices = 8, slice thickness = 1mm]. The imaging plane was referenced to the boundary between the tumor and underlying muscle. A diffusion-weighted, spin-echo (SE) sequence was used to acquire the images at six b-values ($b = 15, 60, 140, 390, 560, 760 \text{ mm}^2 \text{ s}^{-1}$) with diffusion sensitization applied along the read (x) direction. Other acquisition parameters were:

TR/TE = 2000.0/53.0 ms, diffusion gradient duration $\delta = 4.0$ ms, diffusion gradient separation $\Delta = 35$ ms, resulting in an effective diffusion time $t_{\text{dif}} = 33.7$ ms. A T_2 -weighted, spin-echo (SE) sequence was used to acquire images at six echo times (TE = 12.2, 20, 35, 50, 65, 90 ms) with TR = 2000.0 ms. The experiment times were 25 min for diffusion and 5 min per TE value for T_2 , yielding a total imaging time of 55 min. During imaging, animals were placed prone in a home-built animal holder with a 4-turn ^1H solenoid coil around the tumor (Fig. 3-6). Multiple coils of variable diameter were constructed (0.95, 1.35, 1.75 cm) to account for tumor volume changes in repeated measures experiments. Animals were anesthetized with 1.5% isoflurane at a rate of 1.5 L/min in breathing quality air. Body temperature was maintained by circulating warm air at $34.0^\circ \pm 1.0^\circ\text{C}$ using a T-type thermocouple and a double-point feedback control system.



Figure 3-5. Bruker Biospin 2.0T/45cm imaging spectrometer equipped with ± 20 G/cm self-shielded gradients. Current software: Paravision 2.1.1.

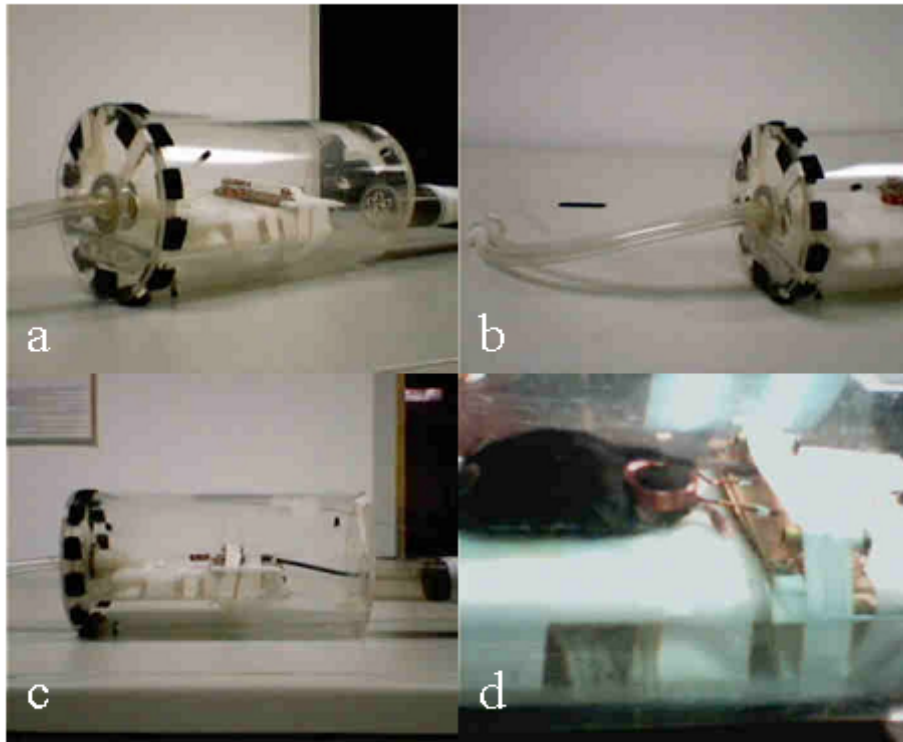


Figure 3-6. Home-built animal holder for murine RIF-1 tumor imaging. (a) Angled-view. (b) Dual-fitted head for delivery and removal of anesthetic (c) Side-view. Thermocouple and circulating tube for warm air and maintenance of body temperature (d) Positioning of solenoid coil to encompass the tumor during imaging.

3.2.4 Data Analysis

Parameter Map Production

Image reconstruction was performed using Paravision's Image Processing and Display Software (Xtip). Image analysis and parameter map production was performed using routines written in IDL (Research Systems Inc., Boulder, CO). ADC, T_2 , and M_0 parameter-map production was performed on a pixel-by-pixel basis based on the relationship between the natural log of the signal intensity and b-value (Eq. 3-1) or signal intensity and echo time (Eq. 3-2), respectively:

$$M(t) = M_0 e^{-bD} \quad (3-1)$$

$$M(t) = M_0 e^{-TE/T_2} \quad (3-2)$$

where M/M_0 is the signal intensity at a particular b-value or TE value; D is the diffusion along a single direction, and T_2 is the spin-spin or transverse relaxation time. A linear

fitting procedure based on the minimization of the chi-square statistic was employed for extraction of MR parameters. Underlying muscle, remaining in the lower imaging slices for (N = 9) animals, was removed by delineation between tissue boundaries using T₂-weighted contrast images (TE = 90ms).

Correction of M₀ Maps

M₀ map correction was performed on a pixel-by-pixel basis using homomorphic unsharp masking (55) and global mean fixation using the following equation:

$$M_0'(i, j) = \frac{\mu_{\text{global}}}{\mu_{\text{roi}}} M_0(i, j) \quad (3-3)$$

where M₀(i,j) is the individual pixel value (i,j), μ_{roi} is the mean for a 23 × 23 ROI centered about (i,j), μ_{global} is the global mean (i.e., a user-defined ‘mean’ applied to all tumor datasets), and M₀'(i,j) is the corrected M₀. Homomorphic unsharp masking (HUM) (23 × 23 kernel) was applied to correct the M₀ maps for distortions due to B₁-field inhomogeneities from tumor extension beyond coil boundaries (55). The global mean of each of the M₀ maps was set to the same arbitrary constant in order to remove temporal variations in M₀, permitting tissue classification based on regional differences in M₀.

3.2.5 K-means Clustering

A 3D feature vector, containing the ADC, T₂, and M₀ parameter maps, was generated for each pixel. KM clustering was performed on a pixel-by-pixel basis using the Euclidean distance measure (52):

$$D = (x - \mu_i)'(x - \mu_i) \quad (3-4)$$

where $x \in \mathbb{R}^3$ is the feature vector and μ_i is the cluster mean, both determined from all of the data (N = 88 datasets, all animals, all timepoints). Prior to KM clustering, feature normalization (mean μ = 0, standard deviation s = 1) was performed for removal of potential scaling differences. Tissue classification was then performed using KM in a hierarchical manner. In the first step of the classification algorithm, KM was applied to separate the data into two clusters (k = 2) of tumor tissue and background noise based on variations in M₀. All voxels classified as noise were set to zero and removed from further processing. In the second step, KM was applied for a varying number of clusters using between one and three features, where f = 1 (ADC), f = 2 (ADC and T₂), f = 3 (ADC, T₂

and M_0), to segment the data into the following: one region each of viable tumor (V1) and necrosis (V2) ($k = 2$); one region of viable tumor (V1) and two regions of necrosis (N1, N2) ($k = 3$), two regions each of viable tumor (V1, V2) and necrosis (N1, N2) ($k = 4$). For KM with 3 features ($f = 3$; ADC, T_2 , and M_0), an additional cluster was added in order to compensate for residual M_0 inhomogeneities missed by HUM correction (i.e., induced by solenoidal coil contact with the tumor edge). All KM methods were then compared with histology in order to determine the optimum number of clusters (k) and features (f).

3.2.6 Histological Analysis

For the control group following imaging, as well as for the radiotherapy group following the final imaging timepoint, animals were euthanized by an overdose of ketamine/zylazine (400 mg/kg:40 mg/kg). The RIF-1 tumors were extracted based on the intersection between the tumor and muscle and frozen for 30 minutes. Sections were taken every 2 mm starting from the base of the tumor, stored in individual tissue cassettes (Microcassettes, VWR International, NJ), and placed in 10% neutral buffered formalin (Fisher Scientific, Pittsburgh, PA). Following fixation, a standard paraffin embedding procedure was used. Tissue cassettes were marked L-R in order to preserve orientation for later correlative analysis between imaging and histology.

Hematoxylin-Eosin (H&E) Histochemistry

For all tumors, three 6 μ m sections, approximately 300 μ m apart, were taken every 1-mm for a total of 24 sections per tumor. Sections were mounted on Poly-L-lysine coated slides (VWR International, West Chester, PA) and dried overnight on a slidewarmer at 37°C. Slides were then stored at room temperature until further processing. Hematoxylin-Eosin (H&E) staining was performed for all sections with digital images (1 \times) taken on a section-by-section basis using a Hewlett-Packard Scanner (Model #3970) at a resolution of 1200dpi. Image analysis and delineation between individual tissue regions (viable, necrotic) was performed using KM clustering and a feature space ($f = 4$) based on the R,G,B image values and texture analysis (56) using the Hurst transform, an image operator used in fractal analysis for the characterization of surface roughness (57). The Hurst transform or coefficient was calculated on a pixel-by-pixel basis using a 7-

pixel-wide neighborhood, and pixel labels identifying groups with the same distance from the central pixel (Fig. 3-7). A linear fitting procedure of log of the distance and versus log of the maximum brightness range between groups in the neighborhood and the central pixel permitted calculation of the Hurst coefficient. In this case, the Hurst coefficient is equivalent to the slope based on the best-fit line and minimization of the chi-square statistic. Additional images were taken at higher resolution (2 \times , 10 \times , 20 \times , and 40 \times) for correspondence with HIF-1 immunohistochemistry using an upright Nikon Eclipse E400 phase contrast microscope (Nikon, Melville, NY) equipped with an RT Color Spot camera (Diagnostic Instruments, Inc., Sterling Heights, MI) for image capture. Spot Analysis 4.0.9 (Diagnostic Instruments, Inc., Sterling Heights, MI) software was employed for optimization of image quality and image acquisition.

Hypoxic Inducible Factor 1 α (HIF-1 α) Immunohistochemistry

For (N = 9) tumors (N = 5 radiotherapy, N = 4 control), additional 6 μ m sections were taken at the approximate 600 μ m mark. Sections were mounted on Poly-L-lysine coated slides (VWR International, West Chester, PA) and dried overnight on a slidewarmer at 37 $^{\circ}$ C. Slides were then stored at room temperature until further processing. Immunohistochemical staining for HIF-1 α was performed using a 1:75 dilution of the mouse monoclonal antihuman HIF-1 α antibody (ab463, ABCam Inc., Cambridge, MA). Optimization of method and immunohistochemical staining was performed by Mass Histology Service (Worcester, MA). Sections were deparaffinized and peroxidase was quenched with 3% H₂O₂ for 15 min. Slide preparation for staining was performed with heat-mediated antigen retrieval (Vector #H-3300 for 20 min.). After rinsing with PBS, slides were incubated overnight at 2 $^{\circ}$ C with the primary antibody. Sections were again rinsed with PBS and incubated with a 1:250 dilution of the secondary antibody (biotin goat anti-mouse IgG, Vector #BA2000) for 1 hr. After rinsing with PBS, detection was performed using a streptavidin-biotin-horseradish peroxidase system (Vector Elite #PK6100 for 1 hr). Sections were again rinsed with PBS and color was developed by a 15-min incubation with 3,3'-diaminobenzidine solution (DAB). Slides were lightly counterstained with hematoxylin. For negative controls, the primary antibody was not applied. Tumor samples with strong cytoplasmic and/or nuclear expression were considered to be positive.

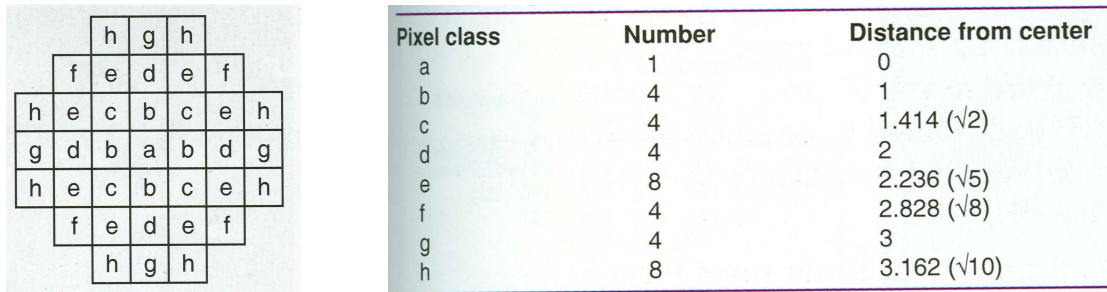


Figure 3-7. Method of analysis using the Hurst operator. Left: 7-pixel-wide neighborhood (37 pixels total) used for calculation of the Hurst coefficient. Pixel labels identify groups with the same distance from the central pixel. Right: Table of pixel classes and their distance from the center pixel.

3.2.8 Statistical Analysis

Data are reported as mean \pm SEM. MS estimates of individual cluster volumes (V_1, V_2, N_1, N_2) as well as viable volume ($V_1 + V_2$) and necrotic volume ($N_1 + N_2$) were compared with H&E histological volumes through computation of Pearson's correlation coefficient to provide the degree of linear association between imaging and histological volume estimates. Histology slices at the 600 μ m point for 1-mm sections from $N = 16$ tumors were analyzed (all other H&E sections had considerable tissue loss). Determination of the best combination of features and clusters was established by finding the method with the best correlation and one-to-one correspondence between KM- and histologically derived tissue-volume estimates. For each cluster/feature combination, the SSD of the data from the model $x = y$ line was calculated (58):

$$\text{SSD} = \sum (\text{Histological \%TTV} - \text{KM\%TTV})^2 \quad (3-5)$$

providing a method for assessment of goodness-of-fit. The cluster/feature combination minimizing the SSD was chosen as the optimum with provision of good correspondence to histology. All subsequent analysis was performed using the optimal cluster/feature combination. The temporal evolution of individual cluster volumes and feature means (ADC, T_2, M_0), as well as total volume and feature mean, were compared on a timepoint-by-timepoint basis between pre-irradiation and post-irradiation by Student's t-tests assuming unequal variances. The relationship between tumor size and percent necrosis, as well as percent necrosis for control and radiotherapy groups was investigated using Pearson's correlation coefficient to provide a measure of the degree of linear correlation between parameters.

3.3 Results

3.3.1 Optimization of KM Method

KM segmentation was applied to divide the data into individual tissue classes based on the Euclidean distance measure (Eq. 3-4). Fig. 3-8a-f shows correlation plots of KM percent necrotic fraction estimated using the following combinations: 1 feature (ADC) and 2 clusters (V1, N1); 1 feature (ADC) and 3 clusters (V1, N1, N2); 2 features (ADC and T₂) and 3 clusters (V1, N1, N2); 2 features (ADC and T₂) and 4 clusters (V1, V2, N1, N2); 3 features (ADC, T₂, and M₀) and 4 clusters (V1, N1, N2, edge); and 3 features (ADC, T₂, and M₀) and 5 clusters (V1, V2, N1, N2, edge). Note that the addition of an ‘edge’ cluster in the KM segmentations including M₀ is necessary in order to account for B₁ field inhomogeneities missed by HUM correction (i.e., generally from the tumor touching the coil edge). The sum of squared differences (SSD) for the KM method with two features (ADC, T₂) and four clusters (V1, V2, N1, N2) for subdivision of both viable and necrotic tissue yielded the minimum SSD, indicating this particular KM tissue segmentation approach was optimal. A quantitative summary of the SSD values for KM percent necrotic fraction versus histologically-derived percent necrotic fraction, as well as the correlation between KM tissue volumes estimates and their corresponding histological volumes are provided in Table 3-1. Although Pearson’s correlation coefficient for KM versus histologically-derived necrotic volumes was the best for using a single feature (ADC) and two clusters ($r = 0.76$), the SSD was the lowest for where two N1, N2). Pearson’s correlation coefficient for KM versus histologically-derived viable volumes was identical for the two methods ($r = 0.94$). In addition, there was a strong correlation between KM versus histologically-derived viable volumes ($r = 0.80$) and a moderate-to-strong correlation between KM and histologically-derived necrotic volumes ($r = 0.61$) as determined on a slice-by-slice basis (Fig. 3-9). These results indicate that the addition of T₂ permits more accurate identification of the total necrotic fraction of the tumor with good slice-by-slice correspondence between KM and histologically-derived necrotic slice volumes; and similar reliability in total viable tissue estimates to ADC alone.

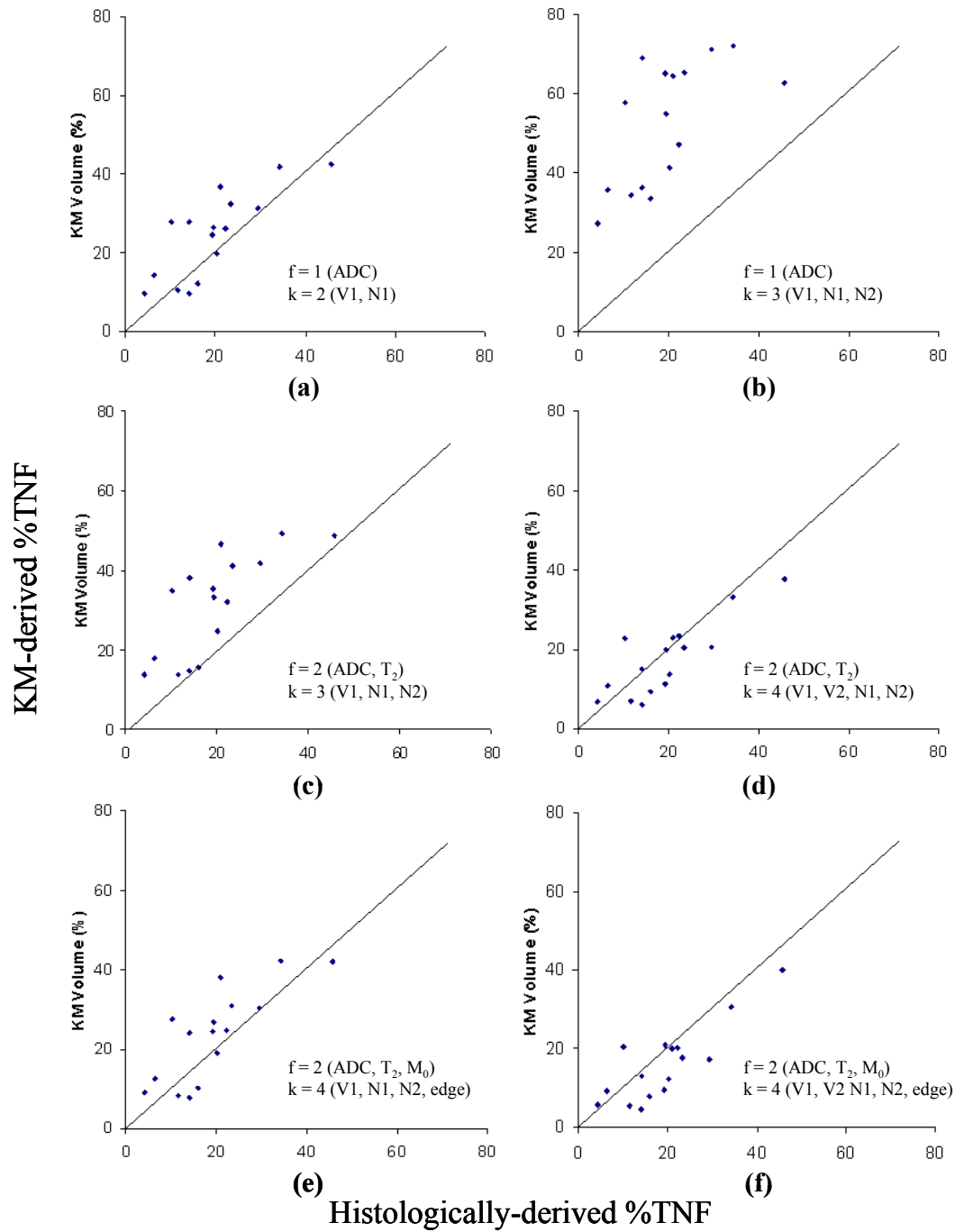


Figure 3-8. Correlation plots of histologically-derived percent-tumor-necrotic fraction (%TNF) versus KM-derived estimates. The $x = y$ line provides a visual reference for the distribution of the data relative to the optimal model, i.e., a one-to-one correspondence. KM feature assignments are labeled on individual plots with designations as follows: f = feature, k = cluster, V1 = viable 1, V2 = viable 2, N1 = necrosis 1, N2 = necrosis 2, and edge = tumor edge (this cluster was added in order to compensate for low M_0 values introduced by the tumor edge touching the coil). The optimum KM method (d) exhibits the smallest deviations from the model $x = y$ line, and therefore, the smallest sum of squared differences (SSD).

Table 3-1. Correlative Summary Between Various KM Methods and Histologically-Derived Estimates of Percent Tumor Necrotic Fraction, Viable Tumor Volume, and Necrotic Volume.

Features	Clusters	SSD (%TNF)	r-value (Viable)	r-value (Necrotic)
ADC	2	1119	0.94	0.76
ADC	3	19441	0.82	0.72
ADC, T ₂	3	3306	0.93	0.75
ADC, T ₂	4	588	0.94	0.69
ADC, T ₂ , and M ₀	4	1053	0.94	0.75
ADC, T ₂ , and M ₀	5	713	0.92	0.68

SSD = sum of squared differences

%TNF = Tumor Necrotic Fraction

r-value = Pearson's correlation coefficient

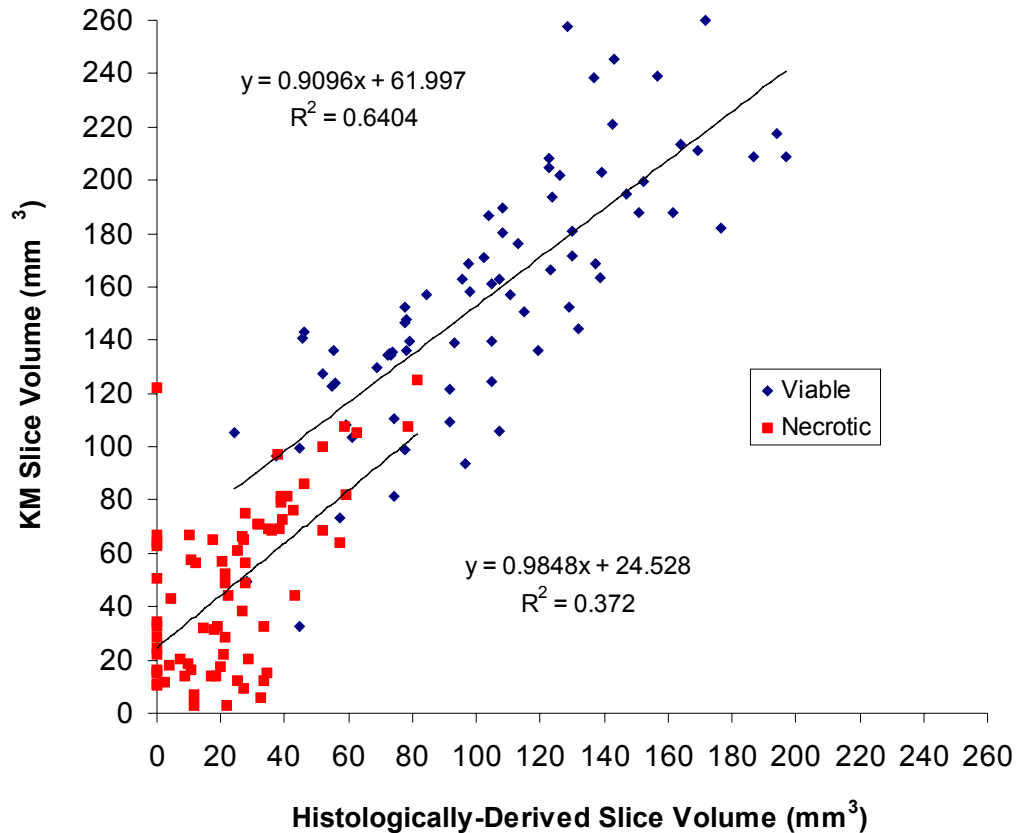


Figure 3-9. Correlation plot of KM volume estimates ($f = 2$, $k = 4$) on a slice-by-slice basis for viable and necrotic tissue populations versus histologically-derived estimates. There was a strong correlation between estimates for viable tissue ($r = 0.80$) and a moderate-to-strong correlation between estimates of necrosis ($r = 0.61$) per determination on a slice-by-slice basis. The non-zero y-intercepts correspond to an overestimation of KM volume versus that of the histologically-derived volume. This overestimation is most likely from tissue shrinkage during histological preparation.

3.3.2 KM Segmentation Results

Based on the optimal KM approach using two features (ADC and T_2) and four clusters, tissue segmentation was performed in a hierarchical manner according to Fig. 3-10. Representative ADC and T_2 parameter maps, their normalized values, and the corresponding KM segmentation map and histological H&E sections are shown in Fig. 3-11. For the KM segmentation map (Fig. 3-11, 5th column), individual tissue regions have been color-coded such that: red = necrotic 1, blue = necrotic 2, green = viable 1, and yellow = viable 2. Mean feature values for individual tissue populations, obtained via clustering of all datasets together ($N = 88$ datasets, over all timepoints), are summarized

in Table 3-2. These results indicate the existence of two unique subpopulations within both viable and necrotic tissue. Both necrotic regions were characterized by high ADC values, but differed based on T_2 . Necrosis 1 had both high ADCs and long T_2 values, whereas necrosis 2 had shorter T_2 values. The viable tissue regions differed in both ADC and T_2 . Viable 1 had both low ADCs and low T_2 values, whereas viable 2 had intermediate ADCs and T_2 values lower than that of viable 1. These KM tissue volume estimates, as described in Section 3.3.1, are well correlated with their corresponding histological estimates. The KM viable volume estimates ($746 \pm 320 \text{ mm}^3$) were strongly correlated ($r = 0.80$, $p < 0.01$) with the histologically-derived viable volumes ($496 \pm 237 \text{ mm}^3$), and the KM necrotic volume estimates ($226 \pm 129 \text{ mm}^3$) were moderately to strongly correlated ($r = 0.61$, $p < 0.01$) with the histologically-derived necrotic volumes ($111 \pm 62 \text{ mm}^3$). The average KM total tumor volume was 972 mm^3 , in comparison to the average histological volume of 607 mm^3 .

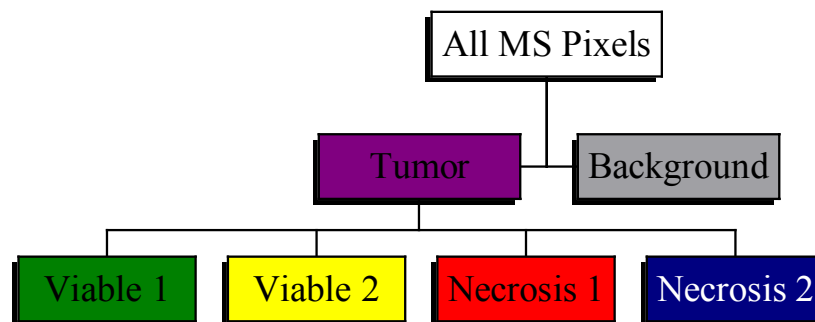


Figure 3-10. Organizational chart diagramming the hierarchical method of KM clustering performed for multiparametric segmentation of tumor into four tissue populations. In the first step ($k = 2$), KM clustering was applied for segmentation of the tumor from background noise voxels based on differences in M_0 . Following removal of the background (by setting values to zero), the remaining tumor voxels were segmented into four tissue populations ($k = 4$), two each for viable tissue and necrosis using a 2-dimensional feature space including ADC and T_2 .

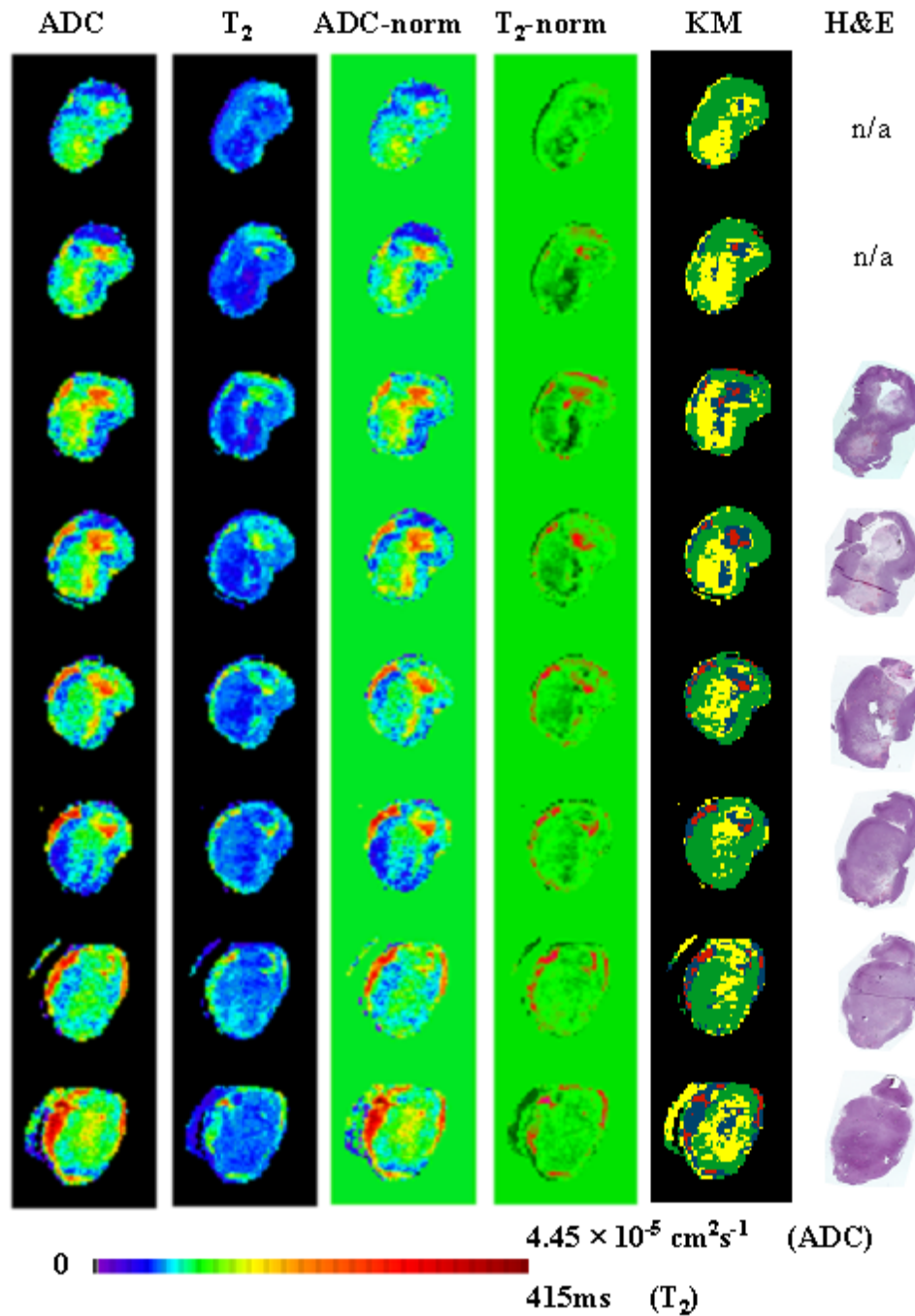


Figure 3-11. KM segmentation results for a representative tumor with corresponding histology via H&E histochemistry. ADC and T₂ parameter maps are shown in the 1st and 2nd columns, with their corresponding normalization maps in the 3rd and 4th columns. These normalization maps were used for MS analysis using KM clustering and the Euclidean distance, with $k = 4$ clusters and $f = 2$ features, namely ADC and T₂. The final KM segmentation map is shown in the 5th column, with color designations such that red = necrosis 1, blue = necrosis 2, green = viable 1, yellow = viable 2. The corresponding H&E histological sections are given in the last column on the right.

Table 3-2. Mean feature values (ADC and T_2) for individual tissue populations following KM segmentation using $k = 4$ clusters.

Features	ADC ($\times 10^{-5} \text{ cm}^2 \text{ s}^{-1}$)	T_2 (ms)	total number of voxels	% of total
Viable 1	0.76 ± 0.05	60 ± 20	627227	56
Viable 2	1.11 ± 0.05	50 ± 20	374936	34
Necrosis 1	2.2 ± 0.4	139 ± 15	11896	1
Necrosis 2	1.8 ± 0.1	68 ± 6	103951	9

Parameters were derived on an animal-by-animal basis based on the clustering of all datasets together ($N = 29$ animals, 88 total datasets over all timepoints). Data are presented as mean \pm SD.

3.3.3 Correlation with Histology

KM Segmentation and H&E Staining of Tumor Morphology

Fig. 3-12 shows the KM segmentation map (Fig. 3-12a) and the corresponding H&E stained section (Fig. 3-12b) for a single-slice, with high-power (20 \times) images for identification of morphological features contributing to the ADC and T_2 values measured in individual regions (Fig. 3-12c-f) labeled as: 1 = necrosis 1, 2a,b = necrosis 2; 3 = viable 1; 4 = viable 2. Necrosis 1 was generally acellular in nature, whereas necrosis 2 had a sparse population of cells intermixed with intact red blood cells (RBCs). Viable 1 was very cell-dense, whereas viable 2 had a slightly reduced cell density with greater vascularity. Fig. 3-13 shows higher power (40 \times) images corresponding to the (20 \times) images in Fig. 3-12c-f. Necrosis 1 (Fig. 3-13a) shows evidence of inflammation, indicated by the presence of neutrophils (blue arrows) recruited to the area to remove residual cellular debris (red arrows). In addition, the remaining structure post-cell death appears to have begun to degrade, and the few remaining cells in the region are in the process of nuclear fragmentation, termed karyorrhexis (yellow arrows). Necrosis 2 (Fig. 3-13b), in contrast to necrosis 1, has a sparse population of cells undergoing apoptotic cell death intermixed with RBCs that have accumulated in the interstitial space either

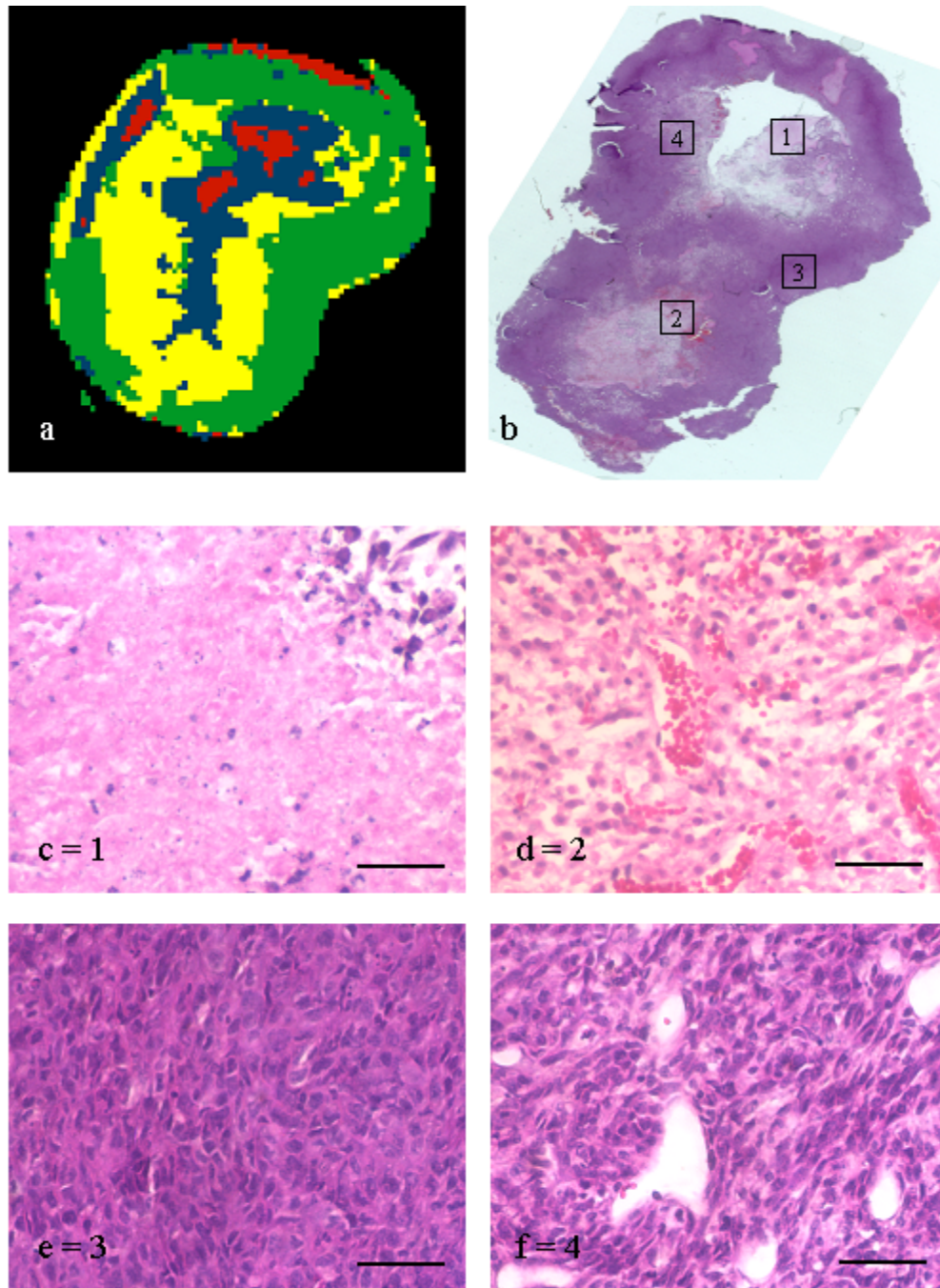


Figure 3-12. KM segmentation map for a single-slice from a representative RIF-1 tumor with corresponding histology. (a) KM map based on segmentation using 2 features (ADC , T_2) and 4 clusters. Individual tissue populations are color-coded such that: red = necrosis 1; blue = necrosis 2; green = viable 1, and yellow = viable 2. (b) H&E stained section. Regions of interests were chosen for investigation of the underlying morphological contribution to the measured ADC and T_2 values, with: 1 = necrosis 1; 2 = necrosis 2; 3 = viable 1; 4 = viable 2. These regions correspond to the 20x images in (c) through (f). Scale bar = $50\mu\text{m}$.

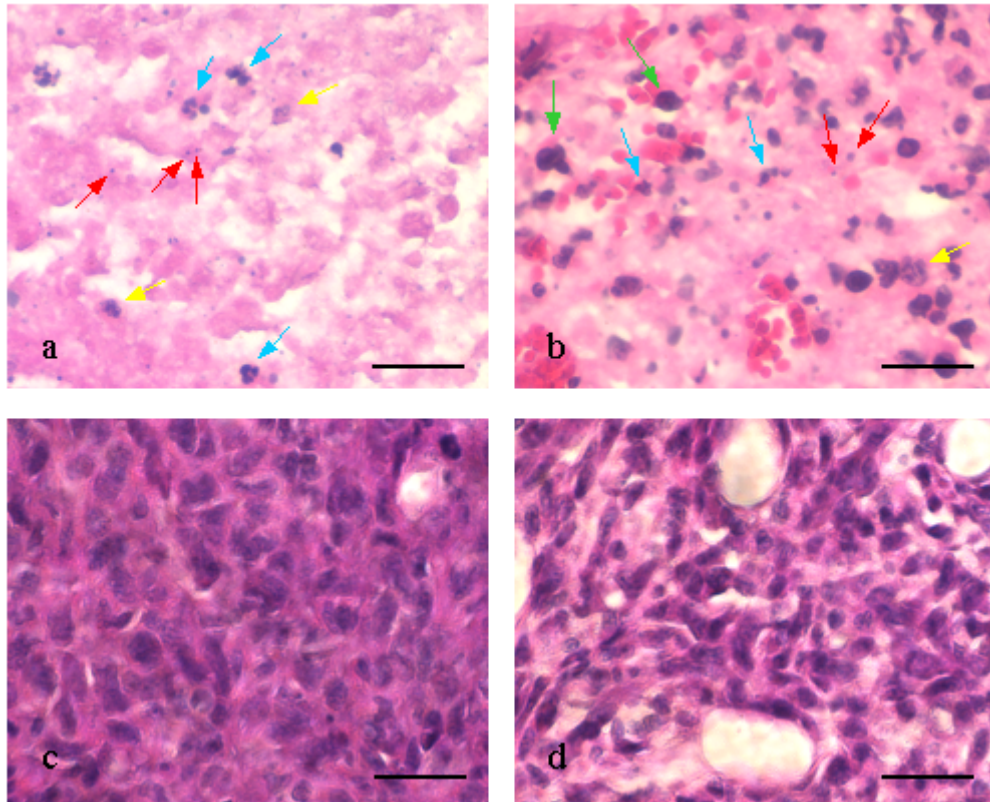


Figure 3-13. H&E images taken at 40 \times magnification, corresponding to the regions specified in Fig. 3-12. (a) Necrosis 1. This region is generally acellular in nature. (b) Necrosis 2. This region is characterized by a sparse population of cells intermixed with red blood cells. (c) Viable 1. This region is fairly cell-dense, with blood vessels around 10 μ m in diameter. (d) Viable 2. This region has a slightly lower cell density than (c), and is characterized by dilated blood vessels of an approximate 25 μ m-diameter. Morphological identification of enzymatic actions and repair mechanisms concomitant with apoptosis and/or necrosis are labeled by arrows: green = pyknosis, yellow = karyorrhexis, blue = neutrophil invasion, red = nuclear dusting. Scale bar = 25 μ m.

from hemorrhage or a leaky vasculature. This accumulation of RBCs leads to inflammation, indicated again by the presence of neutrophils (yellow arrows). Cells in this region are undergoing nuclear karyorrhexis (yellow arrows) or pyknosis (green arrows). Pyknotic nuclei exhibit degradation of both nuclear DNA and cytoplasmic RNA, resulting in nuclear shrinkage. Unlike the necrotic regions, Viable 1 (Fig. 3-13c) is extremely cell-dense, with no evidence of inflammation or RBC accumulation. Viable 2 (Fig. 3-13d), on the other hand, has a slightly reduced cell-density over that of viable 1, with an abundance of dilated blood vessels. These blood vessels are approximately 25 μ m in diameter in comparison to 10 μ m for viable 1.

HIF-1 α Immunohistochemistry and Identification of Hypoxia

Fig. 3-14 shows high power (10 \times , 20 \times , and 40 \times) images for control slides receiving only the secondary antibody (i.e., no anti HIF-1 α). Note that viable tissue (V) and necrosis (N) showed neither positive staining nor any residual background staining. Fig. 3-15 shows high power (10 \times , 20 \times , and 40 \times) images for HIF-1 α immunostaining and the corresponding H&E stained regions. Nuclei staining an intense brown (Fig. 3-15e, black arrows) indicate upregulated HIF-1 α expression specific to hypoxia. Cells with overexpression of HIF-1 α were generally located in peri-necrotic regions, although some cells in areas more distal to necrosis did have some HIF-1 α activity. These cells stained a faint brown (Fig. 3-15e, brown arrow), and likely had HIF-1 α expression unrelated to hypoxia. This is reiterated in Fig. 3-16. The first image (Fig. 3-16a) shows the viable tumor region for a control slide receiving only the secondary antibody (i.e., no anti HIF-1 α). The next image (Fig. 3-16b) shows the viable tumor region, which is presumably non-hypoxic, with a diffuse light brown staining of cells with some HIF-1 α activity. The cells with light staining have no characteristic spatial pattern. Fig. 3-16c, unlike the diffuse staining in Fig. 3-16b, exhibits cells with intense brown staining located specifically in peri-necrotic regions. This HIF-1 α activity is specific to hypoxia.

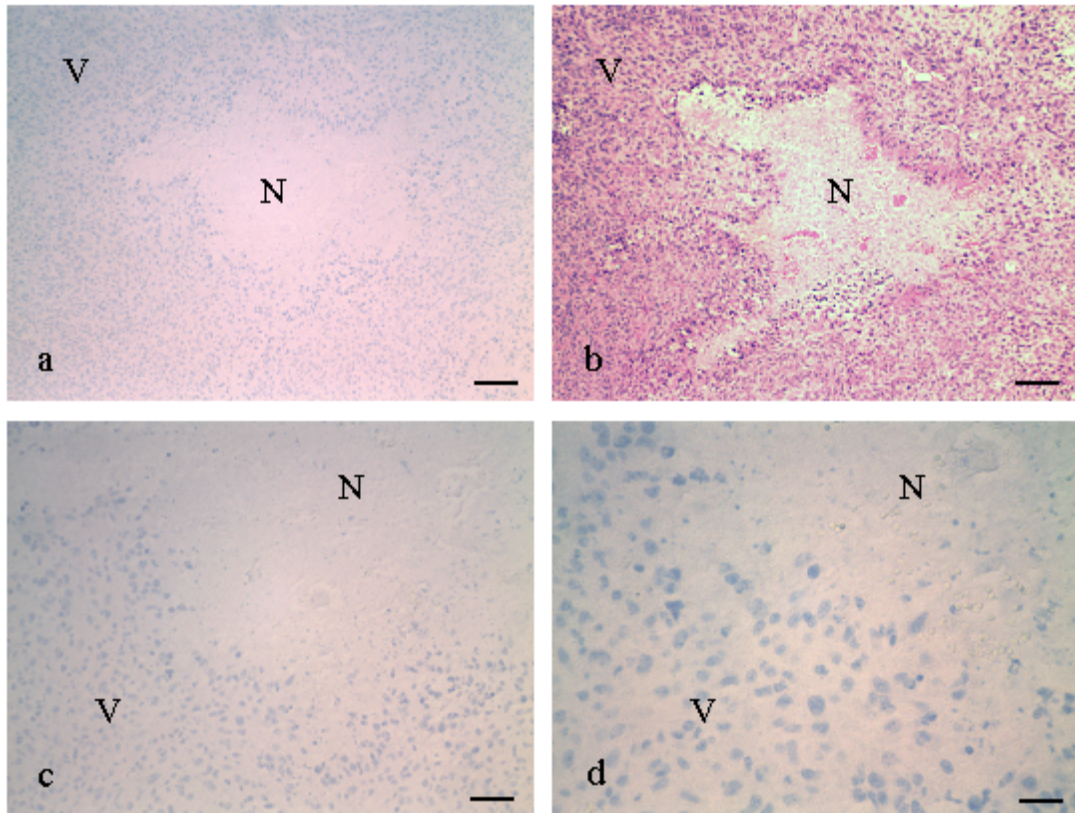


Figure 3-14. Negative control slides for HIF-1 α immunostaining with corresponding H&E histochemistry. (a) HIF-1 α negative control image (10 \times) denoting viable tissue (V) and necrosis (N). (b) Corresponding H&E stained section. (c) HIF-1 α negative control image (20 \times). (d) HIF-1 α negative control image (40 \times). Scale bar = 100 μ m for (a) and (b), 50 μ m for (c), and 25 μ m for (d).

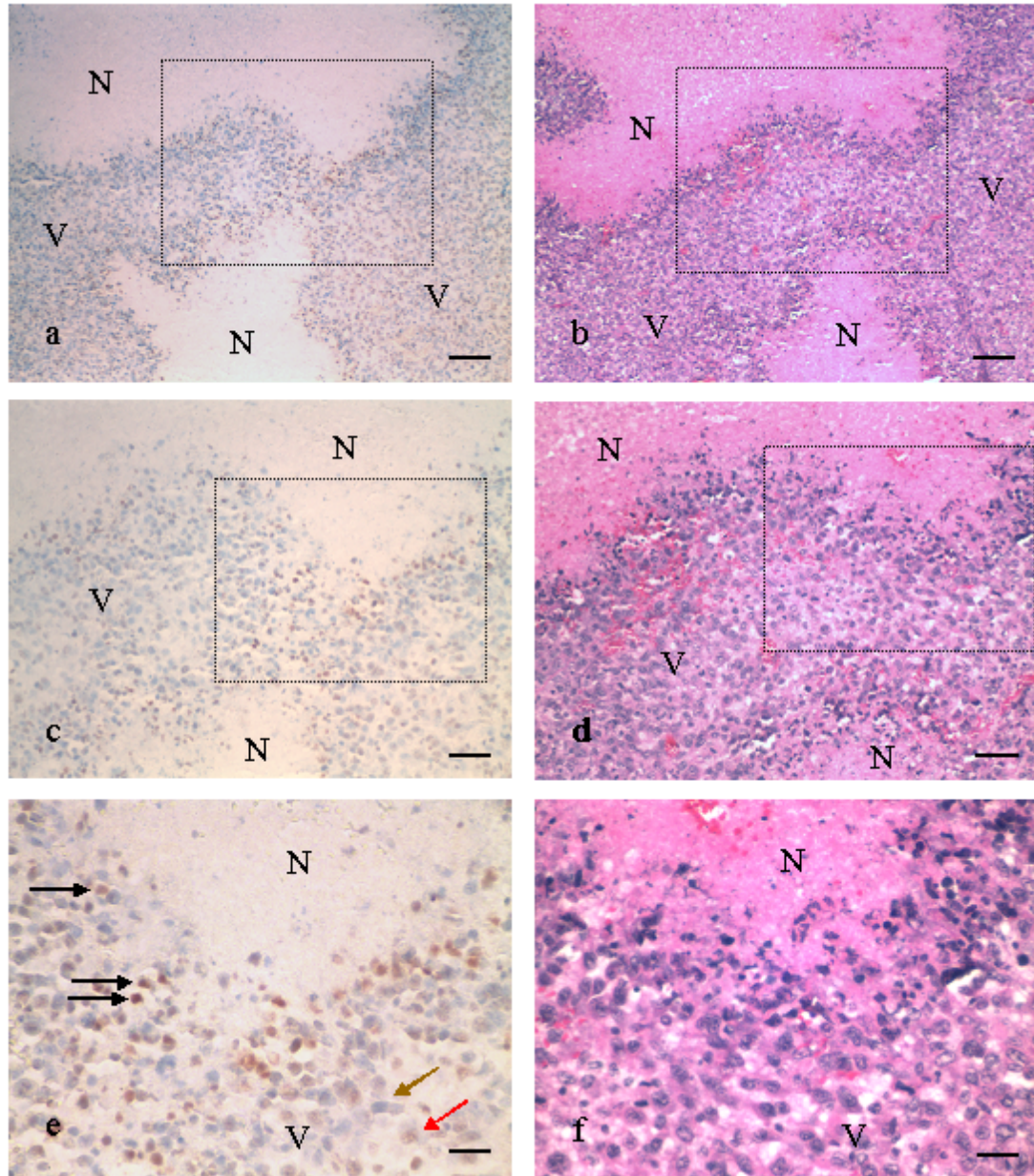


Figure 3-15. HIF-1 α immunostaining with corresponding H&E histochemistry. (a) HIF-1 α image (10 \times) denoting viable tissue (V) and necrosis (N). (b) Corresponding H&E stained section. (c) HIF-1 image (20 \times) from inset in (a). (d) Corresponding H&E stained section. (e) HIF-1 α image (40 \times) from inset in (c). (f) Corresponding H&E stained section. HIF-1 α positive nuclei in peri-necrotic regions stain an intense brown (black arrows), HIF-1 α negative nuclei stain light blue (from the hematoxylin counterstain, brown arrow), and nuclei with non-specific HIF-1 α activity (i.e., unrelated to hypoxia) stain a faint brown (red arrow). Scale bar = 100 μ m for (a) and (b), 50 μ m for (c) and (d), and 25 μ m for (e) and (f).

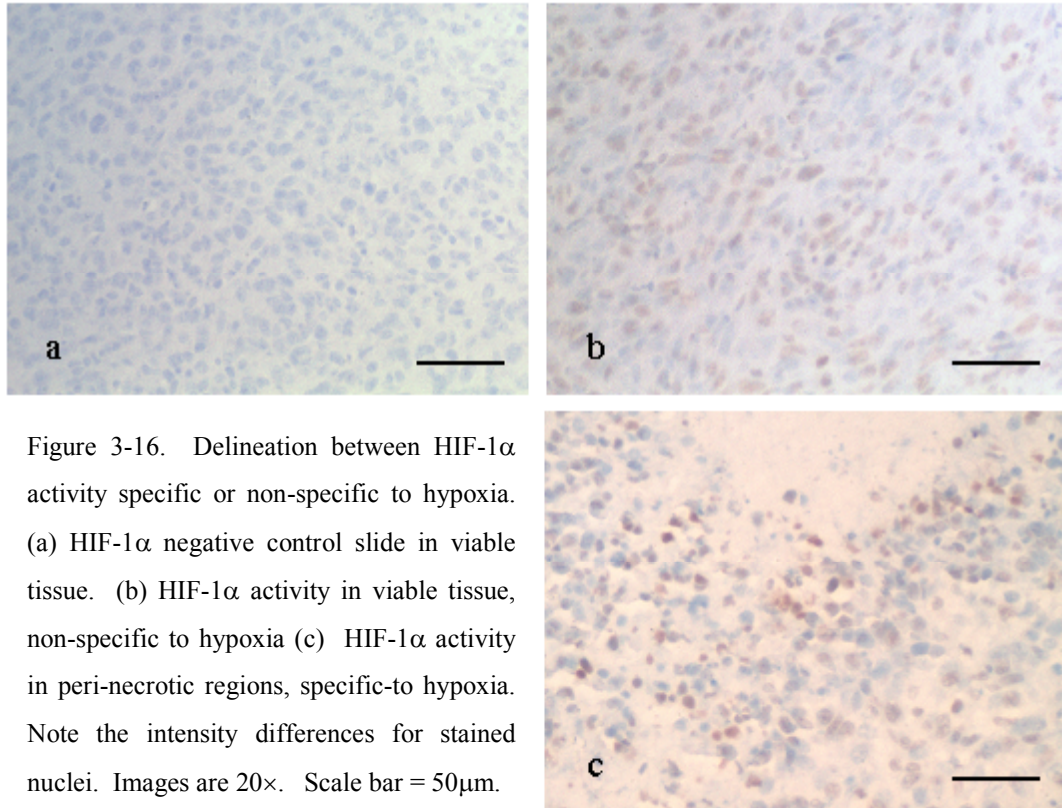


Figure 3-16. Delineation between HIF-1 α activity specific or non-specific to hypoxia. (a) HIF-1 α negative control slide in viable tissue. (b) HIF-1 α activity in viable tissue, non-specific to hypoxia (c) HIF-1 α activity in peri-necrotic regions, specific-to hypoxia. Note the intensity differences for stained nuclei. Images are 20 \times . Scale bar = 50 μ m.

3.3.4 Temporal Evolution of KM Volume

Fig. 3-17 illustrates the temporal evolution of individual KM volume estimates pre- as well as post-irradiation. The overall trend of the total KM volume is a volume decrease to day 2, followed by tumor regrowth from day 2 to day 8. Changes in KM viable volume mirror the changes in total KM volume. In contrast, KM necrotic volume consistently increases out to 2d post-irradiation, at which point it levels off. With the decrease in viable 1 out to day 2 there was a concomitant increase in viable 2. After day 2, both viable 1 and viable 2 slowly but steadily increased. In terms of individual necrotic regions, necrosis 1 remained unchanged with time, whereas necrosis 2 increased in volume to day 4, after which it leveled off. This trend for necrosis 2 followed very closely to that of the total volume, not surprising as the majority of the necrotic volume was necrosis 2 versus necrosis 1.

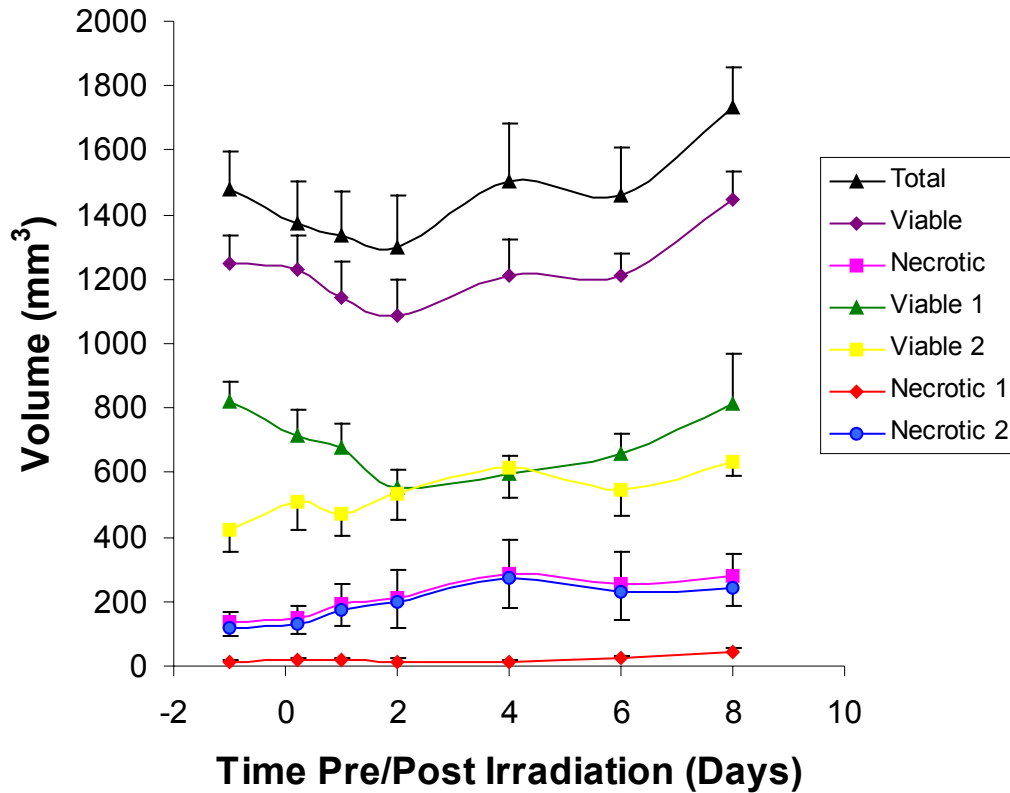


Figure 3-17. Temporal evolution of individual KM cluster volumes pre- and post-irradiation. The overall volume decreases post-irradiation out to day 2, with subsequent tumor regrowth post day 2. The underlying contributions to changes in tumor volume are visible by inspection of individual tissue populations (viable, necrotic), as well as the subpopulations within both viable and necrotic tissue. Data are presented as mean \pm SEM. Values for each timepoint are based on the radiotherapy animals ($n = 11, 12, 9, 8, 9, 8$ for 5h, 1d, 2d, 4d, 6d, and 8d respectively). Differences in number of animals per timepoint are based on tumors reaching 2.0cc, considered a burden for the animal.

3.4 Discussion

3.4.1 Determination of Optimum KM Method

In order to address the issue of tumor heterogeneity, MS analysis using ADC, T_2 , and M_0 parameter maps and the KM clustering algorithm was performed. Subdivision into individual tissue populations was based on similarities in feature space using the Euclidean distance measure (Eq. 3-4). The optimum number of clusters and features providing the best segmentation of tumor tissue is unknown *a priori*. Since the number(s) of clusters are chosen by the user, it is extremely important to identify the optimum number of clusters for tissue segmentation before further analysis. Selection of too few or too many clusters will result in reduced sensitivity to tissue heterogeneity and/or poor correspondence with histology. For this reason, both the number of clusters and the number of features were varied in order to determine the optimal KM method for addressing intra- and inter-tumor heterogeneity. The results for individual cluster/feature combinations are diagrammed in Fig. 3-8. Correlation plots of KM Volume presented as percent-tumor-necrotic fraction (%TNF) versus histologically-derived %TNF show that the option using 2 features (ADC, T_2) and 4 clusters minimized the sum of squared differences (SSD) to a value of 588 over all other methods (Table 3-1). The addition of T_2 over that of segmentation using ADC alone reduced the SSD from 1119 to 588, permitting more accurate division between viable and necrotic tissue. Both segmentation methods, ADC alone or ADC with T_2 , showed the same correlation between viable-volume estimates ($r = 0.94$) and similar values for necrotic-volume estimates ($r = 0.76$ for ADC alone and $r = 0.69$ for ADC with T_2). Although Pearson's correlation coefficient was slightly lower with the addition of T_2 , the 2-feature method provided a better estimate for the necrotic fraction (i.e., less overestimation) than ADC alone (Fig. 3-8a versus Fig. 3-8d). For segmentation with ADC and T_2 , besides a strong total volume correlation between viable and necrotic tissue estimates (Fig. 3-8d), there was also a good slice-by-slice correlation between KM viable ($r = 0.81$, $p < 0.01$) and necrotic ($r = 0.61$, $p < 0.01$) estimates and their corresponding histologically-derived volume estimates (Fig. 3-9). These values were generally overestimated (~38%), probably a result of tissue shrinkage from histological preparation using formalin fixation versus section loss.

Formalin is known to cause tissue shrinkage and deformation (59). The addition of M_0 didn't change the SSD or correlation values by a significant amount. Since segmentation including M_0 required an additional cluster to compensate for reduced M_0 values at the tumor edge (i.e., from B_1 field inhomogeneities), it was concluded that M_0 only added potential variability in the segmentation process and would compromise the ability to translate this technique to other oncological models.

3.4.2 KM Delineation Between Viable Tissue and Necrosis

Following methodological optimization, analysis of results from the 2-feature, 4-cluster method (ADC and T_2 with subdivision into two regions each of viable tissue and necrosis) was performed. The final KM segmentation according to normalized ADC and T_2 values and the corresponding histology via H&E is shown in Fig. 3-11, with a quantitative summary of the data in Table 3-2.

KM Subdivision of Necrosis

Superior to ADC alone, the addition of T_2 to the MS feature space permitted segmentation of both viable tissue (well-oxygenated vs. hypoxic) and necrosis (acellular vs. mixed). Using ADC alone for division between viable and necrotic tissue tended to overestimate the size of the necrotic region (Fig. 3-8a), and attempts at further subdivision of the necrotic region failed, resulting in gross overestimation of %TNF (Fig. 3-8b). With the addition of T_2 , two necrotic regions were identifiable. Because necrosis 1 is generally acellular (Figs. 3-12c and 3-13a), the T_2 values tend to be relatively long due to short correlation times (τ_c) and a homogeneous environment with properties close to that of bulk water. Necrosis 2 (Figs. 3-12d and 3-13b), on the other hand, is characterized by a sparse population of cells intermixed with RBCs. The intact RBCs, present from hemorrhage and/or a leaky vasculature (60), recruit neutrophils to the area (Fig. 3-13b, blue arrows). Most likely, this combination of RBCs, protein accumulation from neutrophil action, and the presence of a small cellular population leads to shorter T_2 values. RBCs with a high deoxyhemoglobin/methemoglobin (Hb/MHb) content are paramagnetic; therefore, they induce small local changes in the magnetic field, dephasing the transverse magnetization and shortening T_2 (61,62). Neutrophil accumulation and the remainder of cells both increase the amount of protein and macromolecules in the area,

which, when complexed with water, lengthen the correlation times and also shorten T_2 . Both necrotic regions had higher ADC values than regions characterized as viable tissue.

KM Subdivision of Viable Tissue

Employment of both ADC and T_2 permitted subdivision of the viable tissue as well. Viable 1 (Fig. 3-12e and 3-13c), presumably well-oxygenated tissue, was extremely cell-dense, free of any inflammation or RBC accumulation. This high cellular density results in increased diffusion restriction through the greater presence of cellular membranes and organelles, leading to ADC values of $\sim 0.76 \times 10^{-5} \text{ cm}^2\text{s}^{-1}$ (Table 3-2). Viable 2 (Fig. 3-12f and 3-13d), on the other hand, differs from viable 1 in both ADC and T_2 . Viable 2 has a slightly reduced cellular density from that of viable 1, with a greater abundance of dilated blood vessels (Fig. 3-13d) than viable 1 (Fig. 3-13c). The viable 2 region of some tumors also showed evidence of RBC accumulation in the interstitial space either from hemorrhage or a leaky vasculature (60), and through cross-sections of vessels present in the area (data not shown). The reduced cellular density and the presence of RBCs account for the elevated ADCs and reduced T_2 values, respectively, in contrast to viable 1 (Table 3-2). Previous reports by Ryschich and coworkers (63,64) show vessel dilation as the first detectable stage of ongoing angiogenesis, prior to vessel sprouting. The authors concluded that vessel dilation permits an increased endothelial diffusion surface for delivery of O_2 to surrounding tissue. This suggests that the presence of vessel dilation in viable 2 to approximately $25\mu\text{m}$ from normal values around $10\mu\text{m}$ to $15\mu\text{m}$ is a compensatory response to a reduced oxygen environment.

3.4.3 KM Identification of Hypoxic Tissue

HIF-1, or hypoxic-inducible factor, is upregulated during hypoxia, inducing transcription of a variety of genes in order to adapt to a low oxygen environment (4-8). HIF-1 itself is composed of two subunits, HIF-1 α and HIF-1 β . In a normal, well-oxygenated setting, these are separate and inactive. Under hypoxic conditions, HIF-1 α upregulation leads to: 1) dimerization with HIF-1 β to form an active transcription factor, 2) interaction with hypoxia response elements (termed HREs), and 3) subsequent genetic transcription (65).

Peri-Necrotic Expression of HIF-1 α

In order to help validate subdivision of the viable tissue into subpopulations, namely well-oxygenated versus hypoxic tissue, HIF-1 α immunohistochemistry was performed. Initial verification of HIF-1 α -specific staining of the nuclei versus non-specific background staining was performed via negative control slides (Fig. 3-14a, no anti-HIF-1 α) with comparison to H&E (Fig. 3-14b) of the same region. No staining of nuclei was observable in viable (V) or necrotic (N) regions (Fig. 3-14c,d). Fig. 3-15 shows images of HIF-1 α expression and the corresponding H&E stained section. HIF-1 α expression was highest in peri-necrotic regions, exhibited by nuclei staining an intense brown (Fig. 3-15e, black arrows), versus normal cells (Fig. 3-15e, brown arrow) or cells with non-specific HIF-1 α activity (Fig. 3-15e, red arrow). Fig. 3-16 further demonstrates the non-specific HIF-1 α expression in comparison to regions adjacent to necrosis (i.e., viable 2). These results are consistent with previous studies reporting concentrated HIF-1 α expression in peri-necrotic regions and a heterogeneous distribution of expression throughout the tumor area (15,24,26,66). Expression throughout the tumor distal to regions of necrosis could potentially be from small hypoxic microenvironments, but HIF-1 α activity in these areas is more likely from genetic upregulation of HIF-1 α rather than hypoxic-mediated expression. Since HIF-1 α expression in viable 1 was either non-existent or heterogeneously distributed (Fig. 3-16b) versus that of the concentrated expression in viable 2 (Fig. 3-16d), the HIF-1 α expression in viable 2 is likely an indirect measure of hypoxia. These results support the delineation between viable 1 and viable 2, as well as the identification of viable 1 as well-oxygenated tissue and viable 2 as hypoxic. Because tumors have varying viability, with well-oxygenated and hypoxic viable tissue and regions of necrosis, by subdividing major regions (viable, necrotic) some of the complexity may be addressed. Although the correspondence between regions of HIF-1 α and KM volume estimates was analyzed in a more qualitative manner, these results suggest that the subdivision of viable tissue into well-oxygenated and hypoxic regions is plausible. Further study at higher resolution using this methodology and the addition of pO₂ and lactate concentration to the feature space should permit a more accurate

assessment of well-oxygenated versus hypoxic tumor tissue and the exact correspondence between KM regions and areas of HIF-1 α expression.

3.4.4 Temporal Evolution of KM Volume

Following radiotherapy, the temporal evolution of individual tissue regions and their overall contribution to tumor regression and regrowth was investigated. Fig. 3-17 diagrams the temporal evolution of total tumor volume, viable and necrotic volume, and the subpopulations within both viable and necrotic tissue. The overall response of the tumors was a reduction in total volume out to day 2, followed by tumor regrowth. Underlying this change, there was a general reduction in viable volume out to day 2, followed by tumor regrowth—this trend for viable tissue followed that of the total tumor response. In addition, the necrotic volume increased post-treatment out to day 4, followed by a plateau. In terms of the subpopulations within viable tissue, there was a decrease in viable 1 volume post-irradiation concomitant with an increase in viable 2 out to day 2. After day 2, both viable 1 and viable 2 increased, although the change in viable 1 was significantly more pronounced. At day 4 viable 2 plateaued, but viable 1 continued to increase. These results indicate tumor regression via a transition from well-oxygenated to hypoxic tissue induced by radiotherapeutic intervention and the formation of necrosis out to day 4, followed by tumor regrowth. The overall change in necrosis from pre- (9%) versus post-irradiation (15%) was substantial, approximately a 67% increase in necrosis following single-dose radiotherapy.

3.4.5 Utility of the KM Method

Advantage of MS Analysis over Single Parameter Approaches

Although several studies have shown that increases in total tumor ADC prior to any change in tumor volume are indicative of a positive-treatment response (40,44-46), the evaluation of the tumor in this manner confounds ones ability to address intra-tumor variability. With a reduction in tumor necrotic fraction, the total tumor ADC approaches ADC values consistent with that of viable tissue. If small sub-populations of necrosis are present, changes in the overall necrosis may be small and would show little to no change in total tumor ADC. In addition, regions of mixed viability exist. Tissue may not necessarily be clearly viable or clearly necrotic. A single feature such as ADC, although

a fairly good estimate for regions that are viable or necrotic, lacks the sensitivity to identify these regions of mixed viability.

Combating Tumor Heterogeneity

Overall, these results indicate that MS analysis using the KM method with ADC and T_2 provides a way of addressing inter- and intra-tumor heterogeneity through identification of individual tumor tissue populations. This particular method was able to identify subpopulations within both viable and necrotic tissue, and more importantly, the delineation between well-oxygenated versus hypoxic tissue. Since both necrosis and hypoxia have been implicated in poor treatment response and reduced patient survival, the quantification of the amount of necrosis and the severity of hypoxia may aid in assignment of a more aggressive treatment regimen. Additionally, through identification of individual tissue regions, their relative contributions to the overall therapeutic response may be investigated, permitting a method for therapeutic monitoring and optimization of drug-dose and timing schemes in pre-clinical animal models.

Acknowledgements

The authors thank Dr. George Pins (Worcester Polytechnic Institute, MA) for the use of his laboratory for histological purposes (paraffin-embedding, microtome sectioning, H&E staining, and slide photography), Brett Downing and Kevin Cornwell (Worcester Polytechnic Institute, MA) for helpful advice and optimization of the H&E protocol, and Dr. Richard A.D. Carano (Genentech, CA) for his advice on the KM clustering algorithm. This work was supported by the Research Advancement Program (K.G.H.) through Worcester Polytechnic Institute.

References

1. Raghunand N, Gatenby RA, Gillies RJ. Microenvironmental and cellular consequences of altered blood flow in tumours. *Br J Radiology* 2003;76:S11-S22.
2. Jain RK. Delivery of molecular and cellular medicine to solid tumors. *Adv Drug Deliv Rev* 2001;46:149-168.
3. Semenza GL. Hypoxia-inducible factor 1: master regulator of O_2 homeostasis. *Curr Opin Genet Dev* 1998;8:588-594.

4. Ebert BL, Firth JD, Ratcliffe PJ. Hypoxia and mitochondrial inhibitors regulate expression of glucose transporter-1 via distinct cis-acting sequences. *J Biol Chem* 1995;270:29083-29089.
5. Rolfs A, Kvietikova I, Gassmann M, Wenger RH. Oxygen-regulated transferrin expression is mediated by hypoxia-inducible factor-1. *J Biol Chem* 1997;272:20055-20062.
6. Lee PJ, Jiang BH, Chin BY, Iyer NV, Alam J, Semenza GL, Choi AM. Hypoxia-inducible factor 1 mediates transcriptional activation of the heme oxygenase-1 gene in response to hypoxia. *J Biol Chem* 1997;272:5375-5381.
7. Liu Y, Cox RS, Morita T, Kourembanas S. Hypoxia regulates vascular endothelial growth factor gene expression in endothelial cells. Identification of a 5' enhancer. *Circ Res* 1995;77:638-643.
8. Ikeda E, Achen MG, Breier G, Risau W. Hypoxia-induced transcriptional activation and increased mRNA stability of vascular endothelial growth factor in C6 glioma cells. *J Biol Chem* 1995;270:19761-19766.
9. Gray LH, Conger AD, Ebert M, Hornsey S, Scott OC. The concentration of oxygen dissolved in tissues at the time of irradiation as a factor in radiotherapy. *Br J Radiol* 1953;26:638-648.
10. Prasad KN. Cellular Radiation Damage. *Handbook of Radiobiology*. Boca Raton: CRC Press; 1995. p 49-59.
11. Fyles AW, Milosevic M, Wong R, Kavanagh MC, Pintilie M, Sun A, Chapman W, Levin W, Manchul L, Keane TJ, Hill RP. Oxygenation predicts radiation response and survival in patients with cervix cancer. *Radiother Oncol* 1998;48:149-156.
12. Rofstad EK, Sundfor K, Lyng H, Trope CG. Hypoxia-induced treatment failure in advanced squamous cell carcinoma of the uterine cervix is primarily due to hypoxia-induced radiation resistance rather than hypoxia-induced metastasis. *Br J Cancer* 2000;83:354-359.
13. Burri P, Djonov V, Aebbersold DM, Lindel K, Studer U, Altermatt HJ, Mazzacchelli L, Greiner RH, Gruber G. Significant correlation of hypoxia-inducible factor-1 α with treatment outcome in cervical cancer treated with radical radiotherapy. *Int J Radiat Oncol Biol Phys* 2003;56:494-501.
14. Nordmark M, Overgaard M, Overgaard J. Pretreatment oxygenation predicts radiation response in advanced squamous cell carcinoma of the head and neck. *Radiother Oncol* 1996;41:31-39.
15. Koukourakis MI, Giatromanolaki A, Skarlatos J, Corti L, Blandamura S, Piazza M, Gatter KC, Harris AL. Hypoxia inducible factor (HIF-1 α and HIF-2 α) expression in early esophageal cancer and response to photodynamic therapy and radiotherapy. *Cancer Res* 2001;61:1830-1832.
16. Cerniglia GJ, Wilson DF, Pawlowski M, Vinogradov S, Biaglow J. Intravascular oxygen distribution in subcutaneous 9L tumors and radiation sensitivity. *J Appl Physiol* 1997;82:1939-1945.
17. Zips D, Eicheler W, Bruchner K, Jackisch T, Geyer P, Petersen C, van der Kogel AJ, Baumann M. Impact of the tumour bed effect on microenvironment, radiobiological hypoxia and the outcome of fractionated radiotherapy of human

- FaDu squamous-cell carcinoma growing in nude mice. *Int J Radiat Biol* 2001;77:1185-1193.
18. Birner P, Schindl M, Obermair A, Breitenecker G, Oberhuber G. Expression of hypoxia-inducible factor 1 α in epithelial ovarian tumors: its impact on prognosis and response to chemotherapy. *Clin Cancer Res* 2001;7:1661-1668.
 19. Erler JT, Cawthorne CJ, Williams KJ, Koritzinsky M, Wouters BG, Wilson C, Miller C, Demonacos C, Stratford IJ, Dive C. Hypoxia-mediated down-regulation of bcl-2 and bax in tumors occurs via hypoxic-inducible factor 1-dependent and -independent mechanisms and contributes to drug resistance. *Mol Cell Biol* 2004;24:2875-2889.
 20. Brown JM. The hypoxic cell: a target for selective cancer therapy. *Cancer Res* 1999;59:5863-5870.
 21. Hockel M, Vaupel P. Tumor hypoxia: definitions and current clinical, biologic, and molecular aspects. *J Natl Cancer Inst* 2001;93:266-276.
 22. Maxwell PH, Dachs GU, Gleadow JM, Nicholls LG, Harris AL, Stratford IJ, Hankinson O, Pugh CW, Ratcliffe PJ. Hypoxia-inducible factor-1 modulates gene expression in solid tumors and influences both angiogenesis and tumor growth. *Proc Natl Acad Sci USA* 1997;94:8104-8109.
 23. Ryan HE, Poloni M, McNulty W, Elson D, Gassmann M, Arbeit JM, Johnson RS. Hypoxia-inducible factor-1 α is a positive factor in solid tumor growth. *Cancer Res* 2000;60:4010-4015.
 24. Zhong H, De Marzo AM, Laughner E, Lim M, Hilton DA, Zagzag D, Buechler P, Isaacs WB, Semenza GL, Simons JW. Overexpression of hypoxia-inducible factor 1 α in common human cancers and their metastases. *Cancer Res* 1999;59:5830-5835.
 25. Chia SK, Wykoff CC, Watson PH, Han C, Leek RD, Pastorek J, Gatter KC, Ratcliffe P, Harris AL. Prognostic significance of a novel hypoxia-regulated marker, carbonic anhydrase IX, in invasive breast carcinoma. *J Clin Oncol* 2001;19:3660-3668.
 26. Vleugel MM, Greijer AE, Shvarts A, van der Groep P, van Berkel M, Aarboodem Y, van Tinteren H, Harris AL, van Diest PJ, van der Wall E. Differential prognostic impact of hypoxia induced and diffuse HIF-1 α expression in invasive breast cancer. *J Clin Pathol* 2005;58:172-177.
 27. Giatromanolaki A, Koukourakis MI, Sivridis E, Pastorek J, Wykoff CC, Gatter KC, Harris AL. Expression of hypoxia-inducible carbonic anhydrase-9 relates to angiogenic pathways and independently to poor outcome in non-small cell lung cancer. *Cancer Res* 2001;61:7992-7998.
 28. Nordmark M, Hoyer M, Keller J, Nielsen OS, Jensen OM, Overgaard J. The relationship between tumor oxygenation and cell proliferation in human soft tissue sarcomas. *Int J Radiat Oncol Biol Phys* 1996;35:701-708.
 29. Lancaster JA, Harris AL, Davidson SE, Logue JP, Hunter RD, Wykoff CC, Pastorek J, Ratcliffe PJ, Stratford IJ, West CM. Carbonic anhydrase (CA IX) expression, a potential new intrinsic marker of hypoxia: correlations with tumor oxygenation measurements and prognosis in locally advanced carcinoma of the cervix. *Cancer Res* 2001;61:6394-6399.

30. Helmer KG, Dardzinski BJ, Sotak CH. The application of porous-media theory to the investigation of time-dependent diffusion in in vivo systems. *NMR Biomed* 1995;8:297-306.
31. Helmer KG, Han S, Sotak CH. On the correlation between the water diffusion coefficient and oxygen tension in RIF-1 tumors. *NMR Biomed* 1998;11:120-130.
32. Lyng H, Haraldseth O, Rofstad EK. Measurement of cell density and necrotic fraction in human melanoma xenografts by diffusion weighted magnetic resonance imaging. *Magn Reson Med* 2000;43:828-836.
33. Helmer KG, Meiler MR, Sotak CH, Petrucci JD. Comparison of the return-to-the-origin probability and the apparent diffusion coefficient of water as indicators of necrosis in RIF-1 tumors. *Magn Reson Med* 2003;49:468-478.
34. Herneth AM, Guccione S, Bednarski M. Apparent diffusion coefficient: a quantitative parameter for in vivo tumor characterization. *Eur J Radiol* 2003;45:208-213.
35. Sun Y, Mulkern RV, Schmidt K, Doshi S, Albert MS, Schmidt NO, Ziu M, Black P, Carrol R, Kieran MW. Quantification of water diffusion and relaxation times of human U87 tumors in a mouse model. *NMR Biomed* 2004;17:399-404.
36. Muti M, Aprile I, Principi M, Italiani M, Guiducci A, Giulianelli G, Ottaviano P. Study on the variations of the apparent diffusion coefficient in areas of solid tumor in high grade gliomas. *Magn Reson Imaging* 2002;20:635-641.
37. Sinha S, Sinha U. Functional magnetic resonance of human breast tumors. *Ann NY Acad Sci* 2002;980:95-115.
38. Zhao M, Pipe JG, Bonnett J, Evelhoch JL. Early detection of treatment response by diffusion-weighted ¹H-NMR spectroscopy in a murine tumor *in vivo*. *Br J Cancer* 1996;73:61-64.
39. Galons JP, Altbach MI, Paine-Murrieta GD, Taylor CW, Gillies RJ. Early increases in breast tumor xenograft water mobility in response to paclitaxel therapy detected by non-invasive diffusion magnetic resonance imaging. *Neoplasia* 1999;1:113-117.
40. Chinnaiyan AM, Prasad U, Shankar S, Hamstra DA, Shanaiah M, Chenevert TL, Ross BD, Rehemtulla A. Combined effect of tumor necrosis factor-related apoptosis-inducing ligand and ionizing radiation in breast cancer therapy. *Proc Natl Acad Sci USA* 2000;97:1754-1759.
41. Jennings D, Hatton BN, Guo J, Galons JP, Trouard TP, Raghunand N, Marshall J, Gillies RJ. Early response of prostate carcinoma xenografts to docetaxel chemotherapy monitored with diffusion MRI. *Neoplasia* 2002;4:255-262.
42. Moffat BA, Hall DE, Stohanovska J, McConville PJ, Moody JB, Chenevert TL, Rehemtulla A, Ross BD. Diffusion imaging for evaluation of tumor therapies in preclinical animal models. *Magma* 2004;17:249-259.
43. Valonen PK, Lehtimaki KK, Vaisanen TH, Kettunen MI, Grohn OH, Yia-Herttuala S, Kauppinen RA. Water diffusion in a rat glioma during ganciclovir-thymidine kinase gene therapy-induced programmed cell death in vivo: correlation with cell density. *J Magn Reson Imaging* 2004;19:389-396.
44. Chenevert TL, McKeever PE, Ross BD. Monitoring early response of experimental brain tumors to therapy using diffusion magnetic resonance imaging. *Clin Cancer Res* 1997;3:1457-1466.

45. Chenevert TL, Stegman LD, Taylor JMG, Robertson PL, Greenberg HS, Rehemtulla A, Ross BD. Diffusion magnetic resonance imaging: an early surrogate marker of therapeutic efficacy in brain tumors. *J Natl Cancer Inst* 2000;92:2029-2036.
46. Dzik-Jurasz A, Domenig C, George M, Wolber J, Padhani A, Brown G, Doran S. Diffusion MRI for prediction of response of rectal cancer to chemoradiation. *Lancet* 2002;360:307-308.
47. Helmer KG, Meiler MM, Sotak CH, Petrucci JD. Comparison of the return-to-origin probability and the apparent diffusion coefficient of water as indicators of necrosis in RIF-1 tumors. *Magn Reson Med* 2003;49:468-478.
48. Tzika AA, Astrakas LG, Zarifi MK, Petridou N, Young-Poussaint T, Goumnerova L, Zurakowski D, Anthony DC, Black PM. Multiparametric MR assessment of pediatric brain tumors. *Neuroradiology* 2003;45:1-10.
49. Clark MC, Hall LO, Goldgof DB, Velthuizen R, Murtagh FR, Silbiger MS. Automatic tumor segmentation using knowledge-based techniques. *IEEE Trans Med Imaging* 1998;17:187-201.
50. Jacobs MA, Barker PB, Bluemke DA, Maranto C, Arnold C, Herskovits EH, Bhujwala Z. Benign and malignant breast lesions: diagnosis with multiparametric MR imaging. *Radiology* 2003;229:225-232.
51. Carano RA, Ross AL, Ross J, Williams SP, Koeppen H, Schwall RH, van Bruggen N. Quantification of tumor tissue populations by multispectral analysis. *Magn Reson Med* 2004;51:542-551.
52. Duda R, Hart P. Pattern classification. New York: John Wiley & Sons; 2001.
53. Carano RA, Takano K, Helmer KG, Tatlisumak T, Irie K, Petrucci JD, Fisher M, Sotak CH. Determination of focal ischemic lesion volume in the rat brain using multispectral analysis. *J Magn Reson Med* 1998;8:1266-1278.
54. Carano RA, Li F, Irie K, Helmer KG, Silva MD, Fisher M, Sotak CH. Multispectral analysis of the temporal evolution of cerebral ischemia in the rat brain. *J Magn Reson Imaging* 2000;12:842-858.
55. Brinkmann BH, Manduca A, Robb RA. Optimized homomorphic unsharp masking for MR grayscale inhomogeneity correction. *IEEE Trans Med Imaging* 1998;17:161-171.
56. Loukas CG, Linney A. A survey on histological image analysis-based assessment of three major biological factors influencing radiotherapy: proliferation, hypoxia, and vasculature. *Comput Methods Programs Biomed* 2004;74:183-199.
57. Russ JC. Fractal analysis. The image processing handbook. 2nd ed. Boca Raton: CRC Press; 1995. p 262-270.
58. Kazemi M, Silva MD, Li F, Fisher M, Cohen Y, Sotak CH. Investigation of techniques to quantify in vivo lesion volume based on comparison of water apparent diffusion coefficient (ADC) maps with histology in focal cerebral ischemia of rats. *Magn Reson Imaging* 2004;22:653-659.
59. Carson FL. Histotechnology: a self-instructional text. Chicago: ASCP Press; 1997.
60. Hashizume H, Baluk P, Morikawa S, McLean JW, Thurston G, Roberge S, Jain RK, McDonald DM. Openings between defective endothelial cells explain tumor vessel leakiness. *Am J Pathol* 2000;156:1363-1380.

61. Gomori JM, Grossman RI, Yu-Ip C, Asakura T. NMR relaxation times of blood: dependence on field strength, oxidation state, and cell integrity. *J Comput Assist Tomogr* 1987;11:684-690.
62. Janick PA, Hackney DB, Grossman RI, Asakura T. MR imaging of various oxidation states of intracellular and extracellular hemoglobin. *Am J Neuroradiol* 1991;12:891-897.
63. Ryschich E, Schmidt J, Hammerling GJ, Klar E, Ganss R. Transformation of the microvascular system during multistage tumorigenesis. *Int J Cancer* 2002;97:719-725.
64. Ryschich E, Schmidt E, Maksan SM, Klar E, Schmidt J. Expansion of the endothelial surface by an increase of vessel diameter during tumor angiogenesis in experimental hepatocellular and pancreatic cancer. *World J Gastroenterol* 2004;10:3171-3174.
65. Gillies RJ, Raghunand N, Karczmar GS, Bhujwala ZM. MRI of the tumor microenvironment. *J Magn Reson Imaging* 2002;16:430-450.
66. Talks KL, Turley H, Gatter KC, Maxwell PH, Pugh CW, Ratcliffe PJ, Harris AL. The expression and distribution of the hypoxia-inducible factors HIF-1 α and HIF-2 α in normal human tissues, cancers, and tumor-associated macrophages. *Am J Pathol* 2000;157:411-421.

CHAPTER 4

MULTISPECTRAL TISSUE CHARACTERIZATION IN A RIF-1 TUMOR MODEL: MONITORING RESPONSE TO SINGLE-DOSE (1000cGy) RADIOTHERAPY

Introduction

- DWI Assessment of Treatment Response
- MS Tissue Characterization
- Tumor Growth Kinetics
- Monitoring Response to Radiotherapy

Methods

- Animal Preparation
- Radiotherapy
- MRI Measurements
- Data Analysis
- K-Means Clustering
- Kinetic Modeling
- Histological Analysis
- Statistical Analysis

Results

- KM Segmentation Results
- Results: Control Group (Untreated)
- Results: Radiotherapy Group (Treated)
- Tumor Growth Kinetics (Control vs. Radiotherapy)
- KM Volume and Treatment Response: TGD and Cell Kill
- KM Volume and Treatment Response: Evolution of ADC and T_2

Discussion

- KM Segmentation Results
- KM Results: Control versus Radiotherapy
- KM Contributions to TGD and Cell Kill
- Underlying Contributions to the ADC Response
- Utility of the KM Method

Multispectral Tissue Characterization in a RIF-1 Tumor Model: Monitoring Response to Single-Dose (1000cGy) Radiotherapy

Erica C. Henning¹, Chieko Azuma², Christopher H. Sotak^{1,3,4}, Karl G. Helmer¹

Departments of Biomedical Engineering¹ and Chemistry & Biochemistry³

Worcester Polytechnic Institute

Worcester, Massachusetts 01609

Department of Clinical Sciences²

Tufts University Veterinary School of Medicine

North Grafton, Massachusetts

Department of Radiology⁴

University of Massachusetts Medical School

Worcester, MA 01655

Part of this work was presented at the 12th and 13th annual meetings of the International Society of Magnetic Resonance in Medicine, Kyoto, Japan, 2004 and Miami Beach, FL, USA, 2005.

Manuscript in Progress

Abstract

Assessment of therapeutic efficacy is confounded by intra-tumor and inter-tumor heterogeneity. Variable pre-treatment tissue composition, tumor size, and growth kinetics, as well as post-treatment cell kill and tumor regrowth complicate dose-optimization and comparative treatment regimens in animal oncology studies. In addition, the roles of various processes (vasogenic edema, reduced cell density, formation of necrosis, and tumor regrowth) with potential contribution to the temporal evolution of the total apparent diffusion coefficient (ADC) are not fully understood. In order to address these issues, a multi-spectral (MS) approach, combining ADC and T_2 parameter maps with k-means (KM) clustering, was employed for estimation of multiple compartments within both viable tumor tissue and necrosis following single-dose (1000 cGy) radiotherapy in a radiation-induced fibrosarcoma (RIF-1) tumor model. The individual contributions of cell kill and tumor growth kinetics (tumor doubling time (TDT) pre- and post-irradiation, tumor growth delay (TGD), cell kill) to the radiotherapy-induced response were investigated. A moderate-to-strong correlation was found between the change in KM total viable volume and the resultant TGD ($r = 0.62$) and cell kill ($r = 0.65$). An increase in pre-treatment viable 1 correlated with a decrease in both TGD ($r = 0.68$) and cell kill ($r = 0.71$). There was no correlation between pre-treatment viable 2 volume and TGD or cell kill. These results suggest that viable 2 is well-oxygenated, radiosensitive tissue, while viable 2 is hypoxic, and therefore, radioresistant. The roles of therapeutically-induced vasogenic edema and formation of necrosis to the early ADC response post-treatment, as well as the role of individual tissue components to the ADC response during tumor-regrowth were investigated. The trend in increased total ADC was observed prior to an increase in necrotic fraction (visible beyond day 4 post-treatment). This trend is driven by the increase in total viable tissue ADC, specifically that of viable 1. Because there are no changes in T_2 , which would be indicative of edema based on changes in water content, these observations suggest that the early increase in total ADC is in fact based on a slight reduction in cell density, and not that of radiation-induced vasogenic edema. This method should be helpful in monitoring the range of tissue viability as a function of time post-treatment, as well as understanding the underlying mechanisms contributing to the temporal evolution of the total ADC response.

Quantitative assessment of individual tissue regions, tumor growth rates (TDT and TGD), and cell kill should provide a more accurate method for therapeutic monitoring and optimization of drug-dose and timing schemes in pre-clinical animal models by eliminating the issue of inter-tumoral variability.

Keywords: RIF-1, tumor, diffusion, multispectral analysis, radiotherapy

4.1 Introduction

Early increases in ADC post-treatment have been hypothesized to indicate a decrease in cell density and formation of necrosis, indicative of a positive treatment response. At this time, the underlying mechanisms that contribute to the total ADC response are not fully understood. This chapter addresses the application of multispectral (MS) analysis using ADC and T_2 parameter maps and the k-means (KM) clustering algorithm to follow the tumor response to radiotherapeutic intervention. The role of individual tissue regions to the total ADC response and their correlation with tumor growth kinetics should provide a better understanding of the physiological dynamics of pre- versus post-treatment tumor response.

4.1.1 DWI Assessment of Treatment Response

Clinical assessment of therapeutic efficacy is generally based on changes in tumor volume. Unfortunately, changes in tumor volume are generally slow, preventing early assessment and modification of therapy based on individual responsiveness. The ability to predict therapeutic response on an individual basis would minimize potentially harmful side-effects and toxicity issues, especially for patients with non-responsive tumors who should be reassigned to an alternative form of treatment. Over the past decade, diffusion imaging has emerged as a powerful contrast for tissue assessment following chemotherapeutic and/or radiotherapeutic treatment in experimental tumor models (1-5), as well as in clinical oncology (6-8). The first major study showing a substantial increase in the tumor apparent diffusion coefficient (ADC) of water post-treatment was done by Zhao *et al.* (1). The authors reported a significant increase in ADC (approximately 30-40% by day 2 for both 150mg/kg and 300mg/kg cyclophosphamide treatment) previous to a reduction in tumor volume using diffusion-weighted $^1\text{H-NMR}$ spectroscopy, likely a result of tumor cytotoxic response. These results, reproduced from reference (1) are diagrammed in Fig. 4-1.

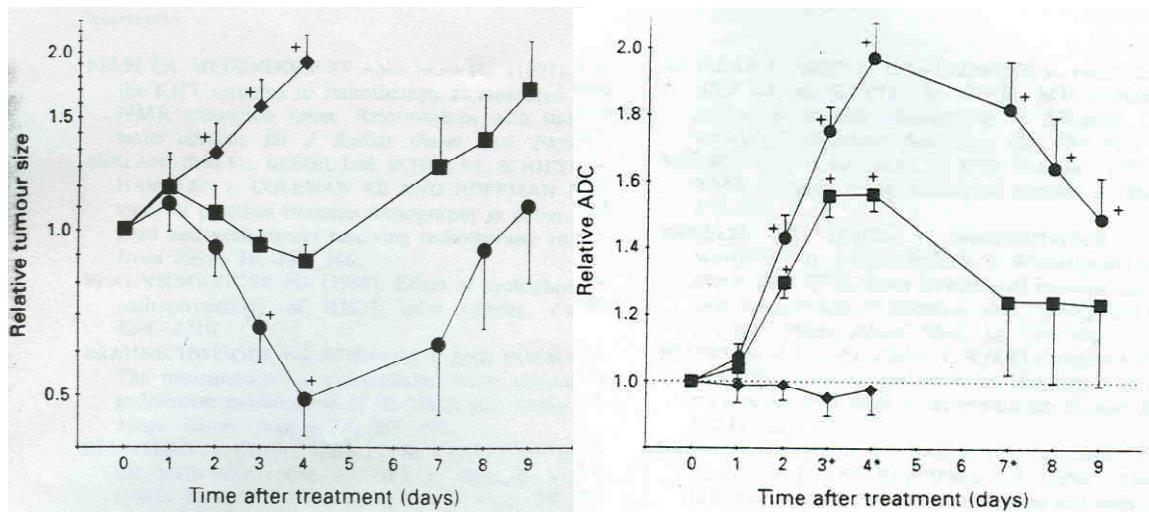


Figure 4-1. Evolution of tumor volume (left) and spectroscopic ADC (right) following chemotherapy in a RIF-1 tumor model. Symbol designations are: diamonds = control tumors; squares = tumors receiving a single dose of 150mg/kg cyclophosphamide (Cp); and circles = tumors receiving 300 mg/kg Cp. A significant increase in ADC was seen previous to any change in tumor volume (day 2), with ADC reversal upon tumor regrowth (post-day 4). Figure reproduced from reference (1).

Changes in ADC Correlate with Changes in Cellular Density

Subsequent studies by Chenevert *et al.* (6,7) investigated the contribution of tumor physiology to this ADC change by comparing the temporal evolution of the therapy-induced ADC increase to histology at each timepoint. The authors reported a strong correlation between the mean ADC of the total tumor volume and values of cellular density, obtained from histological examination of hematoxylin-eosin (H&E) stained sections in a rat 9L glioma model. They concluded that the early ADC increase was a result of reduced cellular density concomitant with the formation of necrosis. Lyng *et al.* (9) confirmed this correlation between ADC, cellular density, and necrotic fraction in four human xenograft lines, although the degree of correlation was dependent on the size of the necrotic region.

Limitations of ADC Calculations Based on Whole-Volume Measurements

Although these reports provide strong evidence that a significant ADC increase correlates with therapeutically-induced changes in cellular density and formation of necrosis, increased ADCs at early timepoints post-treatment may also result from other

therapeutically-induced changes in ADC such as vasogenic edema. Spectroscopic ADCs or mean ADC calculations based on total tumor volume do not assess tissue heterogeneity, and therefore mask the complex tissue response. Helmer *et al.* (10) attempted to address this issue of heterogeneity by analyzing tissue that was either clearly viable or clearly necrotic, determined from H&E-stained sections. Tissue having a mixture of viable cells and acellular regions was excluded from analysis. The authors suggested that multiple MR parameters should increase the ability to identify these regions, although success would depend on their size as well as image resolution.

4.1.2 Multispectral Tissue Characterization

Variable pre-treatment tissue composition, tumor size, and growth kinetics, as well as post-treatment cell kill and tumor regrowth complicate dose-optimization and comparison of treatment regimens in animal oncological studies. With this in mind, a multispectral (MS) approach using multiple MR parameters should provide greater power than previous single-parameter studies. Recent multiparametric studies in brain (11,12) and breast (13) cancer provide promising results for pathological assessment. Subsequent to these studies, Carano *et al.* (14) reported on a multispectral (MS) analysis approach using ADC, T_2 , and M_0 parameter maps for identification of viable versus necrotic tissue in COLO205 tumor xenografts in immuno-compromised mice. The authors reported that ADCs permitted differentiation between viable tissue and necrosis; and with the addition of T_2 , further subdivision of necrotic tissue was possible. They noted that although their MS estimates of viable and necrotic volumes correlated well with the corresponding histological estimates, the MS viable volume provided a more stable efficacy endpoint. Their KM volume results are reproduced in Fig. 4-2. There was a significant reduction in MS viable volume by day 10 for two of the treatment groups, but similar values of necrotic fraction regardless of the presence or type of therapeutic intervention. Carano and coworkers suggested that the necrotic fraction results might be merely a characteristic of the cell line, as these types of tumors tend to grow rapidly and form large regions of necrosis.

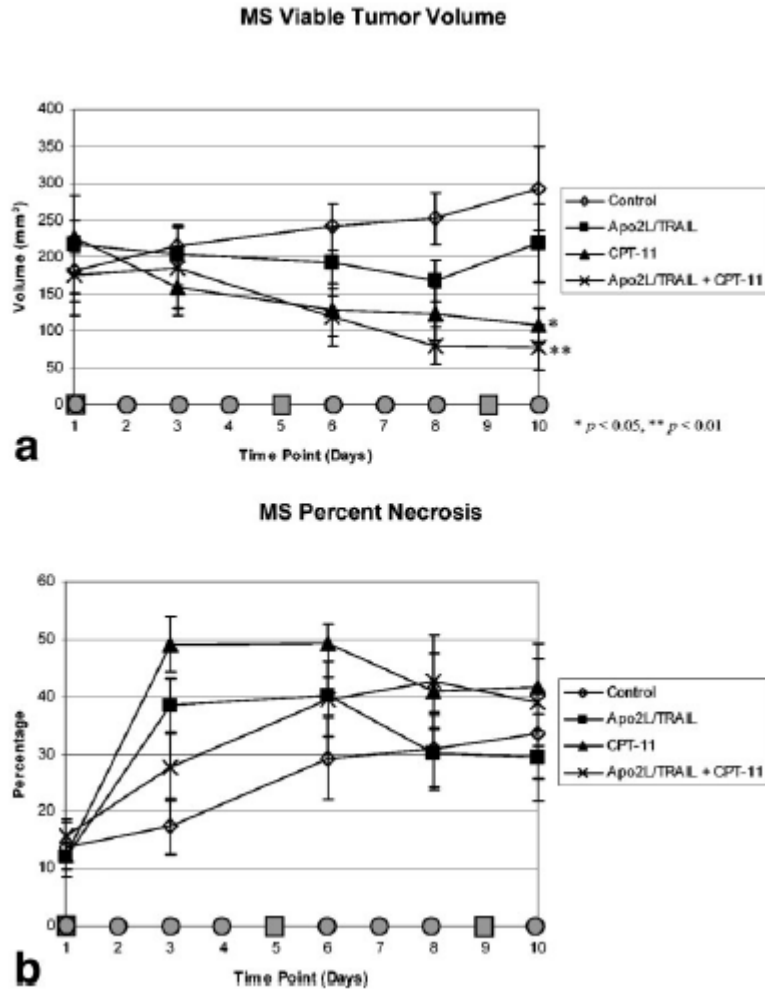


Figure 4-2. The temporal evolution of mean MS estimates of viable tumor volume (a) and percent necrosis (b) in response to Apo2L/TRAIL and CPT-11 therapy. Animals were treated with 60mg/kg Apo-2/TRAIL (circle) on days 1-4 and 6-10. 80mg/kg CPT-11 (square) was administered on days 1, 5, and 9. *p < 0.05, ** p < 0.01, significant difference relative to control (diamond) based on Dunnett’s test of multiple comparisons. Figure reproduced from reference (14).

4.1.3 Tumor Growth Kinetics

Previous tumor growth studies in experimental animal models (14-19) and the clinical setting (20,21) have demonstrated that serial MRI measurements permit the non-invasive evaluation of tumor growth kinetics and a method for monitoring treatment response. Ross *et. al.* (16) provided a model for assessment of tumor doubling time (TDT), tumor

growth delay (TGD), and log cell kill without the requirement that the rate of tumor regrowth be identical to the pretreatment growth rate. The authors concluded that MRI quantification of these three parameters provides a non-invasive way of accounting for inter-animal variability. With this in mind, combining MS methods for tissue characterization with tumor growth kinetics and cell kill measurements should provide a better understanding of the physiological dynamics of treated tumors. In addition, subdivision of individual tissue types should also permit investigation of the relative contributions of each tissue population to the response pre- versus post-treatment.

4.1.4 Monitoring Response to Radiotherapy

There were two goals of this study. First, in order to gain insight into the various processes whose combination yield the total ADC response over time; second, to identify the contribution of tissue heterogeneity (viable, necrotic) to the treatment response and changes in tumor growth kinetics and cell kill. To this end, we performed MS analysis using a 2-dimensional feature space (ADC, T_2) and the k-means clustering algorithm (22) for identification of multiple compartments within both viable and necrotic tissue. Hematoxylin-eosin (H&E) staining was performed for identification two types of viable tissue (V1, V2) and two types of necrosis (N1, N2). Immunohistochemical staining for hypoxic-inducible factor-1 alpha ($HIF-1\alpha$) was performed for differentiation of viable tissue into well-oxygenated (V1) and hypoxic (V2) regions. This method, a 2-feature, 4-cluster segmentation using k-means clustering and the Euclidean distance, was found to be optimal following analysis of the correlation between KM parameter maps and the corresponding histology (details provided in Ch. 3). The temporal evolution of individual tissue populations was investigated in order to understand the underlying mechanisms of treatment response pre- versus post-radiotherapeutic intervention.

4.2 Methods

4.2.1 Animal Preparation

The present study was approved by the Institute Animal Care and Use Committee (IACUC) of the University of Massachusetts Medical School (IACUC protocol A-544). Twenty-nine 6-8 week-old female C3H mice (20-25g; Taconic Farms, Germantown, NY) were initially anesthetized with an intraperitoneal injection of ketamine/zylazine (100 mg/kg:10 mg/kg). All mice were inoculated with 1×10^6 RIF-1 cells (0.15 ml), delivered through a subcutaneous injection into the right hind leg. Tumors were allowed to develop for 3-4 weeks, yielding an approximate 1.0 cc starting volume. Tumor volume was determined from caliper measurements, taken 2-3 times per week, of the three perpendicular axes (length, width, height) and the equation for calculating the volume of an ellipsoid where $V = (\pi/6) (l \times w \times h)$. Animals were subsequently divided into two groups: a control group (N = 16) and a treatment group (N = 13). For the control group (N = 16), tumors of varying volumes (1.0 cc to 2.0 cc) were imaged at a single timepoint and then extracted for histological examination. For the treatment group (N = 13), tumors of an approximate 1.0 cc starting volume were irradiated with 1000 cGy at a rate of 300 cGy/min (Siemens Mevatron 77, 6 MeV electrons, Tufts University School of Veterinary Medicine, North Grafton, MA). Imaging for the treatment group was performed at 1d pre-treatment, 5 hr, 1d, 2d post-treatment, and every 2d thereafter until tumor doubling (maximum 14d post-treatment) or until tumors reached a 2.0 cc volume (considered a burden for the animal).

4.2.2 Radiotherapy

Prior to radiotherapy, animals were anesthetized with an intraperitoneal injection of ketamine/zylazine (100 mg/kg:10 mg/kg). Animals were placed prone on a plastic board, with movement restricted by securing the forepaws and hindlegs down using medical tape (Fig. 3-4a). The right hind leg was pulled away from the body for preparation. First, a 0.5-cm-thick bolus of tissue-substitute (Bolx-II, MED-TEC, Inc., Orange City, IA), with the center cut out, was placed around the tumor and filled with gel (Fig. 3-4b). In order to deliver the desired dose to the tumor center without exposing the underlying tissue and bone, an additional 0.5-1.0-cm-thick bolus of tissue-substitute was

placed over the top, depending on the measured tumor height (Fig. 3-4c). Based on tumor length and width, custom-made cutouts from 2.0-3.0 cm in diameter were used for the cone size in order to limit the radiation to the tumor versus the surrounding tissue (Fig. 3-4d). Following preparation, tumors were irradiated with 1000 cGy at a rate of 300 cGy/min (Siemens Mevatron 77, 6 MeV electrons, Tufts University School of Veterinary Medicine, North Grafton, MA). At the conclusion of single-dose radiotherapy, animals were returned to their cage where they recovered from anesthesia and were provided with food and water.

4.2.3 MRI Measurements

MR experiments were performed with a Bruker Biospin 2.0T/45cm imaging spectrometer operating at 85.56 MHz for ^1H and equipped with ± 20 G/cm self-shielded gradients (Fig. 3-5). The experiments involved multi-slice image acquisition along the coronal plane [matrix size = 128×128 , FOV = $3\text{cm} \times 3\text{cm}$, slices = 8, slice thickness = 1mm]. The imaging plane was referenced to the boundary between the tumor and underlying muscle. A diffusion-weighted, spin-echo (SE) sequence was used to acquire the images at six b-values ($b = 15, 60, 140, 390, 560, 760 \text{ mm}^2 \text{ s}^{-1}$) with diffusion sensitization applied along the read direction. Other acquisition parameters were: TR/TE = 2000.0/53.0 ms, diffusion gradient duration $\delta = 4.0$ ms, diffusion gradient separation $\Delta = 35$ ms, resulting in an effective diffusion time $t_{\text{dif}} = 33.7$ ms. A T_2 -weighted, spin-echo (SE) sequence was used to acquire images at six echo times (TE = 12.2, 20, 35, 50, 65, 90 ms) with TR = 2000.0 ms. The experiment times were 25 min for diffusion and 5 min per TE value for T_2 , yielding a total imaging time of 55 min. During imaging, animals were placed prone in a home-built animal holder with a 4-turn ^1H solenoid coil around the tumor (Fig. 3-6). Multiple coils of variable diameter were constructed (0.95, 1.35, 1.75 cm) to account for tumor volume changes in repeated measures experiments. Animals were anesthetized with 1.5% isoflurane at a rate of 1.5 L/min in breathing quality air. Body temperature was maintained by circulating warm air at $34.0^\circ \pm 1.0^\circ\text{C}$ using a T-type thermocouple and a double-point feedback control system.

4.2.4 Data Analysis

Parameter Map Production

Image reconstruction was performed using Paravision's Image Processing and Display Software (Xtip). Image analysis and parameter map production was performed using routines written in IDL (Research Systems Inc., Boulder, CO). ADC, and T_2 parameter-map production was performed on a pixel-by-pixel basis based on the relationship between the natural log of the signal intensity and b-value (Eq. 4-1) or signal intensity and echo time (Eq. 4-2), respectively:

$$M(t) = M_0 e^{-bD} \quad (4-1)$$

$$M(t) = M_0 e^{-TE/T_2} \quad (4-2)$$

where M/M_0 is the signal intensity at a particular b-value or TE value; D is the diffusion along a single direction, and T_2 is the spin-spin or transverse relaxation time. A linear fitting procedure based on the minimization of the chi-square statistic was employed for extraction of MR parameters. Underlying muscle, remaining in the lower imaging slices for ($N = 9$) animals, was removed by delineation between tissue boundaries using T_2 -weighted contrast images ($TE = 90\text{ms}$).

4.2.5 K-means Clustering

A 2D feature vector, containing ADC and T_2 parameter maps, was generated. KM clustering was performed on a pixel-by-pixel basis using the Euclidean distance measure (22):

$$D = (x - \mu_i)^t (x - \mu_i) \quad (4-3)$$

where $x \in R^3$ is the feature vector and μ_i is the cluster mean, both determined from all of the data ($N = 88$ datasets, all animals, all timepoints). Prior to KM clustering, feature normalization ($\mu = 0$, $s = 1$) was performed for removal of potential scaling differences. Tissue classification was then performed using KM in a hierarchical manner. In the first step of the classification algorithm, KM was applied to separate the data into two clusters ($k = 2$) of tumor tissue and background noise based on variations in M_0 . All voxels classified as noise were set to zero and removed from further processing. In the second step, KM was applied ($k = 4$) to segment the data into the following two regions each of viable tumor ($V1, V2$) and necrosis ($N1, N2$).

4.2.6 Kinetic Modeling

Growth kinetic calculations and cell kills were determined using an exponential model of tumor growth (23) and the mathematical model proposed by Ross *et al.* (16). In this model (Fig. 4-3), tumor volumes, $V(t)$, are plotted versus time post-cell implantation, t , using the natural log of the following equation:

$$V(t) = V_0 e^{\frac{\ln 2}{T_d} t} \quad (4-4)$$

where T_d is the volumetric doubling time and V_0 is the initial viable tumor volume (at first measurement). To determine the pre-treatment and post-treatment doubling times of the tumors, $T_{d_{pre}}$ and $T_{d_{post}}$, Eq. 4 was fit to the initial exponential growth curve and the regrowth curve of the total tumor evolution plot. By inserting the $T_{d_{pre}}$ into the equations determined by the fits for exponential growth and regrowth, the difference in time will be equivalent to the tumor growth delay, or TGD. The effective volume of tumor surviving immediately after treatment, V_{post} , was derived by extrapolation of the regrowth curve to the day of treatment. This permits calculation of the ratio of the volumes pre- and post-treatment, and subsequent determination of log cell kill:

$$\text{Log Cell Kill} = \log_{10} \left[\frac{V_{pre}}{V_{post}} \right] \quad (4-5)$$

This approach does not have the constraint requiring that the rate of tumor regrowth be identical to the pre-treatment growth rate, thereby making it more applicable to situations with inherent heterogeneity such as the case in animal oncological models.

4.2.7 Histological Analysis

For the control group following imaging, as well as for the radiotherapy group following the final imaging timepoint, animals were euthanized by an overdose of ketamine/zylazine (400 mg/kg:40 mg/kg). The RIF-1 tumors were extracted based on the intersection between the tumor and muscle and frozen for 30 minutes. Sections were taken every 2 mm starting from the base of the tumor, stored in individual tissue cassettes (Microcassettes, VWR International, NJ), and placed in 10% neutral buffered formalin (Fisher Scientific, Pittsburgh, PA). Following fixation, a standard paraffin embedding procedure was used. Tissue cassettes were marked L-R in order to preserve orientation for later correlative analysis between imaging and histology.

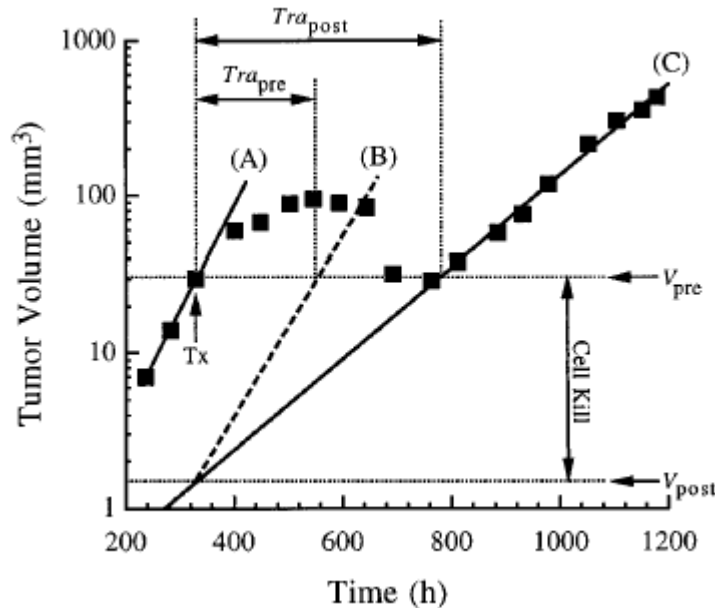


Figure 4-3. Demonstration of the mathematical analysis of tumor growth and treatment. Data points are actual values obtained for a 9L tumor treated with BCNU. The line marked A is the least-squares fit of the pre-treatment growth points according to Eq. 4-4. The line marked C is the fit of the post-treatment growth points. Line C is extrapolated back to the time of treatment to give V_{pre} . Log cell kill is the log of the ratio $V_{\text{pre}}/V_{\text{post}}$ (Eq. 4-5). The line marked B is the theoretical tumor regrowth curve assuming $Td_{\text{post}} = Td_{\text{pre}}$. The relative contributions of cell kill and tumor growth rates are related to the calculated repopulation intervals, Tra_{pre} and Tra_{post} (these are not included in our analysis). Figure reproduced from reference (16).

Hematoxylin-Eosin (H&E) Histochemistry

For all tumors, three $6\mu\text{m}$ sections, approximately $300\mu\text{m}$ apart, were taken every 1-mm for a total of 24 sections per tumor. Sections were mounted on Poly-L-lysine coated slides (VWR International, West Chester, PA) and dried overnight on a slidewarmer at 37°C . Slides were then stored at room temperature until further processing. Hematoxylin-Eosin (H&E) staining was performed for all sections with digital images ($1\times$) taken on a section-by-section basis using a Hewlett-Packard Scanner (Model #3970) at a resolution of 1200dpi. Image analysis and delineation between individual tissue regions (viable, necrotic) was performed using KM clustering and a feature space ($f = 4$) based on the R,G,B image values and texture analysis (24) using the Hurst transform, an

image operator used in fractal analysis for the characterization of surface roughness (25). The Hurst transform or coefficient was calculated on a pixel-by-pixel basis using a 7-pixel-wide neighborhood, and pixel labels identifying groups with the same distance from the central pixel (Fig. 3-8). A linear fitting procedure of log of the distance and versus log of the maximum brightness range between groups in the neighborhood and the central pixel permitted calculation of the Hurst coefficient. In this case, the Hurst coefficient is equivalent to the slope based on the best-fit line and minimization of the chi-square statistic. Additional images were taken at higher resolution (2 \times , 10 \times , 20 \times , and 40 \times) for correspondence with HIF-1 immunohistochemistry using an upright Nikon Eclipse E400 phase contrast microscope (Nikon, Melville, NY) equipped with an RT Color Spot camera (Diagnostic Instruments, Inc., Sterling Heights, MI) for image capture. Spot Analysis 4.0.9 (Diagnostic Instruments, Inc., Sterling Heights, MI) software was employed for optimization of image quality and image acquisition.

Hypoxic Inducible Factor 1 α (HIF-1 α) Immunohistochemistry

For (N = 9) tumors (N = 5 radiotherapy, N = 4 control), additional 6 μ m sections were taken at the approximate 600 μ m mark. Sections were mounted on Poly-L-lysine coated slides (VWR International, West Chester, PA) and dried overnight on a slidewarmer at 37 $^{\circ}$ C. Slides were then stored at room temperature until further processing. Immunohistochemical staining for HIF-1 α was performed using a 1:75 dilution of the mouse monoclonal antihuman HIF-1 α antibody (ab463, ABCam Inc., Cambridge, MA). Optimization of method and immunohistochemical staining was performed by Mass Histology Service (Worcester, MA). Sections were deparaffinized and peroxidase was quenched with 3% H₂O₂ for 15 min. Slide preparation for staining was performed with heat-mediated antigen retrieval (Vector #H-3300 for 20 min.). After rinsing with PBS, slides were incubated overnight at 2 $^{\circ}$ C with the primary antibody. Sections were again rinsed with PBS and incubated with a 1:250 dilution of the secondary antibody (biotin goat anti-mouse IgG, Vector #BA2000) for 1 hr. After rinsing with PBS, detection was performed using a streptavidin-biotin-horseradish peroxidase system (Vector Elite #PK6100 for 1 hr). Sections were again rinsed with PBS and color was developed by a 15-min incubation with 3,3'-diaminobenzidine solution (DAB). Slides were lightly counterstained with hematoxylin. For negative controls, the primary antibody was not

applied. Tumor samples with strong cytoplasmic and/or nuclear expression were considered to be positive.

4.2.8 Statistical Analysis

Data are reported as mean \pm SEM. MS estimates of individual cluster volumes (V_1, V_2, N_1, N_2) as well as total viable volume (V_1+V_2) and total necrotic volume (N_1+N_2) were compared with H&E histological volumes through computation of Pearson's correlation coefficient to provide the degree of linear association between imaging and histological volume estimates. Histology slices at the 600 μ m point for 1-mm sections from $N = 16$ tumors were analyzed (all other H&E sections had considerable tissue loss). The temporal evolution of individual cluster volumes and feature means (ADC, T_2), as well as total volume and feature mean, were compared on a timepoint-by-timepoint basis between pre-irradiation and post-irradiation by two-tailed t-tests assuming unequal variances. The relationship between tumor size and percent necrosis, as well as percent necrosis for control and radiotherapy groups was investigated using Pearson's correlation coefficient to provide a measure of the degree of linear correlation between parameters.

4.3 Results

4.3.1 KM Segmentation Results

Fig. 4-4 shows representative ADC and T_2 parameter maps (Fig. 4-4a,b), the KM segmentation map (Fig. 4-4c), and the corresponding histological H&E section (Fig. 4-4d). For the KM segmentation map, individual tissue regions have been color-coded such that: red = necrotic 1, blue = necrotic 2, green = viable 1, and yellow = viable 2. Mean feature values for individual tissue populations, obtained via clustering of all datasets together ($N = 88$ datasets, over all timepoints), are summarized in Table 4-1. These results indicate the existence of two unique subpopulations within both viable and necrotic tissue. Fig. 4-5 shows high-power images corresponding to the regions labeled on the H&E section in Fig. 4-4. Necrosis 1 (Fig. 4-5a), characterized by high ADCs and high T_2 values was generally acellular in nature. It showed some signs of inflammation,

indicated by the presence of neutrophils (blue arrows) recruited to the area to remove residual cellular debris (red arrows). In addition, the remaining structure post-cell death appears to have begun to degrade, and the few remaining cells in the region are in the process of nuclear fragmentation, termed karyorrhexis (yellow arrows). Necrosis 2 (Fig. 4-5b), in contrast to necrosis 1, is characterized by low T_2 values. It has a sparse population of cells undergoing apoptotic cell death intermixed with red blood cells (RBCs) that have accumulated in the interstitial space either from hemorrhage or a leaky vasculature (26). This accumulation of RBCs leads to inflammation, indicated again by the presence of neutrophils (blue arrows). Cells in this region are undergoing karyorrhexis (yellow arrows) or pyknosis (green arrows). Pyknotic nuclei exhibit degradation of both nuclear DNA and cytoplasmic RNA, resulting in nuclear shrinkage. Unlike the necrotic regions, viable 1 (Fig. 4-5c) is extremely cell-dense, with no evidence of inflammation or RBC accumulation. Viable 2 (Fig. 4-5d), on the other hand, has a slightly reduced cell-density over that of viable 1, with an abundance of dilated blood vessels. These blood vessels are approximately $25\mu\text{m}$ in comparison to $10\mu\text{m}$ for viable 1. Fig. 4-5e,f diagram the resultant HIF-1 α expression via comparison of HIF-1 α immunohistochemistry and H&E histochemistry for the same location. HIF-1 α expression, denoted by the intensely stained brown nuclei (black arrows), is hypoxic-specific, whereas the lightly stained nuclei (red arrow) are from non-specific genetic upregulation of HIF-1 α . The regions with the most concentrated HIF-1 α expression were located in per-necrotic areas.

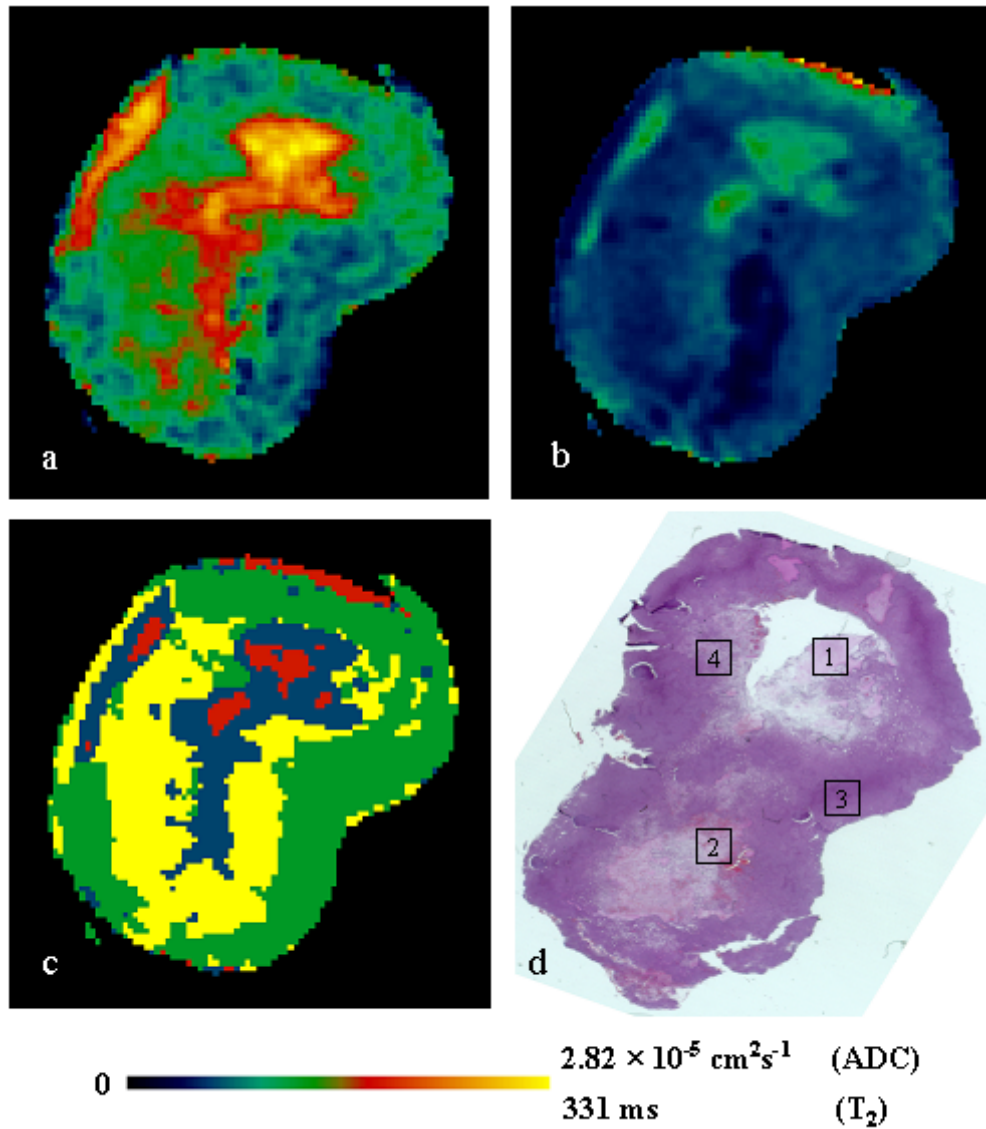


Figure 4-4. KM segmentation results for a single-slice of a representative tumor with corresponding histology via H&E histochemistry. ADC and T₂ parameter maps are shown in (a) and (b) respectively, with the corresponding KM segmentation map in (c), and the corresponding H&E stained section in (d). Color designations for the KM map are: red = necrosis 1, blue = necrosis 2, green = viable 1, yellow = viable 2. Regions of interest were chosen for investigation of the underlying morphology contribution to the measured ADC and T₂ values, with: 1 = necrosis 1; 2 = necrosis 2; 3 = viable 1; 4 = viable 2. High-power images of these regions are displayed in Fig. 4-5.

Table 4-1. Mean feature values (ADC and T_2) for individual tissue populations following KM segmentation using $k = 4$ clusters.

Features	ADC ($\times 10^{-5} \text{ cm}^2 \text{ s}^{-1}$)	T_2 (ms)	total number of voxels	% of total
Viable 1	0.76 ± 0.05	60 ± 20	627227	56
Viable 2	1.11 ± 0.05	50 ± 20	374936	34
Necrosis 1	2.2 ± 0.4	139 ± 15	11896	1
Necrosis 2	1.8 ± 0.1	68 ± 6	103951	9

Parameters were derived on an animal-by-animal basis based on the clustering of all datasets together ($N = 29$ animals, 88 total datasets over all timepoints). Data are presented as mean \pm SEM.

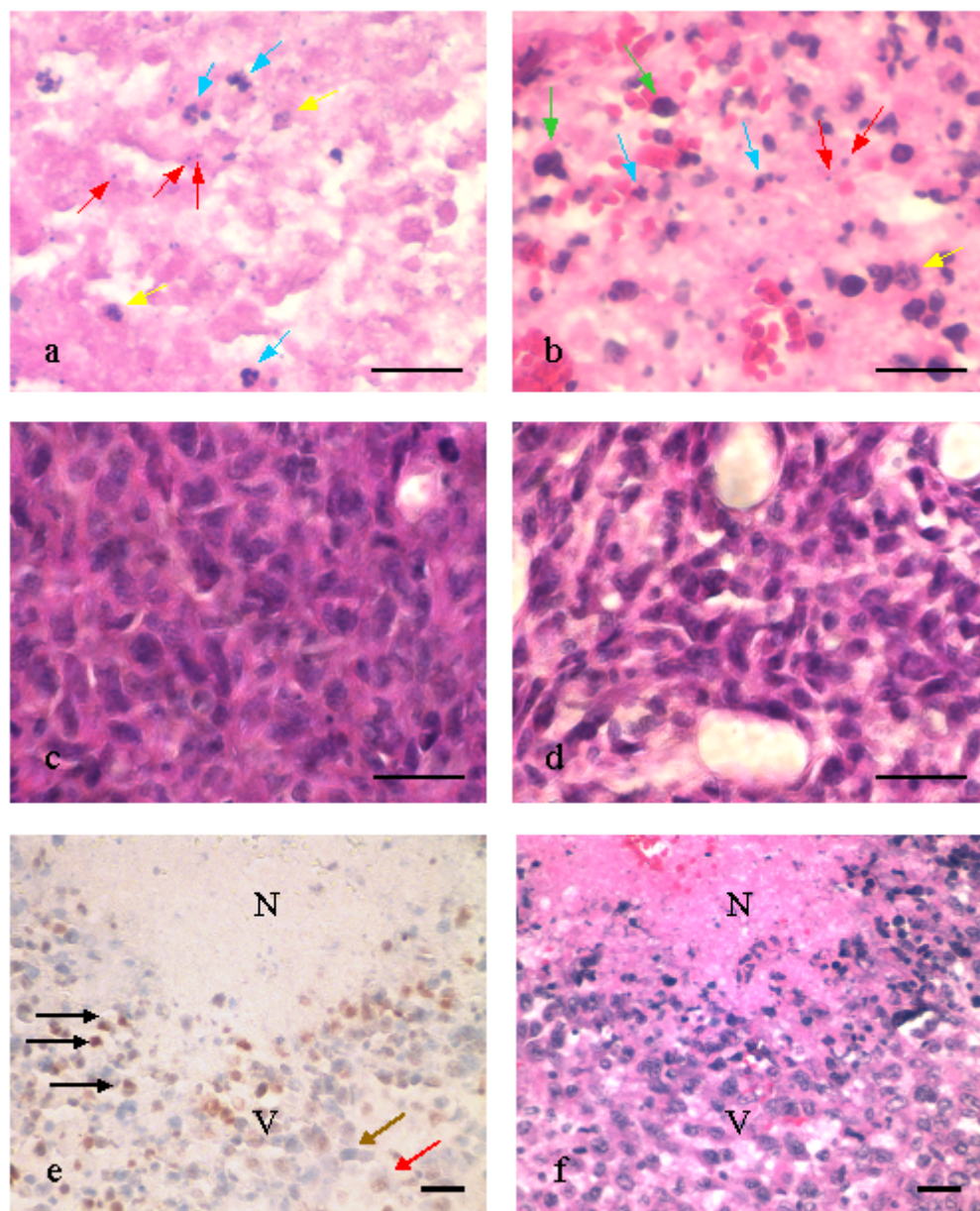


Figure 4-5. H&E images taken at 40 \times magnification (a-d) corresponding to the regions specified in Fig. 4-4, and 20 \times magnification (e-f) for identification of hypoxic nuclei via HIF-1 α immunohistochemistry. (a) Necrosis 1. (b) Necrosis 2. (c) Viable 1. (d) Viable 2. Morphological identification of enzymatic actions and repair mechanisms concomitant with apoptosis and/or necrosis are labeled by arrows: green = pyknosis, yellow = karyorrhexis, blue = neutrophil invasion, red = nuclear dusting. (e) HIF-1 α immunohistochemistry with the corresponding H&E stained region (f). HIF-1 α positive nuclei in perinecrotic regions stain an intense brown (black arrows), negative nuclei stain light blue (from hematoxylin counterstain, brown arrow), and nuclei with non-specific HIF-1 α activity (i.e., unrelated to hypoxia) stain a faint brown (red arrow). Scale bar = 25 μ m. for (a-d) and 50 μ m for (e-f).

4.3.2 Results: Control Group (Untreated)

Fig. 4-6 shows various correlation plots for the control group of animals (N = 13, 3 animals excluded from analysis because of misregistration between ADC and T₂ parameter maps). There was a strong correlation between KM volume and caliper volume estimates ($r = 0.70$, Fig. 4-6a). In terms of the relationship between total-tumor-mean ADC and KM volume estimates, there was a weak correlation between the total-tumor-mean ADC and KM total volume ($r = 0.48$, Fig. 4-6b) and total-tumor-mean ADC and KM viable volume ($r = 0.43$, Fig. 4-6c). Fig. 4-6d shows a modest-to-strong correlation ($r = 0.55$) between total tumor ADC and KM percent-tumor-necrotic fraction (%TNF). Table 4-2 provides a quantitative summary of mean feature values (ADC, T₂) for individual tissue populations of the control group only. From these results, the existence of two unique subpopulations within both viable and necrotic tissue is evident, consistent with the results in Table 4-1.

4.3.3 Results: Radiotherapy Group (Treated)

Table 4-3 gives a quantitative summary of mean feature values (ADC, T₂) for individual tissue populations for the radiotherapy group pre-treatment (-1d) and at 8-days post-treatment. The pre-treatment values are very close to the values listed in Table 4-2 for the control group. Both had comparable percentages of viable and necrotic tissue, with equally similar values of ADC and T₂ on a population-by-population basis. Note that both groups (control, pre-treatment) had 10% necrosis. By 8-days post-treatment, there was an increase in necrotic fraction to an average of 16%, with a jump in volume by a factor of 2. In addition to radiation-induced necrotic formation, there was an increase in viable 2 volume by 50%. Viable 1 remained constant. In terms of the ADCs and T₂ values pre- versus post-treatment, all values remained fairly constant except for necrosis 1, there was an increase in ADC by approximately 24%.

Temporal Evolution of KM Volume

Fig. 4-7 illustrates the temporal evolution of individual KM volume estimates pre- as well as post-irradiation for the radiotherapy group. The overall trend of the total KM volume is a volume decrease out to day 2, followed by tumor regrowth out to day 8. Changes in KM viable volume mirror the changes in total KM volume. In contrast, KM

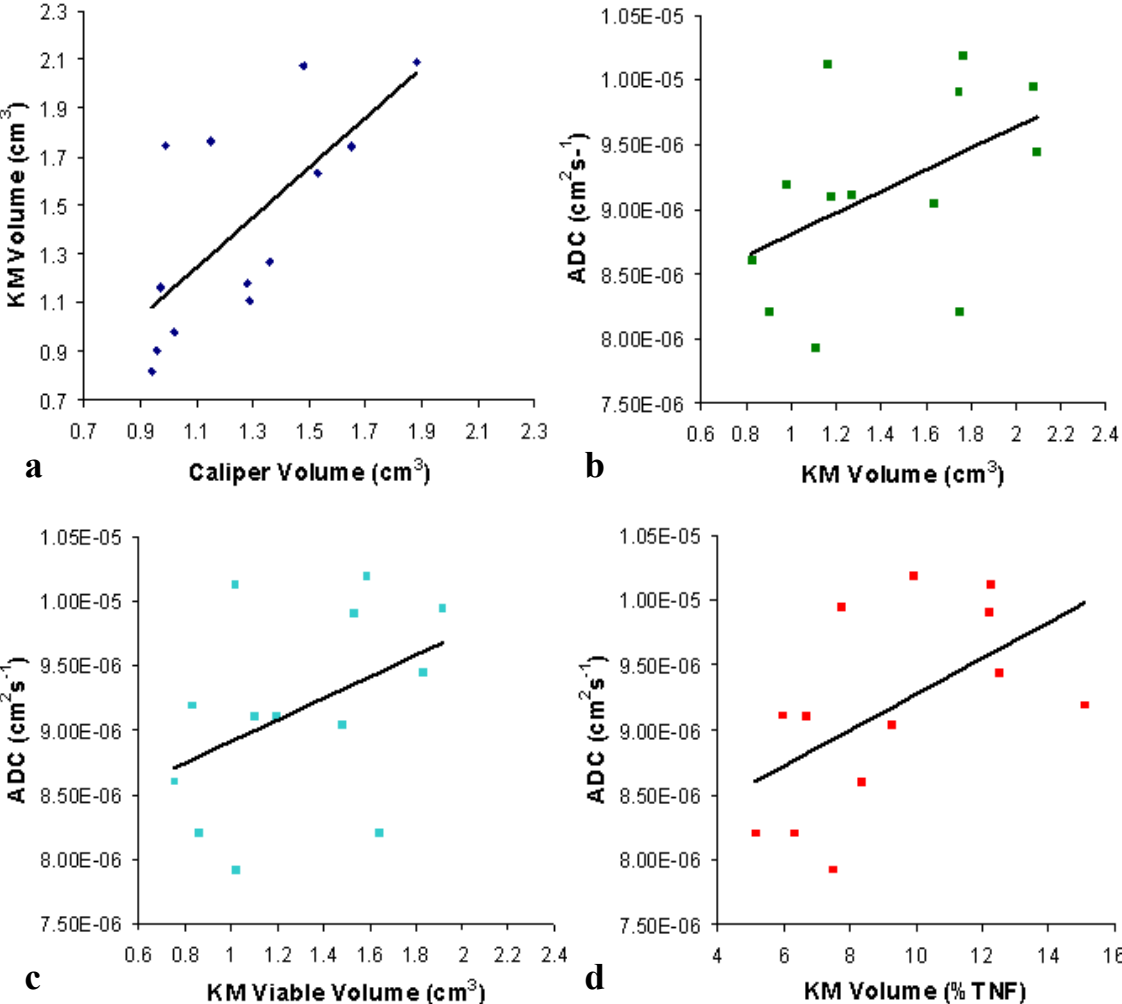


Figure 4-6. Correlation plots of KM volume versus caliper volume (a), total tumor ADC versus KM volume (b), ADC versus KM viable volume (c), and ADC versus percent-tumor-necrotic fraction, %TNF (d). There is a strong correlation between KM and caliper volume estimates ($r = 0.70$). There are relatively weak correlations between ADC and KM volume ($r = 0.48$) and ADC and KM viable volume ($r = 0.43$), with a moderate-to-strong correlation between ADC and %TNF ($r = 0.55$). Data are plotted for 13 of the 16 control animals. The remaining three were excluded because of miresgistration between ADC and T₂ parameter maps.

Table 4-2. Control group mean feature values (ADC and T₂) for individual tissue populations.

Features	ADC ($\times 10^{-5} \text{ cm}^2 \text{ s}^{-1}$)	T ₂ (ms)	Volume (mm ³)	% of total
Viable 1	0.71 ± 0.01	64 ± 1	890 ± 60	63
Viable 2	1.09 ± 0.04	50 ± 0.4	400 ± 60	28
Necrosis 1	2.0 ± 0.1	137 ± 2	21 ± 4	2
Necrosis 2	1.8 ± 0.11	73 ± 1	110 ± 15	8

Parameters were derived on an animal-by-animal basis based on the clustering of all datasets together (N = 29 animals, 88 total datasets over all timepoints). Data are presented as mean ± SEM.

Table 4-3. Radiotherapy group mean feature values (ADC and T₂) for individual tissue populations at 1-day pre-treatment (Pre-Tx) and 8-days post-treatment (8d).

Timepoint	Features	ADC ($\times 10^{-5} \text{ cm}^2 \text{ s}^{-1}$)	T ₂ (ms)	Volume (mm ³)	% of total
Pre-Tx (-1d)	Viable 1	0.70 ± 0.02	62 ± 1	820 ± 60	60
	Viable 2	1.1 ± 0.01	50 ± 1	420 ± 70	31
	Necrosis 1	2.1 ± 0.06	144 ± 5	16 ± 6	1
	Necrosis 2	1.8 ± 0.02	68 ± 1	120 ± 30	9
Post-Tx (8d)	Viable 1	0.79 ± 0.04	63 ± 1	810 ± 150	47
	Viable 2	1.1 ± 0.01	52 ± 1	640 ± 40	37
	Necrosis 1	2.6 ± 0.06	146 ± 5	40 ± 10	2
	Necrosis 2	1.8 ± 0.01	72 ± 1	240 ± 60	14

Parameters were derived on an animal-by-animal basis based on the clustering of all datasets together (N = 29 animals, 88 total datasets over all timepoints). Data are presented as mean ± SEM.

necrotic volume consistently increases out to day 2 post irradiation, after which point it levels off. With the decrease in viable 1 out to day 2 there was a concomitant increase in viable 2. After day 2, both viable 1 and viable 2 slowly but steadily increased. In terms of individual necrotic regions, necrosis 1 remained unchanged with time, whereas necrosis 2 increased in volume to day 4, after which it leveled off. This trend for necrosis 2 followed very closely to that of the total necrotic volume, not surprising as the majority of the necrosis was necrosis 2 versus necrosis 1.

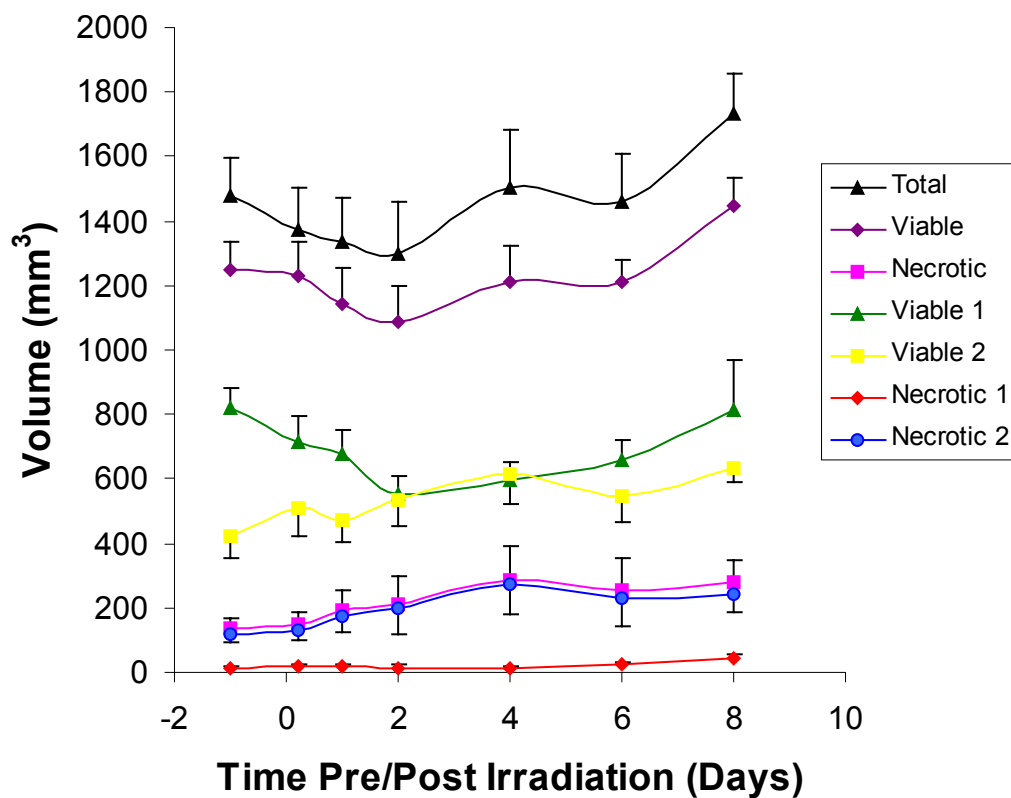


Figure 4-7. Temporal evolution of individual KM cluster volumes pre- and post-irradiation. The overall volume decreases post-irradiation out to day 2, with subsequent tumor regrowth post day 2. The underlying contributions to changes in tumor volume are visible by inspection of individual tissue populations (viable, necrotic), as well as the subpopulations within both viable and necrotic tissue. Values for each timepoint are based on the radiotherapy animals ($n = 11, 12, 9, 8, 9, 8$ for 5h, 1d, 2d, 4d, 6d, and 8d respectively). Differences in number of animals per timepoint are based on tumors reaching 2.0cc, considered a burden for the animal.

4.3.4 Tumor Growth Kinetics (Control vs. Radiotherapy)

Fig. 4-8 shows the method of mathematical analysis of tumor growth and treatment for a representative animal from the radiotherapy group. From this plot, the tumor doubling time (TDT) pre- and post-irradiation may be determined, as well as the tumor growth delay (TGD), and log cell kill. For this animal, $TDT_{pre} = 2.7$ days, $TDT_{post} = 3.6$ days, $TGD = 5.6$ days, and $\log \text{ cell kill} = 0.46$. Fig. 4-9 shows the tumor growth curves for control versus radiotherapy animals as determined from caliper tumor volume measurements (Fig. 4-9a,b) and the corresponding TDT results (Fig. 4-9c,d). The control group TDT was 3.7 ± 0.5 days. In this group, one of the animal's TDT was 10.2 days—if this is removed, the control group TDT = 3.1 ± 0.2 days. For the radiotherapy group, the pre-treatment TDT was 2.3 ± 0.1 days, versus a post-treatment TDT of 6.5 ± 0.7 , with a significant difference between the two ($p < 0.001$). From these results, the single-dose (1000cGy) radiotherapy induced a 3-fold delay in tumor growth.

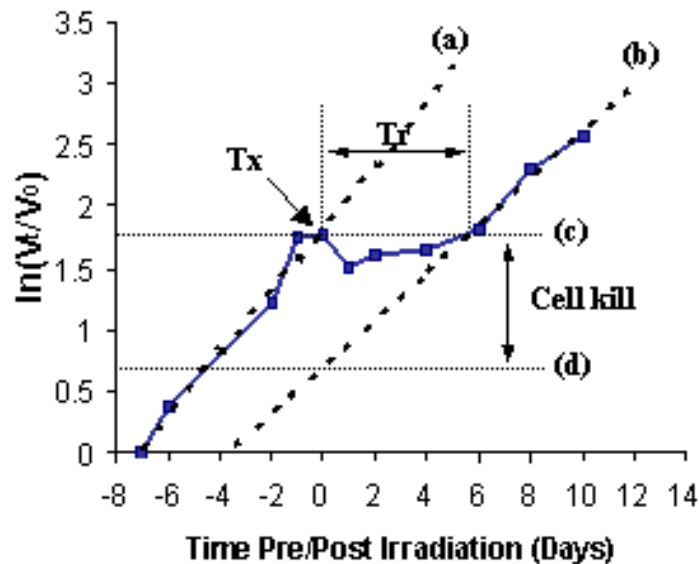


Figure 4-8. Sample plot for a representative RIF-1 tumor demonstrating the mathematical analysis employed for tumor growth and treatment. The line marked (a) is the least-squares fit of the pre-treatment growth points to Eq. 4-4. The line marked (b) is the least-squares fit of the post-treatment growth points to Eq. 4-4. (c) and (d) permit extrapolation of the V_{t-pre} and V_{t-post} , and subsequent calculation of the log cell kill according to Eq. 4-5. Tr , the repopulation interval, is the time required for recovery of the cell population killed by treatment, i.e., the tumor growth delay (TGD).

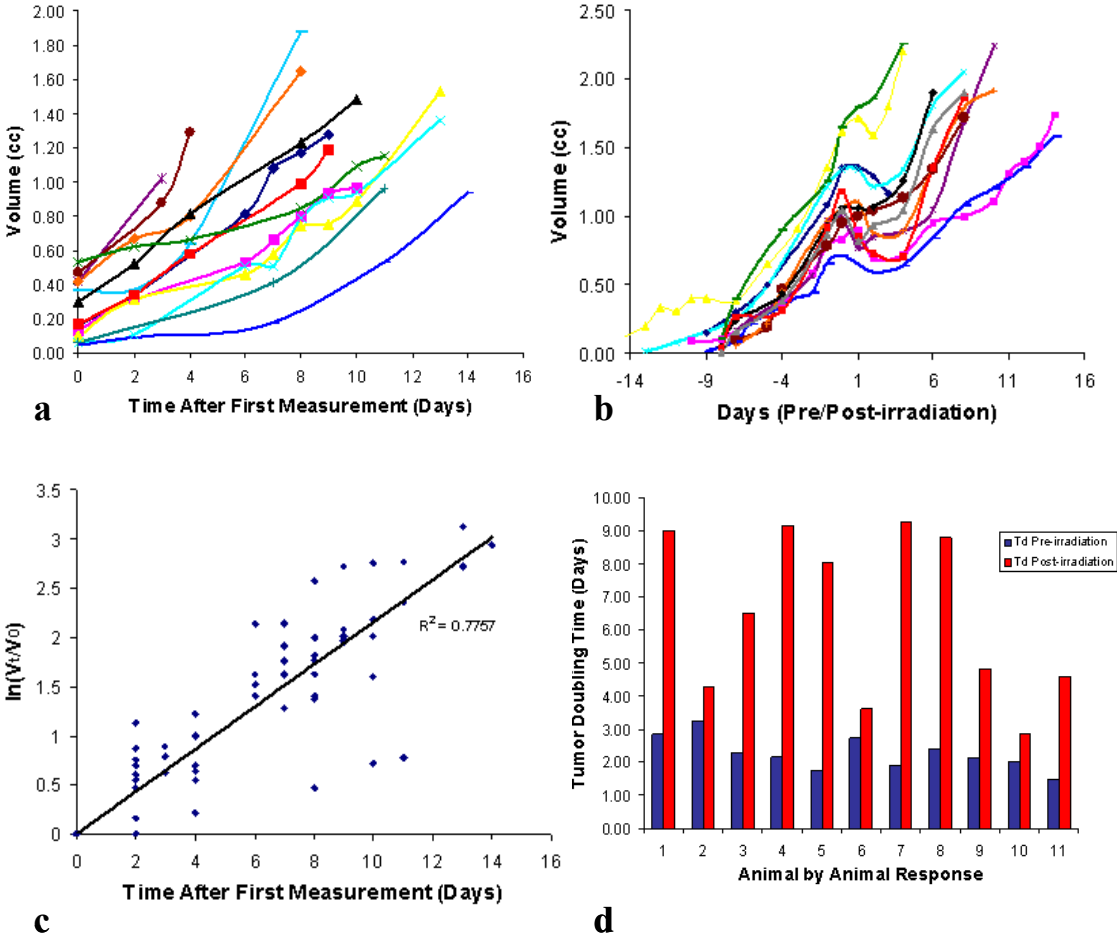


Figure 4-9. Tumor growth curves on an animal-by-animal basis for control (a) and radiotherapy (b) groups, with the corresponding tumor doubling time (TDT) plots. (c) control group TDT = 3.7 ± 0.5 days. One animal's TDT was 10.2 days. If this is removed, the group TDT = 3.1 ± 0.1 . (d) radiotherapy group TDTs on an animal-by-animal basis. There was a significant difference ($p < 0.001$) between pre-treatment TDT (2.3 ± 0.1) versus post-treatment TDT (6.5 ± 0.7).

4.3.5 KM Volume and Treatment Response: TGD and Cell Kill

Fig. 4-10 shows the relationship between the changes in tumor volume between day 0 and the point at which the tumor volume reached a minimum (ranged between day 1 and 4 post-irradiation) and the resultant tumor growth delay (TGD) and log cell kill. For the total tumor volume, determined via caliper measurements, there was a strong correlation between an increase in volume and decreased TGD ($r = 0.91$) and decreased cell kill ($r = 0.85$). Similar correlations were found for the change in KM volume versus TGD and cell kill, although the correlations were to a lesser degree ($r = 0.62$ and $r = 0.65$, respectively). In order to understand which viable regions are contributing to the TGD and cell kill, the relationships between changes in viable 1 and viable 2 versus TGD and cell kill were investigated. There was a moderate-to-strong correlation between a change in viable 1 volume and both TGD ($r = 0.68$) and cell kill ($r = 0.71$), but there was no correlation between these kinetic parameters and viable 2. In addition to the changes in total and/or individual volumes playing a role in the TGD and cell kill, the pre-treatment volumes of individual tissue populations may also play a role in the overall radiotherapeutic response. Fig. 4-11 shows the relationship between pre-treatment values for viable 1 and viable 2 and the TGD and cell kill results. A strong correlation was found between the pre-treatment viable 1 volume and TGD ($r = 0.81$), with a moderate-to-strong correlation between pre-treatment viable 1 and log cell kill ($r = 0.55$). No correlation was found between pre-treatment viable 2 volume and TGD or log cell kill.

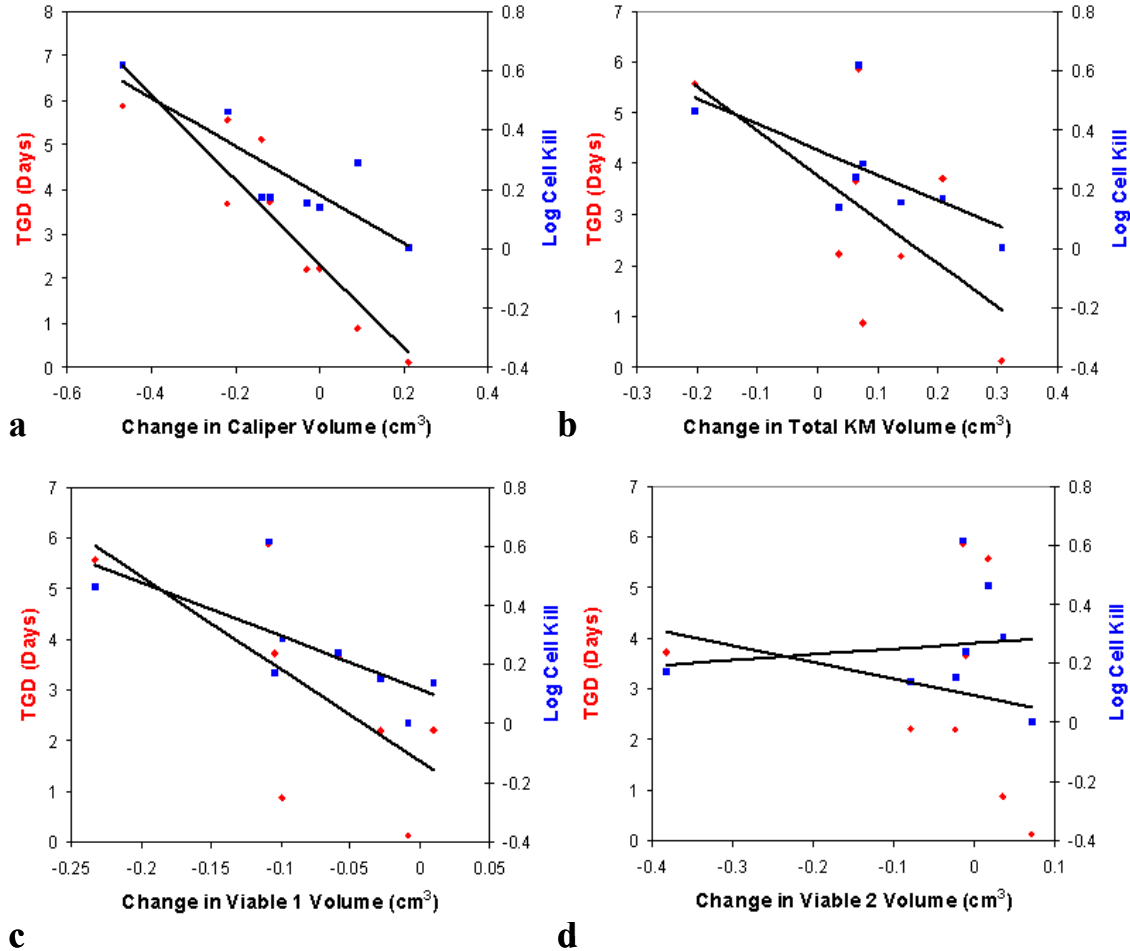


Figure 4-10. The correlation plots for changes in KM volume at day 0 versus the timepoint resulting in a minimum volume (between day 1 and day 4 post-treatment depending on the animal). (a) Volume changes based on caliper measurements were highly correlated with both TGD ($r = 0.91$) and cell kill ($r = 0.85$). (b) Changes in total KM volume were moderate-to-strongly correlated with TGD ($r = 0.62$) and cell kill ($r = 0.65$). Upon investigation of the subpopulations of the viable tissue, it was determined that decreases in viable 1 volume pre- versus post-irradiation correlate well with increased TGD ($r = 0.68$) and increased cell kill ($r = 0.71$). There was no correlation between TGD, cell kill, and viable 2.

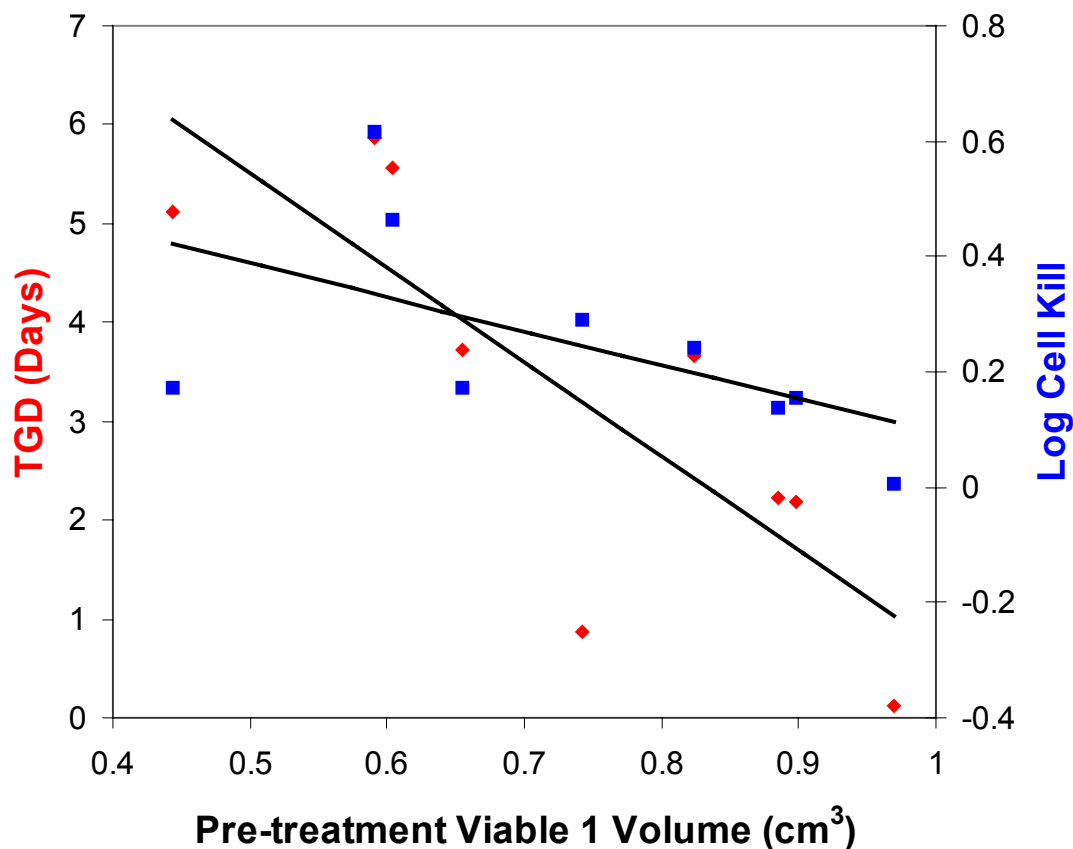


Figure 4-11. The correlation plot for pre-treatment viable 1 volume versus the tumor growth delay (TGD) and log cell kill induced by radiotherapeutic intervention. A strong correlation was found between the pre-treatment viable 1 volume and TGD ($r = 0.81$), with a moderate-to-strong correlation between pre-treatment viable 1 and log cell kill ($r = 0.55$). No correlation was found between pre-treatment viable 2 volume and TGD or log cell kill.

4.3.6 KM Volume and Treatment Response: Evolution of ADC and T_2

Fig. 4-12 shows the temporal evolution of mean ADCs and mean T_2 values for individual KM volumes for the radiotherapy group. The total tumor ADC showed a significant increase by day 2, with a leveling off by day 4 post-treatment. Underlying this change, the trend in KM viable volume followed closely with the total tumor values. This was mainly driven by the change in viable 1 ADC, as viable 2 ADC did not change appreciably. In terms of the necrotic tissue ADC, there was no significant change until day 8. Based on these results, it seems that the early ADC increase (day 0 to 4) is due to changes in ADC in the viable tissue region, with the increase at later timepoints (post-

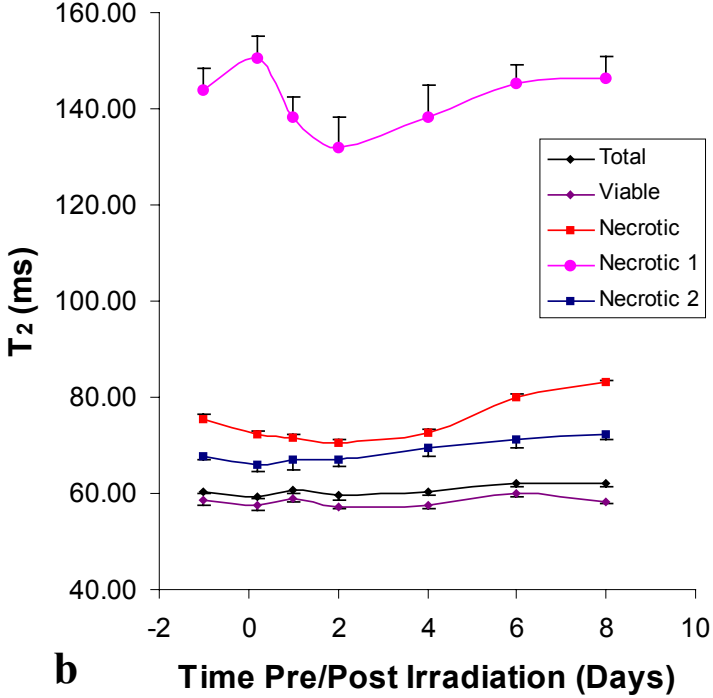
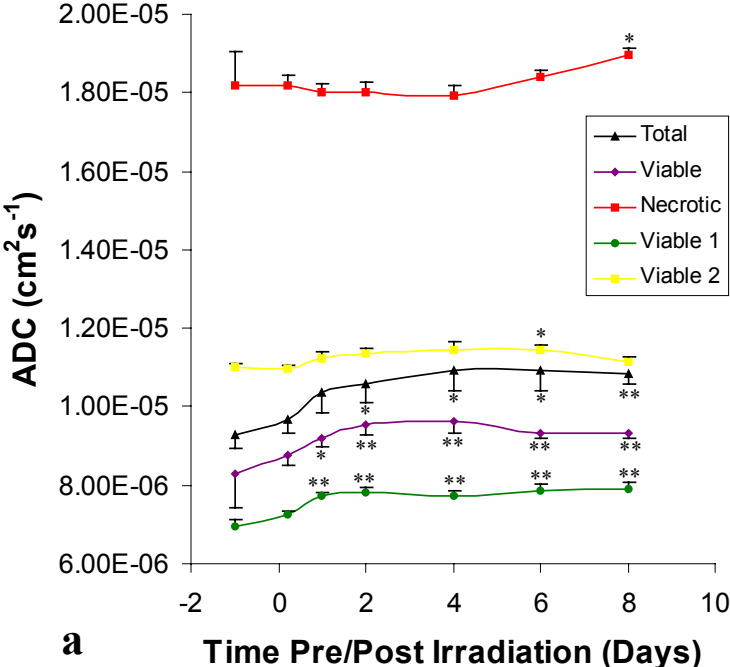


Figure 4-12. Temporal evolution of ADC and T₂ for individual tissue populations pre- versus post-irradiation for the radiotherapy group. Asterisks denote significance based on 2-tailed t-tests assuming unequal variances, for comparisons between values pre-irradiation and every timepoint thereafter. * p < 0.05. ** p < 0.01. Data are presented as mean ± SEM. Values for each timepoint are based on the radiotherapy animals (n = 11, 12, 9, 8, 9, 8 for 5h, 1d, 2d, 4d, 6d, and 8d respectively).

day-4) from the increase in necrotic ADC. The corresponding changes in T_2 values (Fig. 4-12b) show no significant changes between timepoints pre-irradiation versus post-irradiation for any of the individual KM volumes. Since there are no significant changes in T_2 at early timepoints post-irradiation, changes in ADC are likely a result of small changes in cellular density over that of radiation-induced vasogenic edema.

4.4 Discussion

4.4.1 KM Segmentation Results

MS analysis using the KM clustering algorithm and a 2-dimensional feature space (ADC and T_2) permitted subdivision of tumor tissue into two regions each of viable tissue (V1, V2) and necrosis (N1, N2) based on differences in mean ADC and T_2 values using the Euclidean distance measure (Eq. 4-3). These results are shown in Figs. 4-4 and 4.5. This cluster/feature combination was determined to be the optimal method of correlation between KM and histologically-derived volume estimates (see Chapter 3 for details). Differences in T_2 permitted subdivision of necrotic tissue into two regions (Fig. 4-5a,b), one generally acellular in nature (necrosis 1), and a second with a sparse population of cells intermixed with intact RBCs from hemorrhage or leaky vasculature (necrosis 2) (26). Differences in both ADC and T_2 permitted subdivision of viable tissue into two regions (Fig. 4-5c,d), one extremely cell-dense, free of inflammation or hemorrhage (viable 1), and a second with a slightly lower cellular density and abundance of dilated blood vessels in comparison to viable 1. Vessel dilation, likely a compensatory mechanism to a reduced oxygen environment, precedes angiogenesis (27,28). Following HIF-1 α immunohistochemistry, HIF-1 α expression (Fig. 4-5e) was found to be concentrated in peri-necrotic areas, generally corresponding to regions of viable 2 from KM segmentation (Fig. 4-4c, viable 2 = yellow). These morphological characteristics, along with the ADC and T_2 values and the peri-necrotic upregulation of HIF-1 α support the contention that viable 2 is hypoxic, and the subdivision of viable tissue in general.

4.4.2 KM Results: Control versus Radiotherapy

In order to understand the effects of radiotherapy on individual tumor tissue populations, separate control and radiotherapy groups were employed. In the control group, varying

tumor sizes between 1.0 cc and 2.0 cc were investigated in order to look at the correlation between tumor volume and various parameters, specifically the degree of necrosis and the corresponding ADC values. A strong correlation was found between KM volume estimates and caliper volume estimates (Fig. 4-6a, $r = 0.70$), indicating that MRI provides an accurate non-invasive measure of tumor volume. With an increase in KM volume there was an increase in tumor ADC (Fig. 4-6b, $r = 0.48$) based on increased percent-tumor-necrotic fraction, %TNF (Fig. 4-6d, $r = 0.55$). These results are consistent with those of Carano and coworkers (14).

Radiation-induced Necrosis and Hypoxia

Through comparison of the quantitative results for the control group (Table 4-2) and radiotherapy group (Table 4-3), a more detailed understanding of the radiotherapy-induced changes in viable and necrotic tissue is possible. The control group and the pre-treatment timepoint (-1d) for the radiotherapy group had comparable ADCs, T_2 values, and volume estimates for individual tissue populations. Note that there was 10% necrosis in either case, with the remaining tumor volume mostly viable tissue. By day-8 post-treatment, there was an increase in necrosis from 10% to 16% with an increase in necrotic volume by a factor of two. Along with radiation-induced necrotic formation, there was a 50% increase in viable 2 volume and little or no change in viable 1 volume. This increase in viable 2 indicates an increase in the amount of hypoxic tissue post-irradiation—in other words, the selective survival of radioresistant tumor cells. These results are consistent with previous studies reporting on a radiation-induced increase in the fraction of hypoxic cells (29-31).

Temporal Evolution of KM Volume

Fig. 4-7 diagrams the temporal evolution of individual KM volumes pre-irradiation versus post-irradiation. The decrease in tumor volume out to day 2, mirrored by a decrease in viable 1, is consistent with radiation-induced cell killing. Concomitant with this decrease is an increase in viable 2. These trends indicate that viable 1, presumably well-oxygenated tissue, is radiosensitive and regresses following irradiation. Viable 2, on the other hand, is radioresistant, and doesn't respond to radiotherapy. In fact, viable 2 increases out to day 4 and then plateaus. This persistent hypoxia may be related to the formation of necrosis, as the trend for viable 2 follows that of the necrotic fraction.

4.4.3 KM Contributions to TGD and Cell Kill

In order to address the relative contributions of individual tissue populations to the overall response, the relationships between KM volume contributions and TGD and cell kill was investigated.

Overall Tumor Growth Kinetics

The overall growth kinetics for the control and radiotherapy groups are shown in Fig. 4-9. Fig. 4-9a,b show the tumor growth curves obtained via caliper measurements for the control and radiotherapy groups, respectively. These plots show the existence of inter-tumoral variability, even though all animals received the same injection of RIF-1 cells for development of the tumor model. The control group TDT was 3.7 ± 0.5 days, consistent with previously reported TDTs within this particular tumor model. For the radiotherapy group, there was a significant difference between pre-treatment TDT (2.3 ± 0.1) and post-treatment TDT (6.5 ± 0.7). These results indicate that a single-dose of 1000cGy induces an approximate 3-fold increase in TDT.

KM Viable Volume Changes and the Radiotherapeutic Response

Changes in volume between day 0 versus the timepoint resulting in a minimum tumor volume (between days 1 and 4 post-treatment depending on the animal) were compared with the resultant TGD and log cell kill on an animal-by-animal basis within the radiotherapy group (Fig. 4-10). There was a moderate-to-strong correlation between the change in total KM volume and these kinetic parameters ($r = 0.62$ for TGD and $r = 0.65$ for cell kill). With a reduction in total KM volume, there was an increase in TGD and cell kill. Changes in viable 1 showed similar levels of correlation, but there was no correlation between viable 2 and TGD or cell kill. This reinforces the previous claim that viable 1 is well-oxygenated, radiosensitive tissue and that viable 2 is radioresistant, and therefore, hypoxic. Because hypoxia induces radioresistance, the relative contributions of viable 1 and viable 2 pre-treatment to the radiotherapeutic response was investigated (Fig. 4-11). There was a strong correlation between pre-treatment viable 1 volume and TGD ($r = 0.81$) and a moderate-to-strong correlation with log cell kill ($r = 0.55$). Again, there was no correlation found between viable 2 and TGD or cell kill.

4.4.4 Underlying Contributions to the ADC Response

In order to understand the underlying contributions whose combination yield the total ADC response following treatment, the temporal evolution of ADCs for individual tissue populations was investigated (Fig. 4-12a). Following radiotherapy, there was an increase in total tumor ADC out to day 4 followed by a plateau. The ADC for necrotic tissue remained constant out to day 4, followed by a significant increase ($p < 0.05$) at day 8. This is most likely from removal of cellular debris and the movement of the total necrotic fraction towards an acellular environment. The ADC increase for viable tissue mirrored that of the total tumor ADC. The underlying contribution to the ADC changes in viable tissue were attributed to the viable 1 fraction, not viable 2. Although there was this slight increase in ADC for viable 1, because there was no corresponding change in T_2 (Fig. 4-12b), it could not be attributed to vasogenic edema. This small change, approximately 10% in magnitude, is most likely from a slight reduction in cellular density. This change was not large enough for a transfer of classification from viable 1 to viable 2 [viable 1 $ADC = 0.76 \pm 0.23$ (mean \pm SD, $\times 10^{-5} \text{ cm}^2\text{s}^{-1}$)]. No significant changes were seen in T_2 for any KM regions, indicating the absence of edema.

4.4.5 Utility of the KM Method

Advantage of MS Analysis over Single Parameter Approaches

Although several studies have shown that increases in mean/volume-averaged tumor ADC prior to any change in tumor volume are indicative of a positive-treatment response (3,6-8), the evaluation of the tumor in this manner does not allow the determination of the origin of the ADC change. With a reduction in tumor necrotic fraction, the mean tumor ADC approaches ADC values consistent with that of viable tissue. If small sub-populations of necrosis are present, changes in the overall necrosis may be small and would show little to no change in mean tumor ADC (9). Because previous studies have also had difficulty in identifying regions of mixed viability (9,10,14), an MS approach aimed at subdividing individual tissue regions, specifically viable tissue, is needed.

MS Analysis and Tumor Growth Kinetics

Overall, these results indicate that the combination of MS analysis with tumor growth kinetics is superior to either approach alone. MS analysis provides a way of addressing

inter- and intra-tumor heterogeneity through identification of individual tumor tissue populations. This particular method was able to identify subpopulations within both viable and necrotic tissue, and more importantly, the delineation between well-oxygenated versus hypoxic tissue. Since both necrosis and hypoxia have been implicated in poor treatment response and reduced patient survival, the quantification of the amount of necrosis and the severity of hypoxia may aid in assignment of a more aggressive treatment regimen. Quantitative assessment of individual tissue regions, tumor growth rates (TDT and TGD), and cell kill should provide a more accurate method for therapeutic monitoring and optimization of drug-dose and timing schemes in pre-clinical animal models by eliminating the issue of inter-tumoral variability.

Acknowledgements

The authors thank Dr. George Pins (Worcester Polytechnic Institute, MA) for the use of his laboratory for histological purposes (paraffin-embedding, microtome sectioning, H&E staining, and slide photography), Brett Downing and Kevin Cornwell (Worcester Polytechnic Institute, MA) for helpful advice and optimization of the H&E protocol, and Dr. Richard A.D. Carano (Genentech, CA) for his advice on the KM clustering algorithm. This work was supported by the Research Advancement Program through Worcester Polytechnic Institute (K.G.H.).

References

1. Zhao M, Pipe JG, Bonnett J, Evelhoch JL. Early detection of treatment response by diffusion-weighted ^1H -NMR spectroscopy in a murine tumor *in vivo*. *Br J Cancer* 1996;73:61-64.
2. Galons JP, Altbach MI, Paine-Murrieta GD, Taylor CW, Gillies RJ. Early increases in breast tumor xenograft water mobility in response to paclitaxel therapy detected by non-invasive diffusion magnetic resonance imaging. *Neoplasia* 1999;1:113-117.
3. Chinnaiyan AM, Prasad U, Shankar S, Hamstra DA, Shanaiah M, Chenevert TL, Ross BD, Rehemtulla A. Combined effect of tumor necrosis factor-related apoptosis-inducing ligand and ionizing radiation in breast cancer therapy. *Proc Natl Acad Sci* 2000;97:1754-1759.
4. Jennings D, Hatton BN, Guo J, Galons JP, Trouard TP, Raghunand N, Marshall J, Gillies RJ. Early response of prostate carcinoma xenografts to docetaxel chemotherapy monitored with diffusion MRI. *Neoplasia* 2002;4:255-262.

5. Moffat BA, Hall DE, Stohanovska J, McConville PJ, Moody JB, Chenevert TL, Rehemtulla A, Ross BD. Diffusion imaging for evaluation of tumor therapies in preclinical animal models. *Magma* 2004;17:249-259.
6. Chenevert TL, McKeever PE, Ross BD. Monitoring early response of experimental brain tumors to therapy using diffusion magnetic resonance imaging. *Clin Cancer Res* 1997;3:1457-1466.
7. Chenevert TL, Stegman LD, Taylor JMG, Robertson PL, Greenberg HS, Rehemtulla A, Ross BD. Diffusion magnetic resonance imaging: an early surrogate marker of therapeutic efficacy in brain tumors. *J Natl Cancer Inst* 2000;92:2029-2036.
8. Dzik-Jurasz A, Domenig C, George M, Wolber J, Padhani A, Brown G, Doran S. Diffusion MRI for prediction of response of rectal cancer to chemoradiation. *Lancet* 2002;360:307-308.
9. Lyng H, Haraldseth O, Rofstad EK. Measurement of cell density and necrotic fraction in human melanoma xenografts by diffusion weighted magnetic resonance imaging. *Magn Reson Med* 2000;43:828-836.
10. Helmer KG, Meiler MR, Sotak CH, Petrucci JD. Comparison of the return-to-the-origin probability and the apparent diffusion coefficient of water as indicators of necrosis in RIF-1 tumors. *Magn Reson Med* 2003;49:468-478.
11. Clark MC, Hall LO, Goldgof DB, Velthuizen R, Murtagh FR, Silbiger MS. Automatic tumor segmentation using knowledge-based techniques. *IEEE Trans Med Imaging* 1998;17:187-201.
12. Tzika AA, Astrakas LG, Zarifi MK, Petridou N, Young-Poussaint T, Goumnerova L, Zurakowski D, Anthony DC, Black PM. Multiparametric MR assessment of pediatric brain tumors. *Neuroradiology* 2003;45:1-10.
13. Jacobs MA, Barker PB, Bluemke DA, Maranto C, Arnold C, Herskovits EH, Bhujwala Z. Benign and malignant breast lesions: diagnosis with multiparametric MR imaging. *Radiology* 2003;229:225-232.
14. Carano RA, Ross AL, Ross J, Williams SP, Koeppen H, Schwall RH, Bruggen NV. Quantification of tumor tissue populations by multispectral analysis. *Magn Reson Med* 2004;51:542-551.
15. Mazurchuk R, Glaves D, Raghavan D. Magnetic resonance imaging of response to chemotherapy in orthotopic xenografts of human bladder cancer. *Clin Cancer Res* 1997;3:1635-1641.
16. Ross BD, Zhao YJ, Neal ER, Ben-Yoseph O, Chenevert TL. Contributions of cell kill and posttreatment tumor growth rates to the repopulation of intracerebral 9L tumors after chemotherapy: an MRI study. *Proc Natl Acad Sci* 1998;95:7012-7017.
17. He Z, Evelhoch JL, Mohammad RM, Adsay NV, Pettit GR, Vaitkevicius VK, Sarkar FH. Magnetic resonance imaging to measure therapeutic response using an orthotopic model of human pancreatic cancer. *Pancreas* 2000;21:69-76.
18. Stegman LD, Rehemtulla A, Hamstra DA, Rice DJ, Jonas SJ, Stout KL, Chenevert TL, Ross BD. Diffusion MRI detects early events in the response of a glioma model to the yeast cytosine deaminase gene therapy strategy. *Gene Therapy* 2000;7:1005-1010.

19. Ross BD, Chenevert TL, Garwood M, Kim B, Stegman LD, Ben-Yoseph O, Zwolshen J, Rehemtulla A, Sunkara PS. Evaluation of (E)-2'-deoxy-2'-(fluoromethylene)cytidine on the 9L rat brain tumor model using MRI. *NMR Biomed* 2003;16:67-76.
20. Lazareff JA, Suwinski R, de Rosa R, Olmstead CE. Tumor volume and growth kinetics in hypothalamic-chiasmatic pediatric low grade gliomas. *Pediatr Neurosurg* 1998;30:312-319.
21. Newman WI, Lazareff JA. A mathematical model for self-limiting brain tumors. *J Theor Biol* 2003;222:361-371.
22. Duda R, Hart P. *Pattern classification*. New York: John Wiley & Sons; 2001.
23. Steele GG. *Growth kinetics of tumors*. Oxford: Clarendon; 1977.
24. Loukas CG, Linney A. A survey on histological image analysis-based assessment of three major biological factors influencing radiotherapy: proliferation, hypoxia, and vasculature. *Comput Methods Programs Biomed* 2004;74:183-199.
25. Russ JC. Fractal analysis. *The image processing handbook*. 2nd ed. Boca Raton: CRC Press; 1995. p 262-270.
26. Hashizume H, Baluk P, Morikawa S, McLean JW, Thurston G, Roberge S, Jain RK, McDonald DM. Openings between defective endothelial cells explain tumor vessel leakiness. *Am J Pathol* 2000;156:1363-1380.
27. Ryschich E, Schmidt J, Hammerling GJ, Klar E, Ganss R. Transformation of the microvascular system during multistage tumorigenesis. *Int J Cancer* 2002;97:719-725.
28. Ryschich E, Schmidt E, Maksan SM, Klar E, Schmidt J. Expansion of the endothelial surface by an increase of vessel diameter during tumor angiogenesis in experimental hepatocellular and pancreatic cancer. *World J Gastroenterol* 2004;10:3171-3174.
29. Hopwood LE, Davies BM, Moulder JE. Drug resistance following irradiation of RIF-1 tumors: influence of the interval between irradiation and drug treatment. *Int J Radiat Oncol Biol Phys* 1990;19:643-650.
30. Gabalski EC, Adam M, Pinto H, Brown JM, Bloch DA, Terris DJ. Pretreatment and midtreatment measurement of oxygen tension levels in head and neck cancers. *Laryngoscope* 1998;108:1856-1860.
31. Rofstad EK, Mathiesen B, Galappathi K. Increased metastatic dissemination in human melanoma xenografts after subcurative radiation treatment: radiation-induced increase in fraction of hypoxic cells and hypoxia-induced up-regulation of urokinase-type plasminogen activator receptor. *Cancer Res* 2004;64:13-18.

CHAPTER 5

HISTORY OF CEREBRAL ISCHEMIA: EVOLUTION AND OUTCOME

Background

Healthy versus Ischemic Brain Tissue
Viability Thresholds in Cerebral Ischemia
Lesion Characterization: Core and Penumbra

Current Therapeutic Targets

rt-PA Therapy
Neuroprotective Therapy
Anti-Inflammatory Agents

Current MRI Methods

Diffusion-weighted Imaging
Perfusion-weighted Imaging
Metabolic Imaging

5.1 Background

Cessation of the cerebral circulation following stroke begins a cascade of physiological events ultimately leading to tissue ischemia and irreversible neuronal damage. Arrested or critically-reduced blood flow is many times a result of vessel occlusion, although it can also be a result of vessel damage (i.e., from traumatic brain injury). Clinically available therapeutic targets, such as standard rt-PA therapy, are limited to the treatment of patients with acute stroke (within 3-5 hours of onset). Unfortunately, the majority of patients presents with symptoms long after this therapeutic window, excluding them from treatment and the potential for improved quality of life. As this leaves clinicians to simple diagnosis and follow-up, methods investigating mechanistic aspects of ischemic progression are necessary in order to provide new therapeutic avenues with potential application at later timepoints from onset of stroke. MRI techniques have been employed in the study of cerebral ischemia since the emergence of the diagnostic utility of DWI in the late 1980s (1) and early 1990s (2,3). Further methods involving PWI and metabolic imaging followed, permitting a more in-depth analysis of the temporal evolution of cerebral ischemia. In order to understand the applicability of MRI methods and the development of potential therapeutic targets for cerebral ischemia, a discussion of healthy versus ischemia brain tissue is required. Additionally, lesion characterization into core and penumbra based on viability thresholds will be covered. This chapter should provide sufficient background for the research presented in Chapters 6 and 7.

5.1.1 Healthy versus Ischemic Brain Tissue

The healthy brain depends on a constant supply of oxygen (O₂) and glucose. Constrained O₂ supply impairs energy production, affecting energy-consuming processes in a sequential manner—impaired functioning is followed by metabolic failure and loss of structural integrity. Depending on the level of perfusion deficit present in ischemic tissue the development of infarction may or may not occur. Residual perfusion from collateral flow can temporarily maintain the limited energy stores in regions with loss of functional integrity but that are structurally intact. These tissue regions are potentially salvageable and serve as a therapeutic target early after stroke onset.

5.1.2 Viability Thresholds in Cerebral Ischemia

The existence of two major thresholds of hypoxia characteristic of cerebral ischemia were suggested by studies revealing that electroencephalographic (EEG) activity is disrupted at significantly higher flow rates than energy state deterioration and failure of ion homeostasis (4-6). A diagram of the various flow thresholds with the corresponding breakdowns of function and metabolism is shown in Fig. 5-1, a modification of Hossmann's (7). Inhibition of protein synthesis (0.55 ml/g/min) is followed by a transition from aerobic to anaerobic glycolysis, with accumulation of lactate (<0.35 ml/g/min) and subsequent reduction of tissue pH (8).

Threshold of Electrical Failure

At flow rates between 0.15 ml/g/min and 0.25 ml/g/min, the spontaneous EEG activity is suppressed. Energy metabolism is moderately reduced from a failing O₂ supply and declined ATP production. Nevertheless, it remains functional and is able to maintain ion homeostasis via the sodium-potassium pump and the Na⁺-K⁺ ATPase enzyme. It is important to note that this tissue region, although compromised, is recoverable because existing neurons are intact. Reperfusion, or the restoration of normal blood flow, could potentially salvage this region's viability.

Threshold of Membrane Failure

At flow rates below 0.15 ml/g/min there is complete failure of energy metabolism, leading to ion pump failure. Unable to maintain existing ion gradients, cells experience a massive efflux of potassium (K⁺) concomitant with an influx of sodium (Na⁺), chloride (Cl⁻), and calcium (Ca²⁺). In response to the massive movement of ionic species (K⁺, Na⁺, Cl⁻, Ca²⁺) across cellular membranes, a shift of extracellular (EC) water to the intracellular (IC) space results in cellular swelling, often referred to as cytotoxic edema. Stimulated release of excitatory neurotransmitters (i.e., glutamate) activates N-methyl-D-aspartate (NMDA) receptors, opening ligand-gated Ca²⁺ channels for further Ca²⁺ influx. Without the necessary energy stores, membrane repolarization and restoration of ion gradients is not possible. Therefore, terminal anoxic depolarizations are characteristic of this region. Intracellular Ca²⁺ accumulation initiates enzymatic activity, the formation of free radicals, and subsequent degradation of cellular components such as DNA. At this point, the loss of structural integrity results in permanent neuronal damage.

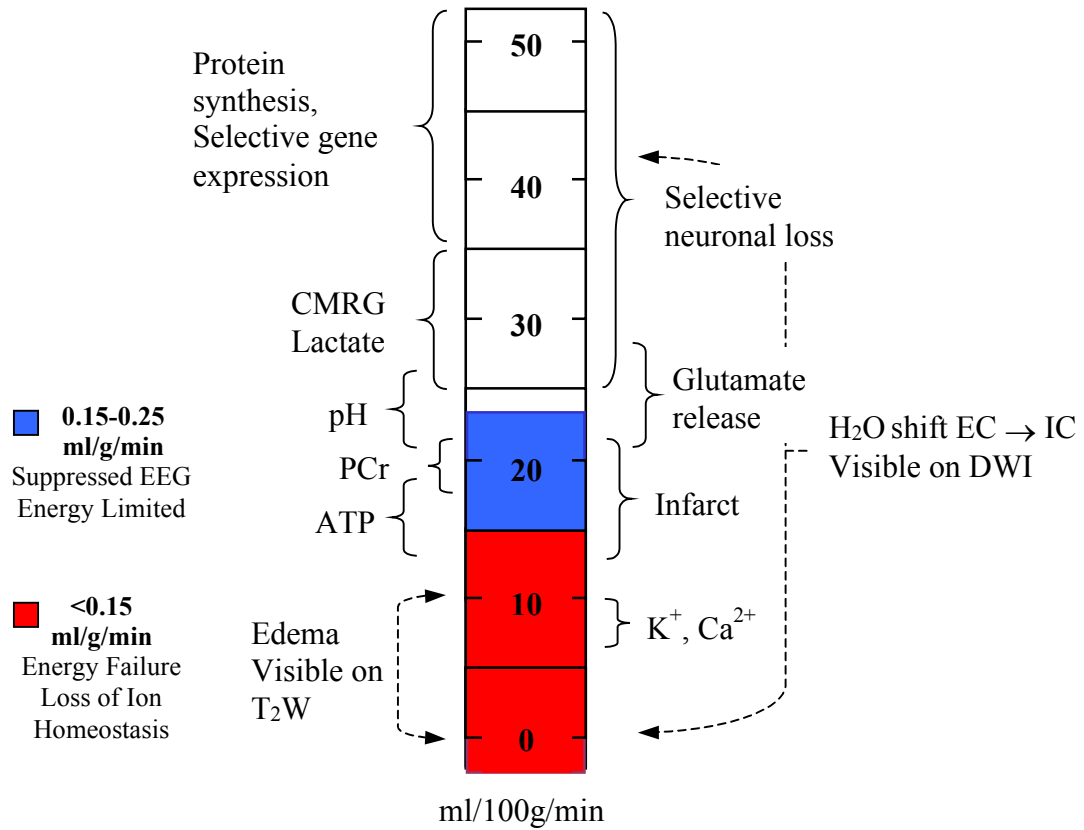


Figure 5-1. Critical flow thresholds of ischemia. Between 0.15 ml/g/min and 0.25 ml/g/min (shaded blue) spontaneous EEG activity is suppressed. Within this flow range, the metabolism remains functional although the energy stores are limited. Transient depolarizations may occur in this region. Below 0.15 ml/g/min (shaded red) there is complete energy failure and severe loss of ion homeostasis. Within this flow range, there is a combined loss of functionality and structural integrity. Terminal anoxic depolarizations are characteristic of this region. CMRG = cerebral metabolic rate of glucose; PCr = phosphocreatine, ATP = adenosine triphosphate. Figure adapted from reference (7).

5.1.3 Tissue Characterization: Core and Penumbra

Defining Ischemic Penumbra

The two critical flow rates, the threshold for electrical failure and the threshold for membrane failure, initiated the idea of a region of potentially viable tissue in which there was functional but not structural injury. This region has been termed the ischemic penumbra (9). An oversimplified model of focal ischemia is shown in Fig. 5-2. Here, the penumbra surrounds a central core of irreversibly damaged tissue (i.e., infarct). Supported by flow from collateral vessels, partial perfusion of the penumbra temporarily maintains its viability in contrast to the core. Lassen *et al.* (10) commented on a temporal dependence for tissue viability, supported by reports of similar lesion sizes in three hours of temporary ischemia versus that of permanent occlusion (11). With this in mind, using a relative cerebral blood flow (rCBF) threshold for delineation between penumbra and core is tricky. Over the years, the evolving definition of penumbra has come to include metrics of metabolism (ATP levels and tissue pH) as well as ionic changes (Ca^{2+} and water movement).

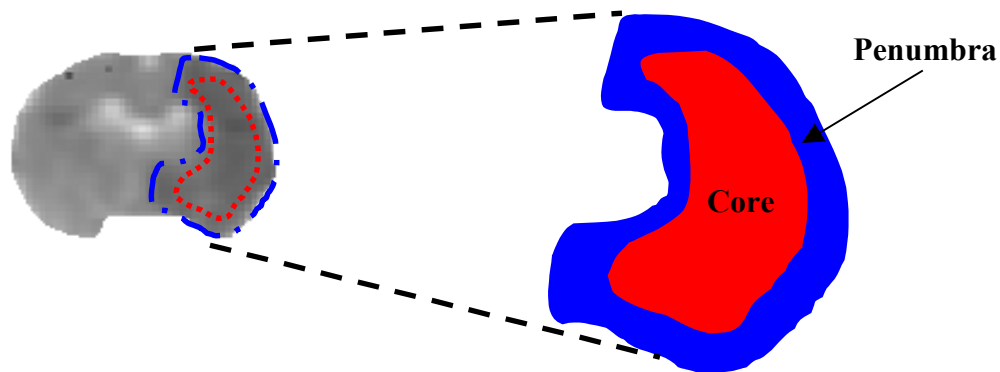


Figure 5-2. Visualization of the Penumbra and Core of Ischemia. Left: ADC parameter map for a single 2-mm axial slice in a rat model of middle cerebral artery occlusion (MCAO). The hypointense region represents the ischemic lesion. The remainder is normal tissue. Right: Cartoon of penumbra tissue (shaded blue) and core (shaded red). The penumbra corresponds to the region of reduced blood flow in which energy metabolism (i.e., ATP production) and ion homeostasis (i.e., the $\text{Na}^+\text{-K}^+$ pump) are preserved. This region is potentially salvageable via therapeutic intervention. The core corresponds to the region of irreversible neuronal damage.

5.2 Current Therapeutic Targets

Potentially salvageable tissue, the penumbra has been of interest for over a decade in the hopes of halting progression to infarct. Current therapies concentrate on mechanisms for improved blood flow, neuroprotection, and anti-inflammation. The overall therapeutic goal is to reduce the progression of cerebral ischemia and the resultant neuronal damage.

5.2.1 Recombinant Tissue Plasminogen Activator (rt-PA) Therapy

Thrombolytic therapy aids in the breakdown of blood clots (emboli) that are suppressing normal cerebral circulation. One such example is recombinant tissue plasminogen activator, or rt-PA. This agent cleaves plasminogen to plasmin, an endogenous substance responsible for fibrinolysis. Although this methodology is effective in the restoration of cerebral blood flow, the high occurrence of intracranial hemorrhage requires extreme care in patient selection. A comparison of intravenous and intraarterial studies in the delivery of rt-PA shows that hemorrhagic transformation results in neurological deterioration in approximately 10% to 15% of patients (12). Despite these safety concerns, rt-PA remains the most successful thrombolytic agent in stroke therapy to date.

5.2.2 Neuroprotective Therapy

The investigation of drugs exhibiting neuroprotective effects is very important in combating failure of energy metabolism and cellular deterioration in cerebral ischemia. Ca^{2+} overload in neurons triggers apoptosis (programmed cell death) and the degradation of cellular components such as DNA, proteins, and phospholipids (13). Wahlgren (14) diagrammed the chain of events resulting in the buildup of intracellular Ca^{2+} , which has been reproduced in Fig. 5-3. Since intracellular Ca^{2+} accumulation leads to permanent neuronal damage, methods aiming to reduce the level of Ca^{2+} influx are of particular interest. This makes Ca^{2+} channels (both voltage-gated and ligand-gated) a therapeutic target.

NMDA Channel Antagonists

The NMDA receptor is the most well known in the excitatory amino acid (EAA) receptor family (Fig. 5-4). This receptor has several binding sites, but the phencyclidine (PCP) recognition site is of particular interest for noncompetitive NMDA channel antagonists such as dizocilpine (MK-801) (15). As stated earlier, glutamate release activates NMDA

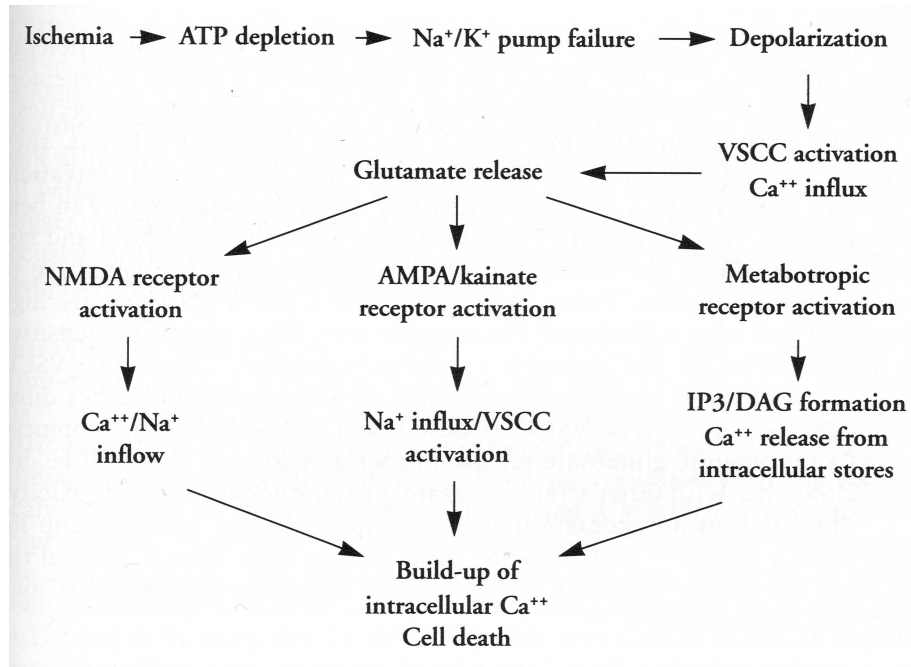


Figure 5-3. Pathophysiological chain of events in cerebral ischemia. These events resulting in a buildup of the intracellular calcium concentration and cell death. Abbreviations are: ATP = adenosine triphosphate, VSCC = voltage-sensitive Ca^{2+} -channels, NMDA = N-methyl-D-aspartate, AMPA = alpha-amino-3-hydroxy-5-methyl-4-isoxazole propionate, IP3 = inositol 1,4,5-trisphosphate, DAG = diacylglycerol (1,2-diacyl-sn-glycerol-3-phosphorylethanolamine). Figure reproduced from reference (14).

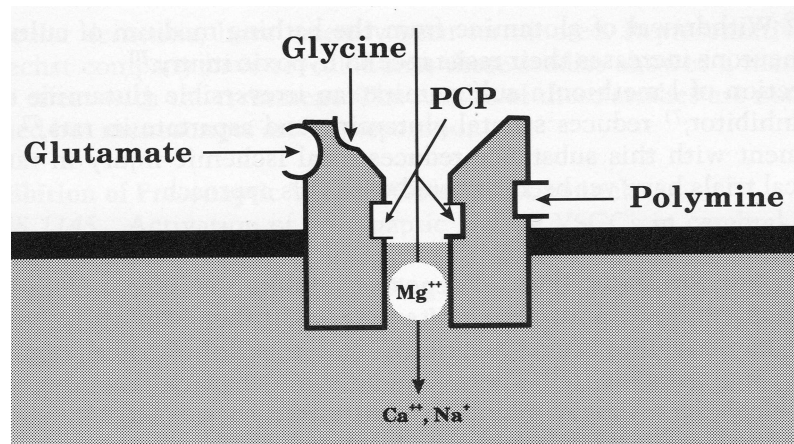


Figure 5-4. Cartoon of the N-methyl-D-aspartate (NMDA) receptor. Individual binding sites (glutamate, glycine, polymine, and phencyclidine (PCP)) are shown. Figure reproduced from reference (14).

receptors, permitting Ca^{2+} influx. Studies of focal cerebral ischemia in animal models have demonstrated significant reductions in infarct volume with MK-801 (16,17). In terms of competitive NMDA channel antagonists (directly blocking the NMDA receptor site), the most extensively tested drug has been CGS-19755. Studies providing CGS-19755 treatment early after ischemic onset reported a significant decrease in Ca^{2+} influx, with differing levels of neuronal protection depending on drug dose and time of delivery (18-20). Subsequent studies comparing the effects of a more recent competitive NMDA receptor antagonist, CGP-40116, with that of CGS-19755 and MK-801 have shown that CGP-40116 is more potent than CGS-19755 with comparable levels of neuroprotection as MK-801 (21-23).

5.2.3 Anti-inflammatory Agents

Although rt-PA therapy improves therapeutic outcome via restoration of blood flow, two retrospective studies performed by the NINDS rt-PA Stroke Study Group (24,25) reported that six percent of patients treated with rt-PA experienced symptomatic intracerebral hemorrhage. In addition, the authors found that the neurological benefit (i.e., minimal or no disability) at 3 months was only 30% better than patients receiving placebo, with similar mortality rates for the two.

Reperfusion Injury and the Inflammatory Response

Reperfusion of ischemic tissue has an associative inflammatory response that may contribute to the development of secondary neuronal damage. Following transient cerebral ischemia, expression of cytokines such as tumor necrosis factor alpha (TNF- α) and interleukin-1 (IL-1) increase the recruitment and activation of leukocytes (26,27). These leukocytes, referred to as polymorphic neutrophils (PMNs), promote blood coagulation by adhesion to endothelial cells and the production of perfusion defects. del Zoppo *et al.* (28) demonstrated that leukocyte accumulation in the microvasculature after reperfusion caused secondary occlusion (i.e., the “no-reflow” phenomenon). Leukocyte accumulation also increases enzymatic activity and the production of oxygen free radicals. These, as discussed earlier, lead to neuronal damage and apoptotic events.

Anti-inflammatory Agents

Because inflammation is the major contributor to reperfusion injury, anti-inflammatory agents targeting adhesion molecules (ICAM-1) or cytokines (TNF- α , IL-1) could reduce the risk of symptomatic ICH following rt-PA therapy. Treatment of cerebral reperfusion injury with anti-ICAM-1 was shown to increase the efficacy of rt-PA in a rabbit model of ischemia (29). Additional studies in IL-1R1 null mice (30) and anti-TNF- α in rat brain (31) reported neuroprotection against reperfusion injury. Further study of antibodies against adhesion molecules such as ICAM-1 and the cytokines listed above should aid in understanding the mechanisms of reperfusion injury and how to combat them.

5.3 Current MRI Methods

MRI techniques such as DWI, PWI, and metabolic imaging permit the rapid definition of ischemic territory and regions of perfusion deficit. These methods are not only useful in investigating the pathophysiology of cerebral ischemia, but also in monitoring therapeutic efficacy and optimizing drug dose and delivery.

5.3.1 Diffusion-weighted Imaging

The emergence of DWI for early detection of ischemic injury, first detected by Moseley and coworkers (2,3), initiated subsequent quantitative assessment of ADCs in normal and ischemic brain tissue. Reduced ADCs, caused by cellular swelling and energy driven processes, permit lesion identification and volumetric analysis. Warach *et al.* (32) reported that ischemic injury was detectable on DWI as early as one hour after onset, previous to any visible hyperintensity on T₂-weighted MRI. A subsequent study by this group reinforced the fact that conventional imaging tends to underestimate the ischemic territory identifiable by ADCs (33). This is because T₂-weighted MRI, which detects alterations in tissue water content, is less sensitive than DWI. T₂ changes are not readily apparent until 4-6 hours after occlusion, when sufficient development of vasogenic edema has occurred. DWI, on the other hand, is able to detect evidence of cytotoxic edema within minutes after occlusion. DWI evaluation of the extent of injury in acute stroke, within 3-5 hours from initial onset, provides the clinician with a diagnostic tool

superior to pre-existing methods; a method for monitoring any therapeutic intervention provided on the patient's behalf.

Reversible versus Irreversible Damage

The ability to differentiate reversible from irreversible damage is important in assessing the severity of stroke at the time of diagnosis and treatment. Ischemic areas with slow diffusion denote permanent injury whereas regions with normal to moderately reduced diffusion suggest salvageable tissue. Minematsu *et al.* (34) noted that MRI with heavy diffusion-weighting was able to differentiate reversible focal ischemic injury from permanent damage in a transient MCAO model in rats. Similar results were reported in cerebral ischemia in gerbils (35).

5.3.2 Perfusion-weighted Imaging

Perfusion deficits due to vascular occlusion are measurable using dynamic contrast-enhanced MRI, described in the latter part of Chapter 1. Several hemodynamic parameters may be measured, such as VTT, rCBV, and CBF_i. Similar to DWI, quantitative assessment of these metrics with perfusion-weighted MRI should help assess the role of collateral circulation in maintaining viability within ischemic tissue. Clinical studies have shown good correlation between reduced rCBV and acute infarcts (36), with a heterogeneous distribution of rCBV values across the lesion (37). Higher rCBV values on the periphery of lesions may indicate less severe damage. Schlaug *et al.* identified a reduction in rCBV (47% of normal) and CBF_i (37% of normal) for the penumbral region, with more severe reductions for the core (19% of normal for rCBV, 12% of normal for CBF_i). These regions with somewhat reduced rCBV or CBF_i and normal to moderately reduced ADCs, termed the “diffusion-perfusion mismatch”, may indicate a treatable area.

Reversible versus Irreversible Damage

Experimental animal studies have investigated changes in this mismatch region using concurrent DWI and PWI, as well as standard T₂-weighted imaging. Carano and coworkers (38,39) reported the delineation between normal and abnormal tissue, as well as penumbra and core, using a multidimensional feature space (ADC, CBF, T₂, and M₀) and cluster analysis. Diffusion and perfusion heterogeneity within the lesion indicates that regions with severely reduced ADCs and CBFs denote the core, whereas regions with normal to moderately reduced ADCs and somewhat reduced CBF denote the

penumbra. Subsequent clinical studies, in defining the diffusion-perfusion mismatch, have used this region as a guideline for therapeutic intervention, with moderate success (40-42). It is important to note that this mismatch is a generalization of the penumbra, and that additional parameters indicative of energy metabolism would improve the delineation between reversible and irreversible injury.

5.3.3 Metabolic Imaging

In the acute stage the diffusion-perfusion mismatch may compromise tissue at both high and low risk. Metabolic imaging offers a method for tracking changes in energy metabolism following ischemia—ATP depletion, tissue acidosis, and increased pH. Concurrent monitoring of these parameters with DWI and PWI should aid in delineating the fraction of mismatch tissue at high risk. Takegami *et al.* (43) observed a region with increased lactate and normal ADC on the periphery of ischemia 20 minutes after MCAO. This region progressed to infarct without treatment. Additional studies (44,45) showed a gradient of cellular metabolic injury; one region with increased lactate in line with the diffusion-perfusion mismatch, a second oligemic region with no change in lactate (both having relatively normal ADC/NAA levels). Since acute lesions may reverse transiently or permanently, or potentially progress to infarct, multiparametric prediction maps are imperative. By combining DWI, PWI, and lactate/NAA imaging, the pathophysiological complexity of ischemia may be elucidated.

References

1. Le Bihan D, Breton E, Lallemand D, Grenier P, Cabanis E, Laval-Jeantet M. MR imaging of intravoxel incoherent motions: application to diffusion and perfusion in neurologic disorders. *Radiology* 1986;161:401-407.
2. Moseley ME, Kucharczyk J, Mintorovitch J, Cohen Y, Kurhanewicz J, Derugin N, Asgari H, Norman D. Diffusion-weighted MR imaging of acute stroke: correlation with T2-weighted and magnetic susceptibility-enhanced MR imaging in cats. *Am J Neuroradiol* 1990;11:423-429.
3. Moseley ME, Cohen Y, Mintorovitch J, Chileuitt L, Shimizu H, Kucharczyk J, Wendland MF, Weinstein PR. Early detection of regional cerebral ischemia in cats: comparison of diffusion- and T2-weighted MRI and spectroscopy. *Magn Reson Med* 1990;14:330-346.
4. Branston NM, Symon L, Crockard HA, Pasztor E. Relationship between the cortical evoked potential and local cortical blood flow following acute middle cerebral artery occlusion in the baboon. *Exp Neurol* 1974;45:195-208.

5. Heiss WD, Hayakawa T, Waltz AG. Cortical neuronal function during ischaemia. Effects of occlusion of one middle cerebral artery on single-unit activity in cats. *Arch Neurol* 1976;33:813-820.
6. Astrup J, Symon L, Branston NM, Lassen NA. Cortical evoked potential and extracellular K⁺ and H⁺ at critical levels of brain ischemia. *Stroke* 1977;8:51-57.
7. Hossmann KA. Viability thresholds and the penumbra of focal ischemia. *Ann Neurol* 1994;36:557-565.
8. Mies G, Ishimaru S, Xie Y, Seo K, Hossmann KA. Ischemic thresholds of cerebral protein synthesis and energy state following middle cerebral artery occlusion in rat. *J Cereb Blood Flow Metab* 1991;11:753-761.
9. Astrup J, Symon L, Siesjo BK. Thresholds in cerebral ischemia: the ischemic penumbra. *Stroke* 1981;12:723-725.
10. Lassen NA, Fieschi C, Lenzi GL. Ischemia, penumbra, and neuronal death: comments on the therapeutic window in acute stroke with particular reference to thrombolytic therapy. *Cerebrovasc Dis* 1991;1:32-35.
11. Kaplan B, Brint S, Tanabe J, Jacewicz M, Wang XJ, Pulsinelli W. Temporal thresholds for neocortical infarction in rats subjected to reversible focal cerebral ischemia. *Stroke* 1991;22:1032-1039.
12. Pessin MS, del Zoppo GJ, Furlan AJ. Thrombolytic treatment in acute stroke: review and update of selective topics. In: Moskowitz MA, Caplan LR, editors. *Cerebrovascular diseases: nineteenth princeton stroke conference*. Boston: Butterworth-Heinemann; 1995. p 409-418.
13. Siesjo BK, Bengtsson F. Calcium fluxes, calcium antagonists and calcium related pathology in brain ischemia, hypoglycemia, and spreading depression: a unifying hypothesis. *J Cereb Blood Flow Metab* 1989;9:127-140.
14. Wahlgren NG. Cytoprotective therapy for acute ischemic stroke. In: Fisher M, editor. *Stroke therapy*. Boston: Butterworth-Heinemann; 1995. p 315-350.
15. Wong EH, Kemp JA, Priestly T, Knight AR, Woodruff GN, Iversen LL. The anticonvulsant MK-801 is a potent N-methyl-D-aspartate antagonist. *Proc Natl Acad Sci* 1986;83:7104-7108.
16. Park CK, Nehls DG, Graham DI, Teasdale GM, McCulloch J. The glutamate antagonist MK-801 reduces focal ischemic damage in the rat. *Ann Neurol* 1988;24:543-551.
17. Hatfield RH, Gill R, Brazell C. The dose-response relationship and therapeutic window for dizocilpine (MK-801) in a rat focal ischaemia model. *Eur J Pharm* 1992;216:1-7.
18. Grotta JC, Picone CM, Ostrow PT, Strong RA, Earls RM, Yao LP, Rhoades HM, Dedman JR. CGS-19755, a competitive NMDA receptor antagonist, reduces calcium-calmodulin binding and improves outcome after global cerebral ischemia. *Ann Neurol* 1990;27:612-619.
19. Swan JH, Meldrum BS. Protection by NMDA antagonists against selective cell loss following transient ischemia. *J Cereb Blood Flow Metab* 1990;10:343-351.
20. Grotta JC, Picone CM, Dedman JR, Rhoades HM, Strong RA, Earls RM, Yao LB. Neuronal protection correlates with prevention of calcium-calmodulin binding in rats. *Stroke* 1990;21:28-31.

21. Sauer D, Allegrini PR, Cosenti A, Pataki A, Amacker H, Fagg GE. Characterization of the cerebroprotective efficacy of the competitive NMDA receptor antagonist CGP40116 in a rat model of focal cerebral ischemia: an in vivo magnetic resonance study. *J Cereb Blood Flow Metab* 1993;13:595-602.
22. Massieu L, Thedinga KH, McVey M, Fagg GE. A comparative analysis of the neuroprotective properties of competitive and uncompetitive N-methyl-D-aspartate receptor antagonists in vivo: implications for the process of excitotoxic degeneration and its therapy. *Neuroscience* 1993;55:883-892.
23. Sauer D, Allegrini PR, Fagg GE. The competitive NMDA receptor antagonist CGP 40116 is a potent neuroprotectant in a rat model of focal ischemia. *J Neural Transm Suppl* 1994;43:81-89.
24. NINDS rt-PA Stroke Study Group T. Tissue plasminogen activator for acute ischemic stroke. *New Engl J Med* 1995;333:1581-1587.
25. NINDS rt-PA Stroke Study Group T. Intracerebral hemorrhage after intravenous t-PA therapy for ischemic stroke. *Stroke* 1997;28:2109-2118.
26. Liu T, Clark RK, McDonnell PC, Young PR, White RF, Barone FC, Feuerstein GZ. Tumor necrosis factor-alpha expression in ischemic neurons. *Stroke* 1994;25:1481-1488.
27. Wang X, Feuerstein GZ, Clark RK, Yue TL. Enhanced leukocyte adhesion to interleukin-1 beta stimulated vascular smooth muscle cells is mainly through intercellular adhesion molecule-1. *Cardiovasc Res* 1994;28:1808-1814.
28. del Zoppo GJ, Schmid-Schonbein GW, Mori E, Copeland BR, Chang CM. Polymorphonuclear leukocytes occlude capillaries following middle cerebral artery occlusion and reperfusion in baboons. *Stroke* 1991;22:1276-1283.
29. Bowes MP, Rothlein R, Fagan SC, Zivin JA. Monoclonal antibodies preventing leukocyte activation reduce experimental neurologic injury and enhance efficacy of thrombolytic therapy. *Neurology* 1995;45:815-819.
30. Basu A, Lazovic J, Krady JK, Mauger DT, Rothstein RP, Smith MB, Levison SW. Interleukin-1 and the interleukin-1 type 1 receptor are essential for the progressive neurodegeneration that ensues subsequent to a mild hypoxic/ischemic injury. *J Cereb Blood Flow Metab* 2005;25:17-29.
31. Lavine SD, Hofman FM, Zlokovic BV. Circulating antibody against tumor necrosis factor-alpha protects rat brain from reperfusion injury. *J Cereb Blood Flow Metab* 1998;18:52-58.
32. Warach S, Chien D, Li W, Ronthal M. Fast magnetic resonance diffusion-weighted imaging of acute human stroke. *Neurology* 1992;42:1717-1723.
33. Warach S, Gaa J, Siewert B, Wielopolski P, Edelman RR. Acute human stroke studied by whole brain echo planar diffusion weighted magnetic resonance imaging. *Ann Neurol* 1995;37:231-241.
34. Minematsu K, Li L, Sotak CH, Davis MA, Fisher M. Reversible focal ischemic injury demonstrated by diffusion-weighted magnetic resonance imaging in rats. *Stroke* 1992;23:1304-1311.
35. Busza A, Allen K, King M, vanBruggen N, Williams S, Gadian D. Diffusion-weighted imaging studies of cerebral ischemia in gerbils. *Stroke* 1992;23:1602-1612.

36. Warach S, Li W, Ronthal M, Edelman RR. Acute cerebral ischemia: evaluation with dynamic contrast-enhanced MR imaging and MR angiography. *Radiology* 1992;182:41-47.
37. Wu RH, Bruening R, Berchtenbreiter C, Weber J, Steiger HJ, Peller M, Penzkofer H, Reiser M. MRI assessment of cerebral blood volume in patients with brain infarcts. *Neuroradiology* 1998;40:496-502.
38. Carano RA, Takano K, Helmer KG, Tatlisumak T, Irie K, Petruccelli JD, Fisher M, Sotak CH. Determination of focal ischemic lesion volume in the rat brain using multispectral analysis. *J Magn Reson Med* 1998;8:1266-1278.
39. Carano RA, Li F, Irie K, Helmer KG, Silva MD, Fisher M, Sotak CH. Multispectral analysis of the temporal evolution of cerebral ischemia in the rat brain. *J Magn Reson Med* 2000;12:842-858.
40. Schlaug G, Benfield A, Baird AE, Siewart B, Lovblad KO, Parker RA, Edelman RR, Warach S. The ischemic penumbra: operationally defined by diffusion and perfusion MRI. *Neurology* 1999;53:1528-1537.
41. Jansen O, Schellinger P, Fiebach J, Hacke W, Sartor K. Early recanalisation in acute ischaemic stroke saves tissue at risk defined by MRI. *Lancet* 1999;353:2036-2037.
42. Sunshine J, Tarr RW, Lanzieri CF, Landis DMD, Selman WR, Lewin JS. Hyperacute stroke: ultrafast MR imaging to triage patients prior to therapy. *Neuroradiology* 1999;212:325-332.
43. Takegami T, Ebisu T, Bito Y, Hirata S, Yamamoto Y, Tanaka C, Mineura K. Mismatch between lactate and the apparent diffusion coefficient of water in progressive focal ischemia. *NMR in Biomed* 2001;14:5-11.
44. Igarashi H, Kwee IL, Nakada T, Katayama Y, Terashi A. ¹H magnetic resonance spectroscopic imaging of permanent focal cerebral ischemia in rat: longitudinal metabolic changes in ischemic core and rim. *Brain Res* 2001;907:208-221.
45. Nicoli F, Lefur Y, Denis B, Ranjeva JP, Confort-Gouny S, Cozzone PJ. Metabolic counterpart of decreased apparent diffusion coefficient during hyperacute ischemic stroke. *Stroke* 2003;34:e82-e87.

CHAPTER 6

VISUALIZATION OF EXPERIMENTAL CORTICAL SPREADING DEPRESSION (CSD) USING MANGANESE-ENHANCED MRI (MEMRI)

Introduction

- Pathophysiology of Cortical Spreading Depression
 - Role of CSD in Neurological Disorders
 - MRI of Experimental CSD
 - Manganese as a Paramagnetic Calcium Analog

Methods

- Animal Preparation
 - MnCl₂ Administration
 - Neuronal Activation via Glutamate
 - Experimental Cortical Spreading Depression
 - MRI Measurements
 - Data Analysis

Results

- MEMRI Enhanced Regions
- Quantitative Summary

Discussion

- Cellular Uptake of Manganese
- Validation of Method
- Derivation of Activation Scheme
- MEMRI Integration Effect
- Role of Apical Dendrites
- Cortical-Subcortical Neuronal Connectivity
- MEMRI or DWI?

Visualization of Cortical Spreading Depression Using Manganese-Enhanced MRI

Erica C. Henning¹, Xiangjun Meng³, Marc Fisher^{3,4}, Christopher H. Sotak^{1,2,4}

Departments of Biomedical Engineering¹ and Chemistry & Biochemistry²

Worcester Polytechnic Institute

Worcester, Massachusetts 01609

Department of Neurology³

University of Massachusetts Memorial Healthcare – Memorial Campus

Worcester, Massachusetts 01605

Department of Radiology⁴

University of Massachusetts Medical School

Worcester, Massachusetts 01655

Part of this work was presented at the 12th annual meeting of the International Society of Magnetic Resonance in Medicine, Kyoto, Japan, 2004.

The majority of this work is published in: *Magn Reson Med* 2005;53:851-857.

Abstract

Cortical spreading depression (CSD) was visualized using manganese-enhanced MRI (MEMRI) following topical application of KCl to the exposed rat cortex. MEMRI signal increase in the ipsilateral cortex relative to the contralateral control region was $60\% \pm 30\%$ following two KCl applications. MEMRI signal increase for a single (40%) versus double (80%) KCl application suggests an integration effect over successive CSD episodes. CSD-induced MEMRI enhancement involved cortical layers containing dense regions of apical dendrites, supporting the contention that these neuronal structures are necessary for propagation of CSDs. Sub-cortical enhancement was present in hippocampal and thalamic regions, most likely a result of neuronal connections with cortical layers 4 and 5. These results are consistent with previous studies of CSD using diffusion-weighted MRI and T_2^* -weighted MRI and should be useful for investigating CSD itself and its role in other neurological disorders.

Keywords: manganese-enhanced MRI, spreading depression, rat brain

6.1 Introduction

The long hypothesized contribution of cortical spreading depression (CSD) to the pathophysiology of neurological disorders such as stroke, head trauma, epilepsy, hypoglycemia, and subarachnoid hemorrhage make it a potential therapeutic target. This chapter will address application of a recently developed MRI method, manganese-enhanced MRI, for the visualization of experimental CSD. The utility of MEMRI for investigating the role of CSDs in the aforementioned conditions will be discussed briefly. The role of peri-infarct depolarizations, similar to CSDs, in the temporal evolution of cerebral ischemia will be covered in Chapter 7, using the methodology developed here.

6.1.1 Pathophysiology of Cortical Spreading Depression

Cortical spreading depression (CSD), a pathophysiological phenomenon of the central nervous system first described by Leao (1,2), is characterized by a spontaneous and reversible depression of electrical activity that spreads from the site of onset as a radial wave across the cortex with a speed of 2 to 5 mm/min. Experimental induction of CSD relies on methods that increase the extracellular K^+ concentration ($[K^+]_o$), leading to depolarization of adjacent presynaptic terminals, neurotransmitter release, and local failure of ion homeostasis (3). The radial wave of depressed cortical electrical activity leads to depolarization of the cellular membrane, causing an abrupt negative shift in direct-current (DC) potential on the order of -5 to -15 mV, followed immediately by a smaller but more prolonged positive phase (4). For the duration of the negative potential shift (approximately one minute), a large increase in $[K^+]_o$ is accompanied by a drop in $[Cl^-]_o$, $[Na^+]_o$, and $[Ca^{2+}]_o$, suggesting that K^+ leaving cells is exchanged against Na^+ and Ca^{2+} that are entering (5). The increase in $[K^+]_o$ to levels of 10 to 60 mmol/L is sufficient to depolarize adjacent neurons in the path of the CSD wave, permitting its continued propagation. Concomitant with the movement of Na^+ and Cl^- into the cell, there is an influx of water, subsequent cellular swelling, and a reduction in extracellular space by 50% (6,7). These transient cellular changes are accompanied by increased cortical perfusion and decreased tissue pO_2 , accounting for the local increase in oxygen consumption required to restore membrane ion gradients (8). Upon passage of the CSD wave, cortical electrical activity renormalizes over the course of several minutes,

permitting additional episodes of CSD following an approximate 3-minute refractory period.

6.1.2 Role of CSD in Neurological Disorders

CSD is of interest because of its contribution to the pathophysiology of stroke, head trauma, epilepsy, hypoglycemia, and subarachnoid hemorrhage (3). Unfortunately, the comprehensive evaluation of CSD in human subjects has not been done, largely in consideration of the challenges involved and the lack of appropriate measuring techniques. The majority of studies investigating the role of CSDs in these conditions have been in animal models, specifically lissencephalic species (mouse, rat, rabbit), versus that of gyrencephalic species (cat, monkey) (5). CSD, which can be elicited by direct chemical, mechanical, or electrical stimulation to the cortex, is produced more readily in lissencephalic species, and, although gyrencephalic species are relatively resistant to CSD propagation, they are by no means immune. Further investigation of the dynamic physiologic changes of CSD could aid in understanding the underlying mechanisms of the aforementioned conditions.

6.1.3 MRI of Experimental CSD

Macroscopic Characterization of CSD

Past studies have used MRI as a non-invasive tool for the characterization of CSD. Gardner-Medwin *et al.* (9) demonstrated the identification of experimentally-induced CSD in a rat model using T_2^* -weighted MRI. The authors suggested that the observed increase in signal intensity (~10%) was a result of sensitivity to alterations in the oxygenation state of hemoglobin within the local cerebral vasculature (10). CSD causes a local increase in cerebral blood flow and tissue oxygenation, yielding increased signal in gradient-echo images (Fig. 6-1). Other studies present observations of a similar phenomenon in which experimentally-induced CSD is characterized by a transient decline in the apparent diffusion coefficient (ADC) of water (11-13). Latour *et al.* (11) characterized the temporal evolution of CSD using DWI. The authors observed a region of declined ADC (~35%) moving across the cortex with a uniform velocity of approximately 3 mm/min (Fig. 6-2). The authors hypothesized that the induced depolarizations of the cellular membrane, resulting in cellular swelling and a decrease in

the extracellular volume fraction, account for the transient decrease in ADC. In line with this study, Busch *et al.* (12) demonstrated the simultaneous recording of EEG, DC potential, and the temporal evolution of CSD using DWI. Their results coincide with those of Latour *et al.* (11), but allow a method of obtaining electrophysiological recordings in the magnet during CSD imaging. For a better understanding of the temporal relation between cell membrane depolarizations and the accompanying hemodynamic response, de Crespigny *et al.* (13) assessed both during CSD using T_2^* -weighted MRI and DWI. The authors found that the transient regional hyperperfusion following the ADC decrease was delayed, suggesting that the perfusion increase is a consequence of elevated ATP requirements for cellular repolarization.

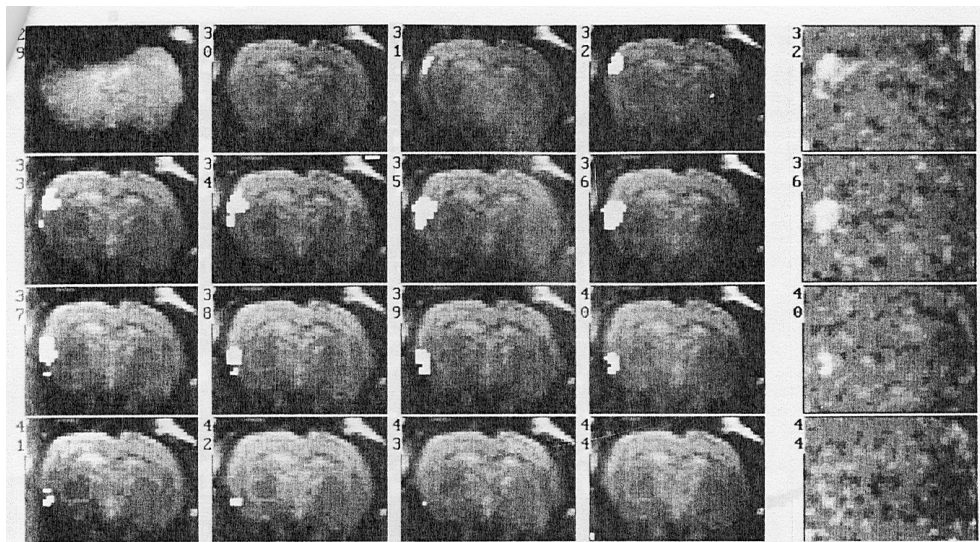


Figure 6-1. Distribution of zones of increased MR signal intensity in successive images (at 12.2-s intervals) following induction of spreading depression. White zones indicate areas with a minimum 5.5% signal increase relative to baseline. A single raw gradient echo image (29) is shown in the top left panel. Regions above the threshold are shown in the remaining images (30-44), superimposed on spin echo anatomical images. Subtraction maps for images 32, 36, 40, and 44 versus baseline are shown in the right-hand column. After application of 3M KCl, a hyperintense region (from decreased T_2^*), approximately 2 mm in size, is clearly visible moving away from the application site to the lower cortex. Figure reproduced from reference (9).

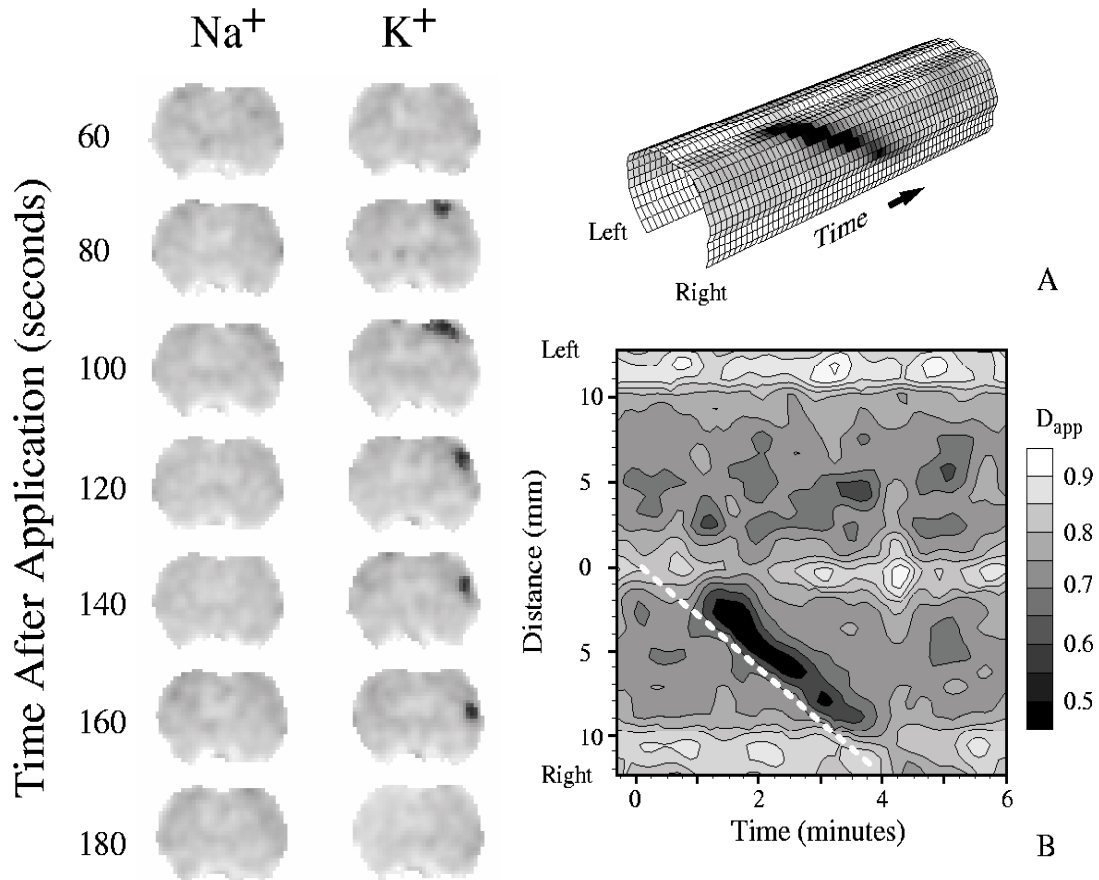


Figure 6-2. Left: Water apparent diffusion coefficient (ADC) maps of a single MRI slice through the rat brain exposed to physiological saline (NaCl) (left) or 3M KCl (right). The gray-scale intensity is proportional to the water ADC and a nonlinear mapping, such that ADC values below $0.55 \times 10^{-5} \text{ cm}^2\text{s}^{-1}$ appear nearly black, was used to exaggerate the affected region. The ADC maps acquired after NaCl application are unchanged, indicative of normal rat brain. After application of 3M KCl, a region of decreased water ADC, approximately 2 mm in size, is clearly visible moving away from the application site to the lower cortex. Right: A 3D intensity plot (top right) for the 30 cortical ROIs, with the corresponding 2D contour plot (bottom right). The slope of the trajectory, indicated by the dashed white line, provides an estimate of the propagation speed ($\sim 3 \text{ mm/min}$). Figure reproduced from reference (11).

Limitations of Real-Time Imaging

Although T_2^* -weighted MRI and DWI have been used to investigate CSD, these studies have limited their spatial resolution and signal-to-noise ratios in order to achieve a reasonable temporal resolution for monitoring the transient changes in ADC and T_2^* concomitant with CSD propagation. T_2^* -weighted MRI also suffers from susceptibility-induced artifacts from the interface between tissue boundaries, degrading image quality. Since DWI and T_2^* methods are based on macroscopic physiological changes (cell swelling and regional blood flow, respectively), they are limited in their ability to characterize the spatial extent of CSD. An MRI method with a higher signal-to-noise ratio for whole-brain imaging of CSD, based on more microscopic physiological changes, would be helpful in order to overcome these limitations.

6.1.4 Manganese as a Paramagnetic Calcium Analog*Manganese and Neuronal Activation*

Recent studies have reported the use of manganese ions (Mn^{2+}) as a membrane-depolarization-dependent contrast agent for monitoring neuronal activation following the application of glutamate (14,15), as well as in the study of focal ischemia (16). Mn^{2+} competitively enters cells through Ca^{2+} -influx pathways such as voltage-gated Ca^{2+} channels (17,18). Lin and Koretsky (14) first demonstrated the utility of paramagnetic Mn^{2+} in monitoring regional brain function using T_1 -weighted MRI. The presence of extracellular Mn^{2+} during neuronal depolarization elicits Mn^{2+} influx through Ca^{2+} channels (Fig. 6-3). Upon repolarization, Ca^{2+} channels close resulting in the ‘permanent’ intracellular uptake of Mn^{2+} . Since Mn^{2+} remains sequestered in previously activated regions, it allows for ‘snapshot’ imaging of brain activation patterns in functional task paradigms performed outside the magnet (14).

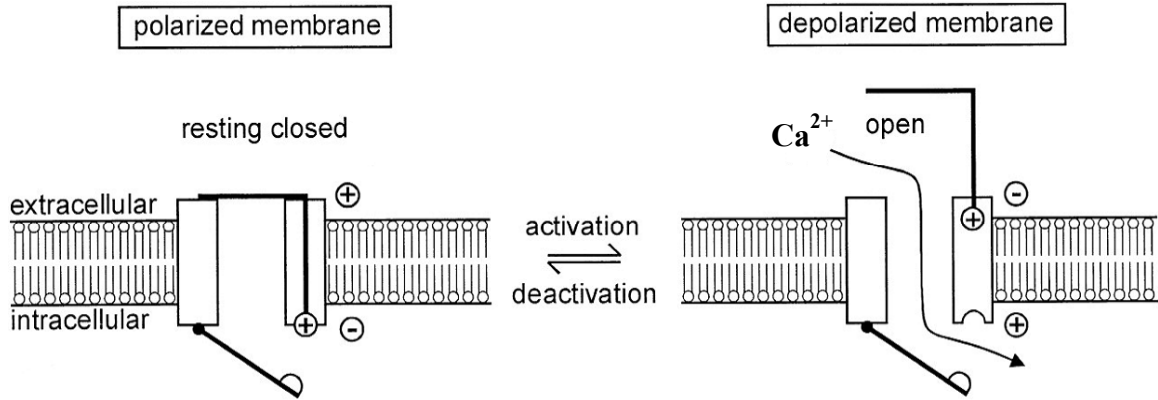


Figure 6-3. Schematic of a voltage-gated Ca^{2+} channel. Following membrane depolarization, both gates open and Ca^{2+} may be exchanged between the intracellular and extracellular spaces. With repolarization, Ca^{2+} channels close resulting in the 'permanent' intracellular uptake of Mn^{2+} .

Manganese and Cortical Spreading Depression

Extracellular accumulation of K^+ , like glutamate, is believed to play a central role in the propagation of CSDs. Whether pathophysiologically or experimentally induced, local increases in $[\text{K}^+]_o$ lead to the depolarization of presynaptic terminals and the opening of Ca^{2+} channels. Mirroring the rise in $[\text{K}^+]_o$, $[\text{Ca}^{2+}]_o$ declines from its normal level of 1.2-1.5 mM to less than 0.3 mM, indicating a Ca^{2+} shift to the intracellular compartment during CSD. Since Mn^{2+} is transported into the cell in a manner similar to Ca^{2+} , it should be possible to use Mn^{2+} to track the spatial distribution of CSD using manganese-enhanced MRI (MEMRI). The purpose of this feasibility study is to demonstrate the utility of Mn^{2+} as a paramagnetic Ca^{2+} analog in the visualization of CSD in the rat brain. MEMRI should be useful for investigating CSD itself as well as its role in the pathophysiology of other neurological disorders.

6.2 Methods

6.2.1 Animal Preparation

The present study was approved by the Institute Animal Care and Use Committee (IACUC) of the University of Massachusetts Medical School (IACUC protocol A-875). Male Sprague-Dawley rats (300-360 g; Taconic Farms, Germantown, NY) were divided into three groups: saline control (N = 4), glutamate (N = 2), and experimental CSD (N = 5). Rats were initially anesthetized with an intraperitoneal injection of chloral hydrate (400 mg/kg). Polyethylene catheters (PE-50, Becton Dickinson, San Jose, CA) were placed in the left femoral vein (i.v.) and the right external carotid artery (ECA) for drug administration. For catheterization of the right ECA, a ventral midline incision was made in the neck. The omohyoid muscle was separated longitudinally and retracted laterally to isolate and expose the right ECA. Following ligation of the vessel, a small incision was made into which the catheter was inserted and secured in place. Cannulation of the right ECA limited drug delivery to the right side of the brain, enabling the left side to serve as a control. The common carotid artery (CCA) was kept intact and open in order to maintain blood flow to regions originally supplied by the right ECA (i.e., face and underlying muscle). Rectal temperature was monitored continuously with a rectal probe and maintained at 37.0°C using a thermostatically-controlled heating lamp (Model 73ATD, YSI Inc., Yellow Spring, OH) during preparation.

6.2.2 MnCl₂ Administration

Physiologically-buffered saline containing 74.5 mM manganese chloride (MnCl₂ • 4H₂O; Sigma, St. Louis, MO) was infused through the left femoral vein at a rate of 3.97 μmol/min (3.2 ml/hr) using a syringe pump (Model 11; Harvard Apparatus, Holliston, MA) for 32 min. The total volume of infused MnCl₂ solution was 1.71 ml (127 μmol). To open the blood-brain barrier (BBB), 25% D-mannitol solution (5 mg/kg; Sigma, St. Louis, MO) was bolus-injected via the right ECA 10 min after the start of the MnCl₂ infusion.

6.2.3 Glutamate Administration

A glutamate administration group (N = 2) was evaluated to validate our use of the MEMRI method previously developed by Aoki *et al* (15), a modification of the original by Lin and Koretsky (14). A solution of L-glutamic acid (0.2 ml of 10 mg/ml; Sigma, St. Louis, MO) was bolus-injected via the right ECA 22 min after the start of the MnCl₂ infusion (Fig. 6-4a). For the corresponding controls (N = 2), physiologically buffered saline (0.2 ml) was injected through the right ECA in place of the glutamate.

6.2.4 Experimental Cortical Spreading Depression

Animal Preparation

For the experimental CSD group (N = 5), rats were mounted prone on a homemade stereotaxic surgical board with a head holder and tooth bar. The frontoparietal cranium was exposed by a midsagittal incision, and a burr hole, 2.0 mm in diameter, was made in the right parietooccipital cortex, 1 mm posterior and 1.5 mm lateral of bregma. Following careful excision of the dura using a 23-gauge needle, two syringes were prepared for cortical application of 4M KCl or 0.9% (w/v) NaCl, respectively.

Single versus Double KCl Applications

In order to evaluate the effects of single versus multiple applications of KCl on CSD-induced MEMRI enhancement, animals were subdivided into two groups: a single 4M KCl application (N = 1) and two 4M KCl applications (N = 4). For the single 4M KCl application, 22 min after the start of MnCl₂ infusion, a 20µl volume of KCl solution was administered over the course of 3 min followed by a saline wash (Fig. 6-4b). For two 4M KCl applications, a 40µl volume of KCl solution was administered in the following manner, 22 min after the start of MnCl₂ infusion: 3-min 4M KCl exposure, saline wash → 3-min waiting period → 3-min 4M KCl exposure, saline wash (Fig. 6-4c). For the corresponding controls (N = 2), 40µl of 0.9% (w/v) NaCl was applied to the exposed cortex in place of the 4M KCl.

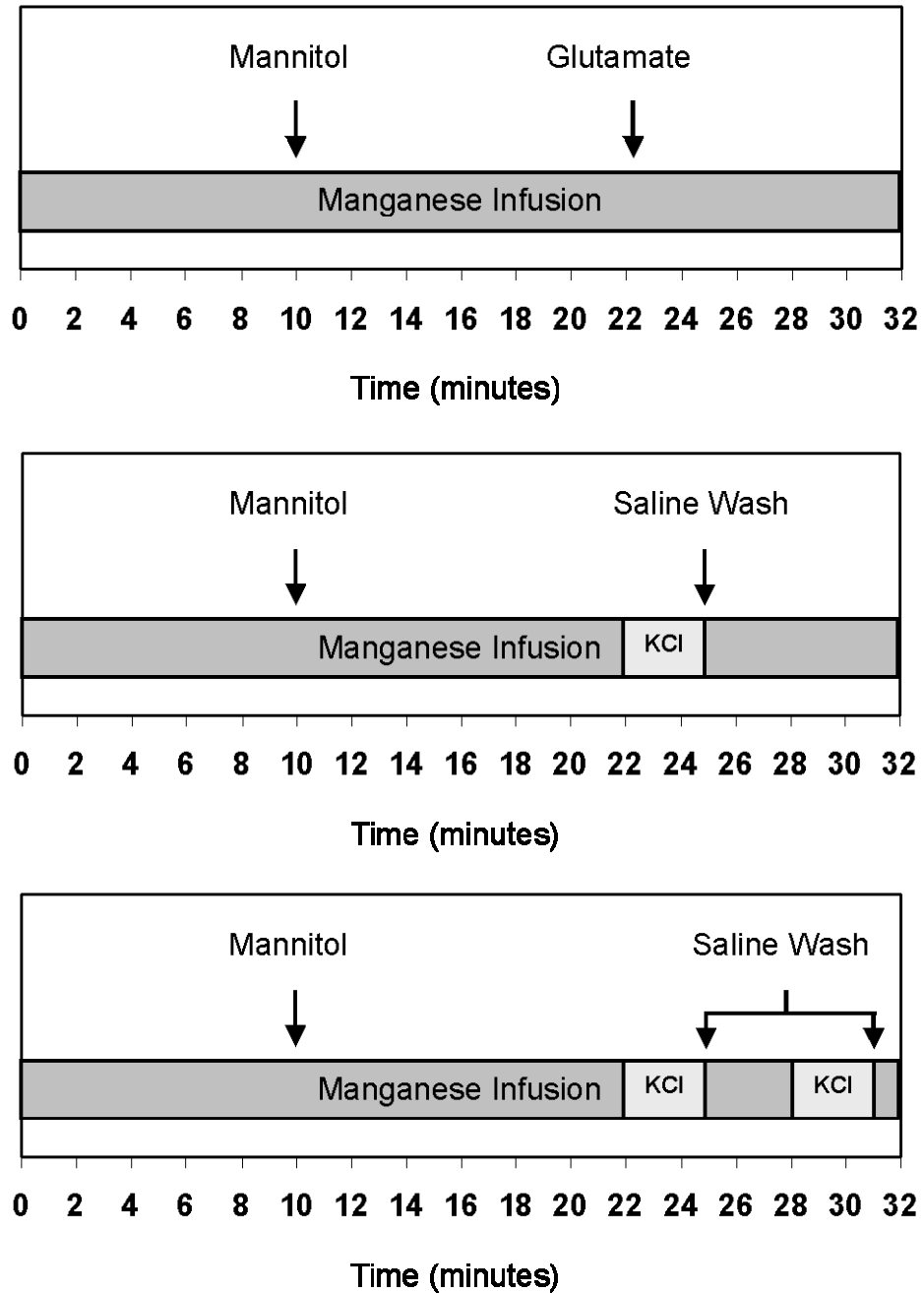


Figure 6-4. Timing of Drug Administration for Glutamate (a), Experimental CSD with one KCl application (b), and Experimental CSD with two KCl applications (c). The time points for starting the $MnCl_2$ infusion, mannitol injection, glutamate injection, KCl applications, and saline washes are indicated by the labeled arrows. For the corresponding controls, physiologically-buffered saline (NaCl) was applied in place of the glutamate or KCl.

6.2.5 MRI Measurements

Data Acquisition and Parameter Setup

MR experiments were performed with a Bruker Biospin 2.0T/45cm imaging spectrometer equipped with ± 20 G/cm self-shielded gradients (Fig. 3-5). T₁-weighted imaging was performed using the following acquisition parameters: TR/TE = 300.0/12.0 ms, FOV = 4 cm \times 4 cm, matrix size = 256 \times 256. The imaging plane was referenced to the rhinal fissure at the boundary of the olfactory bulb. For the glutamate administration group and controls, six 3-mm slices were acquired with NEX = 2. For the experimental CSD group and controls, eight 2-mm slices were acquired with NEX = 4. The total experiment times were 2.6 min and 5.2 min for the glutamate and experimental CSD experiments, respectively.

Imaging Setup and Physiological Monitoring

During imaging, animals were placed supine in a home-built animal holder (Fig. 6-5a). The head of the animal was fixed inside a 2.0 cm \times 3.5 cm rectangular ¹H surface coil shaped to conform to the curvature of the skull (Fig. 6-5b). Animals were anesthetized with 1.0% isoflurane delivered at 1.0 L/min in breathing-quality air (Fig. 6-5c). Body temperature was maintained at $37.0 \pm 1.0^\circ\text{C}$ by circulated warm air using a T-type thermocouple and a double-point feedback control system (Fig. 6-5d).

6.2.6 Data Analysis

Image analysis, image reconstruction and region of interest (ROI) calculations were performed using Paravision's Image Processing and Display Software (Xtip). The spatial extent of MEMRI-enhanced regions (cortical, sub-cortical) were determined by correlation to a standard rat brain atlas (19) based on the slice location in terms of distance from bregma. ROIs were user-defined to delineate between MEMRI-enhanced cortical regions and normal tissue. Percent signal increase was calculated through comparison of the ipsilateral cortex to the equivalent contralateral control region on a slice-by-slice basis:

$$\text{Signal Increase (\%)} = \frac{\text{SI}_{\text{IC}} - \text{SI}_{\text{CC}}}{\text{SI}_{\text{CC}}} \times 100 \quad (6-1)$$

where SI_{IC} is the signal intensity for the ROI in the ipsilateral cortex and SI_{CC} is the signal

intensity for the ROI in the contralateral cortex. Data are presented as mean \pm standard deviation (SD), with a separate term for the inter-slice signal variability (IS-SD).

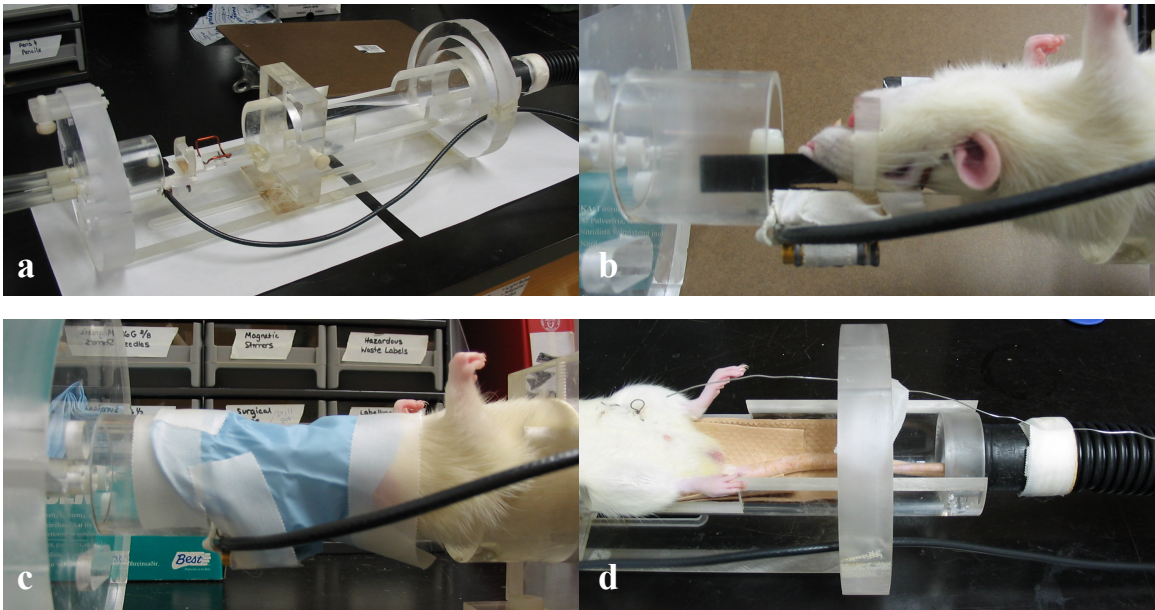


Figure 6-5. Home-built animal holder for rat brain imaging studies. (a) Angled view. The holder is dual-fitted with PVC tubing for delivery and removal of anesthetic, a cradle equipped with nose holder and tooth bar, a 2.0 cm \times 3.5 cm rectangular curved surface coil for ^1H imaging, and a heat tube for maintenance of body temperature using a T-type thermocouple. (b) Side view. The animal is placed supine in the holder such that the surface coil conforms to the curvature of the skull. The nose holder and tooth bar maintain positioning of the animal's head during imaging. (c) Anesthetic Delivery. Anesthetic is delivered to the animal via the PVC tubing in 1.0L/min breathing quality air. A glove is used to restrict delivery of anesthetic to the animal's face. (d) Temperature Maintenance. Body temperature is maintained at $37.0 \pm 1.0^\circ\text{C}$ by circulated warm air using a T-type thermocouple and a double-point feedback control system.

6.3 Results

6.3.1 MEMRI Enhanced Regions

Regional Coverage of Cortical and Ventricular Enhancement

Fig. 6-6 shows the multi-slice T₁-weighted MEMRI for the glutamate group, experimental CSD group, and the corresponding controls at a single time-point 1.5 hours after the start of MnCl₂ infusion. Fig. 6-6a shows the signal enhancement from T₁-weighted MEMRI following neuronal activation via glutamate administration. The average percentage increase in cortical signal intensity was 29% ± 3%, with a similar increase seen in the ventricles. Cortical enhancement was visible across five of the six imaging slices, resulting in approximately 15 mm of coverage (4.5 mm anterior to 10.5 mm posterior of bregma). Fig. 6-6c shows the signal enhancement from T₁-weighted MEMRI of experimental CSD following two applications of 4M KCl. The region of MEMRI enhancement was confined to a 0.6-1.2-mm-thick cortical layer, appearing as a hyperintense streak extending radially from the CSD induction site (solid arrows). The average percentage increase in cortical signal intensity was 60% ± 30%. Cortical enhancement was visible across six of the eight imaging slices, resulting in approximately 12 mm of coverage (2.5 mm anterior to 9.5 mm posterior of bregma).

Regional Coverage of Subcortical Enhancement

In a few of the slices (Fig. 6-6b, open arrows), sub-cortical enhancement was present that did not match with the regional ventricular enhancement of the NaCl control (3.5 mm to 9.5 mm posterior of bregma). Areas of sub-cortical enhancement included hippocampal regions CA1-3, subiculum, and dentate gyrus, as well as the thalamic nucleus, superior and inferior colliculi, and geniculate nucleus. No significant changes in cortical signal intensity were detected for the saline controls (Figs. 6-6b and 6-6d), but the same degree of ventricular enhancement was present.

Comparison of Single versus Double KCl Applications

Fig. 6-7 illustrates the effect of single versus multiple applications of KCl on CSD-induced MEMRI enhancement. Three representative axial images are shown for each animal (solid arrows indicate the image located coincident with the KCl application site). Fig. 6-7a shows the signal enhancement from T₁-weighted MEMRI following a single

application of 4M KCl. The average percentage increase in cortical signal intensity was 40% for this particular animal. Fig. 6-7b shows the signal enhancement from T₁-weighted MEMRI following two applications of 4M KCl. The average percentage increase in cortical signal intensity was 80% for this particular animal ($60\% \pm 30\%$ for N = 4); double that of the single 4M KCl application. Both animals had similar levels of ventricular enhancement.

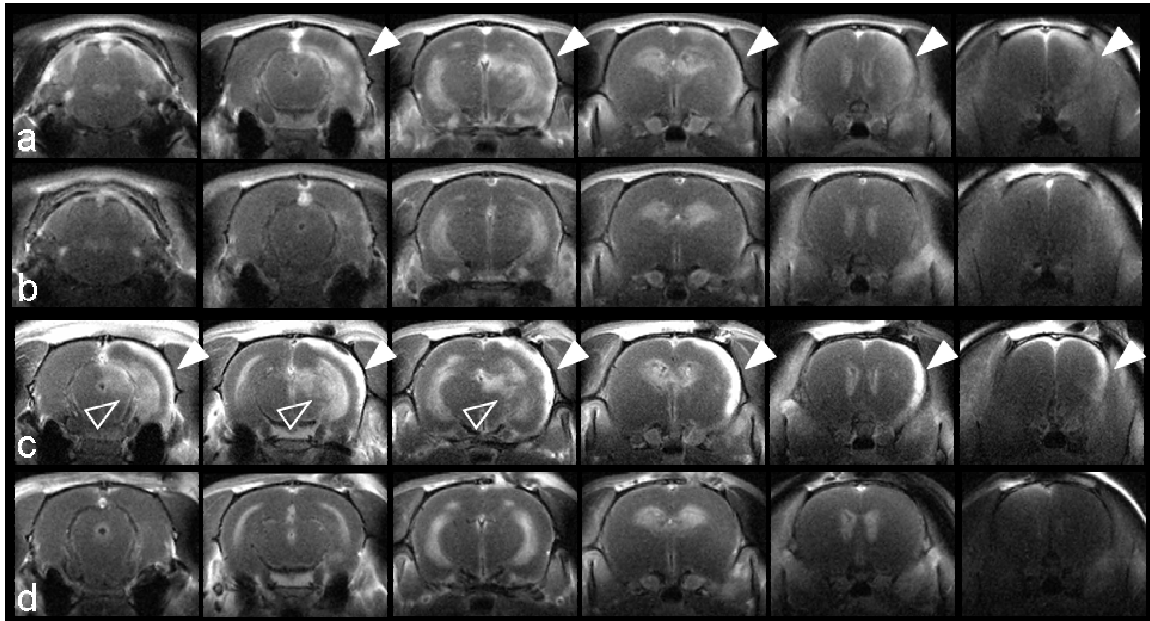


Figure 6-6. T₁-weighted MEMRI following glutamate administration and experimental CSD. a) Neuronal activation following glutamate administration. Glutamate administration results in heterogeneous cortical enhancement ($29\% \pm 3\%$ signal increase) in five out of six images (solid arrows). Slice thickness = 3 mm. b) Saline control for glutamate experiments. c) Cortical signal enhancement following two 4M KCl applications. Two 4M KCl applications result in a thin layer of cortical enhancement ($60\% \pm 30\%$ signal increase) in six out of eight images (solid arrows). Slice thickness = 2 mm. Only images exhibiting enhancement are shown. Signal enhancement following CSD in the presence of Mn²⁺ is clearly visible in the right cortex. Regions of CSD-induced MEMRI enhancement appear as a hyperintense streak extending dorsolaterally from RSG (retrosplenial granular cortex) or FR2 (frontal cortex, area 2) to Pir (piriform cortex) or PRh (perirhinal cortex) depending on the location anterior-posterior with respect to bregma. Regions of sub-cortical enhancement (open arrows) include CA1-3 (Ammon's Horn), the subiculum, and the dentate gyrus of the hippocampus, in addition to the thalamic nucleus, superior and inferior colliculi, and geniculate nucleus. Sub-cortical enhancement is thought to be due to neuronal connections between these particular regions and the cortex. d) NaCl control for experimental CSD.

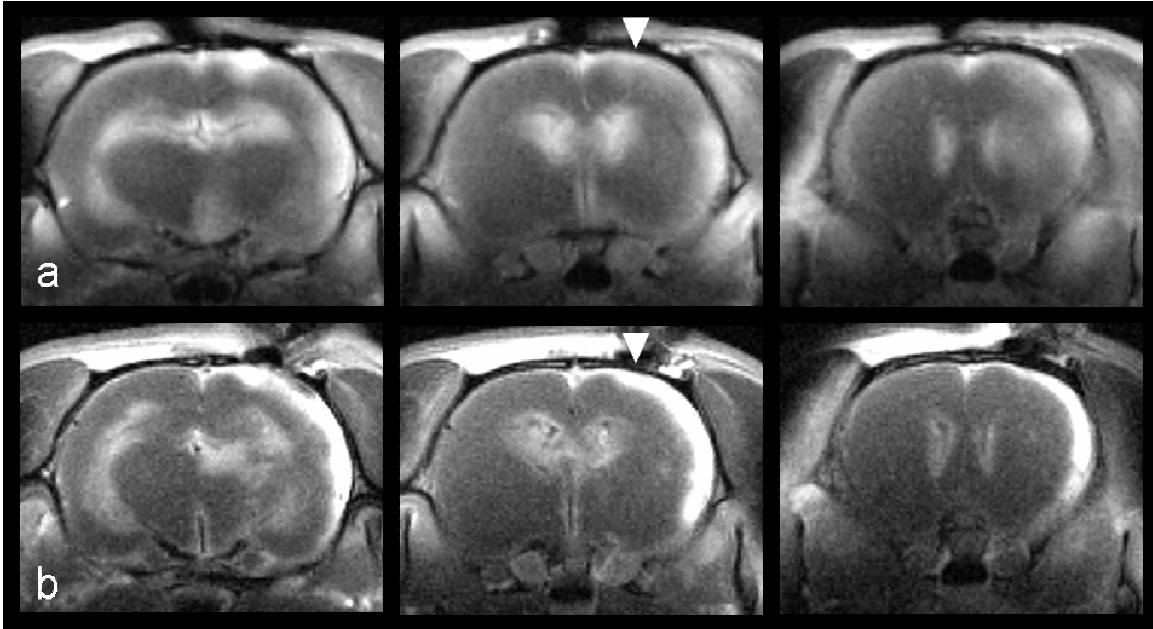


Figure 6-7. Effect of single versus double KCl applications on MEMRI appearance. a) MEMRI enhancement following a single application of 4M KCl. One KCl application results in a thin layer of cortical enhancement (40% signal increase for this particular animal). b) MEMRI enhancement following two applications of 4M KCl. Two applications of KCl induce multiple episodes of CSD, resulting in an integration of MEMRI cortical signal intensity (80% signal increase for this particular animal; $60\% \pm 30\%$ for $N = 4$). MEMRI enhancement was visible across six out of eight images for both the single and double KCl application. Representative axial images coincident with and adjacent to the KCl application site are shown. Solid arrows indicate the location of the KCl application site.

6.3.2 Quantitative Summary

Table 6-1 summarizes the average percentage signal intensity increase for different brain regions for the glutamate administration group, experimental CSD group, and the corresponding controls. In the glutamate administration group, changes in signal intensity in the ipsilateral cortex were comparable to that of the ventricles. Animals in the experimental CSD group that received two applications of 4M KCl exhibited no significant difference in percentage signal increase between the ipsilateral cortex and the ventricles ($p > 0.32$, $N = 4$). A similar trend was seen for the single application of 4M KCl. For both sets of controls, changes in cortical and ventricular signal intensity were comparable, indicating experimental reproducibility.

Table 6-1: Average Signal Increase (%) from T₁-weighted MRI for Different Brain Regions (relative to a homologous region in the contralateral hemisphere) Following Various Stimuli.

Type of Stimulus	Average Signal Increase (%) (using Eq. 6-1)			
	Cortex		Ventricles	
	Mean ± SD	ISSD ^a	Mean ± SD	ISSD ^a
Glutamate Administration (N = 2)	29 ± 3	5	21 ± 6	10
Saline Control (N = 2)	6 ± 1	4	29 ± 9	20
Experimental CSD				
Single KCl Application (N = 1)	40	20	40	20
Two KCl Applications (N = 4)	60 ± 30 [*]	20	46 ± 3	10
NaCl Control (N = 2)	20 ± 10	4	50 ± 10	20

^aTo account for intra-animal variability, the inter-slice standard deviation (ISSD) was calculated from values for the average signal increase (%) across affected slices.

^{*}MEMRI signal intensity changes in the ipsilateral cortex were not significantly different from the ventricles (P > 0.32, N = 4) in the experimental CSD group receiving two KCl applications.

6.4 Discussion

6.4.1 Cellular Uptake of Manganese

Mn²⁺ is paramagnetic and has been used for MRI tissue contrast enhancement by oral or intravenous administration of MnCl₂ or Mn complexes. Mn²⁺ mimics Ca²⁺ uptake in many biological systems and is known to enter cells through ligand- or voltage-gated Ca²⁺ channels during nerve action potentials (17). Following experimental induction of CSD, membrane depolarization facilitates opening of voltage-gated Ca²⁺ channels and a concomitant influx of Mn²⁺. Upon deactivation, channels return to their closed resting state, resulting in the entrapment of intracellular Mn²⁺. This phenomenon is supported by the observation that the specific action of verapamil, a voltage-gated Ca²⁺ channel blocker, inhibits influx of Mn²⁺ into cells (18).

6.4.2 Validation of Method

In the present work, validation of Mn^{2+} as an activation-specific contrast agent was done through glutamate administration in the presence of a compromised BBB using the methodology of Aoki *et al.* (15). For simplicity, all surgical procedures and drug administration were performed outside the magnet with image acquisition at 1.5 hours after the start of $MnCl_2$ infusion. Fig. 6-6a demonstrates that the infusion of $MnCl_2$ during glutamate activation causes cortical and ventricular contrast enhancement of similar magnitude and regional coverage when compared to previous MEMRI studies (14,15). Aoki *et al.* (15) reported a relative signal enhancement of 174% for the right hemisphere (excluding the ventricles) and 155% for the ventricles alone following glutamate administration. These results were based on the comparison of the relative signal intensities in the ipsilateral cortex measured at baseline (prior to injection of mannitol) and following glutamate administration (Fig. 6-8). If instead a comparison is drawn between the relative signal intensities of the ipsilateral cortex and the contralateral cortex following glutamate administration, the relative signal enhancement is approximately 120%. This estimated increase (20%) is consistent with the values reported in Table 1. After drawing a similar comparison between the relative signal intensities of the ventricles and the contralateral cortex, the relative signal enhancement is approximately 135%. Lin and Koretsky (14) reported a steady-state ventricular signal enhancement of 149% following infusion of $MnCl_2$. These increases (35% and 49%) are close to the changes in ventricular signal intensity seen in the experimental groups listed in Table 1.

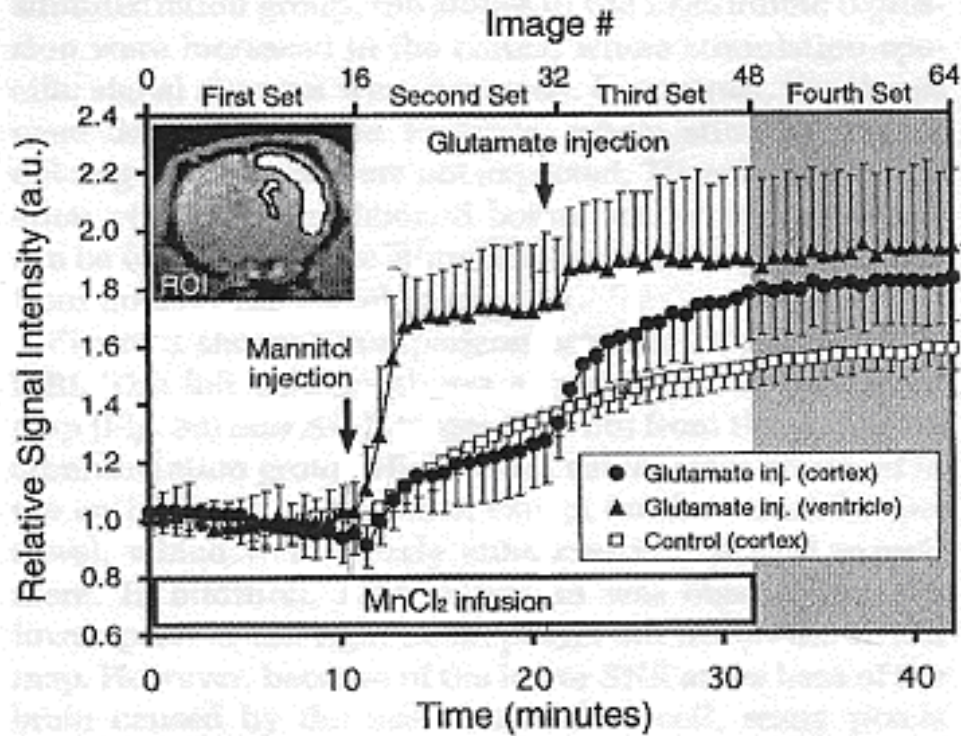


Figure 6-8. Time-course of relative signal intensities in the cortex and ventricle obtained from the glutamate administration (filled symbols) and control (open square) groups. The inset indicates typical ROIs. Timing for $MnCl_2$ infusion, mannitol injection, and glutamate injection are indicated by the labeled arrows. Figure reproduced from reference (15).

6.4.3 Derivation of Activation Scheme

For the experimental CSD group, an activation scheme with a set waiting period was devised (Fig. 6-4c) to account for the approximate 3-min refractory period between initiation of individual episodes of CSD. During the first application of 4M KCl, the local increase in $[K^+]_o$ induces depolarization of presynaptic terminals, opening of voltage-gated Ca^{2+} channels, and the intracellular accumulation of Mn^{2+} . This takes place during the negative phase of the DC-potential shift over the course of 1-2 min. Upon repolarization, the Ca^{2+} channels close resulting in the retention of Mn^{2+} inside the cell. While this repolarization occurs locally, the increase in $[K^+]_o$ is thought to depolarize adjacent neurons, allowing propagation of the CSD wave along the entire extent of the cortex. During the 3-min wait period, restoration of ion gradients occurs with normalization of spontaneous electrical activity, after which a second CSD episode may be induced. Although electrophysiological recordings were not performed, previous work employing this experimental-CSD model reported induction of a single CSD event following one 3-min KCl application (20). Based on these results, one CSD event is expected for the single 3-min KCl application and a minimum of two CSD events are expected for the double KCl application. Each CSD event results in the intracellular accumulation of Mn^{2+} . With multiple CSD events there is an integration effect where the total amount of $[Mn^{2+}]_i$ accumulated is proportional to the signal intensity in T_1 -weighted MRI. As MEMRI ‘records’ all cortical regions having undergone CSD-induced depolarizations, CSDs appear as a hyperintense streak down the cortex (Fig. 6-6c).

6.4.4 MEMRI Integration Effect

Correlation Between MEMRI Enhancement and Degree of Neuronal Activation

An MEMRI integration effect was first demonstrated following brain activation using multiple injections of glutamate (14). The authors followed the temporal evolution of T_1 -weighted MRI signal intensity changes in the cortex from rats undergoing $MnCl_2$ infusion, mannitol injection, and two injections of glutamate. They reported an average signal enhancement of 123% and 238% for prestimulation and following two glutamate injections, respectively. The time-course diagram from this work (Fig. 6-9), for a single representative rat, showed cortical signal intensities of approximately 135%, 200%, and 250% for prestimulation, following a single injection of glutamate, and following two

glutamate injections, respectively. These signal intensity changes suggest a correlation between the number of administered doses of glutamate, or the degree of glutamate-induced Mn^{2+} influx, and the MEMRI signal enhancement.

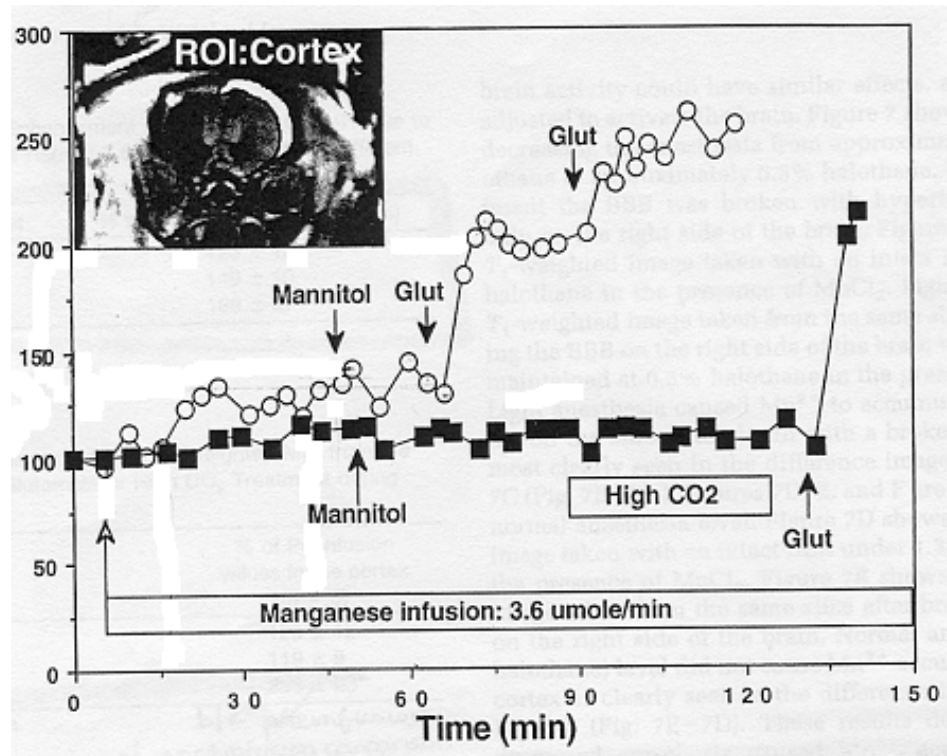


Figure 6-9. Time course of T₁-weighted MRI signal intensity changes in the cortex from two individual rats after addition of glutamate or increased CO₂ in the presence of Mn²⁺ and a broken BBB. Filled circles represent the cortical signal intensity taken from the rat undergoing mannitol and glutamate (glut) injections, and open squares represent signal intensity taken from the rat undergoing mannitol, CO₂, and glutamate (glut) injections. The timepoints for MnCl₂ infusion, mannitol injection, glutamate injection, or high CO₂ are indicated by the labeled arrows. Figure reproduced from reference (14).

Correlation Between MEMRI Enhancement and CSD-induced Manganese Influx

In order to investigate the integration effect for CSD, comparisons were made between animals receiving a single or double application of 4M KCl. Results of a single KCl application versus two KCl applications for experimental induction of CSDs support this relationship between $[Mn^{2+}]_i$ accumulation and the signal enhancement in T_1 -weighted MRI. Fig. 6-7 shows the integration effect of multiple CSD events for representative axial images located coincident with and adjacent to the KCl application site. Following a single 3-min application of 4M KCl, the average percentage increase in cortical signal intensity was 40% (Fig. 6-7a). Following two 3-min applications of 4M KCl, the average percentage increase in cortical signal intensity was 80% ($60\% \pm 30\%$ for $N = 4$) (Fig. 6-7b), double that of the single 4M KCl application. Both had comparable levels of ventricular enhancement, suggesting similar steady-state levels of Mn^{2+} in the CSF space. Although the average percentage increase in cortical signal intensity was $60\% \pm 9\%$ for $N = 4$ in the double 4M KCl application, the average percentage increase for one of the animals was 30%. That particular animal may in fact have only experienced a single CSD episode instead of two CSD episodes, resulting in an average percentage increase more comparable with the animal receiving a single 4M KCl application (40%). Further study comparing single versus multiple applications of 4M KCl in conjunction with electrophysiological measurements will be required to verify the relationship between the number of CSD episodes, $[Mn^{2+}]_i$ accumulation, and MEMRI enhancement.

6.4.5 Role of Apical Dendrites

Cortical Structure and Composition

Previous studies suggest that pyramidal cell dendrites are critical to CSD propagation (21), and that cortical layers containing proximal apical dendrites are more susceptible to CSD than those containing basilar dendrites or distal apical dendritic branches (22). The cortex itself consists of six layers, diagrammed in Fig. 6-10. Layer 1, the molecular or plexiform layer, contains Cajal-Retzius (CR) neurons which establish synaptic contacts to the apical dendritic bouquets of all pyramidal neurons regardless of size, function, location, or cortical depth (23). Layers 2 and 3 contain small, medium, and large pyramidal cells characterized by networks of vertically oriented apical dendrites

extending into layer 1, as well as basilar dendrites extending into deeper cortical layers. Layer 4, the granular layer, contains a large number of small and tightly packed pyramidal cells, whereas layer 5 contains a thin layer of small pyramidal cells with large pyramidal cells scatter throughout, which extend up into layer 1. Layers 4 and 5 have some nonpyramidal cells as well. Layer 6, the multiform layer, contains multiform and fusiform cells arranged in columns by radial fiber bundles, with a sparse population of pyramid-like cells characterized by apical dendrites.

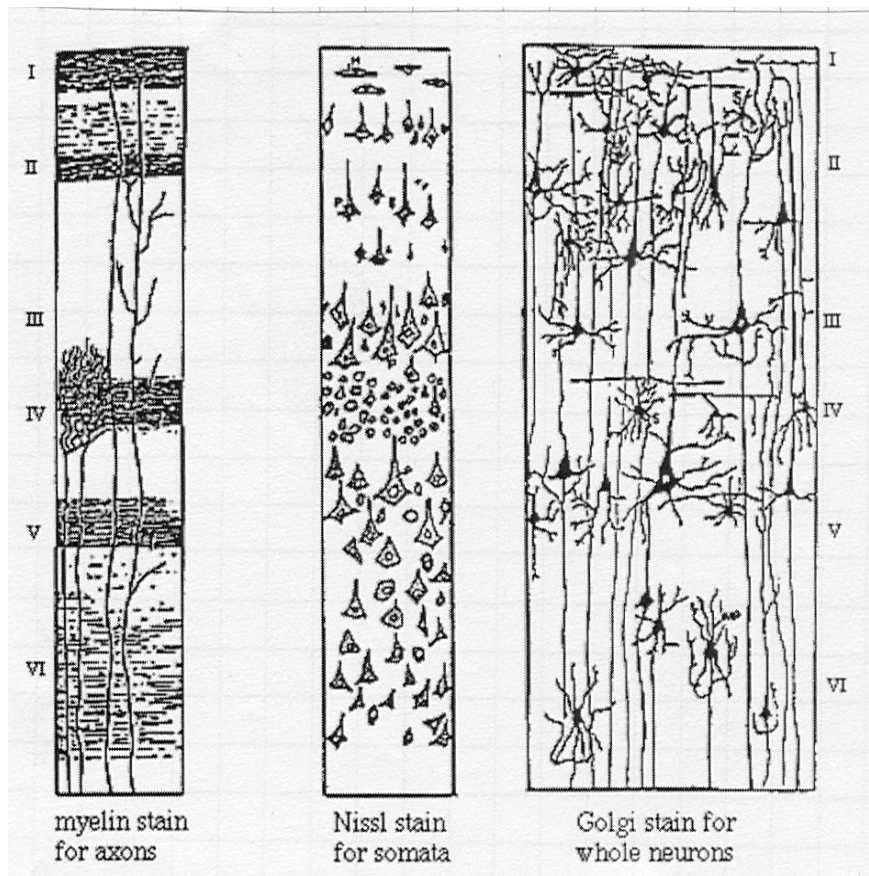


Figure 6-10. Cortical Layer Structure and Composition. The individual composition of cortical layers 1-6 is diagrammed according to a myelin stain for axons (left), Nissl stain for somata (middle), and a Golgi stain for whole neurons (right).

Layer Specific Enhancement

Cortical regions exhibiting MEMRI enhancement following experimental CSD included layers 1-5, extending dorsolaterally from RSG (retrosplenial granular cortex) or FR2 (frontal cortex, area 2) to Pir (piriform cortex) or PRh (perirhinal cortex) depending on the location anterior-posterior with respect to bregma. Layer 6 remained unaffected. Restriction of MEMRI enhancement to cortical layers 1-5 is consistent with the contention that pyramidal cell (apical) dendrites are necessary for the propagation of CSDs through individual layers of the cortex. Note that the apical dendrites in layers 2-5 are generally thick, have a dense covering of spines, and consist of pyramid-shaped cell bodies extending vertically to the pial surface. In contrast to these, the limited number of apical dendrites in layer 6 comes in two forms. The first group is thick and spiny like the apical dendrites of layer 4, but tends to develop horizontally elongated cell bodies instead of pyramid shaped ones whose axons follow curved courses with termination in layer 3 or 4 (24). The second group of apical dendrites in layer 6 are thin, moderately covered by spines, with branching limited to layer 5 before termination in layer 1 (25). These differences in apical dendritic structure for layers 2-5 versus layer 6, degree of extension within these layers and into layer 1, may account for differences in synaptic connectivity, and why layer 6 is not expected to have MEMRI enhancement.

6.4.6 Cortical-Subcortical Neuronal Connectivity

In addition to the cortical enhancement in the experimental CSD group, there was some sub-cortical enhancement visible extending well beyond the ventricular space (Fig. 6-6c, open arrows). This enhancement was different from the non-specific ventricular enhancement observed in the control (Fig. 6-6d). Regions of sub-cortical enhancement included CA1-3 (Ammon's Horn), the subiculum, and the dentate gyrus of the hippocampus, in addition to the thalamic nucleus, superior and inferior colliculi, and geniculate nucleus (Fig. 6-11a-c).

Hippocampal regions CA1-3, Subiculum, and Dentate Gyrus

Harris *et al* (26) reported on the intrinsic connectivity of the rat subiculum, specifically the apical dendritic morphology and patterns of axonal arborization. Following neurobiotin-labelling, the existence of axonal varicosities and extensions found on axons provided evidence of projection cells connecting the entorhinal cortex with CA1. Naber

et al. (27) showed the existence of direct and indirect projections from the perirhinal cortical regions to areas CA1-3 and subiculum of the hippocampus through electrical stimulation and current source density analysis. The authors noted additional projections between the postrhinal cortical region and the dentate gyrus. These connections may explain the MEMRI enhancement in hippocampal regions CA1-3, subiculum, and dentate gyrus following experimental CSD.

Thalamic Nucleus, Superior and Inferior Colliculi, and Geniculate Nucleus

Additional regions of subcortical enhancement included the thalamic nucleus, superior and inferior colliculi, and geniculate nucleus. Previous studies report connections between a high percentage of projection and pyramidal neurons in cortical layers 4 and thalamic nuclei (28,29). Levesque *et al.* (30) reported corticothalamic projections arising from cortical layers 4 and 5 following biocytin-labelling techniques. Other reports describe connections between cortical layer 5 and the superior (31) and inferior (32) colliculi, with neuronal projections extending from the superior colliculus to the geniculate nucleus (33). During CSD, signal propagation descending the pial surface along apical dendrites into cortical layers 4 and 5, and then through the various connections described, may explain the thalamic, superior/inferior collicular, and geniculate nuclear enhancement seen in the MEMRI images.

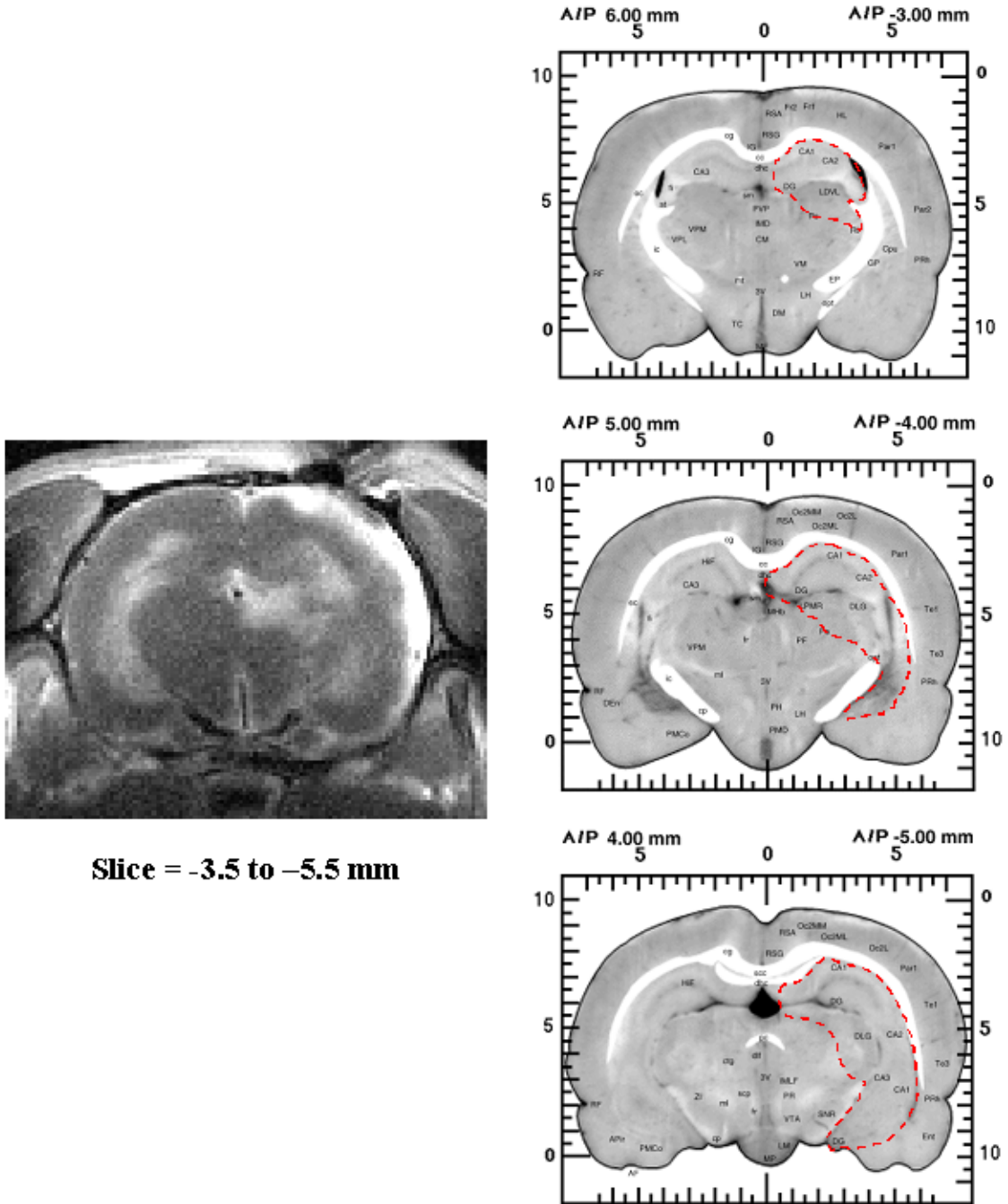


Figure 6-11a. MEMRI Subcortical Enhancement. The T₁-weighted image for slice location -3.5 mm to -5.5 mm from bregma is shown in the left-hand column. The corresponding anatomical maps for -3 mm, -4 mm, and -5 mm from bregma are shown in the right-hand column. Regions of subcortical enhancement (outlined in red) include: hippocampal regions CA1-3, subiculum (S), dentate gyrus (DG), geniculate nucleus (DLG), and thalamic nucleus (LDVL, LMPR). Rat atlas images in the right-hand column were reproduced from the Laboratory of NeuroImaging, UCLA <http://www.loni.ucla.edu/Research/Atlases/RatAtlas.html>.

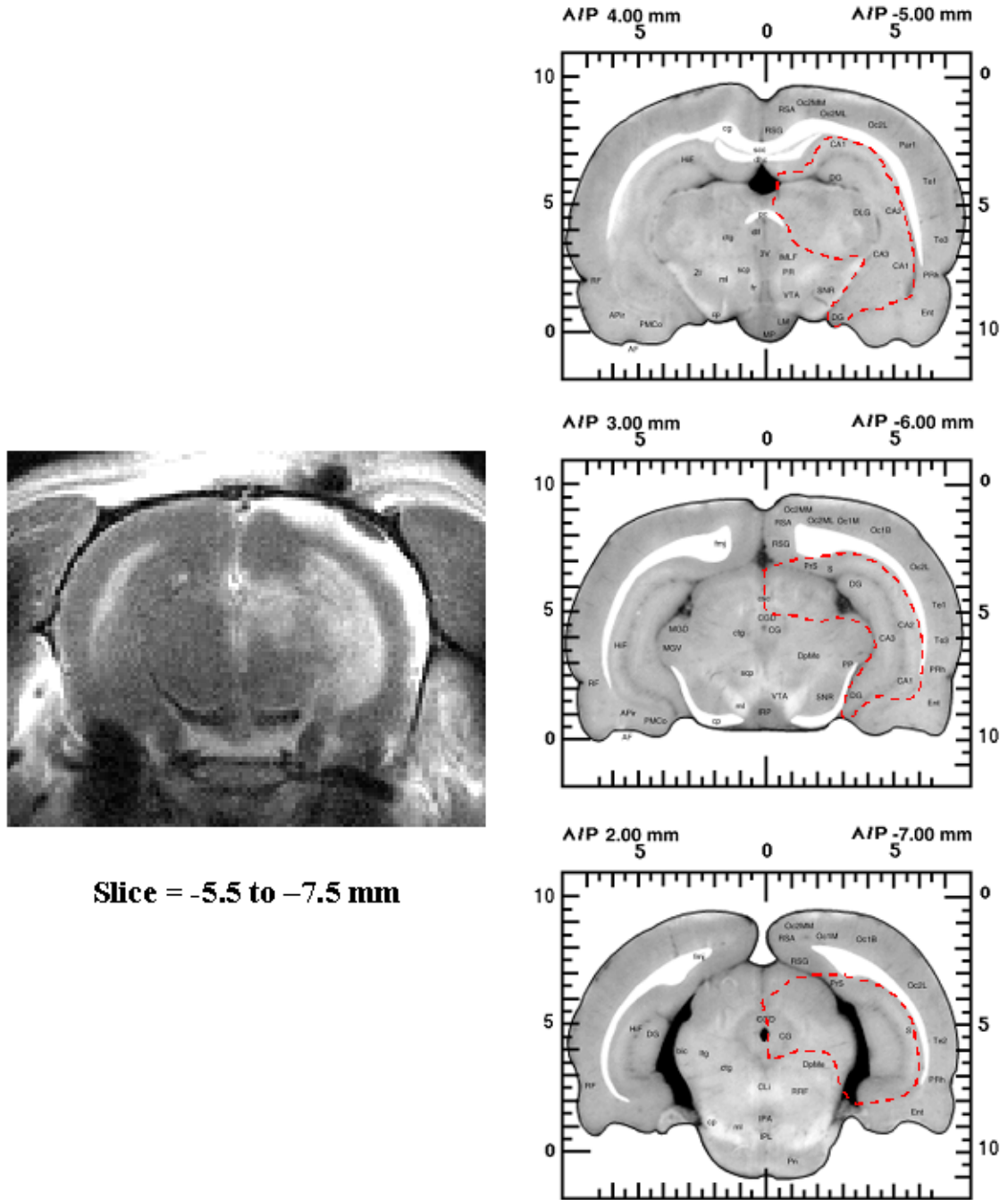
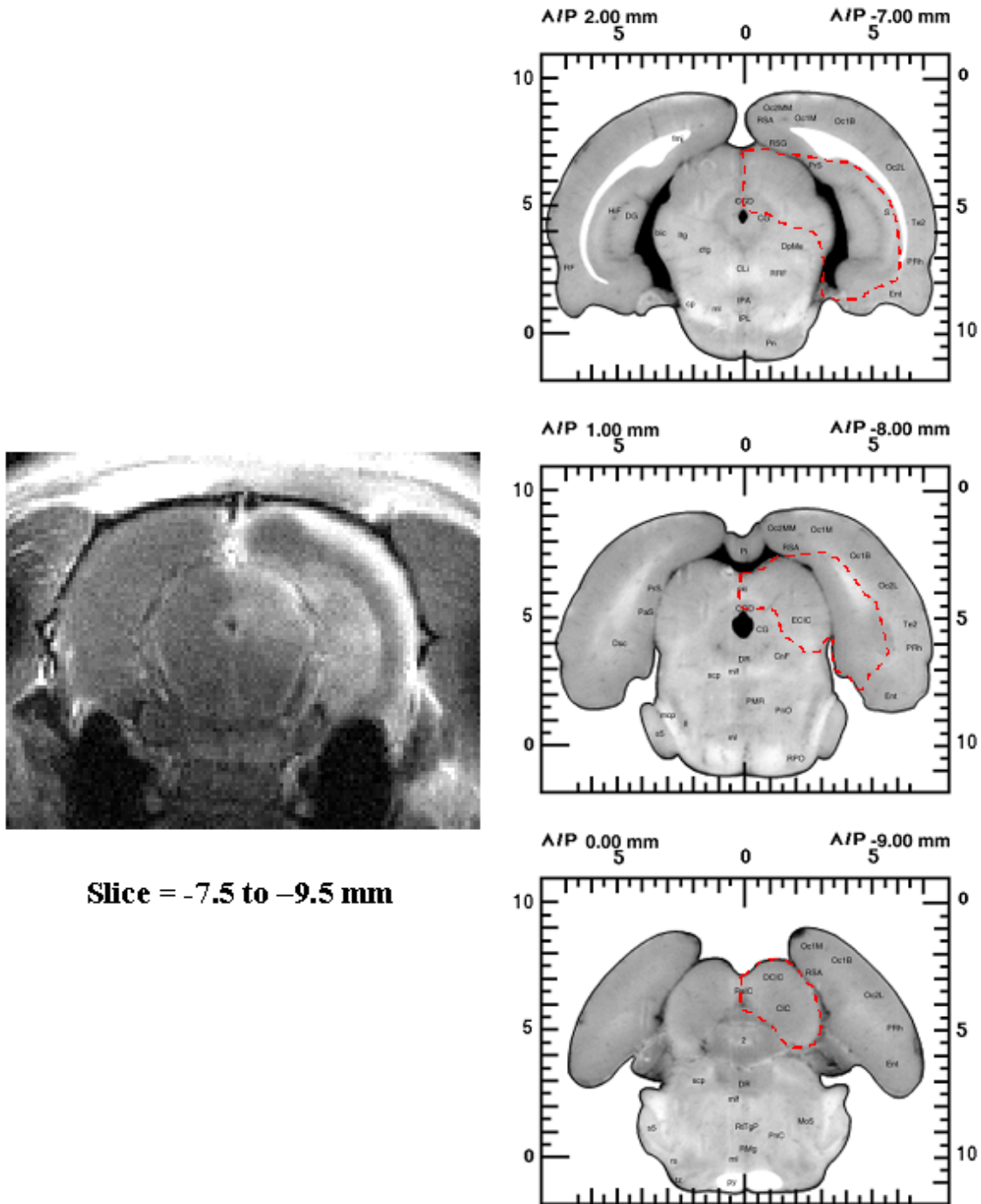


Figure 6-11b. MEMRI Subcortical Enhancement. The T₁-weighted image for slice location -5.5 mm to -7.5 mm from bregma is shown in the left-hand column. The corresponding anatomical maps for -6 mm, -7 mm, and -8 mm from bregma are shown in the right-hand column. Regions of subcortical enhancement (outlined in red) include: hippocampal regions CA1-3, subiculum (PrS, S), dentate gyrus (DG), and geniculate nucleus (DLG). Rat atlas images in the right-hand column were reproduced from the Laboratory of NeuroImaging, UCLA <<http://www.loni.ucla.edu/Research/Atlases/RatAtlas.html>>.



Slice = -7.5 to -9.5 mm

Figure 6-11c. MEMRI Subcortical Enhancement. The T₁-weighted image for slice location -7.5 mm to -9.5 mm from bregma is shown in the left-hand column. The corresponding anatomical maps for -7 mm, -8 mm, and -9 mm from bregma are shown in the right-hand column. Regions of subcortical enhancement (outlined in red) include: subiculum (PrS, S), superior colliculus (SuG, IntG, DpG), and inferior colliculus (CIC, DCIC, ECIC). Rat atlas images in the right-hand column were reproduced from the Laboratory of NeuroImaging, UCLA <<http://www.loni.ucla.edu/Research/Atlases/RatAtlas.html>>.

6.4.7 MEMRI or DWI?

Comparison of MEMRI and DWI of Experimental CSD

The MEMRI signal enhancement in the cortex, described to contain cortical layers 1-5, was 0.6-1.2 mm in thickness and extended radially from the induction site. Zhu (34) reported an average apical dendritic length of 1.2 mm in the neocortex of adult rats. The thickness of MEMRI cortical enhancement is similar to this value and suggests that apical dendrites support CSD propagation. Furthermore, these results are consistent with previous studies of CSD using diffusion-weighted MRI (DWI) (Fig. 6-2), in which a region of decreased water apparent diffusion coefficient (ADC), approximately 2 mm in size, propagated away from the application site to the lower regions of the cortex. The discrepancy in the observed thickness of the affected cortical region reported by MEMRI versus DWI may be attributed to volume-averaging effects from differences in image spatial resolution (400 μ m for DWI versus 156 μ m for MEMRI, in-plane). Although MEMRI and DWI both allow for visualization of CSDs, MEMRI has a clear advantage over that of DWI. Because of the relatively rapid propagation of CSDs and the transiently-induced changes in EC space, DWI is limited to real-time imaging. With intracellular retention of Mn²⁺ and a slow clearance rate, MEMRI may be performed after application of the stimulus outside of the magnet. Consequently, longer experiment times allow for data acquisition at higher spatial resolutions with longer signal averaging and increased signal-to-noise ratios. MEMRI may also be used for tracking real-time changes in-bore.

Utility of MEMRI in Monitoring Experimental or Pathological CSD

In summary, MEMRI is a useful technique for the visualization of experimental CSD using paramagnetic Mn²⁺ as a depolarization-dependent contrast agent in conjunction with T₁-weighted imaging. Topical application of 4M KCl in the presence of extracellular Mn²⁺ and a compromised BBB allowed differentiation between CSD-specific cortical signal enhancement and the non-specific enhancement present in the ventricular space. MEMRI is specific to Ca²⁺ channel activity and the intracellular accumulation of Mn²⁺. Consequently, MEMRI may be a more direct method for imaging the spatial extent of CSD compared with DWI or T₂^{*}-weighted imaging, which are based on more macroscopic physiological changes (cell swelling and regional blood flow,

respectively). Since the Mn^{2+} clearance is relatively slow, MEMRI may be useful for imaging CSD and its contribution to the temporal evolution of other neurological disorders.

Acknowledgements

The authors thank Drs. Karl Helmer (Worcester Polytechnic Institute, MA), Matthew Silva (Millenium Pharmaceuticals, MA), and Jeremy Wellen (GlaxoSmithKline, PA) for helpful advice and encouragement.

References

1. Leao AAP. Spreading depression of activity in the cerebral cortex. *J Neurophysiol* 1944;7:359-390.
2. Leao AAP. Further observations on the spreading depression of activity in the cerebral cortex. *J Neurophysiol* 1947;10:409-414.
3. Hansen AJ, Lauritzen M. The role of spreading depression in acute brain disorders. *An Acad Bras Cienc* 1984;56:457-479.
4. Leao AAP. The slow voltage variation of cortical spreading depression of activity. *Electroencephalogr Clin Neurophysiol* 1951;3:315-321.
5. Somjen GG. Mechanisms of spreading depression and hypoxic spreading depression-like depolarization. *Physiol Rev* 2001;81:1065-1096.
6. Van Harreveld A, Khattab FI. Changes in cortical extracellular space during spreading depression investigated with the electron microscope. *J Neurophysiol* 1967;30:911-929.
7. Hansen AJ, Olsen CE. Brain extracellular space during spreading depression and ischemia. *Acta Physiol Scand* 1980;108:355-365.
8. Lauritzen M. Long-lasting reduction of cortical blood flow of the rat brain after spreading depression with preserved autoregulation and impaired CO_2 response. *J Cereb Blood Flow Metab* 1984;4:546-554.
9. Gardner-Medwin AR, van Bruggen N, Williams SR, Ahier RG. Magnetic resonance imaging of propagating waves of spreading depression in the anaesthetized rat. *J Cereb Blood Flow Metab* 1994;14:7-11.
10. Ogawa S, Lee TM, Nayak AS, Glynn P. Oxygen-sensitive contrast in magnetic resonance image of rodent brain at high magnetic fields. *Magn Reson Med* 1990;14:68-78.
11. Latour LL, Hasegawa Y, Formato JE, Fisher M, Sotak CH. Spreading waves of decreased diffusion coefficient after cortical stimulation in the rat brain. *Magn Reson Med* 1994;32:189-198.
12. Busch E, Hoehn-Berlage M, Eis M, Gyngell ML, Hossmann KA. Simultaneous recording of EEG, DC potential, and diffusion-weighted NMR imaging during

- potassium induced cortical spreading depression in rats. *NMR Biomed* 1995;8:59-64.
13. de Crespigny A, Rother J, van Bruggen N, Beaulieu C, Moseley ME. Magnetic resonance imaging assessment of cerebral hemodynamics during spreading depression in rats. *J Cereb Blood Flow Metab* 1998;18:1008-1017.
 14. Lin YJ, Koretsky AP. Manganese ion enhances T₁-weighted MRI during brain activation: an approach to direct imaging of brain function. *Magn Reson Med* 1997;38:378-388.
 15. Aoki I, Tanaka C, Takegami T, Ebisu T, Umeda M, Fukunaga M, Fukuda K, Silva AC, Koretsky AP, Naruse S. Dynamic activity-induced manganese-dependent contrast magnetic resonance imaging (DAIM MRI). *Magn Reson Med* 2002;48:927-933.
 16. Aoki I, Ebisu T, Tanaka C, Katsuta K, Fujikawa A, Umeda M, Fukunaga M, Takegami T, Shapiro EM, Naruse S. Detection of the anoxic depolarization of focal ischemia using manganese-enhanced MRI. *Magn Reson Med* 2003;50:7-12.
 17. Drapeau P, Nachshen DA. Manganese fluxes and manganese-dependent neurotransmitter release in presynaptic nerve endings isolated from rat brain. *J Physiol* 1984;348:493-510.
 18. Narita K, Kawasaki F, Kita H. Mn and Mg influxes through Ca channels of motor nerve terminals are prevented by verapamil in frogs. *Brain Res* 1990;510:289-295.
 19. Paxinos G, Watson C. *The Rat Brain in Stereotaxic Coordinates*. Orlando: Academic Press; 1986.
 20. Takano K, Latour LL, Formato JE, Carano RA, Helmer KG, Hasegawa Y, Sotak CH, Fisher M. The role of spreading depression in focal ischemia evaluated by diffusion mapping. *Ann Neurol* 1996;39:308-318.
 21. Ochs S, Hunt K. Apical dendrites and propagation of spreading depression in cerebral cortex. *J Neurophysiol* 1960;23:434-444.
 22. Herreras O, Somjen GG. Propagation of spreading depression among dendrites and somata of the same cell population. *Brain Res* 1993;610:276-282.
 23. Marin-Padilla M, Marin-Padilla TM. Origin, prenatal development, and structural organization of layer I of the human cerebral (motor) cortex. *Anat Embryol* 1982;164:161-206.
 24. Jones EG. Varieties and distribution of non-pyramidal cells in the somatic sensory cortex of the squirrel monkey. *J Comp Neurol* 1975;160:205-267.
 25. Katz LC. Local circuitry of identified projections neurons in cat visual cortex brain slices. *J Neurosci* 1987;7:1223-1249.
 26. Harris E, Witter MP, Weinstein G, Stewart M. Intrinsic connectivity of the rat subiculum: I. dendritic morphology and patterns of axonal arborization by pyramidal neurons. *J Comp Neurol* 2001;436:490-505.
 27. Naber PA, Witter MP, Lopes da Silva FH. Evidence for a direct projection from the postrhinal cortex to the subiculum in the rat. *Hippocampus* 2001;11:105-117.
 28. Kelly JP, Wong D. Laminar connections of the cat's auditory cortex. *Brain Res* 1981;212:1-15.
 29. Hersch SM, White EL. Quantification of synapses formed with apical dendrites of golgi-impregnated pyramidal cells: variability in thalamocortical inputs, but

- consistency in the ratios of asymmetrical to symmetrical synapses. *Neuroscience* 1981;6:1043-1051.
30. Levesque M, Gagnon S, Parent A, Deschenes M. Axonal arborizations of corticostriatal and corticothalamic fibers arising from the second somatosensory area in the rat. *Cereb Cortex* 1996;6:759-770.
 31. Kasper EM, Larkman AU, Lubke J, Blakemore C. Pyramidal neurons in layer 5 of the rat visual cortex. I. Correlation among cell morphology, intrinsic electrophysiological properties, and axon targets. *J Comp Neurol* 1994;339:459-474.
 32. Games KD, Winer JA. Layer V in rat auditory cortex: projections to the inferior colliculus and contralateral cortex. *Hear Res* 1988;34:1-25.
 33. Perez-Samartin AL, Sendino-Rodriguez J, Martinez-Millan L, Donate-Oliver F. Morphological characteristics of neurons in the superficial layers of the rabbit's superior colliculus projecting to the ipsilateral dorsal lateral geniculate nucleus. *Arch Ital Biol* 1995;133:177-195.
 34. Zhu JJ. Maturation of layer 5 neocortical pyramidal neurons: amplifying salient layer 1 and layer 4 inputs by Ca^{2+} action potentials in adult rat tuft dendrites. *J Neurophysiol* 2000;526:571-587.

CHAPTER 7

MANGANESE-ENHANCED MRI (MEMRI) OF CEREBRAL ISCHEMIA: ROLE OF PERI-INFARCT DEPOLARIZATIONS (PIDs) IN THE PROGRESSION TO INFARCT

Introduction

- Peri-infarct Depolarizations
- Role of PIDs in Cerebral Ischemia
- MRI Identification of PIDs
- Manganese as a Paramagnetic Calcium Analog

Methods

- Animal Preparation
- Optimization of BBB Opening
- MCAO Procedure
- MRI Measurements
- Data Analysis
- Tissue Characterization

Results

- Optimization of BBB Opening
- Temporal Evolution of Ischemia
- MEMRI and Ischemia

Discussion

- Cellular Uptake of Manganese
- Heterogeneity of BBB Opening
- Temporal Evolution of Ischemia
- MEMRI and Ischemia
- Utility of MEMRI for PID Identification

Abstract

The role of peri-infarct depolarizations, or PIDs, in the temporal evolution of cerebral ischemia is not fully understood. When confounded with the time-varying nature of individual MR parameters, the ability to accurately characterize the ischemic territory becomes difficult. In order to assess the role of PIDs versus that of terminal anoxic depolarizations in tissue progression to infarct with and without therapeutic intervention, a multispectral (MS) approach may provide greater power than that of a single parameter approach. For this reason, MEMRI and DWI were performed for preliminary analysis of the utility of MEMRI in studying the temporal evolution of cerebral ischemia over that of standard DWI. The method for optimum delivery of Mn^{2+} into the extracellular space following BBB disruption was determined to be the following: 6 ml/kg of 25% (w/v) mannitol injected at 0.9 ml/min → 10 min. wait period → 2 ml/kg of 50mM $MnCl_2$ injected at 0.9 ml/min. Following optimization of BBB opening, MEMRI was employed in the characterization of cerebral ischemia. Preliminary results show significant MEMRI enhancement previous to the development of a diffusion deficit, indicating that MEMRI may be useful in identifying tissue presumably at risk. Since PIDs are one of the many aggravating factors in progression of penumbra tissue to infarct, MEMRI may be employed for studying methods suppressing the frequency and duration of PIDs.

7.1 Introduction

Peri-infarct depolarizations (PIDs), similar in many respects to experimentally-induced cortical spreading depressions (CSDs), are one of the many aggravating factors in progression of the ischemic penumbra to infarction. For this reason, methods suppressing the frequency and duration of PIDs should reduce total infarct volume. This chapter will address the development of manganese-enhanced MRI for the visualization of PIDs and their role in the temporal evolution of cerebral ischemia.

7.1.1 Peri-Infarct Depolarizations

Spreading Depression-Like Depolarizations in Ischemia

In cerebral ischemia, regions with severely compromised blood flow (~20% of control) suffer from energy breakdown and failure of ion homeostasis (1-3). Unable to maintain existing ion gradients, there is a massive K^+ shift from the IC to EC space. This increase in extracellular K^+ is of sufficient magnitude to induce neuronal depolarization, opening voltage-gated Ca^{2+} channels for Ca^{2+} influx (4,5). The resultant intracellular Ca^{2+} overload then triggers the release of excitatory neurotransmitters (i.e., glutamate) into the EC space (6,7). Since both K^+ and glutamate elicit spreading depression, a phenomenon first described by Leao (8,9) in the 1940s, it makes sense that increased levels of these substances in ischemia would cause such depolarizations to occur. The existence of these spreading depression-like depolarizations was first described by Nedergaard and Astrup (10) in a rat MCAO model of focal ischemia. The authors reported the occurrence of repetitive DC potential deflections throughout the infarct rim, similar to experimentally-induced spreading depression from 3M KCl application to the cortical surface.

Frequency and Duration of Depolarization

Within the ischemic core, membrane repolarization and restoration of ion gradients is not possible. The lack of necessary energy stores leaves this region in a state of permanent depolarization, termed terminal anoxic depolarization. The anoxic release of K^+ and excitatory neurotransmitters such as glutamate within the infarct core initiate the spread of these depolarizations to the lesion periphery (11). Within the penumbra, the limited flow supplied by collateral vessels cannot adequately meet the metabolic demands of repetitive depolarizations. Successive events tend to be of increasing duration—the

upregulated glucose utilization within an already oxygen-deficient environment leads to transient tissue hypoxia and a lengthened time required for repolarization (12,13). The necessitation for anaerobic glycolysis further aggravates lactate accumulation as well as tissue acidosis (14,15). These exacerbating effects of repetitive transient depolarizations within penumbral tissue, termed peri-infarct depolarizations (PIDs), could potentially transition the tissue into a terminal state (12,16,17).

7.1.2 Role of PIDs in Cerebral Ischemia

Correlation Between PIDs and Infarct Size

Nedergaard and Astrup (10) first hypothesized that peri-infarct depolarizations (PIDs) were the likely cause for progression of penumbral tissue to infarct. A subsequent study by Mies *et al.* (18) reported a direct correlation between the number of depolarizations and infarct volume, with a 13 mm³ increase in infarct size per depolarization. The authors noted that with each depolarization, there was an increase in both DC shift duration and recovery time.

Mechanisms for Progression to Infarct

In addition to episodic tissue hypoxia and increasing acidosis from lactate accumulation, recent studies have reported that cyclooxygenase-2 (COX-2) is transiently-induced following spreading depression (19) and focal ischemia (19,20). COX-2 is a key enzyme in the conversion of arachidonic acid to prostaglandins and thromboxanes—mediators of glutamate release and free radical formation (i.e., nitric oxide). Since all of these contribute to neuronal damage, repetitive PIDs within the penumbra region increase the likelihood of tissue progression to infarct.

7.1.3 MRI Identification of PIDs

DWI Correlation with PIDs and Infarct Size

Following the study by Mies and coworkers (18), several researchers employed DWI methods for the non-invasive investigating of PIDs and their role in the spatiotemporal evolution of cerebral ischemia. Experimental elicitation of CSDs, measured as a region of transiently declined ADCs moving radially away from the initiation site with a propagation speed of ~3 mm/min, results in larger infarct volumes in instances of focal ischemia (21,22). Serial ADC measurements made by Busch *et al.* (22) and the

corresponding increase in infarct size are diagrammed in Fig. 7-1. Dijkhuizen *et al.* (23) confirmed this correlation between ischemia-induced PIDs and the development of neuronal damage. The authors reported a good correlation between the degree of ADC reduction, total depolarization time, and ischemic lesion volume. These results indicate that the severity of cytotoxic edema, and therefore, the magnitude of the ADC change detectable by DWI, increases according to the total duration rather than the frequency of depolarization.

DWI Correlation with PIDs and COX-2 Expression

Transient reductions in ADC, as described above, can be caused by PIDs in acute cerebral ischemia. In light of these findings and those of Miettinen *et al.* (19) and Collaco-Moraes *et al.* (20), it is not surprising that these transient reductions in ADC have an associated increase in COX-2 mRNA expression. Following 60 minutes of MCA occlusion, Mancuso and coworkers (24) reported the expression of COX-2 mRNA in cortical regions that had experienced transient ADC reductions (penumbra), but not in regions with persistent ADC reduction (core). These results are diagrammed in Fig. 7-2. Since PID-induced COX-2 expression supports the expansion of infarct, COX-2 inhibitors and/or methods of PID-suppression could play an important role in preventing injury.

Limitations of Real-Time Imaging

Although DWI has been used to investigate the role of PIDs in ischemia, these studies have limited their spatial resolution and signal-to-noise ratios in order to achieve a reasonable temporal resolution for monitoring the transient changes in ADC concomitant with PIDs. In addition, DWI methods are based on macroscopic physiological changes (cell swelling from cytotoxic edema), limiting the ability to characterize the spatial extent of PIDs in the acute stage of focal ischemia. An MRI method with a higher signal-to-noise ratio based on more microscopic physiological changes (i.e., Ca²⁺ channel activity), would be helpful in order to overcome these limitations.

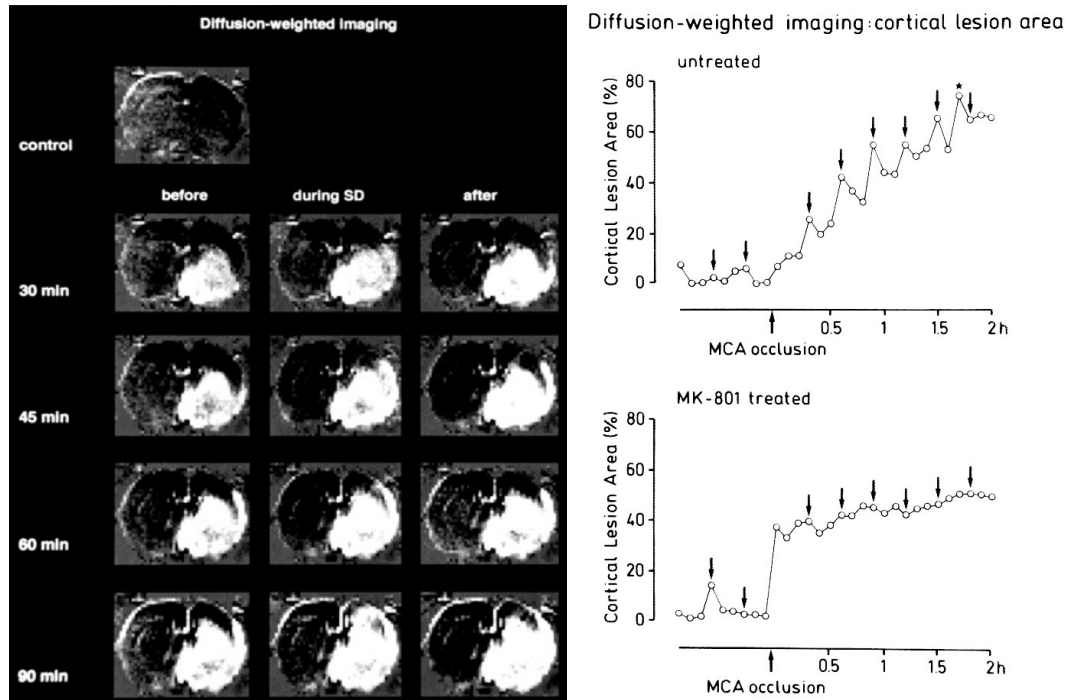


Figure 7-1. Diffusion-weighted imaging of experimentally-induced SD and its role in ischemic progression. Left: Evolution of the ischemia-induced hyperintense area in DWI before, during, and after the passage of SD. Every SD was associated with an expansion of the area of increased DWI signal intensity. Right: Quantitative evaluation of the cortical lesion areas in DWI before and during the first 2 h after MCA occlusion. Arrows indicate timepoints of 0.15M KCl intracortical injection. One late spontaneous SD is indicated by the star. In the untreated animal, every SD was associated with an expansion of cortical lesion area. In the MK-801 treated animal, only the first potassium injection, before MK-801 application, resulted in a SD. Figure reproduced from reference (22).

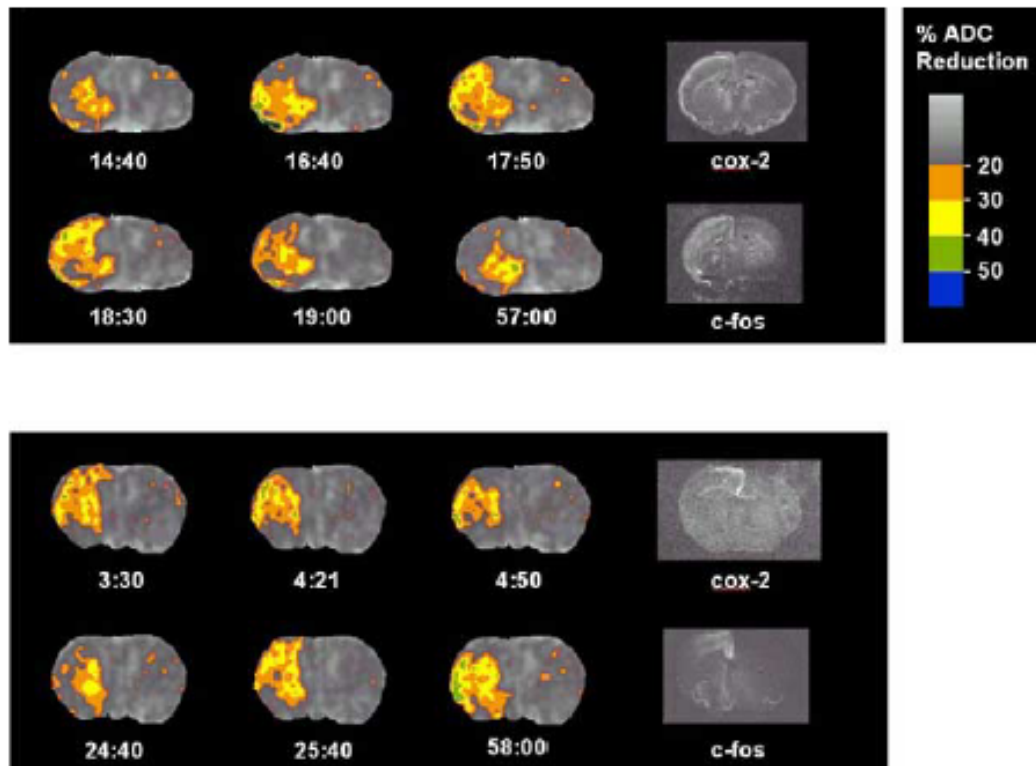


Figure 7-2. ADC Maps for two rats subjected to 60-min MCA occlusion, with corresponding COX-2 and c-fos autoradiography. The ADC lesion (regions with at least 20% reduction relative to the non-ischemic hemisphere) is shown in color. Note the transient reductions in ADC within cortical regions for both animals. COX-2 mRNA and c-fos were expressed in regions having experienced transient reductions in ADC. Figure reproduced from reference (24).

7.1.4 Manganese as a Paramagnetic Calcium Analog

Manganese Action and Intracellular Uptake

Within the past ten years, manganese ions (Mn^{2+}) have gained widespread use as a membrane-depolarization-dependent contrast agent for monitoring functional activation (25-28), neuronal architecture (29), and neuronal tract tracing (30-33). Mn^{2+} , having an ionic radius and charge similar to Ca^{2+} , competitively enters cells through Ca^{2+} -influx pathways such as voltage-gated or ligand-gated Ca^{2+} channels (34,35), with further accumulation within mitochondria (36). Recently, Aoki *et al.* (37) employed Mn^{2+} as a surrogate marker for Ca^{2+} influx in the study of focal ischemia. The authors reported a hyperintense region on T_1 -weighted MRI smaller than the area of reduced ADC (Fig. 7-3). From these results, Aoki and coworkers hypothesized that the T_1 -weighted signal enhancement was indicative of anoxic depolarization, and therefore, the infarct core.

Manganese and Peri-infarct Depolarizations

Although terminal anoxic depolarizations within the core result in Ca^{2+} influx (4), transient depolarizations (PIDs) within the penumbral region yield intracellular accumulation of Ca^{2+} as well (16,38). Ohta *et al.* (16) reported the existence of two distinct regions following permanent MCAO in cats—the first with persistent depolarization (i.e., core) and declined levels of extracellular Ca^{2+} ; the second with repetitive transient depolarizations along the periphery of the first (i.e., penumbra). The authors noted reductions in extracellular Ca^{2+} from 1.2 mM to 0.15 mM concomitant with each depolarization (Fig. 7-4). Since repetitive PIDs resulted in a progressive breakdown of neuronal function and ion homeostasis (i.e., penumbral progression to infarct), Ohta and coworkers suggested that PID-induced intracellular Ca^{2+} accumulation is a contributing factor for neuronal injury. Further understanding of the mechanisms of Ca^{2+} -mediated cell injury in cerebral ischemia is necessary, particularly in the exact role of PIDs in the progression of penumbral tissue to infarct and the potential for therapeutic intervention in the acute stage of ischemia. Since manganese-enhanced MRI (MEMRI) methods have recently been shown to aid in the visualization of experimental CSD in the rat brain (39), MEMRI should be useful for investigating the role of PIDs in the temporal evolution of cerebral ischemia. The aim of this feasibility study is to demonstrate the utility of MEMRI in the visualization of PIDs following ischemic onset.

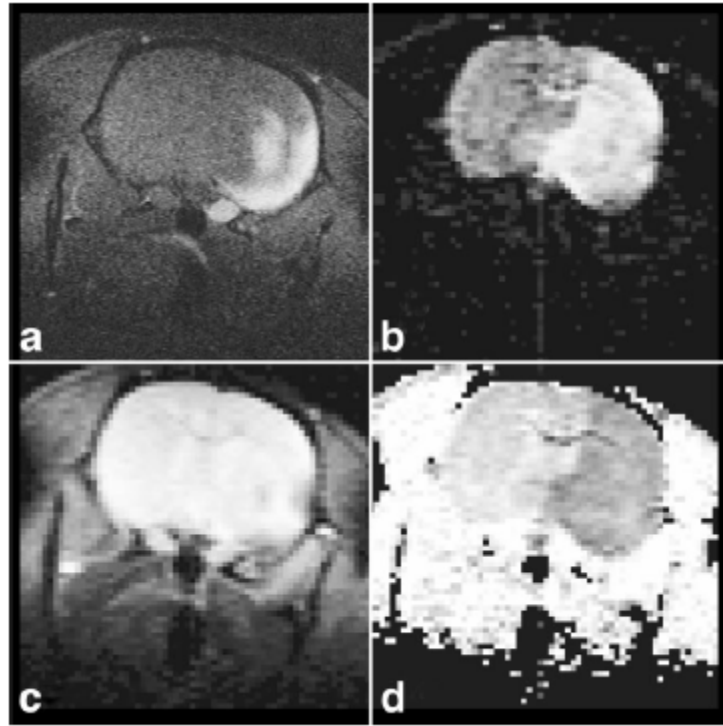


Figure 7-3. Comparison of MEMRI, DWI, T₂-weighted MRI, and ADC images on the same rat following permanent MCAO. The high intensity area localized within the lateral side of caudate-putamen and lateral cortex on MEMRI (a) was smaller than both DWI hyperintensity (b) and decreased ADC (d). Slight hypointensity was visible on T₂-weighted MRI (c). Figure reproduced from reference (37).

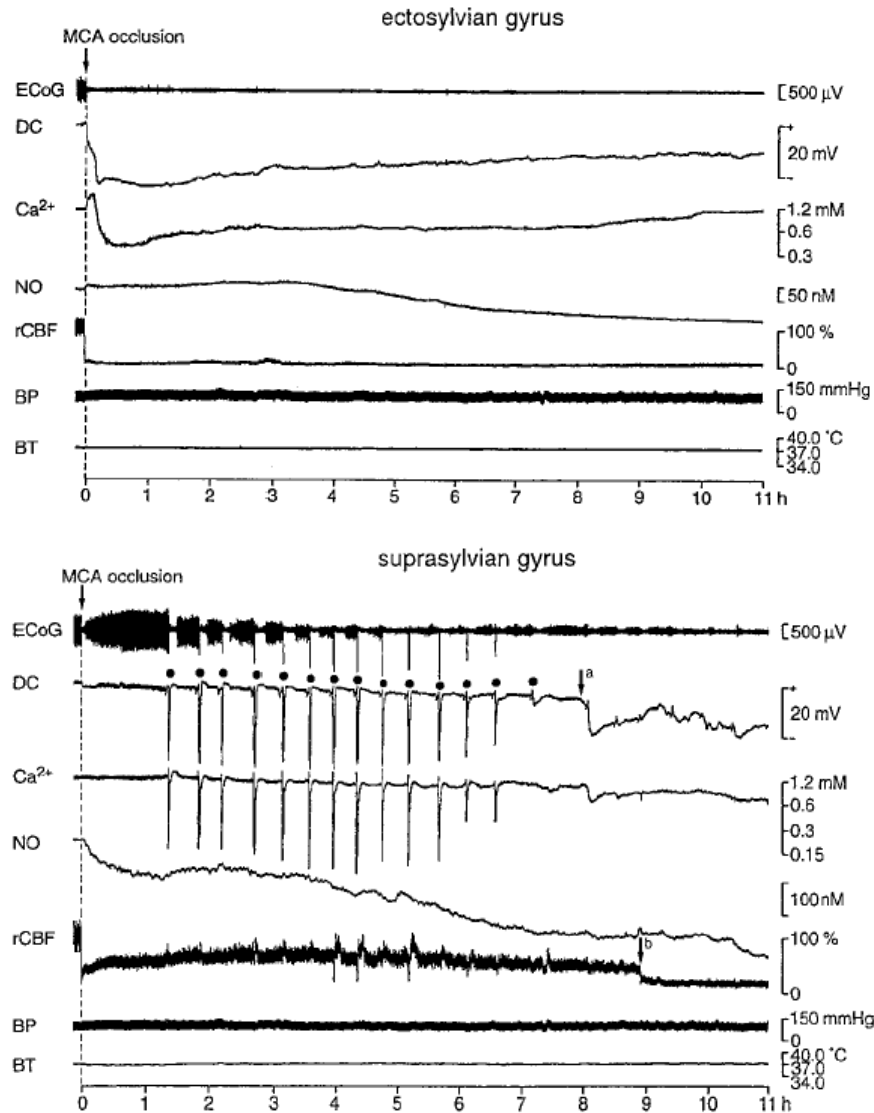


Figure 7-4. Plot of electrophysiological recordings in ectosylvian and suprasylvian gyri. The horizontal axis indicates time (hrs) post-MCAO. (top) In the ectosylvian gyrus, which is proximal to the MCA territory, persistent depolarization was present with permanent negative DC deflection and severely decreased extracellular Ca^{2+} levels. (bottom) In the suprasylvian gyrus, which is more distal to the MCA territory, transient depolarizations were present (indicated by the dots). Concomitant with each depolarization there was a transient decrease in extracellular Ca^{2+} from approximately 1.2 mM to 0.15 mM. The 'a' and 'b' labeled arrows indicate the transition into persistent depolarization and the deterioration of cerebral circulation, respectively. Figure adapted from reference (16).

7.2 Methods

7.2.1 Animal Preparation

The present study was approved by the Institute Animal Care and Use Committee (IACUC) of the University of Massachusetts Medical School (IACUC protocol A-875). Male Sprague-Dawley rats (300-360 g; Taconic Farms, Germantown, NY) were divided into three groups: Optimization of BBB Opening (N = 10), MCAO control (N = 2), and MCAO with MnCl₂ administration (N = 2). Rats were initially anesthetized with an intraperitoneal injection of chloral hydrate (400 mg/kg). A modified PE-50 polyethylene catheter with a PE-10 catheter tip (PE-10 & PE-50, Becton Dickinson, San Jose, CA) was placed in the right external carotid artery (ECA) for drug administration. For catheterization of the right ECA, a ventral midline incision was made in the neck. The omohyoid muscle was separated longitudinally and retracted laterally to isolate and expose the right ECA. Following ligation of the vessel, a small incision was made into which the catheter was inserted and secured in place. Cannulation of the right ECA limited drug delivery to the right side of the brain, enabling the left side to serve as a control. The common carotid artery (CCA) was kept intact and open in order to maintain blood flow to regions originally supplied by the right ECA (i.e., face and underlying muscle). Rectal temperature was monitored continuously with a rectal probe and maintained at 37.0°C using a thermostatically-controlled heating lamp (Model 73ATD, YSI Inc., Yellow Spring, OH) during preparation.

7.2.2 Optimization of BBB Opening

In order to ascertain the regional coverage and heterogeneity present following blood-brain-barrier (BBB) opening, a mixture of glutamate and MnCl₂ was employed in this experimental group (N = 10). The optimum drug dose-timing schedule was determined by assigning animals a set rate (ml/min) and dose (mg/kg) for both D-mannitol and the MnCl₂/Glu combination, with a waiting period (min) between injections (Table 7-1). In addition, the CCA flow dependence of mannitol delivery was tested by advancing the catheter from the ECA into the ICA (BBB-1, BBB-2), keeping the catheter in the ECA only (BBB-3 → BBB-10), or by clamping the CCA during mannitol injection (BBB-8). Following the initial operation, 25% D-mannitol solution (Sigma, St. Louis, MO) was

injected via the right ECA. Individual animals, five or ten minutes after ECA injection of D-mannitol, were administered a mixture of 50 mM MnCl_2 ($\text{MnCl}_2 \cdot 4\text{H}_2\text{O}$; Sigma, St. Louis, MO) and 15 mg/ml L-glutamic acid solution (Sigma, St. Louis, MO). All syringes were prepared and maintained at 37°C prior to injection using an incubator (Isotemp 500 Series, Fisher Scientific, Hampton, NH). Individual drug administration was performed using a syringe pump (Model 11; Harvard Apparatus, Holliston, MA). Heparinized saline (0.1-0.2ml, 37°C) was injected pre- and post-mannitol delivery to prevent clot formation and mannitol recrystallization within the tubing.

7.2.3 MCAO Procedure

For both MCAO groups ($N = 4$), permanent focal ischemia was induced by the intraluminal monofilament MCAO model. Both the right ECA and right CCA were ligated proximally and permanently. Temporarily, the CCA and internal carotid artery (ICA) distal to the ECA were ligated. A 4-0 silicone-coated (Bayer Inc.) suture (Ethilon Nylon Suture, ETHICON, Inc.) with a heat-rounded tip was introduced into the stump of the CCA. Next, the suture was advanced into the ICA approximately 16-18 mm beyond the carotid bifurcation until lodged in the anterior cerebral artery (ACA), blocking blood flow to the middle cerebral artery (MCA). Rectal temperature was monitored continuously with a rectal probe and maintained at 37.0°C using a thermostatically-controlled heating lamp (Model 73ATD, YSI Inc., Yellow Spring, OH) during MCA occlusion. For the MCAO control group ($N = 2$), prior to MCA occlusion, a polyethylene catheter (PE-50, Becton Dickinson, San Jose, CA) was placed in the left femoral vein for Gd injection-based PWI. For the MCAO with MnCl_2 administration group ($N = 2$), in order to investigate the role of Ca^{2+} -mediated activity in the progression of cerebral ischemia, animals received MnCl_2 prior to MCA occlusion. A 25% D-mannitol solution (6 ml/kg, Sigma, St. Louis, MO) was injected via the right ECA. Ten minutes after ECA injection of D-mannitol, 50 mM MnCl_2 (2ml/kg, Sigma, St. Louis, MO) was administered. Both D-Mannitol and MnCl_2 were injected at a rate of 0.9ml/min using a syringe pump (Model 11; Harvard Apparatus, Holliston, MA). Within five minutes after stopping the MnCl_2 infusion, the silicon-coated nylon suture was inserted from the right CCA for MCA occlusion.

Table 7-1. Experimental Setup for Optimization of Blood-Brain-Barrier (BBB) Opening.

Animal #	Mannitol Dose (ml/kg) / Rate (ml/min)	MnCl ₂ /Glu Combo Dose (ml/kg) /Rate (ml/min)	Time Between Injections (min)	Placement of PE-50/PE-10 Combo Tubing	CCA Status During Mannitol Injection
BBB-1	5/1.8	2/1.8	10	ECA into ICA ^a	Flow-limited ^b
BBB-2	5/1.8	2/1.8	5	ECA into ICA ^a	Flow-limited ^b
BBB-3	5/1.8	2/1.8	10	ECA	Open
BBB-4	5/0.9	2/0.9	10	ECA	Open
BBB-5	6/0.9	2/1.8	10	ECA	Open
BBB-6; BBB-7	6/0.9	2/0.9	10	ECA	Open
BBB-8	6/0.9	2/0.9	10	ECA	Clamped
BBB-9	6/0.9	2/0.9	5	ECA	Open
BBB-10	7.5/0.9	2/0.9	10	ECA	Open

^aAnimals with placement of tubing from the ECA into the ICA had a non-modified PE-50 polyethylene catheter. All other animals had a modified PE-50 polyethylene catheter with a PE-10 catheter tip.

^bThe flow from the CCA to the ICA was limited due to placement of the PE-50 tubing from the ECA into the ICA.

7.2.4 MRI Measurements

Data Acquisition and Parameter Setup

MR experiments were performed with a Bruker Biospin 2.0T/45cm imaging spectrometer equipped with ± 20 G/cm self-shielded gradients (Fig. 3-5). Following acquisition of a gradient-echo tripilot, the imaging plane was referenced to the rhinal fissure at the boundary of the olfactory bulb. Image acquisition was performed along the axial plane [number of slices = 6, slice thickness = 2 mm].

Optimization of BBB Opening ($N = 10$)

For the optimization of BBB opening group, a T_1 -weighted SE sequence was used to acquire images using a TR/TE = 300.0/11.0 ms, FOV = 4 cm \times 4 cm, matrix size = 256 \times 256, and NEX = 4. Imaging was performed approximately 30-min post drug administration, with a total experiment time of 10m24s.

MCAO Control Group ($N = 2$)

For the MCAO control group, a DW, SE-EPI sequence was used to acquire images at six b-values ($b = 23 \rightarrow 1471$ s mm^{-2}) along the three principal directions (read(x), phase(y), slice(z)) with TR/TE = 2000/51 ms, $\delta = 6$ ms, and $\Delta = 24.31$ ms, resulting in an effective diffusion time $t_{\text{dif}} = 21.31$ ms. A PW, SE-EPI sequence was used to acquire images pre- and post-contrast Gd-injection with TR/TE = 800/51 ms. A total of 40 repetitions were acquired, with injection of 0.35ml Magnevist (gadopentetate dimeglumine; Berlex, Montville, NJ) at the start of the 10th repetition using a syringe pump (PHD 2000; Harvard Apparatus, Holliston, MA) and a rate of 17 ml/min. A T_2 W, SE-CPMG sequence was used to acquire images at ten echo times (TE = 10 \rightarrow 150 ms) with TR = 2000 ms. For DWI, PWI, and T_2 WI, images were acquired at 30-, 60-, 90-, 120-, and 180-min post-MCAO using matrix size = 64 \times 64, FOV = 2.56 cm \times 2.56 cm, with NEX = 8 for DWI and NEX = 2 for T_2 WI. The total experiment times for DWI, PWI, and T_2 WI were 4m48s (1m36s per direction), 36s, and 4m34s, resulting in an approximate 10-minute temporal resolution.

MCAO with MnCl_2 Administration ($N = 2$)

For the MCAO with MnCl_2 administration group, DWI was performed in the same manner as that of the MCAO control group. A T_1 -weighted SE sequence was used to acquire images using a TR/TE = 300.0/7.0 ms, FOV = 2.56 cm \times 2.56 cm, matrix size =

64×64 , and $NEX = 4$. The total experiment times for DWI and T_1WI were 4m48s (1m36s per direction) and 1m17s, resulting in an approximate 6-minute temporal resolution.

Imaging Setup and Physiological Monitoring

During imaging, animals were placed supine in a home-built animal holder (Fig. 6-5a). The head of the animal was fixed inside a 2.0 cm x 3.5 cm rectangular 1H surface coil shaped to conform to the curvature of the skull (Fig. 6-5b). Animals were anesthetized with 1.2% isoflurane delivered at 1.0 L/min in breathing-quality air (Fig. 6-5c). Body temperature was maintained at $37.0 \pm 1.0^\circ C$ by circulated warm air using a T-type thermocouple and a double-point feedback control system (Fig. 6-5d).

7.2.5 Data Analysis

Optimization of BBB Opening (N = 10)

Image reconstruction was performed using Paravision's Image Processing and Display Software (Xtip). ROIs were user-defined to delineate between MEMRI-enhanced regions and normal tissue using ImageJ (Version 1.33; NIH, Bethesda, MD). Additional ROIs were drawn for hemispheric and total brain volume calculations. Percent hemispheric enhancement was calculated through comparison of the ipsilateral and contralateral hemispheres on a slice-by-slice basis:

$$\text{Hemispheric Enhancement (\%)} = \frac{SI_{IH} - SI_{CH}}{SI_{CH}} \times 100 \quad (7-1)$$

where SI_{IH} is the signal intensity for the ipsilateral hemisphere (side with BBB disruption) and SI_{CH} is the signal intensity in the contralateral hemisphere (side with intact BBB). Percent hemispheric coverage was calculated through a volumetric comparison of the MEMRI-enhanced regions and the ipsilateral hemisphere on a slice-by-slice basis:

$$\text{Hemispheric Coverage (\%)} = \frac{V_E}{V_{IH}} \times 100 \quad (7-2)$$

where V_E is the volume of the MEMRI-enhanced region and V_{IH} is the volume of the ipsilateral hemisphere. Percent regional enhancement was calculated through a comparison of the MEMRI-enhanced region and the contralateral hemisphere:

$$\text{Regional Enhancement (\%)} = \frac{\text{SI}_E - \text{SI}_{\text{CH}}}{\text{SI}_{\text{CH}}} \times 100 \quad (7-3)$$

Data are presented as mean \pm inter-slice signal variability (IS-SD). Additional variance calculations were performed for MEMRI-enhanced regions on an animal-by-animal basis.

MCAO Control (N = 2)

Image reconstruction was performed using Paravision's Image Processing and Display Software (Xtip). Image analysis and parameter map production was performed using routines written in IDL (Research Systems Inc., Boulder, CO). ADC and T_2 parameter-map production was performed on a pixel-by-pixel basis based on the relationship between the log of the signal intensity and b-value (Eq. 7-4) or signal intensity and echo time (Eq. 7-5), respectively, using a linear fitting procedure based on the minimization of the chi-square statistic:

$$M(t) = M_0 e^{-bD} \quad (7-4)$$

$$M(t) = M_0 e^{-TE/T_2} \quad (7-5)$$

where M/M_0 is the signal intensity at a particular b-value or TE value; D is the diffusion along a single direction, and T_2 is the spin-spin or transverse relaxation time. Following ADC parameter map production for the three principal directions (x, y, and z), spatial maps of the mean diffusivity (i.e., ADC_{avg}) were constructed for a scalar measure of isotropic diffusion:

$$\langle D \rangle = \frac{D_1 + D_2 + D_3}{3} \quad (7-6)$$

CBF parameter-map production was performed on a pixel-by-pixel basis based on the change in the relaxation rate ΔR_2 as a function of time pre- versus post-contrast injection:

$$\Delta R_2(t) = -\frac{1}{TE} \times \ln \left[\frac{M(t)}{M_0} \right] \quad (7-7)$$

where $M(t)$ is the signal intensity at a time t during bolus passage of the contrast agent (repetitions 11-40), M_0 is the signal intensity value at baseline pre-contrast (average of repetitions 1-10), and TE is the echo time. First, a mean filter (3 \times 3) was applied to the

data to lower the noise level. Second, the ΔR_2 values calculated using Eq. 7-7 were fit to the following gamma-variate function using non-linear regression (40,41):

$$\Delta R_2(t) = Q t^r e^{-(t/b)} \quad (7-8)$$

where t is the time and Q , r , and b are the three unknown parameters. Third, estimates of relative cerebral blood volume (rCBV) and vascular transit time (VTT) were obtained by calculating the area (Eq. 7-9) and the first moment (Eq. 7-10) of the $\Delta R_2(t)$ versus time curve, respectively:

$$\text{rCBV} = \int_0^{\infty} \Delta R_2(t) dt = Q b^{r+1} \Gamma(r+1) \quad (7-9)$$

$$\text{VTT} = \int_0^{\infty} t \Delta R_2(t) dt = b(r+1) \quad (7-10)$$

where t is the time, Q , r , and b are the three parameters determined from non-linear regression, and $\Gamma(r+1)$ is the gamma function from Eq. 7-8 evaluated at time $t = r+1$. Finally, the CBF index (CBF_i) was calculated on a pixel-by-pixel basis by taking the ratio of Eqs. 7-9 and 7-10.

MCAO with MnCl_2 Administration ($N = 2$)

Image reconstruction was performed using Paravision's Image Processing and Display Software (Xtip). Image analysis and parameter map production was performed using routines written in IDL (Research Systems Inc., Boulder, CO). ADC parameter-map production was performed per previous description according to Eq. 7-4.

7.2.6 Tissue Characterization

Tissue characterization using multispectral (MS) analysis and the k-means (KM) clustering algorithm (42) was employed for subdivision of tissue into normal and abnormal (penumbra, core) populations based on methodology developed by Carano and coworkers (43,44).

MCAO Control ($N = 2$)

A 3D feature vector, containing the ADC, CBF, and T_2 parameter maps, was generated. KM clustering was performed on a pixel-by-pixel basis using the Euclidean distance measure (42):

$$D = (x - \mu_i)^t (x - \mu_i) \quad (7-10)$$

where $x \in R^3$ is the feature vector and μ_i is the cluster mean, both determined from all of the data ($N = 2$ datasets, 5 timepoints per dataset). Incorporation of the inverse covariance matrix accounts for variability across features, allowing data classification via hyperplane decision boundaries without an orthogonality requirement. Prior to KM clustering, the background was removed based on the delineation between the brain and surrounding tissue using the M_0 maps from the T_2 -fitting procedure and ImageJ (Version 1.33; NIH, Bethesda, MD). Feature normalization ($\mu = 0, s = 1$) was then performed for removal of potential scaling differences. Following background removal and normalization steps, KM ($k = 3$) was applied to segment the data into three regions, one each for normal and abnormal tissue, and one for cerebrospinal fluid (CSF). Following segmentation, the abnormal tissue region was then subdivided into penumbra and core.

MCAO with $MnCl_2$ Administration ($N = 2$)

ADC lesion area was determined by pixels exhibiting values of $0.53 \times 10^{-5} \text{ cm}^2\text{s}^{-1}$ or less, based on a previously derived percent-reduction threshold ($\sim 33\%$) for estimating lesion volume (45). MEMRI lesion area was determined by pixels with signal intensities greater than the mean + 2 standard deviations (SDs) in the contralateral hemisphere. The correspondence between ADC and MEMRI was determined through generation of a parameter map with separate color designations for the following: ADC lesion and MEMRI lesion, ADC lesion and normal MEMRI, MEMRI lesion and normal ADC, and normal MEMRI and normal ADC. Data are presented as mean \pm SD.

7.3 Results

7.3.1 Optimization of BBB Opening ($N = 10$)

Fig. 7-5 shows the regional coverage and relative MEMRI enhancement for the BBB optimization group at a single time-point 30 minutes post drug administration (Fig.7-5a-j correspond to BBB-1-10 in Table 7-1). A quantitative summary for percent average hemispheric enhancement, percent average hemisphere coverage, and percent average regional enhancement are provided in Table 7-2.

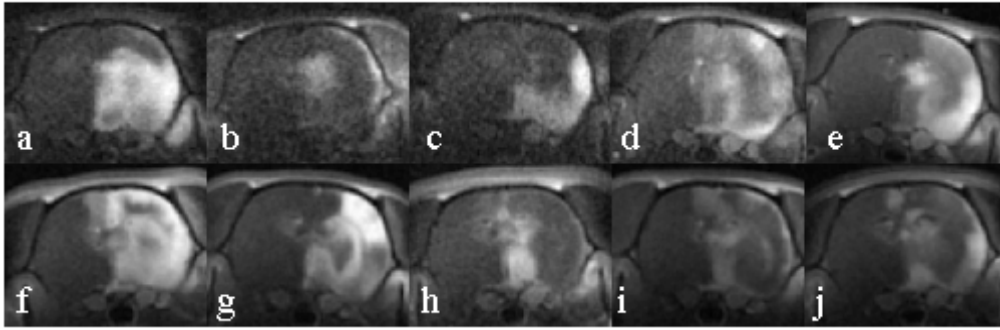


Figure 7-5. T_1 -weighted MEMRI following $MnCl_2$ /Glu combo administration for the BBB opening optimization group. a) \rightarrow j) correspond to BBB-1 \rightarrow BBB-10 in Table 7-1. A single axial image is shown for each animal. Individual images were contrast-enhanced for optimum viewing. Slice thickness = 2mm.

Effect of Timing of Drug Administration on BBB Opening

Although results for a wait period of 5-min versus 10-min for BBB-1 (Fig.7.5a) versus BBB-2 (Fig.7b) at injection rates of 1.8ml/min were not significantly different, two of the six imaging slices for the 5-min wait period exhibited no enhancement at all in comparison to coverage across all six slices for the 10-min wait period. Comparison of a wait period of 5-min versus 10-min for BBB-9 (Fig.7.5i) versus BBB-6 (Fig.7.5f) at injection rates of 0.9ml/min showed significantly greater hemispheric enhancement (i.e., more effective BBB opening) as well as increased regional enhancement (i.e., greater Mn^{2+} uptake in regions of BBB opening) for the 10-min waiting period ($p < 0.01$, two-tailed t-test assuming unequal variance).

Effect of Rate of Drug Administration on BBB Opening

Comparison of rates of 1.8ml/min (BBB-3, Fig.7.5c) and 0.9ml/min (BBB-4, Fig.7-5d) for drug administration showed significantly better hemispheric coverage, greater than a factor two difference ($p < 0.001$) between them.

Effect of Mannitol Dose on BBB Opening

Three doses of 25% (w/v) mannitol were compared, that being 5ml/kg (BBB-4, Fig.7-5d), 6ml/kg (BBB-6, Fig.7-5f), and 7.5ml/kg (BBB-10, Fig.7-5j) at injection rates of 0.9ml/min and a waiting period of 10-min between mannitol injection and delivery of the $MnCl_2$ /Glu combination. The 6ml/kg dose resulted in significantly greater hemispheric coverage than that of the 5ml/kg or 7.5ml/kg doses ($p < 0.01$). Although there was no

Table 7-2. Quantitative Summary of Percent Hemispheric Enhancement, Hemispheric Coverage, and Regional Enhancement for the Optimization of BBB Opening Group (N = 10).

Animal #	% Hemispheric Enhancement (using Eq. 7-1)		% Hemispheric Coverage (using Eq. 7-2)		% Regional Enhancement (using Eq. 7-3)	
	Mean	ISSD	Mean	ISSD	Mean	ISSD
BBB-1	145	20	77	14	180	15
BBB-2	87	61	47	42	154	54
BBB-3	64	19	50	22	113	15
BBB-4	101	36	110	9	112	30
BBB-5	106	27	90	8	116	24
BBB-6;	130;	35;	115;	10;	123;	31;
BBB-7	118	31	64	23	185	41
BBB-8	55	30	44	43	73	66
BBB-9	66	18	109	10	14	31
BBB-10	90	12	92	13	99	18

significant difference between the levels of hemispheric enhancement between the three, the animal receiving the 6ml/kg dose had a mean hemispheric enhancement of 130% that was slightly higher than the remaining two (101% and 90% for the 5ml/kg and 7.5ml/kg doses, respectively).

Effect of MnCl₂/Glu Injection Rate on BBB Opening

Comparison of two different rates of MnCl₂/Glu injection, 1.8ml/min (BBB-5, Fig.7-5e) and 0.9ml/min (BBB-6, Fig.7-5f), yielded significantly better hemispheric coverage on the part of the 0.9ml/min injection rate ($p < 0.001$). Although there was no significant difference in hemispheric enhancement or regional MEMRI enhancement between the two, since the MnCl₂/Glu dose and the Mannitol dose/rate were identical, this was not surprising.

Effect of CCA Flow on BBB Opening

Three experimental setups were tested in order to ascertain the effect of the CCA flow on the heterogeneity of BBB opening. Three separate animals received the following: BBB-1 (Fig.7-5a) had the catheter placed in the ECA, which was then advanced into the ICA, limiting the CCA flow; BBB-6 (Fig.7-5f) had the catheter in the ECA only, permitting CCA flow; and BBB-8 (Fig.7-5h) had the catheter in the ECA only, but the CCA was clamped to stop CCA flow during mannitol injection. BBB-6 exhibited significantly greater levels of both hemispheric enhancement and coverage than that of BBB-1 or BBB-8 ($p < 0.01$).

Effect of Animal Variability on BBB Opening

BBB-6 (Fig.7-5e) and BBB-7 (Fig.7-5f) received the same protocol, but BBB-6 had significantly higher values of regional MEMRI enhancement ($p = 0.01$) and greater hemispheric coverage ($p < 0.01$) than BBB-7.

7.3.2 Temporal Evolution of Ischemia

Temporal Evolution of Lesion Volume

Fig. 7-6 shows the temporal evolution of the ischemic territory between 30-min and 3h post MCA-occlusion. For the 30-min timepoint post MCA occlusion, the abnormal population was subdivided into core and penumbra. The multislice parameter maps for $\langle D \rangle$, CBF_i , and T_2 are diagrammed in the left three columns. In the fourth column of Fig.7-6, the KM segmentation map is shown, with subdivision of the brain into normal

tissue, CSF, and two populations of abnormal tissue (i.e., core and penumbra). The penumbral region represents the tissue that is ‘at risk’ for progression to infarction and permanent neuronal injury. For the 3h timepoint post MCA occlusion, the $\langle D \rangle$ and KM maps (5th and 6th columns of Fig.7-6) are shown, with the corresponding TTC-stained sections at 24h (images taken for both the front and back of the stained slices, designated ‘f’ and ‘b’). These results indicate a progression of the penumbral region to infarct by the 3h-timepoint.

Temporal Evolution of Individual MR Parameters

Fig. 7-7 diagrams the evolution of $\langle D \rangle$ (Fig.7-7a), CBF_i (Fig.7-7b), and T_2 (Fig.7-7c) as a function of time post MCA-occlusion. Mean values for individual tissue populations were calculated based on a pixel-by-pixel comparison between the KM segmentation map and individual MR parameters. Fig.7-7a shows a trend of decreased $\langle D \rangle$ with the passage of time for the abnormal tissue population. Note that the mean $\langle D \rangle$ values for the core at 30-min and 60-min are very close to the values of the total abnormal region from 90-min on. This is expected because the core denotes permanently damaged tissue. Beyond 1hr post MCA-occlusion, tissue assigned to the abnormal population is expected to be core with no salvageable tissue remaining (i.e., no penumbra). Fig.7-7b shows a slight trend of decreased CBF_i for the abnormal population concomitant with an increase in CBF_i for the normal population. Increased CBF_i for normal tissue is likely from hyperperfusion in an attempt to compensate for the existing perfusion deficit. Fig. 7-7c shows relatively invariant T_2 values for all tissue regions. Pathologically induced changes in T_2 (i.e., edema) generally do not present until later timepoints, such as at 12h or 24h.

KM Correspondence with Histological Estimates

Fig. 7-8 shows the slice-by-slice correlation between KM percent hemispheric lesion volume at 3hr (%TBV) and TTC volume at 24hr (%TBV) for a representative animal. KM and TTC volumes were both found to be 28% of TBV, with good slice-by-slice correspondence (highly correlated, $r = 0.89$).

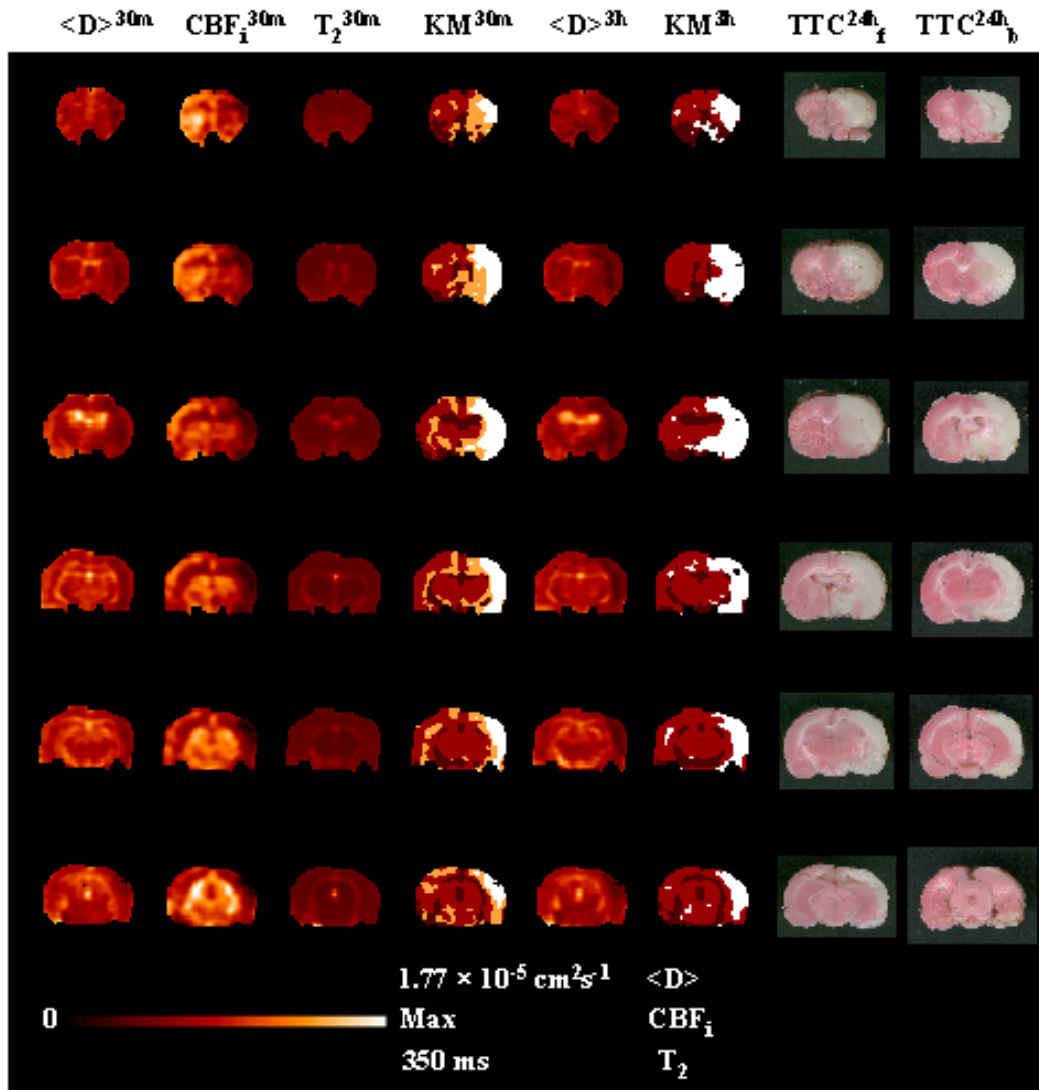


Figure 7-6. k-means (KM) segmentation of the ischemic rat brain into normal, abnormal (core, penumbra), and CSF at 30-min post MCA-occlusion. Multislice parameter maps are shown for $\langle D \rangle$, CBF_i , and T_2 in the first three columns, respectively. In the fourth column, the KM segmentation map is diagrammed with red = normal, brown = CBF, white = core, and peach = penumbra. The penumbra represents tissue at risk, i.e., potentially salvageable with therapeutic intervention. In the fifth and sixth columns, $\langle D \rangle$ and KM are shown for the 3h timepoint. Since this is a permanent MCAO model, the penumbra progresses to infarct. This is visible by comparison of the KM maps at 30-min and 3h. In the last two columns, the front (f) and back (b) of the TTC-stained sections are shown, demonstrating a good correspondence on a slice-by-slice basis with the 3h-KM map.

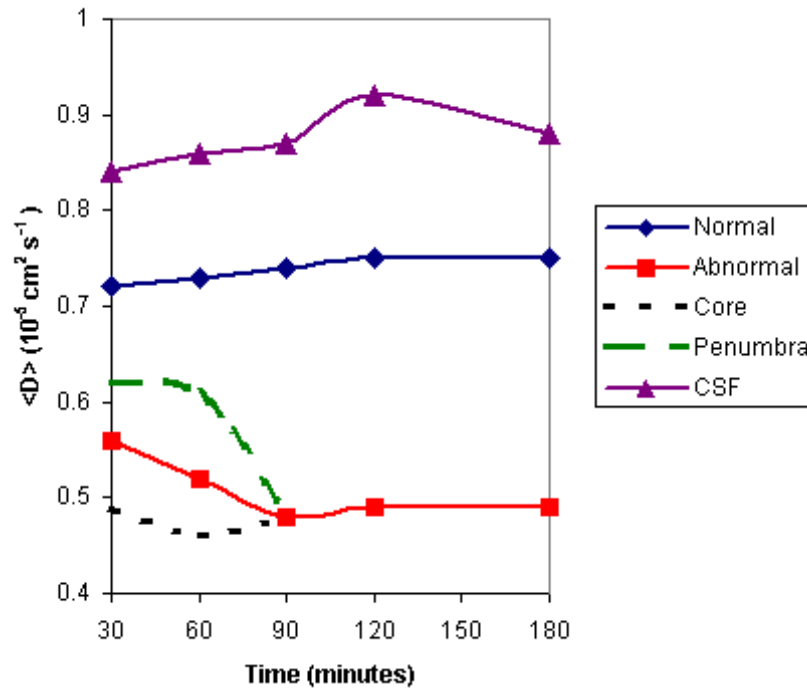


Figure 7-7a. Temporal evolution of $\langle D \rangle$ post MCA-occlusion. Mean values were determined from individual tissue populations based on KM segmentation.

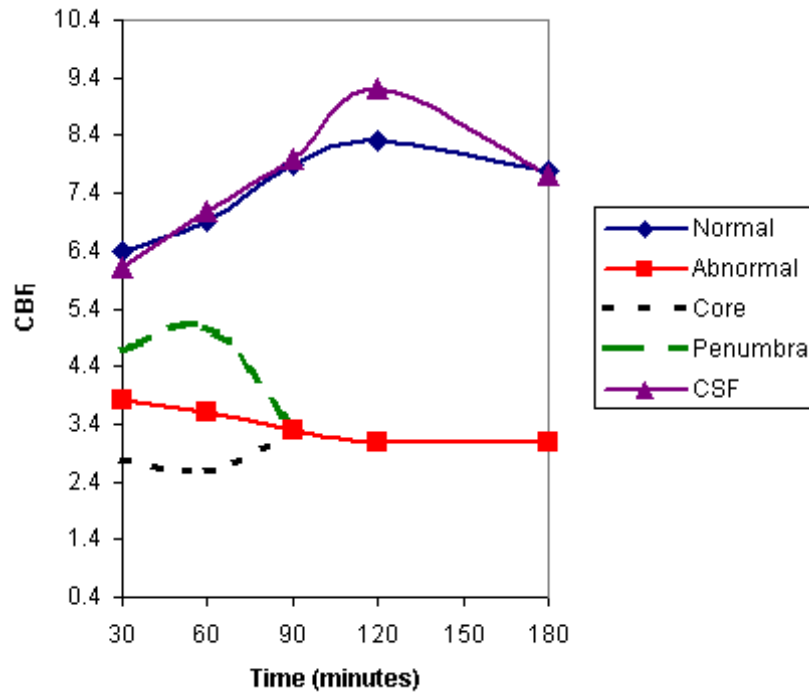


Figure 7-7b. Temporal evolution of CBF_i post MCA-occlusion. Mean values were determined from individual tissue populations based on KM segmentation.

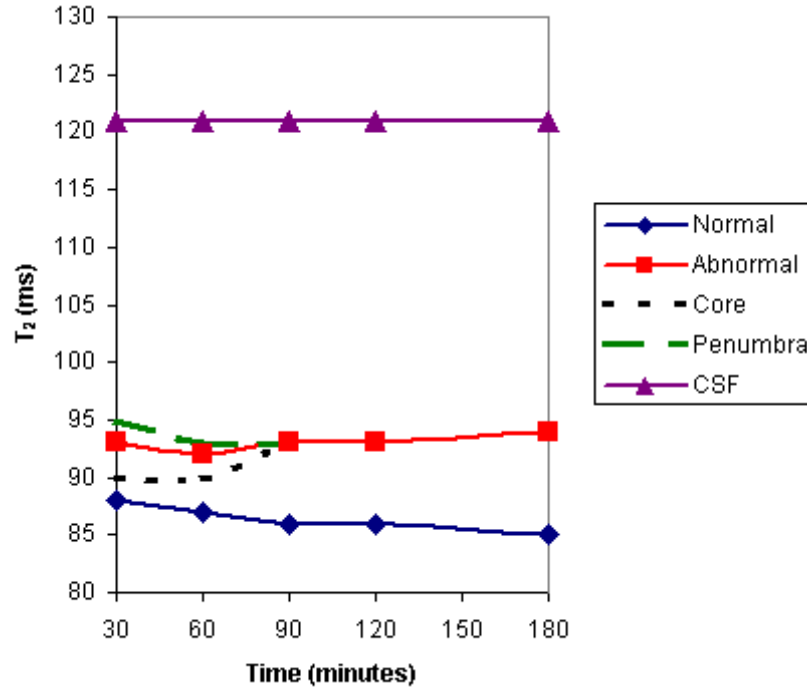


Figure 7-7c. Temporal evolution of T₂ post MCA-occlusion. Mean values were determined from individual tissue populations based on KM segmentation.

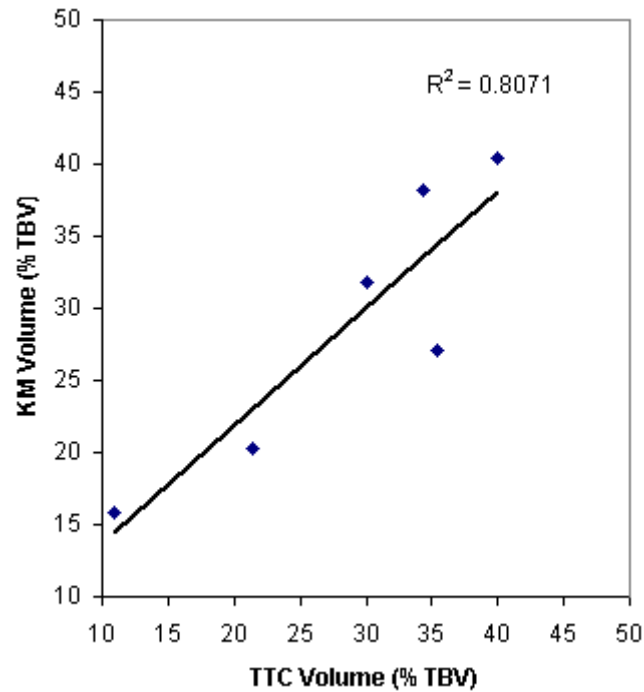


Figure 7-8. Scatter plot of KM-derived lesion volume (at 3hr) versus TTC-derived lesion volume (at 24hr) on a slice-by-slice basis for a representative animal. Values were highly correlated ($r = 0.89$).

7.3.3 MEMRI and Ischemia

Temporal Evolution of Lesion Volume

Fig. 7-9 shows the temporal evolution of the ischemic territory between 30-min and 60-min post MCA-occlusion. For both timepoints, the brain was divided into four regions based on the correspondence between the $\langle D \rangle$ lesion estimate and the MEMRI lesion estimate. The multislice parameter maps for $\langle D \rangle$ and the corresponding T_1W images are diagrammed in the 1st and 2nd columns for 30-min and the 4th and 5th columns for 60-min. The 3rd and 6th columns show the color-coded maps, with blue = normal, red = $\langle D \rangle/T_1W$ lesion, yellow = T_1W lesion, and orange = $\langle D \rangle$ lesion. For the 30-min timepoint, there is a large lesion on T_1W , but nothing on $\langle D \rangle$ (Fig.7-9, 3rd column, yellow). By 60-min, a central core region (Fig.7-9, 6th column, red) with abnormal $\langle D \rangle$ and MEMRI enhancement is evident, surrounded by a peripheral region (Fig.7-9, 6th column, yellow) with significant MEMRI enhancement but $\langle D \rangle$ values around 0.60 to $0.65 \times 10^{-5} \text{ cm}^2\text{s}^{-1}$.

Quantitative Summary of Individual Tissue Regions

Table 7-3 provides a quantitative summary of $\langle D \rangle$ and T_1W values for individual tissue regions. Values are presented as mean \pm SD. For the 30-min timepoint, since no pixels were assigned to the $\langle D \rangle$ lesion (orange), there are no values for $\langle D \rangle$ or T_1W percentage increase. For the central core region (Fig.7-9, red), characterized by severely reduced $\langle D \rangle$ and significant hyperintensity on T_1W , there seems to be no appreciable change in $\langle D \rangle$ or T_1W percentage signal increase between 30-min and 60-min. For the peripheral region (Fig.7-9, yellow), characterized by significant hyperintensity on T_1W with close to normal values for $\langle D \rangle$, there is an additional 20% increase in signal intensity on T_1W between 30-min and 60-min, accompanied by an approximate 10% decline in $\langle D \rangle$. There were no appreciable changes for normal brain (Fig.7-9, blue).

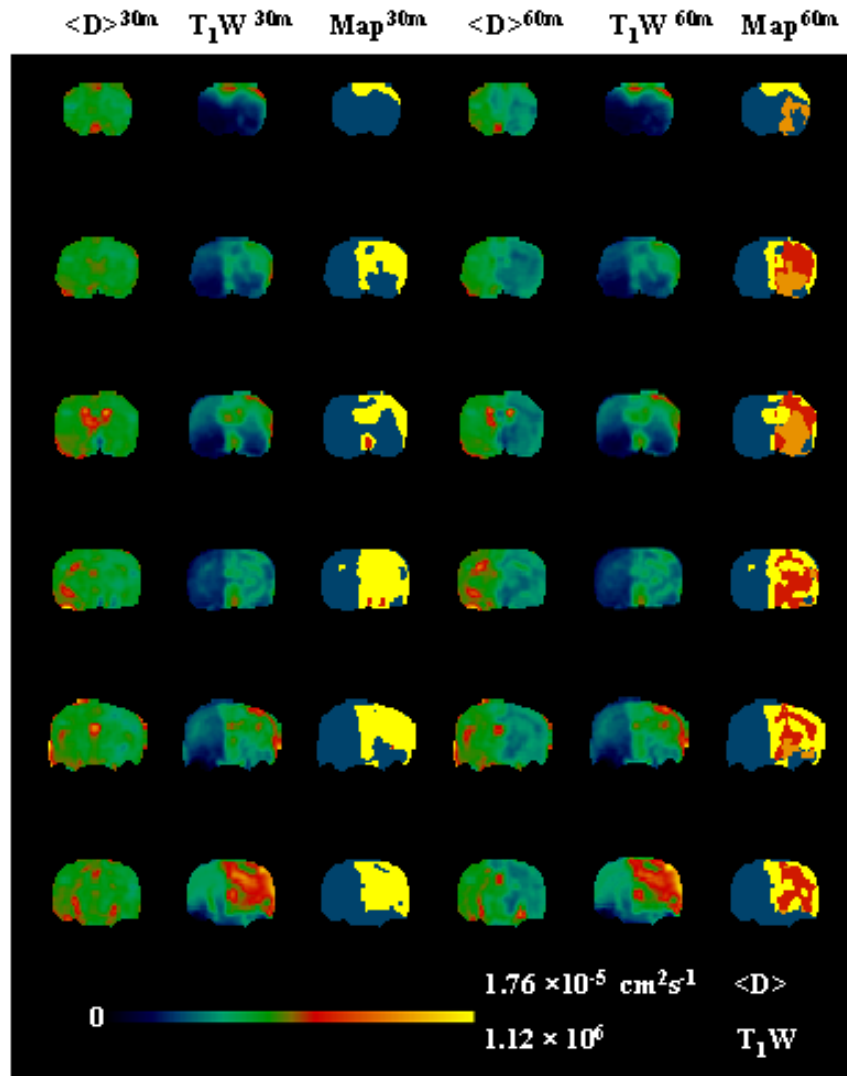


Figure 7-9. Segmentation of the ischemic rat brain into normal and abnormal regions at 30-min and 60-min post MCA-occlusion. Multislice parameter maps are shown for $\langle D \rangle$ (1st and 4th columns), with the corresponding T_1 -weighted MEMRI images (2nd and 5th columns). In the 3rd and 6th columns, color-coded maps were generated based on the correspondence between regions exhibiting lesion on $\langle D \rangle$ (values less than or equal to $0.52 \times 10^{-5} \text{ cm}^2 \text{ s}^{-1}$) and lesion on the T_1 -weighted MEMRI (values greater than mean + 2 SD of the contralateral hemisphere). Color designations are as follows: blue = normal $\langle D \rangle$ and normal T_1W , yellow = abnormal T_1W , orange = abnormal $\langle D \rangle$, and red = abnormal $\langle D \rangle$ and abnormal T_1W . The color maps demonstrate that MEMRI enhancement precedes the development of an ADC lesion (yellow region, 30-min), making it a potential marker for tissue ‘at risk’. For the 60-min timepoint, regions that are lesion on both $\langle D \rangle$ and MEMRI (red) likely represent the infarct core, whereas regions that are lesion only on MEMRI (yellow) may indicate tissue at risk (i.e., peri-infarct depolarization).

Table 7-3. Quantitative Summary of $\langle D \rangle$ and MEMRI enhancement for individual tissue populations based on a threshold of $0.52 \times 10^{-5} \text{ cm}^2\text{s}^{-1}$ for $\langle D \rangle$ and a threshold of the mean + 2 SD (based on the contralateral hemisphere).

Tissue Region	30-min post MCA-occlusion		60-min post MCA-occlusion	
	$\langle D \rangle$ ($10^{-5} \text{ cm}^2\text{s}^{-1}$)	T ₁ W Increase (%)	$\langle D \rangle$ ($10^{-5} \text{ cm}^2\text{s}^{-1}$)	T ₁ W Increase (%)
Normal	0.8 ± 0.1	40 ± 50	0.8 ± 0.1	40 ± 50
$\langle D \rangle$ and T ₁ W lesion	0.46 ± 0.05	170 ± 60	0.47 ± 0.07	180 ± 80
T1W lesion	0.7 ± 0.1	180 ± 80	0.6 ± 0.1	200 ± 100
$\langle D \rangle$ lesion	n/a*	a/a*	0.47 ± 0.03	60 ± 40

*There were no pixels below the $\langle D \rangle$ threshold at 30-min post MCA-occlusion, therefore, there are no mean \pm SD values for $\langle D \rangle$ or T₁W percentage increase.

7.4 Discussion

7.4.1 Cellular Uptake of Manganese

Mechanisms of Manganese Uptake During Ischemia

Two types of depolarization occur during the temporal evolution of cerebral ischemia: terminal anoxic depolarizations (present in the infarct core) and transient depolarizations (present at the core periphery, i.e., the penumbra). In the case of terminal anoxic depolarization, both ligand-gated (ex. NMDA-receptor mediated) and voltage-gated Ca^{2+} channels are activated, permitting Ca^{2+} influx. Buildup of $[\text{Ca}^{2+}]_i$ triggers the release of excitatory neurotransmitters, such as glutamate, as well as an increase in $[\text{K}^+]_o$. Both of these, glutamate and K^+ , have been shown to induce cellular depolarization; therefore, their spread to the edge of the core likely induce PIDs. Individual PIDs yield transient activation of voltage-gated Ca^{2+} channels, permitting Ca^{2+} influx until which time cellular

repolarization and channel closing occurs. Mn^{2+} , a paramagnetic Ca^{2+} analog shown to enter cells via Ca^{2+} -mediated pathways (34,35), has recently been employed in the visualization of experimental CSD (39) and for the characterization of cerebral ischemia (37). Since MEMRI is able to identify experimentally-induced CSDs, it should be able to identify pathologically-induced depolarizations—both anoxic and peri-infarct. Although Aoki's study of focal ischemia (37) was able to identify the ischemic territory using MEMRI, there was a temporal discrepancy between T_1 -weighted MRI and DWI data acquisition of approximately one hour. As there is considerable lesion progression within the first 1-2 hours following permanent MCA occlusion, this time may account for the smaller manganese-enhanced area seen on T_1 -weighted MRI versus that of DWI. Since both anoxic and peri-infarct depolarizations induce Ca^{2+} influx, the volume of MEMRI enhancement should be larger than the DWI lesion at acute timepoints, with temporal progression of the diffusion deficit to match the initial MEMRI-enhanced region. In order to assess the MEMRI-DWI 'mismatch', increased temporal resolution is necessary.

7.4.2 Heterogeneity of BBB Opening

Manganese as an Intracellular Marker

Since accumulated $[Mn^{2+}]_i$ is retained following a specific stimulus (i.e., functional activation, experimentally-induced CSD, or cerebral ischemia), and since there is negligible MEMRI enhancement when Mn^{2+} is restricted to the interstitial space, any resultant MEMRI enhancement is likely from an increase in $[Mn^{2+}]_i$. Mn^{2+} has several coordination sites for water binding, and when inside the cell it tends to be complexed with macromolecules such as proteins. This makes for longer τ_c correlation times, increasing the relaxivity and significantly shortening T_1 . While outside the cell, Mn^{2+} is in a free state, and with relatively fast exchange rates, it has a relatively minimal effect on relaxivity and T_1 values. It is for these reasons that Mn^{2+} may serve as a powerful intracellular marker.

Dependence of Manganese Accumulation on BBB Disruption

Although this is the case, the intracellular accumulation of Mn^{2+} requires the presence of Mn^{2+} in the interstitium at the time of stimulus. In order to get Mn^{2+} into the interstitial space, the BBB is osmotically disrupted using a hypertonic mannitol solution. Since

BBB opening via mannitol is reversible, over the time course at which the BBB is disrupted there exists a window of opportunity for drug delivery. This is based on maximum osmotic shrinkage of the endothelial cells and widening of intercellular tight junctions. Previous reports have indicated the onset of optimal BBB opening to be up to 15-min post mannitol administration (46,47), with dependence on mannitol concentration, dose, and rate of injection. Additional factors affecting BBB opening via mannitol include temperature and blood pressure. In order to ascertain the optimum BBB-opening methodology, various drug dose, timing, and rates of administration were tested (Table 7-1). Based on the results for the optimization of BBB-opening group (Fig.7-5 and Table 7-2), it was determined that 6ml/kg of 25% (w/v) mannitol delivered at a rate of 0.9ml/min, followed by a 10-min waiting period, provided the best overall hemispheric enhancement and coverage (BBB-6, Fig.7-5f). Following optimization of mannitol administration, the rate of MnCl_2 administration was tested. A rate of 0.9ml/min (BBB-6, Fig.7-5f) resulted in significantly better hemispheric coverage ($p < 0.001$) than a rate of 1.8ml/min (BBB-5, Fig.7-5e). Although there was no significant differences in regional enhancement (i.e., degree of enhancement in regions of BBB opening), because the dose of MnCl_2 was kept constant, the amount of accumulated $[\text{Mn}^{2+}]_i$ could potentially be the same for the two.

CCA Flow Dependence on BBB Opening

Limitations imposed on CCA flow (i.e., partial blockage from catheter placement or clamping of the vessel) during mannitol delivery resulted in poor hemispheric coverage and enhancement (flow-limited = BBB-1 and BBB-2, Fig.7-5a and Fig.7-5b; no flow = BBB-8, Fig.7-5h). These results indicate that maintenance of CCA flow is extremely important for effective BBB disruption and a homogeneous distribution of Mn^{2+} in the interstitial space prior to application of the desired stimulus. Placement of the catheter in the ICA or CCA clamping reduces the flow, resulting in inefficient delivery of mannitol to the hemisphere-of-interest. This results in patchy enhancement or no enhancement at all. Since flow is affected by physiological variables such as body temperature and blood pressure, it is extremely important to keep the animals warm while also maintaining a constant level of anesthesia.

Issue of Intra-animal Variability

Even with optimization of the MEMRI protocol, it is important to keep in mind that intra-animal variability in terms of vessel architecture, brain volume, age, and weight may also affect BBB opening. In a recent report by Aoki and coworkers (48), several methodological issues with MEMRI were identified, such as potential brain swelling from mannitol injection, anesthetic level effect on enhancement, as well as the contribution of intra-animal variability to heterogeneous BBB opening. The effect of inter-animal variability is evident in the comparison of two animals having receiving the optimized protocol described above. Both BBB-6 (Fig.7-5f) and BBB-7 (Fig.7-5g) received the same protocol, but differed significantly in regional MEMRI enhancement ($p = 0.01$) and hemispheric coverage ($p < 0.01$).

7.4.3 Temporal Evolution of Ischemia

KM segmentation provides a time-invariant method of tissue segmentation requiring minimal user intervention for subdivision of the brain into normal tissue, abnormal tissue (with subdivision into core and penumbra at early timepoints [30-min, 60-min] post MCAO), and CSF (Fig.7-6). Delineation between the infarct core, regions exhibiting severely reduced $\langle D \rangle$ and CBF_i values, and the penumbra, regions with decreased CBF_i and slightly reduced $\langle D \rangle$, permits identification of tissue at risk. Since this is a permanent MCAO model, all tissue identified as penumbra (Fig.7-6, 4th column, peach) progresses to infarct by 3hr (Fig.7-6, 6th column, white). KM may provide a method for severity assessment and potential therapeutic intervention. Additional studies employing permanent and transient MCAO with and without therapeutic intervention, and the tracking of the penumbral region (i.e., prediction of tissue fate), would be required in order to ascertain the overall utility and clinical relevance.

7.4.4 MEMRI and Ischemia

The goal of this study was to demonstrate the utility of MEMRI for characterizing the ischemic territory. Based on the correspondence between the MEMRI-defined lesion and the $\langle D \rangle$ -defined lesion, four tissue regions were identified and color-coded (Fig.7-9). The first region was characterized by severely reduced $\langle D \rangle$ and significant MEMRI enhancement (Fig.7-9, 6th column, red). This region is presumably core because the

severely reduced $\langle D \rangle$ values are reflective of cytotoxic edema and the hyperintensity on T_1W is most likely from terminal anoxic depolarization and massive influx of Mn^{2+} . Coverage included sub-cortical regions such as the caudate-putamen and globus pallidus of the basal ganglia, which tends to be infarcted in both animal models of ischemia as well as in the clinical setting. The second region was characterized by normal to slightly reduced $\langle D \rangle$ values and significant MEMRI enhancement (Fig.7-9, 6th column, yellow). Coverage was generally along the periphery of the core. This region, presumably salvageable tissue, most likely represents a region experiencing transient PIDs. This is supported by the additional 20% signal intensity increase on MEMRI with a concomitant 10% decrease in $\langle D \rangle$ between the 30-min and 60-min timepoints. These results indicate that repetitive PIDs yield further Mn^{2+} influx and depletion of energy metabolism to restore membrane-ion gradients. Since the area exhibiting significant MEMRI enhancement (Fig.7-9, 3rd column, yellow) preceded the development of $\langle D \rangle$ lesion, MEMRI may provide an additional technique for identifying tissue at risk for infarction at acute timepoints post-ischemic onset.

7.4.4 Utility of MEMRI for PID Identification

In order to determine MEMRI visualization of PIDs versus that of anoxic depolarization, a multispectral (MS) approach investigating the temporal evolution of $\langle D \rangle$, CBF_i , T_2 , and MEMRI needs to be performed with histological validation. MS analysis provides an improved estimate of ischemic lesion volume over that obtained from $\langle D \rangle$ alone (43,44,49). Jacobs and coworkers (50,51) demonstrated that MS analysis using the ISODATA technique (similar to KM, but doesn't require *a priori* knowledge of the number of clusters) performed equally well to single parameter methods (DWI, PWI, and T_2WI). MS analysis, in addition to being as robust as standard methodology, permits subdivision of the ischemic territory into infarct core and a penumbral region that is potentially salvageable, opening the window for therapeutic assessment. Although T_1 -weighted MEMRI has been employed for the visualization of experimentally-induced CSDs and in the characterization of cerebral ischemia, it only provides a relative measure of $[Mn^{2+}]_i$ accumulation based on changes in signal intensity. Acquisition of a T_1 -dataset would provided a more quantitative assessment of $[Mn^{2+}]_i$. Preliminary results shown here indicate that MEMRI is a potentially useful method for identifying tissue at risk for

infarction, and may provide a way for visualizing PIDs and their role in the temporal evolution of cerebral ischemia with and without pharmacological intervention (such as MK-801, a NMDA-receptor antagonist).

Acknowledgements

Thanks to David Bennett (Worcester Polytechnic Institute, MA) for collaborative acquisition of data for the optimization of BBB opening group and Dr. Ichio Aoki (Meiji University, Kyoto, Japan) for helpful advice on optimizing the MEMRI protocol.

References

1. Astrup J, Symon L, Branston M, Lassen NA. Cortical evoked potential and extracellular K^+ and H^+ at critical levels of brain ischemia. *Stroke* 1977;8:51-57.
2. Branston NM, Strong AJ, Symon L. Extracellular potassium activity, evoked potential and tissue blood flow: relationships during progressive ischemia in baboon cortex. *J Neurol Sci* 1977;32:305-321.
3. Hansen AJ. Effect of anoxia on ion distribution in the brain. *Phys Rev* 1985;65:101-148.
4. Harris RJ, Symon L, Branston NM, Bayhan M. Changes in extracellular calcium activity in cerebral ischaemia. *J Cereb Blood Flow Metab* 1981;1:203-209.
5. Hansen AJ, Zeuthen T. Extracellular ion concentrations during spreading depression and ischemia in the rat brain cortex. *Acta Phys Scand* 1981;113:437-445.
6. Schwartz NE, Alford S. Physiological activation of presynaptic metabotropic glutamate receptors increases intracellular calcium and glutamate release. *J Neurophysiol* 2000;84:415-427.
7. Jeremic A, Jeftinija K, Stevanovic J, Glavaski A, Jeftinija S. ATP stimulates calcium-dependent glutamate release from cultured astrocytes. *J Neurochem* 2001;77:664-675.
8. Leao AAP. Spreading depression of activity in the cerebral cortex. *J Neurophysiol* 1944;7:359-390.
9. Leao AAP. Further observations on the spreading depression of activity in the cerebral cortex. *J Neurophysiol* 1947;10:409-414.
10. Nedergaard M, Astrup J. Infarct rim: effect of hyperglycemia on direct current potential and [^{14}C]2-deoxyglucose phosphorylation. *J Cereb Blood Flow Metab* 1986;6:607-615.
11. Hossmann KA. Periinfarct depolarizations. *Cerebrovasc Brain Metab Rev* 1996;8:195-208.
12. Graf R, Saito R, Hubel K, Fujita T, Rosner G, Heiss WD. Spreading depression-like DC-negativations turn into terminal depolarization after prolonged focal ischemia in rats. *J Cereb Blood Flow Metab* 1995;15(suppl 1):S15.

13. Rother J, deCrespigny A, D'Arceuil H, Yoshikawa J, Iwai K, Moseley S, Moseley M. Transient ADC changes in periinfarct tissue in rat. *J Cereb Blood Flow Metab* 1995;15(suppl 1)(S361).
14. Gyngell ML, Busch E, Schmitz B, Kohno K, Back T, Hoehn-Berlage M, Hossmann KA. Evolution of acute focal cerebral ischaemia in rats observed by ¹H-MRS, diffusion-weighted MRI, and electrophysiological monitoring. *NMR Biomed* 1995;8:206-214.
15. Back T, Hoehn M, Mies G, Busch E, Schmitz B, Kohno K, Hossmann KA. Penumbra tissue alkalosis in focal cerebral ischemia: relationship to energy metabolism, blood flow, and steady potential. *Ann Neurol* 2000;47:485-492.
16. Ohta K, Graf R, Rosner G, Heiss W-D. Calcium ion transients in peri-infarct depolarizations may deteriorate ion homeostasis and expand infarction in focal cerebral ischemia in cats. *Stroke* 2000;32:535-543.
17. Pinard E, Nallet H, MacKenzie ET, Seylaz J, Roussel S. Penumbra microcirculatory changes associated with peri-infarct depolarizations in the rat. *Stroke* 2001;33:606-612.
18. Mies G, Iijima T, Hossmann KA. Correlation between peri-infarct DC shifts and ischaemic neuronal damage in rat. *Neuroreport* 1993;4:709-711.
19. Miettinen S, Fusco FR, Yrjanheikki J, Keinanen R, Hirvonen T, Roivainen R, Narhi M, Hokfelt T, Koistinaho J. Spreading depression and focal brain ischemia induce cyclooxygenase-2 in cortical neurons through N-methyl-D-aspartic acid-receptors and phospholipase A₂. *Proc Natl Acad Sci* 1997;94:6500-6505.
20. Collaco-Moraes Y, Aspey B, Harrison M, deBelleruche J. Cyclo-oxygenase-2 messenger RNA induction in focal cerebral ischemia. *J Cereb Blood Flow Metab* 1996;16:1366-1372.
21. Takano K, Latour LL, Formato JE, Carano RAD, Helmer KG, Hasegawa Y, Sotak CH, Fisher M. The role of spreading depression in focal ischemia evaluated by diffusion mapping. *Ann Neurol* 1996;39:308-318.
22. Busch E, Gyngell ML, Eis M, Hoehn-Berlage M, Hossmann KA. Potassium-induced cortical spreading depressions during focal cerebral ischemia in rats: contribution to lesion growth assessed by diffusion-weighted NMR and biochemical imaging. *J Cereb Blood Flow Metab* 1996;16:1090-1099.
23. Dijkhuizen RM, Beekwilder JP, van der Worp HB, Berkelbach van der Sprenkel JW, Tulleken KAF, Nicolay K. Correlation between tissue depolarizations and damage in focal ischemic rat brain. *Brain Res* 1999;840:194-205.
24. Mancuso A, Derugin N, Hara K, Marsh TA, Kong D, Sharp FR, Weinstein PR. Cyclooxygenase-2 mRNA expression is associated with c-fos mRNA expression and transient water ADC reduction detected with diffusion MRI during acute focal ischemia in rats. *Brain Res* 2003;961:121-130.
25. Lin YJ, Koretsky AP. Manganese ion enhances T₁-weighted MRI during brain activation: an approach to direct imaging of brain function. *Magn Reson Med* 1997;38:378-388.
26. Duong TQ, Silva AC, Lee SP, Kim SG. Functional MRI of calcium-dependent synaptic activity: cross correlation with CBF and BOLD measurements. *Magn Reson Med* 2000;53:383-392.

27. Aoki I, Tanaka C, Takegami T, Ebisu T, Umeda M, Fukunaga M, Fukuda K, Silva AC, Koretsky AP, Naruse S. Dynamic activity-induced manganese-dependent contrast magnetic resonance imaging (DAIM MRI). *Magn Reson Med* 2002;48:927-933.
28. Morita H, Ogino T, Seo Y, Fujiki N, Tanaka K, Takamata A, Nakamura S, Murakami M. Detection of hypothalamic activation by manganese ion contrasted T₁-weighted magnetic resonance imaging in rats. *Neurosci Lett* 2002;326:101-104.
29. Aoki I, Wu YJL, Silva AC, Lynch RM, Koretsky AP. In vivo detection of neuroarchitecture in the rodent brain using manganese-enhanced MRI. *Neuroimage* 2004;22:1046-1059.
30. Tjalve H, Mejare C, Borg-Neczak K. Uptake and transport of manganese in primary and secondary olfactory neurones in pike. *Pharmacol Toxicol* 1995;77:23-31.
31. Pautler RG, Silva AC, Koretsky AP. In vivo neuronal tract tracing using manganese-enhanced magnetic resonance imaging. *Magn Reson Med* 1998;40:740-748.
32. Pautler RG, Koretsky AP. Tracing odor-induced activation in the olfactory bulbs of mice using manganese-enhanced magnetic resonance imaging. *Neuroimage* 2002;16:441-448.
33. Saleem KS, Pauls JM, Augath M, Trinath T, Prause BA, Hashikawa T, Logothetis NK. Magnetic resonance imaging of neuronal connections in the macaque monkey. *Neuron* 2002;34:685-700.
34. Drapeau P, Nachshen DA. Manganese fluxes and manganese-dependent neurotransmitter release in presynaptic nerve endings isolated from rat brain. *J Physiol* 1984;348:493-510.
35. Narita K, Kawasaki F, Kita H. Mn and Mg influxes through Ca channels of motor nerve terminals are prevented by verapamil in frogs. *Brain Res* 1990;510:289-295.
36. Chapman RA, Ellis D. Uptake and loss of manganese from perfused frog ventricles. *J Physiol* 1977;272:355-366.
37. Aoki I, Ebisu T, Tanaka C, Katsuta K, Fujikawa A, Umeda M, Fukunaga M, Takegami T, Shapiro EM, Naruse S. Detection of the anoxic depolarization of focal ischemia using manganese-enhanced MRI. *Magn Reson Med* 2003;50:7-12.
38. DeGraba TJ, Ostrow PT, Grotta JC. Threshold of calcium disturbances after focal cerebral ischemia in rats: implications of the window of therapeutic opportunity. *Stroke* 1993;24:1212-1216.
39. Henning EC, Meng X, Fisher M, Sotak CH. Visualization of cortical spreading depression using manganese-enhanced MRI. *Magn Reson Med* 2005;53:851-857.
40. Benner T, Heiland S, Erb G, Forsting M, Sartor K. Accuracy of gamma-variate fits to concentration-time curves from dynamic susceptibility-contrast enhanced MRI: influence of time resolution, maximal signal drop, and signal-to-noise. *Magn Reson Imaging* 1997;15:307-317.
41. Hamberg LM, Macfarlane R, Tasmiroglu E, Boccalini P, Hunter GJ, Belliveau JW, Moskowitz MA, Rosen BR. Measurement of the cerebrovascular changes in

- cats after transient ischemia using dynamic magnetic resonance imaging. *Stroke* 1993;24:444-451.
42. Duda RO, Hart PE, Stork DG. *Pattern classification*. New York: Wiley; 2001.
 43. Carano RA, Takano K, Helmer KG, Tatlisumak T, Irie K, Petrucci JD, Fisher M, Sotak CH. Determination of focal ischemic lesion volume in the rat brain using multispectral analysis. *J Magn Reson Imaging* 1998;8:1266-1278.
 44. Carano RA, Li F, Irie K, Helmer KG, Silva MD, Fisher M, Sotak CH. Multispectral analysis of the temporal evolution of cerebral ischemia in the rat brain. *J Magn Reson Imaging* 2000;12:842-858.
 45. Kazemi M, Silva MD, Li F, Fisher M, Sotak CH. Investigation of techniques to quantify in vivo lesion volume based on comparison of water apparent diffusion coefficient (ADC) maps with histology in focal cerebral ischemia of rats. *Magn Reson Imaging* 2004;22:653-659.
 46. Cosolo WC, Martinello P, Louis WJ, Christophidis N. Blood-brain barrier disruption using mannitol: time course and electron microscopy studies. *Am J Physiol* 1989;256:R443-R447.
 47. Rapoport SI. Advances in osmotic opening of the blood-brain barrier to enhance CNS chemotherapy. *Expert Opinion on Investigational Drugs* 2001;10:1809-1818.
 48. Aoki I, Naruse S, Tanaka C. Manganese-enhanced magnetic resonance imaging (MEMRI) of brain activity and applications to early detection of brain ischemia. *NMR Biomed* 2004;17:532-543.
 49. Jacobs MA, Zhang ZG, Knight RA, Soltanian-Zadeh H, Goussev AV, Peck DJ, Chopp M. A model for multiparametric MRI tissue characterization in experimental cerebral ischemia with histological validation in rat. *Stroke* 2001;32:943-949.
 50. Jacobs MA, Mitsias P, Soltanian-Zadeh H, Santhakumar S, Ghanei A, Hammond R, Peck DJ, Chopp M, Patel S. Multiparametric MRI tissue characterization in clinical stroke with correlation to clinical outcome. Part 2. *Stroke* 2001;32:950-957.
 51. Mitsias PD, Jacobs MA, Hammoud R, Pasnoor M, Santhakumar S, Papamitsakis NIH, Soltanian-Zadeh H, Lu M, Chopp M, Patel SC. Multiparametric MRI ISODATA ischemic lesion analysis. Correlation with the clinical neurological deficit and single-parameter MRI techniques. *Stroke* 2002;33:2839-2844.

CHAPTER 8

SUMMARY

The research presented within this dissertation focused on two major areas of research: monitoring the response to single-dose radiotherapy in a RIF-1 tumor model and the role of cortical spreading depression in the evolution of ischemic stroke. In Chapters 3 and 4, the apparent diffusion coefficient (ADC), spin-spin relaxation time (T_2), and proton density (M_0) were employed for the characterization of the radiotherapeutic response in a radiation-induced fibrosarcoma (RIF-1) tumor model. Chapter 3 described application of multispectral (MS) analysis using the k-means (KM) clustering algorithm for tumor tissue characterization, with histological validation via hematoxylin-eosin (H&E) staining and hypoxic-inducible factor-1alpha ($HIF-1\alpha$) immunohistochemistry. Following optimization, Chapter 4 described the application of the methodology in Chapter 3 in monitoring the radiotherapeutic response (i.e., the temporal evolution of the apparent diffusion coefficient (ADC)). In Chapters 6 and 7, manganese-enhanced MRI (MEMRI) was employed for the characterization of both experimental and pathological cortical spreading depression (CSD). Chapter 6 described the utility of MEMRI in the visualization of experimental CSD. Chapter 7 then employed similar methodology to monitor the temporal evolution of ischemia, specifically the role of peri-infarct depolarizations (PIDs) in the evolution of penumbral tissue to infarction. A brief description for the two major areas of research presented within this dissertation is provided on the following pages.

Part 1: Monitoring Response to Single-Dose Radiotherapy in a RIF-1 Tumor Model

Assessment of therapeutic efficacy is confounded by intra-tumor and inter-tumor heterogeneity. Variable pre-treatment tissue composition, tumor size, and growth kinetics, as well as post-treatment cell kill and tumor regrowth complicate dose-optimization and the comparison of treatment regimens in animal oncological studies. In addition, the roles of various processes (vasogenic edema, reduced cell density, formation of necrosis, and tumor regrowth) with potential contribution to the temporal evolution of the total apparent diffusion coefficient (ADC) are not fully understood.

In order to address these issues, two major goals were developed: first, to gain insight into the various processes whose combination yield the total ADC response over time; second, to identify the contribution of tissue heterogeneity (viable, necrotic) to the treatment response and changes in tumor growth kinetics and cell kill. To this end, a multi-spectral (MS) approach, combining ADC and T_2 parameter maps with k-means (KM) clustering, was employed for estimation of multiple compartments within both viable tumor tissue and necrosis following single-dose (1000 cGy) radiotherapy in a radiation-induced fibrosarcoma (RIF-1) tumor model. Results were compared with conventional histology via the hematoxylin-eosin (H&E) staining procedure (for identification of regions of viable tumor versus necrosis), as well as via hypoxic-inducible factor-1alpha (HIF-1 α) immunohistochemistry (for identification of regions of hypoxia versus well-oxygenated tissue).

The results of this study demonstrate that the MS analysis provides: (1) an improved tissue segmentation method over results obtained from conventional single-parameter approaches, (2) subdivision based on the degree of necrosis, as well as delineation between well-oxygenated and hypoxic viable tissue, (3) good correlation with both H&E staining and HIF-1 α immunohistochemistry, and (4) a method for monitoring the range of tissue viability as a function of time post-treatment, with the potential for predicting therapeutic efficacy.

Part 2: Role of Spreading Depression in Ischemic Stroke

At present, the mechanisms by which focal ischemia evolves into infarction remain poorly understood. Past studies suggest a causative role of spreading depression (SD) in the evolution of focal brain ischemia. Recent studies have reported the use of manganese ions (Mn^{2+}) as a depolarization-dependent contrast agent in monitoring brain activation through the application of glutamate, as well as in the study of focal ischemia. Since SD or SD-like depolarizations induce calcium (Ca^{2+}) influx following loss of ion homeostasis, and knowing that Mn^{2+} , having an ionic radius similar to that of Ca^{2+} , is handled in a similar manner to Ca^{2+} , these studies suggest the possible use of Mn^{2+} in tracking SD or SD-like depolarizations in the evolution of focal brain ischemia.

In order to determine the utility of Mn^{2+} as a marker for SD, experimental SD was elicited by chemical stimulation (KCl application to exposed rat cortex) and compared with control conditions. This study demonstrated that (1) Mn^{2+} is a more accurate marker for SD than DWI or T_2^* methods, (2) cortical restriction of MEMRI enhancement supports the contention that apical dendrites are necessary for SD propagation. (3) subcortical enhancement was a result of cortical-subcortical neuronal connectivity. Based on these results, preliminary experiments involving the study of SD in ischemia using Mn^{2+} were performed. Initial results indicate: (1) MEMRI may provide a method for estimating the likelihood of progression to infarction at acute timepoints post onset of stroke. These studies provide a foundation for further investigation into the role of SD in stroke, and the application of Mn^{2+} towards the design of therapeutic strategies targeting SD inhibition.

Conclusions and Medical Significance

The research within this dissertation employed magnetic resonance imaging techniques for monitoring the temporal evolution of pathological disease states such as focal ischemia and cancer, with and without therapeutic intervention. Optimization of these techniques in experimental models will open the possibility for future application in a clinical setting. Clinical availability of these non-invasive methods, with the ability to detect an early therapeutic response or to provide staging and prediction of tissue fate, would greatly aid in patient management of both cancer and stroke.

APPENDIX

Erica C. Henning

Home Address

214K E. Mountain St., Apt. 158
Worcester, MA 01606
(508) 335-2327

E-mail Address

ehenning@wpi.edu

Work Address

Worcester Polytechnic Institute
Biomedical Engineering Dept.
100 Institute Road
Worcester, MA 01609
(508) 752-3110
FAX: (508) 831-5541

EDUCATION

2000 – 2005 Worcester Polytechnic Institute (WPI) and UMASS Medical School,
Worcester, MA
Ph.D. in Biomedical Engineering and Medical Physics
GPA = 3.8/4.0

1996 – 2000 Florida State University, Tallahassee, FL
B.S. in Physics
GPA = 3.4/4.0

DOCTORAL THESIS

Dissertation Title: “NMR Characterization of Pathological Disease States: Monitoring Response to Single Dose Radiotherapy in a RIF-1 Tumor Model and The Role of Cortical Spreading Depression in the Evolution of Ischemic Stroke” with Christopher H. Sotak.

This dissertation involves applied research in biomedical science using nuclear magnetic resonance spectroscopy (MRS) and imaging (MRI). Research topics include: multi-parametric tissue characterization in a RIF-1 tumor model with histological validation; characterization of the radiotherapeutic response in a RIF-1 tumor model using multispectral analysis; visualization of experimental cortical spreading depression using manganese-enhanced MRI; investigation of the role of cortical spreading depression in the temporal evolution of stroke. Responsibilities in this position include: general maintenance of a Bruker Biospin 2T imaging spectrometer; design and fabrication of RF coils; sequence optimization and data acquisition, source code development for data processing and image analysis using IDL programming.

Experience with animal models include the RIF-1 tumor model in C3H mice and the MCAO model in SD rats. Responsibilities for the RIF-1 tumor model include: general handling of C3H mice, delivery of anesthetic (personal experience with chloral hydrate, ketamine/zylazine, and isoflurane), subcutaneous cell inoculations, tumor extraction and sectioning, paraffin embedded histology, microtome sectioning, hemotoxylin-eosin staining. Responsibilities for the MCAO model include: general handling of SD rats, deliver of anesthetic (personal experience with chloral hydrate and isoflurane), brain sectioning and triphenyl tetrazolium chloride (TTC) staining. Able to perform femoral vein catheterizations and MCA occlusion in rats and tail-vein injections in mice.

WORK EXPERIENCE

2000 – Present **Graduate Research Assistant**, Biomedical Engineering Department, WPI, Worcester, MA
Applied research investigating water diffusion in animal models of cancer and stroke. Experience with RF coil design, sequence optimization, data acquisition, image processing and analysis.

- Fall 2002, 2004 **Graduate Teaching Assistant**, Biomedical Engineering Department, WPI, Worcester, MA
BE 582. Principles of *In Vivo* Nuclear Magnetic Resonance Imaging. Responsibilities include: conversion of the laboratories from a GE CSI-II system
- Fall 2002 **Graduate Teaching Assistant**, Biomedical Engineering Department, WPI, Worcester, MA
BE 4201. Biomedical Imaging. Responsibilities include: teaching the laboratories in which the students perform basic image processing techniques using IDL programming.
- 1999 – 2000 **Directed Research**, Institute of Molecular Biophysics, Florida State University, Tallahassee, FL
Research assessing the cell-cycle dependence of radiation-induced damage of CHO cells using the comet assay. Experience with cell culture and electrophoresis.
- Summer 1999 **Summer Undergraduate Research Fellow**, Mayo Clinic, Rochester, MN
Research on improvement of existing motion correction algorithms. Experience with C programming
- Summer 1998 **Summer Undergraduate Research Fellow**, Roswell Park Cancer Institute, Buffalo, NY
Research investigating the role of brain metabolite concentrations in apoptosis and the progression of cancer. Experience with NMR spectra and general processing with Analyze.
- 1997 – 1998 **Webpage Editor**, Physics Department, Florida State University, Tallahassee, FL
Course webpage development and maintenance using HTML. Experience with UNIX

FELLOWSHIPS AND GRANTS

1. Pierson Fellowship, 08/15/00-05/15/01. Worcester Polytechnic Institute, Worcester, MA
2. GAANN Fellowship, 05/15/01-Present. Worcester Polytechnic Institute, Worcester, MA

HONORS AND AWARDS

1. Student Travel Stipend Award, 12th Scientific Meeting of the International Society of Magnetic Resonance in Medicine, Kyoto, Japan, May 2004.
2. Student Travel Stipend Award, Gordon Research Conference: In Vivo Magnetic Resonance, Lewiston, Maine, July 2004.
3. Student Travel Stipend Award, 13th Scientific Meeting of the International Society of Magnetic Resonance in Medicine, Miami Beach, Florida, May 2005.

PUBLICATIONS

1. Visualization of Cortical Spreading Depression (CSD) Using Manganese-Enhanced MRI (MEMRI), E.C. Henning, X. Meng, M. Fisher, C.H. Sotak, *Magn. Reson. Med.* 2005;53:851-857.
2. Multispectral Quantification of Tissue Types in a RIF-1 Tumor Model with Histological Validation: Part 1, E.C. Henning, C. Azuma, C.H. Sotak, K.G. Helmer, *In Preparation*

3. Multispectral Tissue Characterization in a RIF-1 Tumor Model: Monitoring Response to Single-Dose (1000cGy) Radiotherapy: Part 2, E.C. Henning, C. Azuma, C.H. Sotak, K.G. Helmer, *In Preparation*

CONFERENCE PROCEEDINGS

1. Characterization of Biocompatible Fluorinated Alginates Using ^{19}F NMR Spectroscopy, Erica C. Henning, Matthew D. Silva, Manssur Yaplani, Christopher H Sotak. Abstract, Poster Presented at the 43rd Experimental NMR Conference, Pacific Grove, California, March 2002.
2. Visualization of Cortical Spreading Depression (CSD) Using Manganese-Enhanced MRI (MEMRI), E.C. Henning, X. Meng, M. Fisher, C.H. Sotak. Abstract, Poster Presented at the 45th Experimental NMR Conference, Pacific Grove, California, April 2004.
3. Multispectral Quantification of Tissue Types in a RIF-1 Tumor Model: Monitoring Response of a Single-Dose (1000cGy) Radiotherapy, E.C. Henning, C. Azuma, C.H. Sotak, K.G. Helmer. Abstract, Poster Presented at the 12th Scientific Meeting of the International Society of Magnetic Resonance in Medicine, Kyoto, Japan, May 2004.
4. Visualization of Cortical Spreading Depression Using Manganese-Enhanced MRI, E.C. Henning, X. Meng, M. Fisher, C.H. Sotak. Abstract, Oral Presentation at the 12th Scientific Meeting of the International Society of Magnetic Resonance in Medicine, Kyoto, Japan, May 2004.
5. Correlation of Tumor Growth Kinetics, Cell Kill, and Radiotherapeutic Response in a RIF-1 Tumor Model Using Multispectral Analysis, E.C. Henning, C. Azuma, C.H. Sotak, K.G. Helmer. Abstract, Poster Presented at the 13th Scientific Meeting of the International Society of Magnetic Resonance in Medicine, Miami Beach, Florida, May 2005.
6. Investigation of Early ADC Changes in Response to Single Dose (1000cGy) Radiotherapy in a RIF-1 Tumor Model, E.C. Henning, C. Azuma, C.H. Sotak, K.G. Helmer. Abstract, Oral Presentation at the 13th Scientific Meeting of the International Society of Magnetic Resonance in Medicine, Miami Beach, Florida, May 2005.

MEMBERSHIPS

2002 – Present	International Society of Magnetic Resonance in Medicine
2003 – 2004	Graduate Student Representative for WPI's 15 th Presidential Search Committee
2005	Sigma Xi Scientific Research Society, inducted April 2005.

Visualization of Cortical Spreading Depression Using Manganese-Enhanced Magnetic Resonance Imaging

Erica C. Henning,¹ Xiangjun Meng,³ Marc Fisher,^{3,4} and Christopher H. Sotak^{1,2,4*}

Cortical spreading depression (CSD) was visualized using manganese-enhanced MRI (MEMRI) following topical application of KCl to the exposed rat cortex. MEMRI signal increase in the ipsilateral cortex relative to the contralateral control region was $60 \pm 30\%$ following two KCl applications. MEMRI signal increase for a single (40%) versus double (80%) KCl application suggests an integration effect over successive CSD episodes. CSD-induced MEMRI enhancement involved cortical layers containing dense regions of apical dendrites, supporting the contention that these neuronal structures are necessary for propagation of CSDs. Subcortical enhancement was present in hippocampal and thalamic regions, most likely a result of neuronal connections with cortical layers 4 and 5. These results are consistent with previous studies of CSD using diffusion-weighted MRI and T_2^* -weighted MRI and should be useful for investigating CSD itself and its role in other neurologic disorders. Magn Reson Med 53:851–857, 2005. © 2005 Wiley-Liss, Inc.

Key words: manganese-enhanced MRI; cortical spreading depression; rat brain; glutamate; calcium channels

Cortical spreading depression (CSD), a pathophysiological phenomenon of the central nervous system first described by Leao (1,2), is characterized by a spontaneous and reversible depression of electrical activity that spreads from the site of onset as a radial wave across the cortex with a speed of 2 to 5 mm/min. Experimental induction of CSD relies on methods that increase the extracellular K^+ concentration ($[K^+]_o$), leading to depolarization of adjacent presynaptic terminals, neurotransmitter release, and local failure of ion homeostasis (3). The radial wave of depressed cortical electrical activity leads to depolarization of the cellular membrane, causing an abrupt negative shift in direct-current (DC) potential on the order of -5 to -15 mV, followed immediately by a smaller but more prolonged positive phase (4). For the duration of the negative potential shift (approximately 1 min), a large increase in $[K^+]_o$ is accompanied by a drop in $[Cl^-]_o$, $[Na^+]_o$, and $[Ca^{2+}]_o$, suggesting that K^+ leaving cells is exchanged

against Na^+ and Ca^{2+} that are entering (5). The increase in $[K^+]_o$ to levels of 10 to 60 mmol/L is sufficient to depolarize adjacent neurons in the path of the CSD wave, permitting its continued propagation. Concomitant with the movement of Na^+ and Cl^- into the cell, there is an influx of water, subsequent cellular swelling, and a reduction in extracellular space by 50% (6,7). These transient cellular changes are accompanied by increased cortical perfusion and decreased tissue pO_2 , accounting for the local increase in oxygen consumption required to restore membrane ion gradients (8). Upon passage of the CSD wave, cortical electrical activity renormalizes over the course of several minutes, permitting additional episodes of CSD following an approximate 3-min refractory period.

CSD is of interest because of its contribution to the pathophysiology of stroke, head trauma, epilepsy, hypoglycemia, and subarachnoid hemorrhage (3). Unfortunately, a comprehensive evaluation of CSD in human subjects has not been performed, largely in consideration of the challenges involved and the lack of appropriate measuring techniques. The majority of studies investigating the role of CSDs under these conditions have been in animal models, specifically lissencephalic species (mouse, rat, rabbit), versus gyrencephalic species (cat, monkey) (5). CSD, which can be elicited by direct chemical, mechanical, or electrical stimulation to the cortex, is produced more readily in lissencephalic species, and, although gyrencephalic species are relatively resistant to CSD propagation, they are by no means immune. Further investigation of the dynamic physiologic changes of CSD could aid in understanding the underlying mechanisms of the aforementioned conditions.

Past studies have used MRI as a noninvasive tool for the characterization of CSD. Gardner-Medwin et al. (9) demonstrated the identification of experimentally induced CSD in a rat model using T_2^* -weighted MRI. The authors suggested that the observed increase in signal intensity ($\sim 10\%$) was a result of sensitivity to alterations in the oxygenation state of hemoglobin within the local cerebral vasculature (10). CSD causes a local increase in cerebral blood flow and tissue oxygenation, yielding increased signal in gradient-echo images. Other studies present observations of a similar phenomenon in which experimentally induced CSD is characterized by a transient decline in the apparent diffusion coefficient (ADC) of water (11–13). Latour et al. (11) characterized the temporal evolution of CSD using diffusion-weighted MRI (DWI). The authors observed a region of declined ADC ($\sim 35\%$) moving across the cortex with a uniform velocity of approximately 3 mm/min. The authors hypothesized that the induced depolarizations of the cellular membrane, resulting in cellular swelling and a decrease in the extracellular volume fraction, account for the transient decrease in ADC. In line

¹Department of Biomedical Engineering, Worcester Polytechnic Institute, Worcester, Massachusetts, USA.

²Department of Chemistry & Biochemistry, Worcester Polytechnic Institute, Worcester, Massachusetts, USA.

³Department of Neurology, University of Massachusetts Memorial Health-care—Memorial Campus, Worcester, Massachusetts, USA.

⁴Department of Radiology, University of Massachusetts Medical School, Worcester, Massachusetts USA.

Presented in part at the 12th Annual Meeting of the International Society of Magnetic Resonance in Medicine, Kyoto, Japan, 2004.

Correspondence to: Christopher H. Sotak, Department of Biomedical Engineering, Worcester Polytechnic Institute, 100 Institute Road, Worcester, MA 01609, USA. E-mail: csotak@wpi.edu

Received 21 July 2004; revised 22 November 2004; accepted 24 November 2004.

DOI 10.1002/mrm.20438

Published online in Wiley InterScience (www.interscience.wiley.com).

© 2005 Wiley-Liss, Inc.

with this study, Busch et al. (12) demonstrated the simultaneous recording of EEG, DC potential, and the temporal evolution of CSD using DWI. Their results coincide with those of Latour et al. (11), but allow a method of obtaining electrophysiological recordings in the magnet during CSD imaging. For a better understanding of the temporal relation between cell membrane depolarizations and the accompanying hemodynamic response, de Crespigny et al. (13) assessed both during CSD using T_2^* -weighted MRI and DWI. The authors found that the transient regional hyperperfusion following the ADC decrease was delayed, suggesting that the perfusion increase is a consequence of elevated ATP requirements for cellular repolarization.

Although T_2^* -weighted MRI and DWI have been used to investigate CSD, these studies have limited their spatial resolution and signal-to-noise ratios in order to achieve a reasonable temporal resolution for monitoring the transient changes in ADC and T_2^* concomitant with CSD propagation. T_2^* -weighted MRI also suffers from susceptibility-induced artifacts from the interface between tissue boundaries, degrading image quality. Since DWI and T_2^* methods are based on macroscopic physiologic changes (cell swelling and regional blood flow, respectively), they are limited in their ability to characterize the spatial extent of CSD. An MRI method with a higher signal-to-noise ratio for whole-brain imaging of CSD, based on more microscopic physiologic changes, would be helpful in order to overcome these limitations.

Recent studies have reported the use of manganese ions (Mn^{2+}) as a membrane-depolarization-dependent contrast agent for monitoring neuronal activation following the application of glutamate (14,15), as well as in the study of focal ischemia (16). Mn^{2+} competitively enters cells through Ca^{2+} -influx pathways such as voltage-gated Ca^{2+} channels (17,18). Lin and Koretsky (14) first demonstrated the utility of paramagnetic Mn^{2+} in monitoring regional brain function using T_1 -weighted MRI. The presence of extracellular Mn^{2+} during neuronal depolarization elicits Mn^{2+} influx through Ca^{2+} channels. Upon repolarization, Ca^{2+} channels close resulting in the "permanent" intracellular uptake of Mn^{2+} . Since Mn^{2+} remains sequestered in previously activated regions, it allows for "snapshot" imaging of brain activation patterns in functional task paradigms performed outside the magnet (14).

Extracellular accumulation of K^+ , like glutamate, is believed to play a central role in the propagation of CSDs. Whether pathophysiologically or experimentally induced, local increases in $[K^+]_o$ lead to the depolarization of presynaptic terminals and the opening of Ca^{2+} channels. Mirroring the rise in $[K^+]_o$, $[Ca^{2+}]_o$ declines from its normal level of 1.2–1.5 mM to less than 0.3 mM, indicating a Ca^{2+} shift to the intracellular compartment during CSD. Since Mn^{2+} is transported into the cell in a manner similar to Ca^{2+} , it should be possible to use Mn^{2+} to track the spatial distribution of CSD using manganese-enhanced MRI (MEMRI). The purpose of this feasibility study is to demonstrate the utility of Mn^{2+} as a paramagnetic Ca^{2+} analog in the visualization of CSD in the rat brain. MEMRI should be useful for investigating CSD itself as well as its role in the pathophysiology of other neurologic disorders.

METHODS

Animal Preparation

The present study was approved by the Institute Animal Care and Use Committee (IACUC) of the University of Massachusetts Medical School (IACUC Protocol A-875). Male Sprague–Dawley rats (300–360 g; Taconic Farms, Germantown, NY) were divided into three groups: saline control ($N = 4$), glutamate ($N = 2$), and experimental CSD ($N = 5$). Rats were initially anesthetized with an intraperitoneal injection of chloral hydrate (400 mg/kg). Polyethylene catheters (PE-50, Becton–Dickinson, San Jose, CA) were placed in the left femoral vein (i.v.) and the right external carotid artery (ECA) for drug administration. For catheterization of the right ECA, a ventral midline incision was made in the neck. The omohyoid muscle was separated longitudinally and retracted laterally to isolate and expose the right ECA. Following ligation of the vessel, a small incision was made into which the catheter was inserted and secured in place. Cannulation of the right ECA limited drug delivery to the right side of the brain, enabling the left side to serve as a control. The common carotid artery was kept intact and open in order to maintain blood flow to regions originally supplied by the right ECA (i.e., face and underlying muscle). Rectal temperature was monitored continuously with a rectal probe and maintained at 37.0°C using a thermostatically controlled heating lamp (Model 73ATD, YSI, Inc., Yellow Spring, OH) during preparation.

MnCl₂ Administration

Physiologically buffered saline containing 74.5 mM manganese chloride ($MnCl_2 \cdot 4H_2O$; Sigma, St. Louis, MO) was infused through the left femoral vein at a rate of 3.97 μ mol/min (3.2 mL/hr) using a syringe pump (Model 11; Harvard Apparatus, Holliston, MA) for 32 min. The total volume of infused $MnCl_2$ solution was 1.71 mL (127 μ mol). To open the blood–brain barrier (BBB), 25% D-mannitol solution (5 mg/kg; Sigma) was bolus-injected via the right ECA 10 min after the start of the $MnCl_2$ infusion.

Glutamate Administration

A glutamate administration group ($N = 2$) was evaluated to validate our use of the MEMRI method previously developed by Aoki et al. (15), a modification of the original by Lin and Koretsky (14). A solution of L-glutamic acid (0.2 mL of 10 mg/mL; Sigma) was bolus-injected via the right ECA 22 min after the start of the $MnCl_2$ infusion (Fig. 1a). For the corresponding controls ($N = 2$), physiologically buffered saline (0.2 mL) was injected through the right ECA in place of the glutamate.

Experimental Cortical Spreading Depression

For the experimental CSD group ($N = 5$), rats were mounted prone on a homemade stereotaxic surgical board with a head holder and tooth bar. The frontoparietal cranium was exposed by a midsagittal incision, and a burr hole, 2.0 mm in diameter, was made in the right parietooccipital cortex, 1 mm posterior and 1.5 mm lateral of bregma. Following careful excision of the dura using a

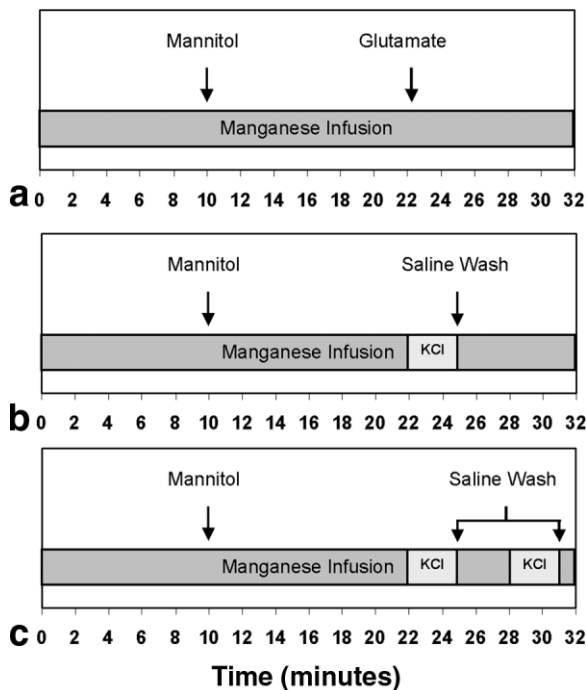


FIG. 1. Timing of drug administration (in minutes) for glutamate (a), experimental CSD with one KCl application (b), and experimental CSD with two KCl applications (c). The time points for starting the MnCl_2 infusion, mannitol injection, glutamate injection, KCl applications, and saline washes are indicated by the labeled arrows. For the corresponding controls, physiologically buffered saline (NaCl) was applied in place of the glutamate or KCl.

23-gauge needle, two syringes were prepared for cortical application of 4M KCl or 0.9% (w/v) NaCl, respectively.

In order to evaluate the effects of single versus multiple applications of KCl on CSD-induced MEMRI enhancement, animals were subdivided into two groups: a single 4 M KCl application ($N = 1$) and two 4 M KCl applications ($N = 4$). For the single 4 M KCl application, 22 min after the start of MnCl_2 infusion, a 20- μL volume of KCl solution was administered over the course of 3 min followed by a saline wash (Fig. 1b). For two 4 M KCl applications, a 40- μL volume of KCl solution was administered in the following manner, 22 min after the start of MnCl_2 infusion: 3-min 4 M KCl exposure, saline wash \rightarrow 3-min waiting period \rightarrow 3-min 4 M KCl exposure, saline wash (Fig. 1c). For the corresponding controls ($N = 2$), 40 μL of 0.9% (w/v) NaCl was applied to the exposed cortex in place of the 4 M KCl.

MRI Measurements

MR experiments were performed with a Bruker Biospin 2.0 T/45 cm imaging spectrometer equipped with ± 20 G/cm self-shielded gradients. T_1 -weighted imaging was performed using the following acquisition parameters: TR/TE = 300.0/12.0 ms, FOV = 4×4 cm, matrix size = 256×256 . The imaging plane was referenced to the rhinal fissure at the boundary of the olfactory bulb. For the glutamate administration group and controls, six 3-mm slices were acquired with NEX = 2. For the experimental CSD

group and controls, eight 2-mm slices were acquired with NEX = 4. The total experiment times were 2.6 and 5.2 min for the glutamate and experimental CSD experiments, respectively. During imaging, animals were placed supine in a homebuilt animal holder. The head of the animal was fixed inside a 2.0×3.5 cm rectangular ^1H surface coil shaped to conform to the curvature of the skull. Animals were anesthetized with 1.2% isoflurane delivered at 1.0 L/min in breathing-quality air. Body temperature was maintained at $37.0 \pm 1.0^\circ\text{C}$ by circulated warm air using a T-type thermocouple and a double-point feedback control system.

Data Analysis

Image analysis, image reconstruction, and region of interest (ROI) calculations were performed using Paravision's Image Processing and Display Software (Xtip). The spatial extent of MEMRI-enhanced regions (cortical, subcortical) was determined by correlation to a standard rat brain atlas (19) based on the slice location in terms of distance from bregma. ROIs were user-defined to delineate between MEMRI-enhanced cortical regions and normal tissue. Percentage signal increase was calculated through comparison of the ipsilateral cortex to the equivalent contralateral control region on a slice-by-slice basis,

$$\text{Signal increase (\%)} = \frac{SI_{\text{IC}} - SI_{\text{CC}}}{SI_{\text{CC}}} \times 100, \quad [1]$$

where SI_{IC} is the signal intensity for the ROI in the ipsilateral cortex and SI_{CC} is the signal intensity for the ROI in the contralateral cortex. Data are means \pm standard deviation (SD), with a separate term for the interslice signal variability (IS-SD).

RESULTS

Figure 2 shows the multislice T_1 -weighted MEMRI for the glutamate group, experimental CSD group, and the corresponding controls at a single time point 1.5 hr after the start of MnCl_2 infusion. Figure 2a shows the signal enhancement from T_1 -weighted MEMRI following neuronal activation via glutamate administration. The average percentage increase in cortical signal intensity was $29 \pm 3\%$, with a similar increase seen in the ventricles. Cortical enhancement was visible across five of the six imaging slices, resulting in approximately 15 mm of coverage (4.5 mm anterior to 10.5 mm posterior of bregma). Figure 2c shows the signal enhancement from T_1 -weighted MEMRI of experimental CSD following two applications of 4 M KCl. The region of MEMRI enhancement was confined to a 0.6- to 1.2-mm-thick cortical layer, appearing as a hyperintense streak extending radially from the CSD induction site (solid arrows). The average percentage increase in cortical signal intensity was $60 \pm 30\%$. Cortical enhancement was visible across six of the eight imaging slices, resulting in approximately 12 mm of coverage (2.5 mm anterior to 9.5 mm posterior of bregma). In a few of the slices (Fig. 2b, open arrows), subcortical enhancement was present that did not match with the regional ventricular enhancement of the NaCl control (3.5 to

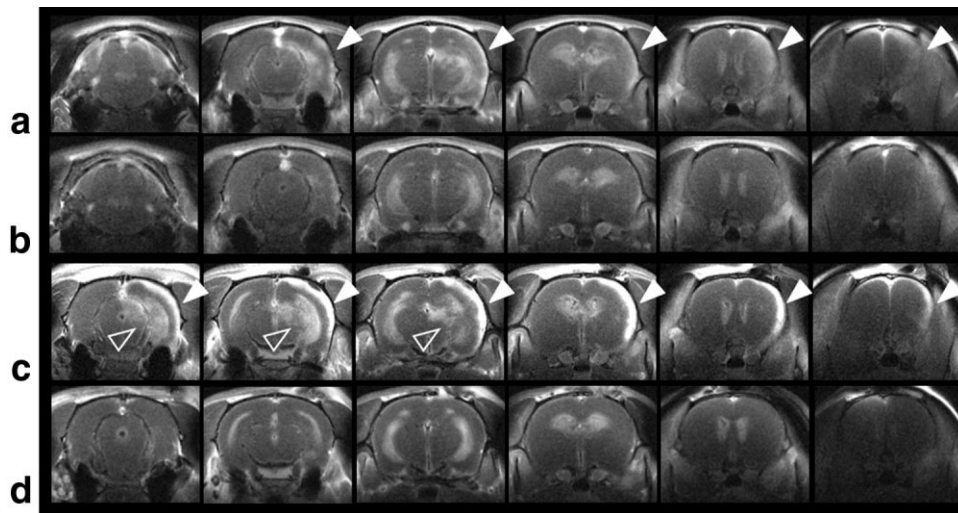


FIG. 2. T_1 -weighted MEMRI following glutamate administration and experimental CSD. (a) Neuronal activation following glutamate administration. Glutamate administration results in heterogeneous cortical enhancement ($29 \pm 3\%$ signal increase) in five of six images (solid arrows). Slice thickness = 3 mm. (b) Saline control for glutamate experiments. (c) Cortical signal enhancement following two 4 M KCl applications. Two 4 M KCl applications result in a thin layer of cortical enhancement ($60 \pm 30\%$ signal increase) in six of eight images (solid arrows). Slice thickness = 2 mm. Only images exhibiting enhancement are shown. Signal enhancement following CSD in the presence of Mn^{2+} is clearly visible in the right cortex. Regions of CSD-induced MEMRI enhancement appear as a hyperintense streak extending dorsolaterally from retrosplenial granular cortex or frontal cortex, area 2, to piriform cortex or perirhinal cortex depending on the location anterior–posterior with respect to bregma. Regions of subcortical enhancement (open arrows) include CA1–3 (Ammon’s horn), the subiculum, and the dentate gyrus of the hippocampus, in addition to the thalamic nucleus, superior and inferior colliculi, and geniculate nucleus. Subcortical enhancement is thought to be due to neuronal connections between these particular regions and the cortex. (d) NaCl control for experimental CSD.

9.5 mm posterior of bregma). Areas of subcortical enhancement included hippocampal regions CA1–3, subiculum, and dentate gyrus, as well as the thalamic nucleus, superior and inferior colliculi, and geniculate nucleus. No significant changes in cortical signal intensity were detected for the saline controls (Fig. 2b and d), but the same degree of ventricular enhancement was present.

Figure 3 illustrates the effect of single versus multiple applications of KCl on CSD-induced MEMRI enhancement. Three representative axial images are shown for each animal (solid arrows indicate the image located coincident with the KCl application site). Figure 3a shows the signal enhancement from T_1 -weighted MEMRI following a single application of 4 M KCl. The average percentage increase in cortical signal intensity was 40% for this par-

ticular animal. Figure 3b shows the signal enhancement from T_1 -weighted MEMRI following two applications of 4 M KCl. The average percentage increase in cortical signal intensity was 80% for this particular animal ($60 \pm 30\%$ for $N = 4$), double that of the single 4 M KCl application. Both animals had similar levels of ventricular enhancement.

Table 1 summarizes the average percentage signal intensity increase for different brain regions for the glutamate administration group, experimental CSD group, and the corresponding controls. In the glutamate administration group, changes in signal intensity in the ipsilateral cortex were comparable to that of the ventricles. Animals in the experimental CSD group that received two applications of 4 M KCl exhibited no significant difference in percentage signal increase between the ipsilateral cortex and the ven-

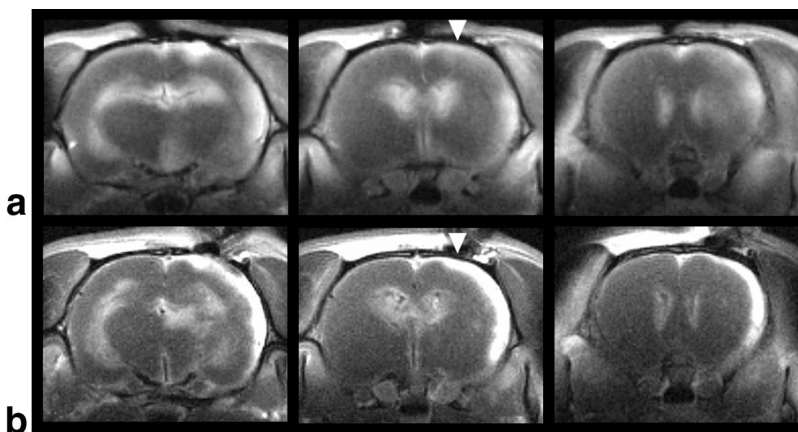


FIG. 3. Effect of single versus double KCl applications on MEMRI appearance. (a) MEMRI enhancement following a single application of 4 M KCl. One KCl application results in a thin layer of cortical enhancement (40% signal increase for this particular animal). (b) MEMRI enhancement following two applications of 4 M KCl. Two applications of KCl induce multiple episodes of CSD, resulting in an integration of MEMRI cortical signal intensity (80% signal increase for this particular animal; $60 \pm 30\%$ for $N = 4$). MEMRI enhancement was visible across six of eight images for both the single and the double KCl application. Representative axial images coincident with and adjacent to the KCl application site are shown. Solid arrows indicate the location of the KCl application site.

Table 1

Average Signal Increase (%) from T_1 -Weighted MRI for Different Brain Regions (Relative to a Homologous Region in the Contralateral Hemisphere) Following Various Stimuli

Type of stimulus	Average signal increase (%) (using Eq. [1])			
	Cortex		Ventricles	
	Mean \pm SD	ISSD ^a	Mean \pm SD	ISSD ^a
Glutamate administration ($N = 2$)	29 \pm 3	5	21 \pm 6	10
Saline control ($N = 2$)	6 \pm 1	4	29 \pm 9	20
Experimental CSD				
Single KCl application ($N = 1$)	40	20	40	20
Two KCl applications ($N = 4$)	60 \pm 30*	20	46 \pm 3	10
NaCl control ($N = 2$)	20 \pm 10	4	50 \pm 10	20

^aTo account for intra-animal variability, the inter slice standard deviation (IS-SD) was calculated from values for the average signal increase (%) across affected slices.

*MEMRI signal intensity changes in the ipsilateral cortex were not significantly different from the ventricles ($P > 0.32$, $N = 4$) in the experimental CSD group receiving two KCl applications.

trices ($P > 0.32$, $N = 4$). A similar trend was seen for the single application of 4 M KCl. For both sets of controls, changes in cortical and ventricular signal intensity were comparable, indicating experimental reproducibility.

DISCUSSION

Mn^{2+} is paramagnetic and has been used for MRI tissue contrast enhancement by oral or i.v. administration of $MnCl_2$ or Mn complexes. Mn^{2+} mimics Ca^{2+} uptake in many biologic systems and is known to enter cells through ligand- or voltage-gated Ca^{2+} channels during nerve action potentials (17). Following experimental induction of CSD, membrane depolarization facilitates opening of voltage-gated Ca^{2+} channels and a concomitant influx of Mn^{2+} . Upon deactivation, channels return to their closed resting state, resulting in the entrapment of intracellular Mn^{2+} . This phenomenon is supported by the observation that the specific action of verapamil, a voltage-gated Ca^{2+} channel blocker, inhibits influx of Mn^{2+} into cells (18).

In the present work, validation of Mn^{2+} as an activation-specific contrast agent was done through glutamate administration in the presence of a compromised BBB using the methodology of Aoki et al. (15). For simplicity, all surgical procedures and drug administration were performed outside the magnet with image acquisition at 1.5 hr after the start of $MnCl_2$ infusion. Figure 2a demonstrates that the infusion of $MnCl_2$ during glutamate activation causes cortical and ventricular contrast enhancement of similar magnitude and regional coverage when compared to previous MEMRI studies (14,15). Aoki et al. (15) reported a relative signal enhancement of 174% for the right hemisphere (excluding the ventricles) and 155% for the ventricles alone following glutamate administration. These results were based on the comparison of the relative signal intensities in the ipsilateral cortex measured at baseline (prior to injection of mannitol) and following glutamate administration. If instead a comparison is drawn between the relative signal intensities of the ipsilateral cortex and the contralateral cortex following glutamate administration, the relative signal enhancement is approximately 120%. This estimated increase (20%) is consistent with the values reported in Table 1. After a similar comparison is drawn between the relative signal intensities of the ven-

trices and the contralateral cortex, the relative signal enhancement is approximately 135%. Lin and Koretsky (14) reported a steady-state ventricular signal enhancement of 149% following infusion of $MnCl_2$. These increases (35 and 49%) are close to the changes in ventricular signal intensity seen in the experimental groups listed in Table 1.

For the experimental CSD group, an activation scheme with a set waiting period was devised (Fig. 1c) to account for the approximate 3-min refractory period between initiation of individual episodes of CSD. During the first application of 4 M KCl, the local increase in $[K^+]_o$ induces depolarization of presynaptic terminals, opening of voltage-gated Ca^{2+} channels, and the intracellular accumulation of Mn^{2+} . This takes place during the negative phase of the DC-potential shift over the course of 1–2 min. Upon repolarization, the Ca^{2+} channels close resulting in the retention of Mn^{2+} inside the cell. While this repolarization occurs locally, the increase in $[K^+]_o$ is thought to depolarize adjacent neurons, allowing propagation of the CSD wave along the entire extent of the cortex. During the 3-min wait period, restoration of ion gradients occurs with normalization of spontaneous electrical activity, after which a second CSD episode may be induced. Although electrophysiological recordings were not performed, previous work employing this experimental-CSD model reported induction of a single CSD event following one 3-min KCl application (20). Based on these results, one CSD event is expected for the single 3-min KCl application and a minimum of two CSD events are expected for the double KCl application. Each CSD event results in the intracellular accumulation of Mn^{2+} . With multiple CSD events there is an integration effect where the total $[Mn^{2+}]_i$ accumulated is proportional to the signal intensity in T_1 -weighted MRI. As MEMRI “records” all cortical regions having undergone CSD-induced depolarizations, CSDs appear as a hyperintense streak down the cortex (Fig. 2c).

A MEMRI integration effect was first demonstrated following brain activation using multiple injections of glutamate (14). The authors followed the temporal evolution of T_1 -weighted MRI signal intensity changes in the cortex from rats undergoing $MnCl_2$ infusion, mannitol injection, and two injections of glutamate. They reported an average signal enhancement of 123 and 238% for prestimulation and following two glutamate injections, respectively. The

time-course diagram from this work, for a single representative rat, showed cortical signal intensities of approximately 135, 200, and 250% for prestimulation, following a single injection of glutamate, and following two glutamate injections, respectively. These signal intensity changes suggest a correlation between the number of administered doses of glutamate, or the degree of glutamate-induced Mn^{2+} influx, and the MEMRI signal enhancement.

In order to investigate the integration effect for CSD, comparisons were made between animals receiving a single or double application of 4 M KCl. Results of a single KCl application versus two KCl applications for experimental induction of CSDs support this relationship between $[Mn^{2+}]_i$ accumulation and the signal enhancement in T_1 -weighted MRI. Figure 3 shows the integration effect of multiple CSD events for representative axial images located coincident with and adjacent to the KCl application site. Following a single 3-min application of 4 M KCl, the average percentage increase in cortical signal intensity was 40% (Fig. 3a). Following two 3-min applications of 4 M KCl, the average percentage increase in cortical signal intensity was 80% ($60 \pm 30\%$ for $N = 4$) (Fig. 3b), double that of the single 4 M KCl application. Both had comparable levels of ventricular enhancement, suggesting similar steady-state levels of Mn^{2+} in the CSF space. Although the average percentage increase in cortical signal intensity was $60 \pm 9\%$ for $N = 4$ in the double 4 M KCl application, the average percentage increase for one of the animals was 30%. That particular animal may in fact have only experienced a single CSD episode instead of two CSD episodes, resulting in an average percentage increase more comparable with the animal receiving a single 4 M KCl application (40%). Further study comparing single versus multiple applications of 4 M KCl in conjunction with electrophysiological measurements will be required to verify the relationship among the number of CSD episodes, $[Mn^{2+}]_i$ accumulation, and MEMRI enhancement.

Previous studies suggest that pyramidal cell dendrites are critical to CSD propagation (21) and that cortical layers containing proximal apical dendrites are more susceptible to CSD than those containing basilar dendrites or distal apical dendritic branches (22). Cortical regions exhibiting MEMRI enhancement following experimental CSD, expected to encompass layers containing these neuronal structures, extended dorsolaterally from retrosplenial granular cortex or frontal cortex, area 2, to piriform cortex or perirhinal cortex depending on the location anterior–posterior with respect to bregma. Cortical restriction of MEMRI enhancement is consistent with the contention that pyramidal cell (apical) dendrites are necessary for the propagation of CSDs through individual layers of the cortex.

In addition to the cortical enhancement in the experimental CSD group, there was some visible subcortical enhancement extending well beyond the ventricular space (Fig. 2c, open arrows). This enhancement was different from the non-specific ventricular enhancement observed in the control (Fig. 2d). Regions of subcortical enhancement included CA1–3 (Ammon's horn), the subiculum, and the dentate gyrus of the hippocampus, in addition to the thalamic nucleus, superior and inferior colliculi, and geniculate nucleus. Previous studies report on the intrinsic connectivity between hippocampal regions and the entorhinal, perirhinal, and post-rhinal cortices (23,24), as well as corticothalamic projections

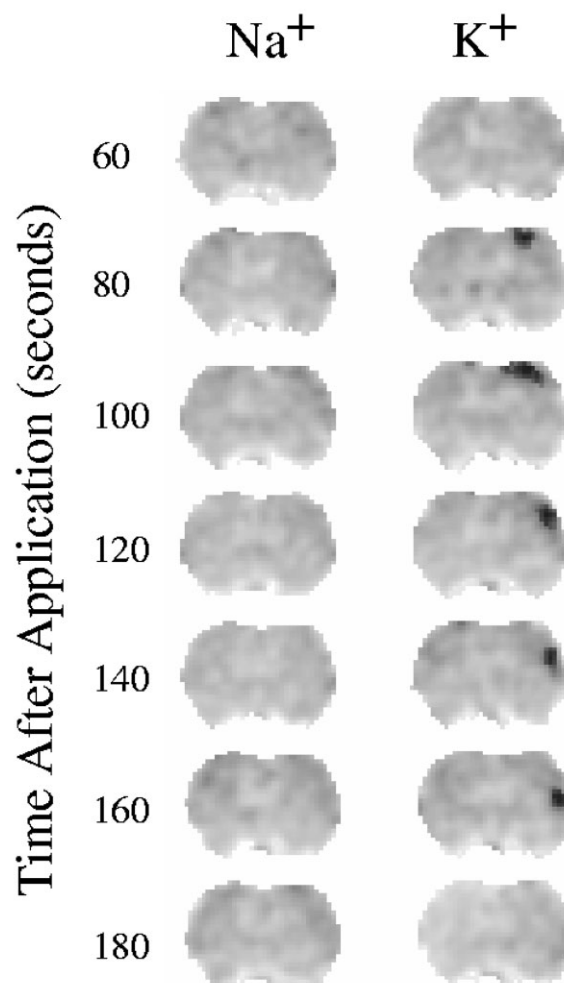


FIG. 4. Water apparent diffusion coefficient (ADC) maps of a single MRI slice through the rat brain exposed to physiologic saline (NaCl) (left) or 3 M KCl (right). The grayscale intensity is proportional to the water ADC and a nonlinear mapping, such that ADC values below $0.55 \times 10^{-5} \text{ cm}^2 \text{ s}^{-1}$ appear nearly black, was used to exaggerate the affected region. The ADC maps acquired after NaCl application are unchanged, indicative of normal rat brain. After application of 3 M KCl, a region of decreased water ADC, approximately 2 mm in size, is clearly visible moving away from the application site to the lower cortex. [Reprinted from Latour LL, Hasegawa Y, Formato JE, Fisher M, Sotak CH. Spreading waves of decreased diffusion coefficient after cortical stimulation in the rat brain. *Magn Reson Med* 1994;32:189–198. Copyright ©1994. Reprinted with permission of Wiley-Liss, Inc., a subsidiary of John Wiley and Sons, Inc.] (11)

arising from cortical layers 4 and 5 (25–27). Other reports describe connections between cortical layer 5 and the superior (28) and inferior (29) colliculi, with neuronal projections extending from the superior colliculus to the geniculate nucleus (30). During CSD, signal propagation descending the pial surface along apical dendrites into individual layers of the cortex, and then through the various connections described, may explain the subcortical enhancement seen in the MEMRI images.

The MEMRI signal enhancement in the cortex was 0.6–1.2 mm in thickness and extended radially from the induction site. Zhu (31) reported an average apical dendritic length of 1.2 mm in the neocortex of adult rats. The thick-

ness of MEMRI cortical enhancement is similar to this value and suggests that apical dendrites support CSD propagation. Furthermore, these results are consistent with previous studies of CSD using DWI (Fig. 4), in which a region of decreased water ADC, approximately 2 mm in size, propagated away from the application site to the lower regions of the cortex. The discrepancy in the observed thickness of the affected cortical region reported by MEMRI versus DWI may be attributed to volume-averaging effects from differences in image spatial resolution (400 μm for DWI versus 156 μm for MEMRI, in-plane). Although MEMRI and DWI both allow for visualization of CSDs, MEMRI has a clear advantage over that of DWI. Because of the relatively rapid propagation of CSDs and the transiently induced changes in EC space, DWI is limited to real-time imaging. With intracellular retention of Mn^{2+} and a slow clearance rate, MEMRI may be performed after application of the stimulus outside of the magnet. Consequently, longer experiment times allow for data acquisition at higher spatial resolutions with longer signal averaging and increased signal-to-noise ratios. MEMRI may also be used for tracking real-time changes in-bore.

In summary, MEMRI is a useful technique for the visualization of experimental CSD using paramagnetic Mn^{2+} as a depolarization-dependent contrast agent in conjunction with T_1 -weighted imaging. Topical application of 4 M KCl in the presence of extracellular Mn^{2+} and a compromised BBB allowed differentiation between CSD-specific cortical signal enhancement and the nonspecific enhancement present in the ventricular space. MEMRI is specific to Ca^{2+} channel activity and the intracellular accumulation of Mn^{2+} . Consequently, MEMRI may be a more direct method for imaging the spatial extent of CSD compared with DWI or T_2^* -weighted imaging, which are based on more macroscopic physiologic changes (cell swelling and regional blood flow, respectively). Since the Mn^{2+} clearance is relatively slow, MEMRI may be useful for imaging CSD and its contribution to the temporal evolution of other neurologic disorders.

ACKNOWLEDGMENTS

The authors thank Drs. Karl Helmer (Worcester Polytechnic Institute, MA), Matthew Silva (Millenium Pharmaceuticals, MA), and Jeremy Wellen (GlaxoSmithKline, PA) for helpful advice and encouragement.

REFERENCES

1. Leao AAP. Spreading depression of activity in the cerebral cortex. *J Neurophysiol* 1944;7:359–390.
2. Leao AAP. Further observations on the spreading depression of activity in the cerebral cortex. *J Neurophysiol* 1947;10:409–414.
3. Hansen AJ, Lauritzen M. The role of spreading depression in acute brain disorders. *An Acad Bras Cienc* 1984;56:457–479.
4. Leao AAP. The slow voltage variation of cortical spreading depression of activity. *Electroencephalogr Clin Neurophysiol* 1951;3:315–321.
5. Somjen GG. Mechanisms of spreading depression and hypoxic spreading depression-like depolarization. *Physiol Rev* 2001;81:1065–1096.
6. Van Harrevelde A, Khattab FI. Changes in cortical extracellular space during spreading depression investigated with the electron microscope. *J Neurophysiol* 1967;30:911–929.
7. Hansen AJ, Olsen CE. Brain extracellular space during spreading depression and ischemia. *Acta Physiol Scand* 1980;108:355–365.
8. Lauritzen M. Long-lasting reduction of cortical blood flow of the brain after spreading depression with preserved autoregulation and impaired CO_2 response. *J Cereb Blood Flow Metab* 1984;4:546–554.
9. Gardner-Medwin AR, van Bruggen N, Williams SR, Ahier RG. Magnetic resonance imaging of propagating waves of spreading depression in the anaesthetized rat. *J Cereb Blood Flow Metab* 1994;14:7–11.
10. Ogawa S, Lee TM, Nayak AS, Glynn P. Oxygenation-sensitive contrast in magnetic resonance image of rodent brain at high magnetic fields. *Magn Reson Med* 1990;14:68–78.
11. Latour LL, Hasegawa Y, Formato JE, Fisher M, Sotak CH. Spreading waves of decreased diffusion coefficient after cortical stimulation in the rat brain. *Magn Reson Med* 1994;32:189–198.
12. Busch E, Hoehn-Berlage M, Eis M, Gyngell ML, Hossmann KA. Simultaneous recording of EEG, DC potential, and diffusion-weighted NMR imaging during potassium induced cortical spreading depression in rats. *NMR Biomed* 1995;8:59–64.
13. de Crespigny A, Rother J, van Bruggen N, Beaulieu C, Moseley ME. Magnetic resonance imaging assessment of cerebral hemodynamics during spreading depression in rats. *J Cereb Blood Flow Metab* 1998;18:1008–1017.
14. Lin YJ, Koretsky AP. Manganese ion enhances T_1 -weighted MRI during brain activation: an approach to direct imaging of brain function. *Magn Reson Med* 1997;38:378–388.
15. Aoki I, Tanaka C, Takegami T, Ebisu T, Umeda M, Fukunaga M, Fukuda K, Silva AC, Koretsky AP, Naruse S. Dynamic activity-induced manganese-dependent contrast magnetic resonance imaging (DAIM MRI). *Magn Reson Med* 2002;48:927–933.
16. Aoki I, Ebisu T, Tanaka C, Katsuta K, Fujikawa A, Umeda M, Fukunaga M, Takegami T, Shapiro EM, Naruse S. Detection of the anoxic depolarization of focal ischemia using manganese-enhanced MRI. *Magn Reson Med* 2003;50:7–12.
17. Drapeau P, Nachshen DA. Manganese fluxes and manganese-dependent neurotransmitter release in presynaptic nerve endings isolated from rat brain. *J Physiol* 1984;348:493–510.
18. Narita K, Kawasaki F, Kita H. Mn and Mg influxes through Ca channels of motor nerve terminals are prevented by verapamil in frogs. *Brain Res* 1990;510:289–295.
19. Paxinos G, Watson C. *The rat brain in stereotaxic coordinates*. Orlando: Academic Press; 1986.
20. Takano K, Latour LL, Formato JE, Carano RAD, Helmer KG, Hasegawa Y, Sotak CH, Fisher M. The role of spreading depression in focal ischemia evaluated by diffusion mapping. *Ann Neurol* 1996;39:308–318.
21. Ochs S, Hunt K. Apical dendrites and propagation of spreading depression in cerebral cortex. *J Neurophysiol* 1960;23:432–444.
22. Herreras O, Somjen GG. Propagation of spreading depression among dendrites and somata of the same cell population. *Brain Res* 1993;610:276–282.
23. Harris E, Witter MP, Weinstein G, Stewart M. Intrinsic connectivity of the rat subiculum: I. Dendritic morphology and patterns of axonal arborization by pyramidal neurons. *J Comp Neurol* 2001;435:490–505.
24. Naber PA, Witter MP, Lopes da Silva FH. Evidence for a direct projection from the postrhinal cortex to the subiculum in the rat. *Hippocampus* 2001;11:105–117.
25. Kelly JP, Wong D. Laminar connections of the cat's auditory cortex. *Brain Res* 1981;212:1–15.
26. Hersch SM, White EL. Quantification of synapses formed with apical dendrites of Golgi-impregnated pyramidal cells: variability in thalamocortical inputs, but consistency in the ratios of asymmetrical to symmetrical synapses. *Neuroscience* 1981;6:1043–1051.
27. Levesque M, Gagnon S, Parent A, Deschenes M. Axonal arborizations of corticostratial and corticothalamic fibers arising from the second somatosensory area in the rat. *Cereb Cortex* 1996;6:759–770.
28. Kasper EM, Larkman AU, Lubke J, Blakemore C. Pyramidal neurons in layer 5 of the rat visual cortex. I. Correlation among cell morphology, intrinsic electrophysiological properties, and axon targets. *J Comp Neurol* 1994;339:459–474.
29. Games KD, Winer JA. Layer V in rat auditory cortex: projections to the inferior colliculus and contralateral cortex. *Hear Res* 1988;34:1–25.
30. Perez-Samartin AL, Sendino-Rodriguez J, Martinez-Millan L, Donate-Oliver F. Morphological characteristics of neurons in the superficial layers of the rabbit's superior colliculus projecting to the ipsilateral dorsal lateral geniculate nucleus. *Arch Ital Biol* 1995;133:177–195.
31. Zhu JJ. Maturation of layer 5 neocortical pyramidal neurons: amplifying salient layer 1 and layer 4 inputs by Ca^{2+} action potentials in adult rat tuft dendrites. *J Physiol* 2000;526:571–587.

Multispectral Quantification of Tissue Types in a RIF-1 Tumor Model: Monitoring Response of a Single-Dose (1000cGy) Radiotherapy

E. C. Henning¹, C. Azuma², C. H. Sotak^{1,3}, K. G. Helmer¹

¹Department of Biomedical Engineering, Worcester Polytechnic Institute, Worcester, MA, United States, ²Department of Clinical Sciences, Tufts University School of Veterinary Medicine, North Grafton, MA, United States, ³Department of Radiology, University of Massachusetts Medical School, Worcester, MA, United States

Introduction

The development of MRI endpoints to detect an early tumor therapeutic response would aid greatly in patient management, opening the possibility for both rapid radio- and chemotherapeutic dose optimization and replacement of ineffective therapies with alternative treatment. Unfortunately, inter- and intra-tumor heterogeneity complicate the quantification of treatment response using MRI. A multi-spectral (MS) analysis approach in combination with ADC and T_2 maps has been shown to aid in the identification of multiple compartments within necrotic tissue.¹ Here we report on a single-dose radiotherapy study using RIF-1 tumors in which MS analysis, using k-means (KM) clustering, was used to identify multiple compartments in both viable and necrotic tissue. The goal is to identify sub-populations in each tissue type to better characterize tissue that includes heterogeneity.

Methods

Twenty-nine 6-8 week-old female C3H mice weighing 20-25g were anesthetized with an intraperitoneal injection of ketamine/xyzylazine (100mg/kg:10mg/kg). All mice were inoculated with 1×10^6 RIF-1 cells (0.15ml), delivered through a subcutaneous injection into the right hind leg. Tumors were allowed to develop for 3-4wks, yielding an approximate 1.0cc starting volume.

Data for both control (n=16) and treatment (n=13) groups were acquired with a Bruker Biospin 2.0T/45 cm imaging spectrometer operating at 85.56 MHz for ¹H and equipped with ± 20 G/cm self-shielded gradients. The experiments involved multi-slice image acquisition along the coronal plane [128x128, FOV=3cm, slices=8, slice thickness=1mm]. A diffusion-weighted, spin-echo (SE) sequence was used to acquire the images at six b-values (b=50, 110, 210, 500, 690, 910 $\text{mm}^2 \text{s}^{-1}$) with diffusion sensitization applied along the read direction. Other acquisition parameters were: TR/TE=2000.0/53.0 msec, diffusion gradient duration $\delta=4.0$ msec, diffusion gradient separation $\Delta=35$ msec, resulting in an effective diffusion time $t_{diff}=33.75$ msec. A T_2 -weighted, SE sequence was used to acquire images at six echo times (TE = 12.2, 20, 35, 50, 65, 90 msec) with TR=2000msec. For the control group, tumors of varying volumes were imaged at a single time point and then extracted for histological examination. For the treatment group, tumors were irradiated with 1000cGy at a rate of 300cGy/min (Siemens Mevatron 77, 6 MeV electrons). Imaging was performed 1d pre-treatment, 5-hr, 1d-, 2d- post-treatment, and every 2d thereafter until tumor doubling (maximum 14d post-treatment).

Image reconstruction and ADC and T_2 parameter-map generation was performed using routines written in IDL[®] (RSI, Boulder, CO). Tissue classification was performed using the k-means (KM) clustering algorithm in a hierarchical manner. In the first step of the classification algorithm, it was applied to separate the data into two clusters (k = 2) of tumor tissue and background noise. All voxels classified as noise were set to zero and removed from further processing. In the second step, KM (k = 4) was applied to the remaining tissue voxels to segment the data into regions of viable tumor and necrosis. Average ADC and T_2 values were calculated for each cluster over all time points.

Results and Discussion

Fig. 1 shows the cluster assignments for a representative RIF-1 tumor. A central necrotic region is visible and is characterized by a small area of high ADC and high T_2 -values surrounded by an area of somewhat lower ADC and T_2 values also associated with necrotic tissue. The viable tissue regions have similar T_2 values, but differing ADCs. The cluster with the higher ADC is adjacent to the necrotic clusters; the cluster with the lower ADC is located at the tumor periphery. The mean MR parameter values for each cluster in Fig. 1 are given in Table 1. Fig. 2 shows the temporal changes in individual cluster volume fractions (percent of total volume) pre- and post-irradiation for the treatment group. The total viable fraction decreased out to Day 4, with a concomitant increase in the total necrotic fraction. This decrease in viable fraction mirrors that of the initial decrease in tumor volume post-irradiation. Tumor volumes began to increase again after Day 4. Tumors that had not yet doubled in size by Day 10 were slower growing and had relatively smaller necrotic fractions. This accounts for suppression of the expected increase in necrotic fraction as the tumor regrows. In conclusion, this method allows the characterization of tissue heterogeneity within the broad categories of viable and necrotic tissue and may be used for tracking changes in tissue viability post-therapeutic intervention.

References

[1] Carano et al. *Proc. Int. Soc. Magn. Reson. Med.*, 490 (2002). [2] Duda RO and Hart PE. *Pattern Classification and Scene Analysis*. New York: John Wiley&Sons, 1973.

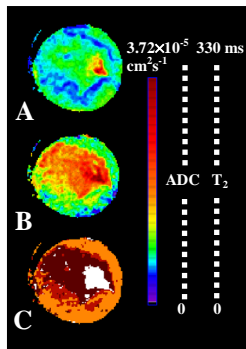


Fig. 1: A multispectral (MS) image of a representative RIF-1 tumor. (A) T_2 parameter map. (B) ADC parameter map. (C) KM map. The map derived by k-means (C) depicts the segmentation of the tumor into two regions of viable tumor and two regions of necrosis. Color assignments are: Viable 1 = Orange; Viable 2 = Red, Necrosis 1 = White; Necrosis 2 = Brown.

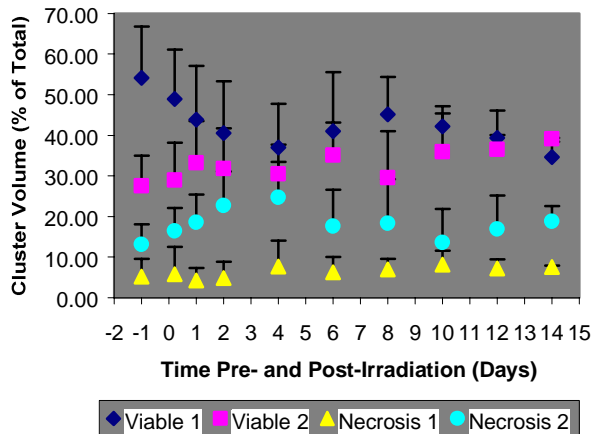


Fig. 2: Plot of the temporal evolution of individual cluster volumes for the treatment group.

Table 1: Mean parameters for the multispectral (MS) tissue classes of the RIF-1 tumor shown in Fig. 1. The measured parameters, ADC and T_2 , are given as the mean \pm standard deviation.

Tissue Cluster	ADC $\times 10^5$ (cm^2s^{-1})	T_2 (ms)
Viable 1	0.9 ± 0.2	60 ± 10
Viable 2	1.4 ± 0.3	50 ± 9
Necrosis 1	1.7 ± 0.3	70 ± 10
Necrosis 2	2.3 ± 0.6	110 ± 50

Visualization of Cortical Spreading Depression Using Manganese-Enhanced MRI

E. C. Henning¹, X. Meng², M. Fisher^{2,3}, C. H. Sotak^{1,3}

¹Department of Biomedical Engineering, Worcester Polytechnic Institute, Worcester, MA, United States, ²Department of Neurology, University of Massachusetts Memorial Healthcare, Worcester, MA, United States, ³Department of Radiology, University of Massachusetts Medical School, Worcester, MA, United States

Synopsis

Cortical spreading depression (CSD) was visualized for the first time using manganese-enhanced MRI (MEMRI) following topical application of 4M KCl to the exposed rat cortex. The region of MEMRI signal enhancement was confined to a 1.0-1.5-mm-thick cortical layer extending radially from the induction site. MEMRI allowed visualization of CSD over the entire cortical layer in the affected hemisphere. These results are consistent with previous studies of CSD using DWI and should be useful for investigating CSD itself as well as its role in cerebral ischemia.

Introduction

Cortical spreading depression (CSD) is characterized by a spontaneous and reversible depression of electrical activity that spreads from the site of onset as a radial wave across the cortex with a speed of 2-5 mm/min.¹ CSD is accompanied by an ionic redistribution across the cell membrane, with efflux of K⁺ and influx of Na⁺, Cl⁻, Ca²⁺ and water. Recent studies have reported the use of Mn²⁺ as a membrane-depolarization-dependent contrast agent for monitoring neuronal activation following the application of glutamate,² as well as in the study of focal ischemia.³ Extracellular accumulation of K⁺ and/or glutamate is believed to play a central role in the propagation of CSDs. Since Mn²⁺ has an ionic radius similar to that of Ca²⁺, and is transported into the cell in a manner similar to Ca²⁺, it should be possible to use Mn²⁺ to track the spatial distribution of CSD using MEMRI.

Methods

Seven male Sprague-Dawley rats weighing 300-350g were anesthetized with an intraperitoneal injection of chloral hydrate (400 mg/kg). Manganese chloride (MnCl₂; Sigma), dissolved to 74.5mM in isotonic saline, was infused through the left femoral vein at a rate of 3.97 μ mol/min (3.2ml/hr) using a syringe pump (model 11; Harvard Apparatus) for 32 min. Ten minutes after start of MnCl₂ infusion, 25% D-mannitol solution (5ml/kg; Sigma) was injected through the external carotid artery (ECA) over 2 min. For glutamate administration (N = 2), L-glutamic acid solution (0.2ml of 10mg/ml; Sigma) was injected through the ECA 22 min. after start of MnCl₂ infusion. For CSD (N = 2), the fronto-parietal cranium was exposed by a midsagittal incision, and a burr hole, 1.5 mm in diameter, was made in the right parietooccipital cortex 1 mm anterior and 1.5 mm lateral of the lambda. The dura was excised with a 23-gauge needle to expose the surface of the cortex. Application of 4M KCl was performed in the following manner, 22 min. after start of MnCl₂ infusion: 3 min. 4M KCl exposure, saline wash \rightarrow 3 min. waiting period \rightarrow 3 min. 4M KCl exposure, saline wash. For the corresponding controls (N = 3), physiologically buffered saline (NaCl) was applied in place of the glutamate or KCl.

MRI experiments were performed with a Bruker Biospin 2.0T/45 cm imaging spectrometer operating at 85.56 MHz for ¹H and equipped with \pm 20G/cm self-shielded gradients. T₁-weighted imaging was performed using the following acquisition parameters: TR/TE = 300.0/12.0 msec, FOV = 4 cm \times 4 cm, matrix size = 256 \times 256. For the glutamate administration group and controls, six 3-mm slices were acquired with NEX = 2. For the CSD group and controls, eight 2-mm slices were acquired with NEX = 4.

Results

Fig.1A shows the signal enhancement from T₁-weighted MEMRI following glutamate administration. Average enhancement in the cortex is 129% \pm 5%. Fig.1C shows the signal enhancement from T₁-weighted MEMRI following CSD. Average enhancement in the cortex is 180% \pm 20%. No significant changes in cortical signal intensity were detected for the saline control (Fig.1B) or the NaCl control for CSD (Fig.1D).

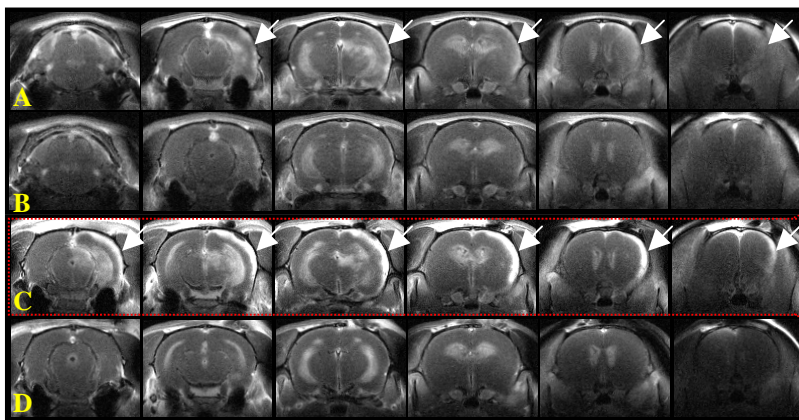


Figure 1: T₁-weighted MEMRI following glutamate administration and CSD. (A) Neuronal activation following glutamate administration. (B) Saline control. (C) Cortical enhancement following 4M KCl application. (D) NaCl application. Signal enhancement following CSD in the presence of Mn²⁺ is clearly visible in the right cortex of (C). Arrows highlight regions of MEMRI enhancement.

Discussion

For CSD, the region of signal enhancement was confined to a 1.0-1.5-mm-thick cortical layer extending radially from the induction site. These results are consistent with previous studies of CSD using DWI (Fig.2), in which a region of decreased ADC, approximately 2mm in size, propagates away from the application site to the lower cortex. In contrast to the transient ADC changes accompanying DWI visualization of CSD, MEMRI "records" all cortical regions that have undergone CSD-induced depolarizations and thus CSDs appear as a hyperintense "streak" down the cortex (Fig.1C). Given the relatively rapid propagation of CSDs relative to DWI acquisition, only a single slice visualization of CSDs is possible using this approach. In contrast, MEMRI has the advantage of multi-slice, whole-brain recording since the spatial history of CSD propagation is permanently recorded by the uptake of Mn²⁺. This method should be useful for investigating CSD itself as well as its role in cerebral ischemia.³

References

- [1] Leao A. *J. Neurophysiol.* **7**, 359-390 (1944).
[3] Aoki I et al. *Magn. Reson. Med.* **48**, 927-933 (2002).

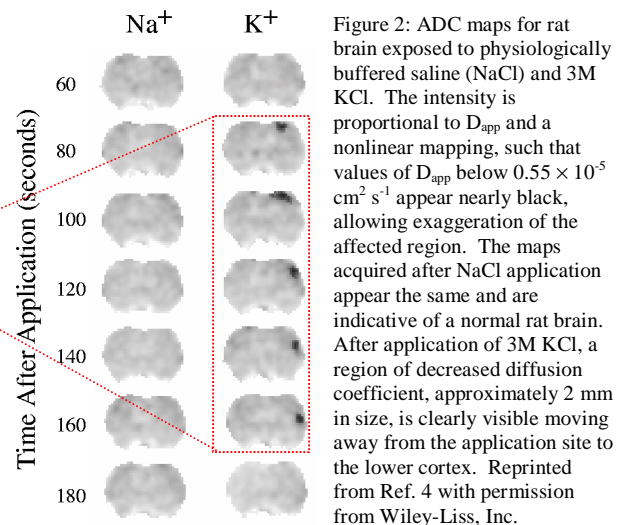


Figure 2: ADC maps for rat brain exposed to physiologically buffered saline (NaCl) and 3M KCl. The intensity is proportional to D_{app} and a nonlinear mapping, such that values of D_{app} below 0.55 \times 10⁻⁵ cm² s⁻¹ appear nearly black, allowing exaggeration of the affected region. The maps acquired after NaCl application appear the same and are indicative of a normal rat brain. After application of 3M KCl, a region of decreased diffusion coefficient, approximately 2 mm in size, is clearly visible moving away from the application site to the lower cortex. Reprinted from Ref. 4 with permission from Wiley-Liss, Inc.

- [2] Lin Y-J, Koretsky A. *Magn. Reson. Med.* **38**, 378-388 (1997).
[4] Latour LL et al. *Magn. Reson. Med.* **32**, 189-198 (1994).

Correlation of Tumor Growth Kinetics, Cell Kill, and Radiotherapeutic Response in a RIF-1 Tumor Model Using Multispectral Analysis

E. C. Henning¹, C. Azuma², C. H. Sotak^{1,3}, K. G. Helmer¹

¹Department of Biomedical Engineering, Worcester Polytechnic Institute, Worcester, MA, United States, ²Department of Clinical Sciences, Tufts University School of Veterinary Medicine, North Grafton, MA, United States, ³Department of Radiology, University of Massachusetts Medical School, Worcester, MA, United States

Introduction

Assessment of therapeutic efficacy is confounded by intra-tumor and inter-tumor heterogeneity. Variable pre-treatment tissue composition, tumor size, and growth kinetics, as well as post-treatment cell kill and tumor regrowth complicate dose-optimization and comparative treatment regimens in animal oncology studies. A multi-spectral (MS) analysis approach using ADC, T₂, and M₀ maps has been shown to aid in the differentiation between viable and necrotic tissue, as well as the identification of multiple compartments within necrotic tissue.¹ Here, we report on a single-dose radiotherapy study using RIF-1 tumors in which MS analysis, using k-means (KM) clustering, was used to identify multiple compartments in both viable and necrotic tissue. This methodology combined with the contributions of cell kill and tumor growth kinetics should provide a better understanding of the physiological dynamics of treated tumors.

Methods

Seven 6-8 week-old female C3H mice weighing 20-25g were anesthetized with an intraperitoneal injection of ketamine/xyzazine (100mg/kg:10mg/kg). All mice were inoculated with 1×10⁶ RIF-1 cells (0.15ml), delivered through a subcutaneous injection into the right hind leg. Tumors were allowed to develop for 3-4wks, yielding an approximate 1.0cc starting volume.

Data were acquired with a Bruker Biospin 2.0T/45cm imaging spectrometer operating at 85.56MHz for ¹H and equipped with ±20G/cm shielded gradients. Image acquisition was performed along the coronal plane [128×128, FOV=3cm, slices=8, slice thickness=1mm]. A DW-SE sequence was used to acquire the images at six b-values (15 → 760 s mm⁻²) with TR/TE=2000/53ms, δ=4ms, Δ=35ms, resulting in an effective diffusion time t_{diff}=33.7ms. A T₂W-SE sequence was used to acquire images at six echo times (12.2 → 90 ms) with TR=2000ms. Tumors were irradiated with 1000cGy at a rate of 300cGy/min (Siemens Mevatron 77, 6 MeV electrons, Tufts University Veterinary School of Medicine). Imaging was performed 1d pre-treatment, 5hr, 1d, 2d post-treatment, and every 2d thereafter until tumor doubling (maximum 10d post-treatment).

ADC, T₂, and M₀ parameter-maps were generated using routines written in IDL[®] (RSI, Boulder, CO). Tissue classification was performed using the k-means (KM) clustering algorithm. KM was applied to segment data into two regions each of viable tumor (V1,V2) and necrosis (N1,N2), and one region of adipose tissue. Growth kinetic calculations and cell kill were determined using an exponential model of tumor growth² and the mathematical model proposed by Ross *et al.*,³ respectively.

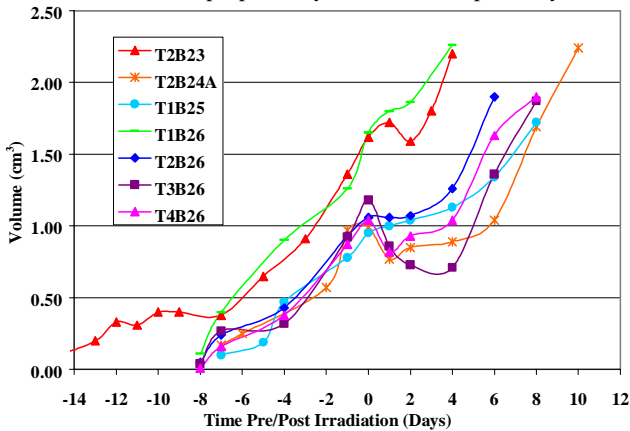


Fig.2: Plot of tumor growth on an animal-by-animal basis pre- and post-irradiation. Individual volumes were calculated from caliper measurements using the equation $V = (\pi/6) * (l * w * h)$ where l = length, w = width, and h = height.

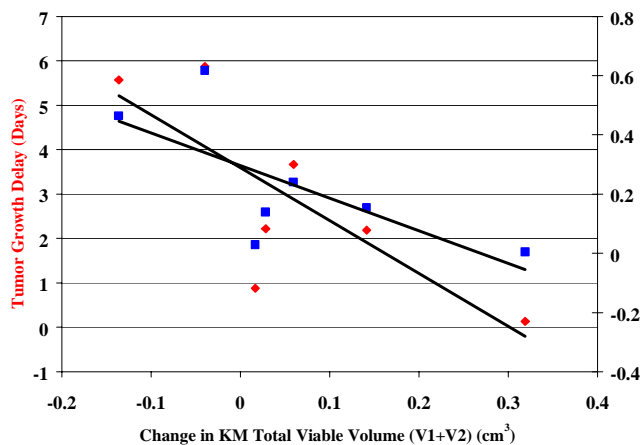


Fig.3: Plot of tumor growth delay and cell kill versus a change in KM viable volume. Volume changes were calculated based on the difference between pre-treatment V1+V2 and the minimum V1+V2 volume post-treatment on an animal-by-animal basis.

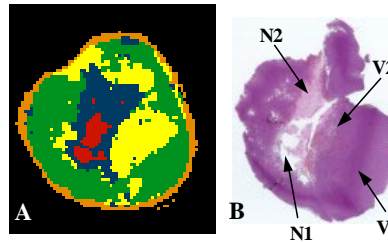


Fig.1: A multispectral (MS) image of a RIF-1 tumor. (A) KM map. (B) Hematoxylin-Eosin (H&E) Image. The map derived by k-means (A) depicts the segmentation of the tumor into two regions of viable tumor and two regions of necrosis. Tissue assignments are: Viable 1 (V1) = Green; Viable 2 (V2) = Yellow, Necrosis 1 = Red (N1); Necrosis 2 (N2) = Blue, Adipose Tissue = Orange.

Results

This method allows identification of tissue heterogeneity within viable tumor and necrosis. Fig.1 shows the cluster assignments for a representative RIF-1 tumor (Fig.1A) and the corresponding H&E image (Fig.1B) at 6d post-treatment. Fig.2 shows the tumor growth curves on an animal-by-animal basis pre- and post-irradiation. Fig.3 shows the correlation between the tumor growth delay (TGD), cell kill, and the change in KM total viable volume (V1+V2) pre-irradiation versus the minimum volume post-irradiation (1d or 2d post depending on the animal). There was a strong correlation between the change in V1+V2 and the resultant TGD (R = 0.78) and cell kill (R = 0.70). The relative contributions of pre-treatment V1 and V2 volumes versus post-treatment kinetic parameters were investigated. An increase in pre-treatment V1 correlated with a decrease in both TGD (R = 0.82) and cell kill (R = 0.83). There was no correlation between pre-treatment V2 volume and TGD or cell kill.

Discussion

These results suggest that V1 is well-oxygenated, radiosensitive tissue, while V2 is hypoxic, and therefore, radioresistant. The assignment of V1 and V2 will be validated using immunohistochemical (IHC) staining for hypoxic-inducible factor 1-alpha (HIF-1α). Since tumor oxygenation is a major factor for effective treatment and can be spatially heterogeneous across the tumor, MS methods should be helpful in monitoring the range of tissue viability as a function of time post-treatment.

References

- [1] Carano RAD et al. Magn Reson Med 2004;51:542-551.
- [2] Steele GG. Growth Kinetics of Tumors. Clarendon: Oxford; 1977.
- [3] Ross BD et al. Proc Natl Acad Sci 1998;95:7012-7017.

Investigation of Early ADC Changes in Response to Single Dose (1000cGy) Radiotherapy in a RIF-1 Tumor Model

E. C. Henning¹, C. Azuma², C. H. Sotak^{1,3}, K. G. Helmer¹

¹Department of Biomedical Engineering, Worcester Polytechnic Institute, Worcester, MA, United States, ²Department of Clinical Sciences, Tufts University School of Veterinary Medicine, North Grafton, MA, United States, ³Department of Radiology, University of Massachusetts Medical School, Worcester, MA, United States

Introduction

Previous studies employing diffusion MRI have shown that rapid changes in the apparent diffusion coefficient (ADC) following therapeutic intervention can indicate a positive therapeutic response.^{1,2} Although tissue ADCs are known to correlate with cell density, increased ADCs at early timepoints post-treatment may be the result of therapeutically-induced changes in ADC such as vasogenic edema. In order to understand the various contributions to the ADC response, we have performed multispectral (MS) analysis using ADC, T_2 and M_0 for subdivision of tissue into regions of viable tumor and necrosis. Tissue segmentation using this methodology provides insight into the various processes whose combination yield the total ADC response over time.

Methods

Seven 6-8 week-old female C3H mice weighing 20-25g were anesthetized with an intraperitoneal injection of ketamine/xyzilazine (100mg/kg:10mg/kg). All mice were inoculated with 1×10^6 RIF-1 cells (0.15ml), delivered through a subcutaneous injection into the right hind leg. Tumors were allowed to develop for 3-4wks, yielding an approximate 1.0cc starting volume.

Data were acquired with a Bruker Biospin 2.0T/45cm imaging spectrometer operating at 85.56MHz for ¹H and equipped with ± 20 G/cm self-shielded gradients. Image acquisition was performed along the coronal plane [128x128, FOV=3cm, slices=8, slice thickness=1mm]. A DW-SE sequence was used to acquire the images at six b-values (15 \rightarrow 760 s mm²) with TR/TE=2000/53ms, δ =4ms, Δ =35ms, resulting in an effective diffusion time t_{diff} =33.7ms. A T_2 -W-SE sequence was used to acquire images at six echo times (12.2 \rightarrow 90 ms) with TR=2000ms. Tumors were irradiated with 1000cGy at a rate of 300cGy/min (Siemens Mevatron 77, 6 MeV electrons, Tufts University Veterinary School of Medicine). Imaging was performed 1d pre-treatment, 5hr, 1d, 2d post-treatment, and every 2d thereafter until tumor doubling (maximum 10d post-treatment).

ADC, T_2 , and M_0 parameter-maps were generated using routines written in IDL[®] (RSI, Boulder, CO). Tissue classification was performed using the k-means (KM) clustering algorithm. KM was applied to segment data into two regions each of viable tumor (V1,V2) and necrosis (N1,N2), and one region of adipose tissue. Average ADC values were calculated on an animal-by-animal basis as well as for individual cluster volumes.

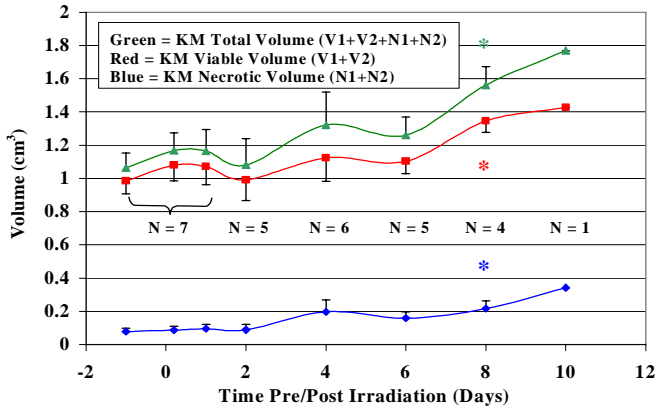


Fig.2: Plot of KM volumes versus time. Labels indicate the number of animals per timepoint. Error bars = SEM. Asterisks denote significance ($p < 0.05$), comparing each timepoint post-irradiation to pre-irradiation values.

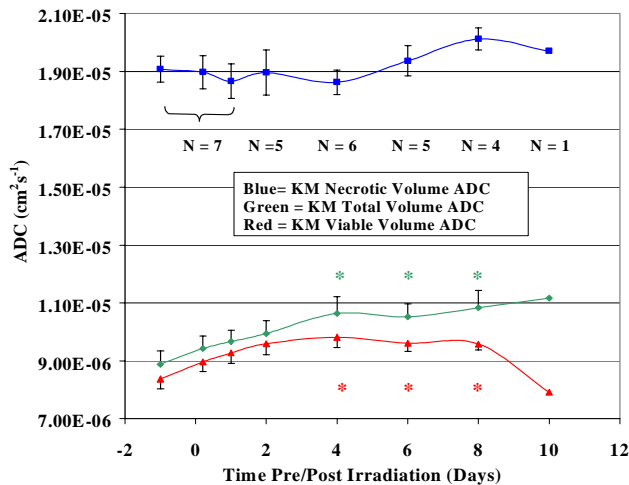


Fig.3: Plot of ADC values versus time. Error bars = SEM. Labels indicate number of animals per timepoint. Asterisks denote significance ($p < 0.05$), comparing each time point post-irradiation to pre-irradiation values.

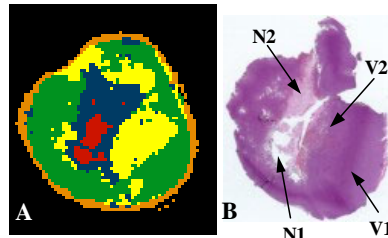


Figure 1: A multispectral (MS) image of a representative RIF-1 tumor. (A) KM map. (B) Hematoxylin-Eosin (H&E) Image. The map derived by k-means (A) depicts the segmentation of the tumor into two regions of viable tumor and two regions of necrosis. Tissue assignments are: Viable 1 (V1) = Green; Viable 2 (V2) = Yellow, Necrosis 1 (N1) = Red; Necrosis 2 (N2) = Blue, Adipose Tissue = Orange.

Results

Fig.1 shows the cluster assignments for a representative RIF-1 tumor (Fig.1A) and the corresponding H&E image (Fig.1B) at 6d post-treatment. Fig.2 shows the total viable (V1+V2) and necrotic (N1+N2) tumor volumes pre- and post-irradiation as determined by the KM algorithm. There was no significant change in KM total tumor volume (V1+V2+N1+N2) until after day 6. From day 8, there was a significant increase in viable and necrotic tissue, respectively. Fig.3 shows the temporal evolution of the ADC in each tissue classification as well as the total tumor ADC.

Discussion

The trend in increased total ADC prior to day 4 is consistent with previous observations, although the radiotherapy-induced ADC increase is less than values reported in studies using chemotherapy.^{1,2} An increase in ADC can result from an increase in the necrotic fraction of the tumor. However, the increase in necrosis is not observed here until after day 8 (Fig.2). In Fig.3, there is an increase in total ADC that occurs prior to the change in necrotic fraction. This trend is driven by the increase in viable tissue ADC; the necrotic tissue ADC remains constant over this period. In Fig.2, the viable tumor regrowth begins after day 6, with an increase in necrosis after day 8. Note that after the initial increase, the viable ADC becomes constant from days 2 – 8 until the point of viable tumor regrowth (day 8). The decrease in viable ADC at day 10 is consistent with an increase in cell density. These observations suggest that the early increase in total ADC is not due to a reduction in cell density, but instead may be a result of radiation-induced vasogenic edema.

References

- [1] Zhao M et al. Br J Cancer 1996;73:61-64.
- [2] Chenevert TL et al. J Natl Cancer Inst 2000;92:2029-2036.